NANOSTRUCTURES FOR BIOAPPLICATION AND TOXIC SPECIES REMEDIATION

By

JERINA MAJEED

CHEM01200904017

Bhabha Atomic Research Centre, Mumbai

A thesis submitted to the

Board of Studies in Chemical Sciences

In partial fulfillment of requirements

for the Degree of

DOCTOR OF PHILOSOPHY

of

HOMI BHABHA NATIONAL INSTITUTE

March 2015

Homi Bhabha National Institute[1]

Recommendations of the Viva Voce Committee

As members of the Viva Voce Committee, we certify that we have read the dissertation prepared by **Jerina Majeed** entitled "**Nanostructures For Bioapplication and Toxic Species Remediation**" and recommend that it may be accepted as fulfilling the thesis requirement for the award of Degree of Doctor of Philosophy.

Chairman: **Dr. D. Das** **Date:**

Guide / Convener: **Dr. A. K. Tyagi** **Date:**

Member 1: **Dr. B. N. Pandey** **Date:**

Member 2: **Dr. Jayshree Ramkumar** **Date:**

Member 3: **Dr. V. Sudarsan** **Date:**

Final approval and acceptance of this thesis is contingent upon the candidate's submission of the final copies of the thesis to HBNI.

I hereby certify that I have read this thesis prepared under my direction and recommend that it may be accepted as fulfilling the thesis requirement.

Date:

Place:

Dr. A. K. Tyagi
(Guide)

STATEMENT BY AUTHOR

This dissertation has been submitted in partial fulfillment of requirements for an advanced degree at Homi Bhabha National Institute (HBNI) and is deposited in the Library to be made available to borrowers under rules of the HBNI.

Brief quotations from this dissertation are allowable without special permission, provided that accurate acknowledgement of source is made. Requests for permission for extended quotation from or reproduction of this manuscript in whole or in part may be granted by the Competent Authority of HBNI when in his or her judgment the proposed use of the material is in the interests of scholarship. In all other instances, however, permission must be obtained from the author.

Jerina Majeed

DECLARATION

I, hereby declare that the investigation presented in the thesis has been carried out by me. The work is original and has not been submitted earlier as a whole or in part for a degree / diploma at this or any other Institution / University.

Jerina Majeed

List of Publications arising from the thesis

Journals

1. Water-dispersible polyphosphate-grafted Fe_3O_4 nanomagnets for cancer therapy
   Jerina Majeed, K. C. Barick, Neena G. Shetake, B. N. Pandey, P. A. Hassan and A. K. Tyagi
   RSC Adv., 2015, 5, 86754-86762.

2. Effect of synthesis protocol on the surface charge of Zinc oxide nanoparticles and its consequence on sorption ability
   Jerina Majeed, Jayshree Ramkumar, S. Chandramouleeswaran
   and A. K. Tyagi
   Sep. Sci. Tech. 2015, 50,404-410.

3. Highly Selective Uptake of Copper (II) Ions from aqueous media using nanosorbents in batch mode
   Jerina Majeed, Jayshree Ramkumar, S. Chandramouleeswaran
   and A. K. Tyagi
   Adv. Porous Mater. 2014, 2, 1-10.

4. Enhanced specific absorption rate in silanol functionalized Fe_3O_4 core - shell nanoparticles: study of Fe leaching in Fe_3O_4 and hyperthermia in L929 and HeLa cells
   Jerina Majeed, L. Pradhan, R. S. Ningthoujam, R. K. Vatsa, D. Bahadur
   and A.K. Tyagi
   Colloids and Surfaces B: Biointerface, 2014, 122, 396-403.

5. Facile synthesis of flower like FePt@ZnO core–shell structure and its bifunctional properties
   Jerina Majeed, O. D. Jayakumar, B. P. Mandal, H. G. Salunke, R. Naik
   and A.K. Tyagi
   J. Alloys Comp., 2014, 59, 95–100.

6. Effect of Mo incorporation in the TiO_2 lattice: A mechanistic basis for photocatalytic dye degradation
   K. Bhattacharyya, **Jerina Majeed**, K. K. Dey, P. Ayyub, A. K. Tyagi
   and S. R. Bharadwaj
   J. Phys. Chem. C, 2014, 118, 15946-15962.

7. Fe_3O_4@SiO_2 core-shell nanoparticles: Synthesis, characterization and application in environmental remediation
   Jerina Majeed, Jayshree Ramkumar, S. Chandramouleeswaran
   and A.K. Tyagi
   AIP Conf. Proc., 2014, 1591, 605-609.

8. Kinetic modeling: dependence of structural and sorption properties of ZnO—crucial role of synthesis
   Jerina Majeed, Jayshree Ramkumar, S. Chandramouleeswaran,
   O. D. Jayakumar and A.K. Tyagi

RSC Adv., 2013, 3, 3365-3373.

9. Magnetism in tetragonal and cubic phase of FePt
Jerina Majeed, O. D. Jayakumar, H. G. Salunke and A. K. Tyagi
AIP Conf. Proc., 2012, 1447, 1247-1248.

10. Direct synthesis of partially ordered tetragonally structured FePt nanoparticles by polyol method for biomedical application
Jerina Majeed, F. Sayed, O. D. Jayakumar, C. Sudakar and A. K. Tyagi
Int. J. Nano Dim. 2011, 2, 61-65.

Conferences

1. "Preparation and characterization of ZnO nanoparticles and their sorption studies for dye uptake"
Jerina Majeed, O. D. Jayakumar, J. Ramkumar, A. K. Tyagi
*International Conference on Recent Trends in Materials Science and Technology (**ICMST-2010**)*, October 29-31, 2010; Thiruvananthapuram, Kerala, India.

2. "Magnetism in tetragonal and cubic phase of FePt"
Jerina Majeed, O.D. Jayakumar, H.G. Salunke, A.K. Tyagi
56th DAE Solid State Physics Symposium, December 19-23, 2011; Tamil Nadu, India

3. "Flower Shaped Bifunctional FePt @ZnO core-shell Nanostructures: Synthesis, Magnetic and Luminescent Properties"
Jerina Majeed, O. D. Jayakumar, H.G. Salunke and A. K. Tyagi *Interdisciplinary Symposium for Material Chemistry (ISMC-2012)*, December 11–15, 2012, BARC, India.

4. "$Fe_3O_4@SiO_2$ Core-shell Nanoparticles: Synthesis, Characterization and Application in Environmental Remediation"
Jerina Majeed, Jayshree Ramkumar, S.Chandramouleeswaran,
and A. K. Tyagi
58th DAE-Solid State Physics Symposium-2013, December 17–21, 2013, Punjab, India.

5. "Zinc oxide nanoparticles: Applications for remediation of ground water system"
Jerina Majeed, Jayshree Ramkumar, S.Chandramouleeswaran, and A. K. Tyagi,"
DAE-BRNS Symposium on Emerging Trends in Separation Science and Technology (SESTEC-2014), February 25- 28, 2014, BARC, India.

Jerina Majeed

Dedicated to………

My Family

ACKNOWLEDGEMENTS

Firstly, I thank Almighty, the most merciful and gracious, for reasons too numerous to mention,

I would like to express my deepest gratitude to my guide, **Dr. A. K. Tyagi**, for his excellent guidance, care, patience, and providing me with an excellent atmosphere for doing research. He has been patient enough to bear my faults and the pressure to match the level of his expectations extracted out the quality and originality of this work.

I express heartwarming thanks to **Dr. T. Mukherjee**, Ex Director, Chemistry Group, BARC, for being a true representative for students, and my Doctoral committee members who have spent time to evaluate my yearly progress and gave valuable comments and positive suggestion throughout my PhD. I would also like to extend my thanks to Director, Chemistry Group, **Dr. B. N. Jagatap** and Head, Chemistry Division, **Dr. V. K. Jain** for their encouragement and support during my tenure in BARC. I am also thankful to **Department of Atomic Energy** for their financial support, without which none of the work would have been possible.

I would like to thank **Dr. Jayshree Ramkumar**, who spends her invaluable time channelizing my understanding in the field of water treatment and practical issues beyond the textbooks, patiently correcting my write-ups and manuscripts. I would like to express my sincere appreciations to **Dr. K. C. Barick** and **Dr. Raghumani** for their enlightening discussions on hyperthermia and drug delivery and their substantial help on surface functionalization of magnetic nanoparticles and other experiments.

I would also like to thank **Dr. O. D. Jayakumar**, for introducing me into the exciting world of synthetic chemistry and **Dr. B. P. Mandal** and **Dr. V. Grover** for their help and encouragement whenever required. I would also like to thank **Dr. S. J. Patwe**, for her care, affection and constant support. My thanks are due to **Mr. R. Shukla** for his valuable suggestions, motivations and help regarding both scientific and non-scientific matters. Other members of Solid State Chemistry Section whom I would like to acknowledge include: **Dr. S. N. Achary**, **Dr. M. Roy**, **Dr. A. Singhal** and **Dr D Dutta**. I am grateful to all my colleagues in the Chemistry Division who helped me in one way or another. I am also thankful to **Dr. M. R. Pai** and **Dr. A. M. Banerjee** for introducing me to the exciting world of research, during the M.Tech project I did with them.

Most of the results described in this thesis would not have been obtained without a healthy collaboration. I owe a great deal of appreciation and gratitude to **Prof. D. Bahadur** (IIT –Bombay) and **Ms. Lina** for their help in the bio experiments, **Dr. Salunke** for magnetic measurements, **Mr. Chandramouleeswaran** for ICP measurements, **Dr. B. N. Pandey** and **Ms. Neena** for cell viability studies. Thanks are also due to **Dr. V. Sudarsan** and **Dr. K. Bhattacharyya** for their guidance and friendly support during the project works I did with them. **Dr. R. K. Vatsa, Dr. S. R. Bharadwaj** and **Dr. P. A. Hassan** are thanked for allowing me to work in their labs and use the instrumental facilities available with them

I would like to thank **Vasundhara**, who as a good friend was always willing to help and give her best suggestions. It would have been a lonely lab without her. **Ms. Suman** is another name I'd be indebted to in many ways. Many thanks to **Farheen**, who haven around in any time of need not only as a senior and friend but more than like a sister, I owe a big thanks to her for making my staying away from family much easier for me by taking me on visits to her family. I also would like to extend my thanks to **Pooja**, **Mohsin**, **Anitha** and **Samatha** for their support and cheerful companionship. I would also like to thank the technical staff and office staff of the department **Ms. Aruna**, **Ms. Mani**, **Ms. Vishaka** and **Ms. Nisha** for their timely help in need

I would also like to thank my friends **Yusuf, Ahmed, Dileep, Vivek, Dinesh, Naidu, Shaguftha, Amresh, Siddarth, Shitaljeeth** and **Avishek** for their encouragement, being there and for providing exciting and fun filled environment during my research years. My research would not have been possible without their helps. I would also like to thank my longtime friends **Lekha**, **Shalini**, **Snehal**, **Arun**, **Sushant**, **Mhejabeen**, **Krishna** and **Prabath** for their help and for making my days in Mumbai fun. **Vinyan** and **Syari** are the other two names I shouldn't forget, who were there with me through my good and bad times, thanks guys for being there when I was in need.

Finally, I would thank my family for being my source of strength. Each word I have jotted out in this dissertation I owe it to my mother **Ms. Suhara Majeed**, who has nutured me to grow to a person I am, with her unconditional love and support throughout my life and for the sacrifices she have made to give me a brighter future. I can never thank enough my father, **Mr. Abdul Majeed**, for being there whenever I needed him. I would also like to thank my sister **Chinnu** and my brother **Jefry** along with my **parents in law, Mr Sainuddin** and **Ms Mariyam**, as well as **Tariq** and **Hiba** who encouraged and supported me during my studying far from home. Without their prayers, wholehearted support and continuous encouragement, I would have never been able to stand at this point in my life.

Also I try to put my thoughts for a very special and deserving person into words, **Hisham** to acknowledge in essence all the support, assurance and care I have received over these years. Thanks for being the true basis of my spirit, for all the sacrifices you have made for me, encouraging me to complete my studies and my regrets for all the time that I was not able to be with you.

Jerina Majeed

Contents

Page No.

Chapter 2: Experimental Techniques 36-75

SYNOPSIS

Conventionally nanoparticles having structural features in between those of atoms/molecules and bulk materials, are defined as the particles whose size at least in one dimension is less than 100 nm [1]. The unique physical and chemical properties of the nanomaterials compared to their bulk counterparts have attracted significant interest among researchers all over the world and has led to the birth of a new area of research and development, known as Nanoscience and Nanotechnology.

The larger surface-to-volume ratio of nanoparticles, compared to the conventional particles, plays an important role in different properties, which are surface sensitive. It has been amply demonstrated by now that the size and shape of the nanomaterials govern their physicochemical properties [1-3]. Synthesis of the nanomaterials and their characterization is an important and challenging activity that helps to develop nanomaterials of optimum size, shape and morphology coupled with desired properties for a specific application.

Accordingly, in the present thesis, in addition to the conventional co-precipitation synthesis, a number of other soft-chemical methods have been employed. This thesis has been focused on the uses of nanostructured oxides as adsorbents and catalysts, explicitly photocatalysts. Other applications involving magnetic materials for various therapeutic procedures are also summarized here. Thus, a prudent selection of the preparative techniques and fine-tuning of process parameters is required to obtain these important nanostructures with the desired properties.

The details of the introductory study material along with the results obtained for individual systems are presented in different chapters are summarized below.

Chapter 1: Introduction

This chapter provides a brief introduction to the history, different types and properties of nanomaterials. Various soft-chemical routes used to synthesize these nanomaterials are briefly described in this chapter. In particular, co-precipitation, sol-gel and combustion methods have been described. A detailed explanation of different steps involved in each synthesis method is presented. The important properties of the nanomaterials are also discussed briefly. The various applications explored within the title of this thesis are discussed in details along with the overview of the literature reports in the applicable areas.

Chapter 2: Experimental techniques

A concise description of the techniques used for the characterization of these materials, an outline to the theory and experimental setup used to investigate the sorption properties, as well as therapeutic properties of the above mentioned samples, are discussed in this chapter. The synthesis processes of various nanomaterials have also been discoursed in this chapter. The basic principle of various instrumental methods such as powder X-ray diffraction (XRD), Transmission Electron Microscopy (TEM), Scanning Electron Microscopy (SEM), Thermogravimetry-Differential thermal analysis (TG-DTA), Fourier Transmission Infrared Spectroscopy (FT-IR), X-ray Photoelectron Spectroscopy (XPS) and Raman Spectroscopy have been discussed in details.

The rapid industrialization and its ensuing by-products have adversely affected the environment by instigating hazardous wastes and poisonous gases being released to the environment. In order to detoxify their effects, various techniques like photocatalytic oxidation, chemical coagulants, electrochemical, bioremediation, ion-exchange resins, reverse osmosis and adsorption have been employed [4-7]. The core issue of such technology is to devise materials that can absorb these ions irreversibly, selectively, efficiently and in large quantities from contaminated sources such as water. Currently, available sorbents such as activated alumina, zeolite, activated carbon, and silica gel cannot fulfill the task of safe disposal. Hence, new and better sorbents are required to meet the challenges. Nano-based adsorbents are the most convenient technologies for removal of pollutants from the aqueous system [8-11]. Thus in chapter 3-6, various sorbent materials and their modifications have been discussed for the removal of some of these toxic species from water.

Chapter 3: ZnO- based nano sorbents

This chapter elucidates the possibility of fine tuning the surface charge by changing the synthesis protocol for the ZnO nanoparticles (ZnO NPs) and in-turn its efficiency as sorbents for removal of various cationic and anionic toxic species was found to improve. ZnO NPs synthesized by different procedures like pyrolysis, gel-combustion and co-precipitation, were characterized in details and their sorption characteristics with respect to different toxic species were studied. The main aim of this study was to bring out the changes on the surface charge of nanoparticles by adopting different synthetic protocols. The ZnO NPs synthesized by two different routes namely pyrolysis and gel combustion results in particles with different physical characteristics such as positive surface charge as compared to the nanoparticles synthesized by co-precipitation method having negative surface charge, thus considerably affecting the sorption properties. The co-precipitation method resulted in ZnO NPs possessing a negative charge and it was tested for sorption of transition metal ion. The adsorbent could be recycled up to five cycles without a significant decrease in its adsorption capacity. Considering the simple synthesis procedure, environmental friendliness, high sorption capability and good regeneration performance of ZnO NPs, it is expected that these nanoparticles have potential application in the sorption and pre-concentration of heavy metal ions and chromates from aqueous system.

Apart from all these advantages, ZnO NPs have a major disadvantage of dissolution in acidic condition. Further, to overcome these drawbacks, in the following chapter the ZnO NPs were stabilized by coating with various functional groups like thiol and silica.

Chapter 4: Surface functionalized ZnO nanoparticles

In order to overcome the poor stability in acidic conditions and to further improve specific physical, chemical and surface properties that allow the selective removal of toxic ions, ZnO-composite nanoparticles were designed. In view of these possibilities, the surface functionalization of ZnO NPs was done using a cost-effective simple one pot co-precipitation method, followed by a facile ligand introduction to bind readily available high affinity ligands onto the nanoparticle surface. This technique allows for tailoring of the surface chemistry to impart the specificity and affinity towards the target analytes (heavy metals of environmental concern).

Thiol and mercapto surface modified ZnO NPs were shown to be highly effective and selective sorbent materials. In present thesis, ZnO-nanocomposites with varying surface functionalities were synthesized, using the appropriate ligand moieties under simple laboratory conditions. The surface functionalization was confirmed by the results of various techniques like IR, TGA, BET surface area and elemental analysis. The efficiency of these nanocomposites for the removal of various heavy metal ions especially Hg(II) and Pb(II) was tested, in a batch mode. The effect of initial metal ions concentration and contact time were also investigated. Different sorption and kinetic isotherm models were fitted using the experimental data. Kinetic modeling analysis, done by fitting the data in the pseudo-first- order and pseudo-second-order, indicated that the pseudo second order equation is the most suitable model for explaining sorption mechanism of metal ions onto the composites, indicating that the adsorption mechanism depends on the adsorbate and adsorbent. Equilibrium data were found to be represented well by the Freundlich isotherm equation, for all the cases suggesting the existence of heterogeneous conditions. The effect of the interfering ions (transition metal ions) on the sorption of Hg(II) and Pb (II) ions was also evaluated with the interfering ions concentration of 10 mg/L, which indicated that there was no interference with the maximum adsorption capacity for Hg(II) and Pb(II) for thiol functionalized nanoparticles.

These sorbents apart from being highly efficient and selective still have the problem of dissolution in highly acidic or alkaline pH. To circumvent these limitations, it was crucial to look for a sorbent stable in diverse pH range.

Chapter 5: $CeVO_4$ based adsorbent

The framework compounds like vanadates and phosphates are known to show good sorption capacities, and to the best of our knowledge, this cerium vanadomolybdate system has not been explored as sorbents. Hence, it was attempted to explore the sorption of unwanted, highly toxic Pb(II) ions from aqueous solutions. In view of this, Chapter 5 endeavours to explore the synthesis of Mo substituted $CeVO_4$ [$Ce(V_{1-x}Mo_x)O_4$ ($0.0 \leq x \leq 0.4$)] nanoparticle, by a simple co-precipitation synthesis. An exhaustive study which probes the solid solution formation mechanism based on X-ray diffraction and spectroscopic techniques like Raman and X-ray photoelectron spectroscopy is presented, which quite evidently supported the formation of substitutional solid solutions by replacement of V by Mo in

$CeVO_4$. The sorption behaviour of these nanoparticles was shown to have tremendous dependence on their morphology. Thus, in order to understand morphology of Mo substituted nanoparticles, the samples were subjected to microscopic studies, which divulged the formation of self-aggregated highly porous 3D spherical structures and the BET surface analysis divulged the mesoporous nature of the sample. This entails investigating their sorption capacities for Pb(II) in batch mode and modeling of sorption and kinetic isotherms. Kinetic studies indicated that $CeVO_4$ could show fast uptake of Pb(II), with 100% uptake achieved in 1 h while the Mo-substituted $CeVO_4$ could depict the same uptake in less than 10 min. Kinetic modeling analysis, done by fitting the data in the pseudo-first-order and pseudo second-order, indicated that the pseudo second order equation is the most suitable model for explaining sorption mechanism of metal ions onto the composites, suggesting chemisorption process as the rate limiting step.

The stability of the sorbent further led us to think about the main problem associated with nanosorbents, recyclability from the aqueous solution due to their smaller particle size and superior dispersive properties. Comparing usual separation methods, including filtration and centrifugation which are time consuming steps and may often lead to loss of the sorbent, magnetic sorbents can be easily and rapidly separated from aqueous solutions using an external magnetic field and regenerated to be used for multiple cycles, thus making it a cost effective sorption method. The next chapter focuses on exploration of magnetic nano- sorbents.

Chapter 6: Magnetic nano-sorbents

This chapter deals with the synthesis, characterization and sorption property evaluation of composites of Fe_3O_4-SiO_2 (SMNPs) with respect to transition metal ions and cationic dyes like methylene blue. The magnetic nanoparticles were prepared and characterized extensively using various techniques like XRD, TEM, IR and BET surface area analysis. The superior magnetic responsivity of the Fe_3O_4 core, aids in easier and faster removal of the sorbent from its aqueous solution using an external magnet as compared to the non-magnetic sorbents. XRD analysis confirms the formation of highly crystalline single phasic structure of Fe_3O_4 with an average crystallite size of ~ 9 nm. The surface modification by the silanol moieties on to the magnetic nanoparticle (MNP) surface was successful as shown from the IR spectra and BET surface area analysis steered to the predominance of 3D network of mesopores. The sorption studies were done at room temperature and near neutral conditions of solution pH. Various experimental aspects were tuned to get optimum conditions to achieve the maximum uptake. The effect of initial metal ion concentration on uptake was studied by varying the concentration between 1-10 mg/L. The sorbent was found to be efficient in removing the toxic metal ions within 30 min of equilibration, whereas; methylene blue was removed within 10 min. The experimentally obtained values of maximum uptake capacity for the different transition metal ions were found to be in the order Co(II) < Ni(II) < Cu(II) <

Zn(II). Concomitantly, different sorption and kinetic isotherm models were fitted using the experimental data. The uptake process was found to be thermodynamically as well as kinetically favorable, and the extensive modeling of data showed that maximum adsorption capacity 115 mg/g and 233 mg/g for Zn(II) ions and methylene blue, respectively, which is in agreement with experimental values and the chemisorption nature of uptake.

Chapter 7: Photocatalytic materials

In the present thesis, attempts have also been made to prepare the nanocrystalline photocatalytic material for degradation of organic contaminants. In this chapter, it has been shown that the photocatalytic properties of anatase TiO_2 under visible light are enhanced by substitutional doping of Mo in the TiO_2 lattice, simultaneously with the presence of a nano dispersed MoO_3. The effect of doping content on the composition, crystallinity, phase and surface morphology were investigated by XRD, TEM, DRS, Raman and XPS techniques. The photocatalytic activity was correlated with several parameters such as the oxidation state, bandgap, surface species, *etc*. The photocatalysis experiments were conducted using a model Rhodamine B (Rh-B) dye and a mechanistic understanding of the photocatalytic degradation of the Rh-B dye with its adsorption properties is described. The usually observed de- alkylation step is completely absent in this case and photo-degradation occurs through other mechanism. Different molecular intermediates involved in the Rh-B photo-degradation are identified by NMR spectroscopy and the structural attributions leading to such a mechanism are discussed. The nanoparticles showed good photocatalytic activity towards degradation of Rh-B dye. These nanoparticles can be further used for degradation of other dyes and removal of toxic metals, such as arsenic.

In the first part of the thesis the environmental applications of nanoparticles have been discussed. In subsequent second part the bio applications of various nanoparticles studied are discussed.

Chapter 8: Silica coated nanoparticles for hyperthemia based treatment

The silica coated magnetic nanoparticles have been synthesized and evaluated for their sorption efficiencies in the earlier part of this thesis. While in this chapter, the strategy to improve the efficacy of the magnetic nanoparticles (MNPs) for hyperthermia treatment has been discussed. The optimization of the surface coating thickness using biocompatible moiety silica (SiO_2), which on encapsulating the magnetite crystal yields a unique magnetic responsivity. Formation of highly crystalline single-phase Fe_3O_4 nanostructures was revealed from XRD as well as TEM analysis and FTIR spectra clearly indicates the presence of SiO_2 coating on MNPs. Induction heating experiments induce the remarkable self-heating efficiency of these MNPs under external AC magnetic field. The temperature achieved by silica coated MNPs is higher than that by uncoated MNPs. It is found that the Specific Absorption Rate (SAR) value decreases with increase in shell thickness. The chemical stability of these samples is analyzed by leaching experiments at pH 2–7. The silica coated samples are stable up to 7 days even at pH 2. Biocompatibility of the MNPs is evaluated *in vitro* by assessing their cytotoxicity on L929 and human cervical cancer cells (HeLa cells) using Sulfo Rhodamine-B assay. Their hyperthermic killing ability is also evaluated in HeLa cells using the same method. Cells treated with MNPs along with induction heating show decrease in viability as compared to that without induction heating. Further, cell death is found to be -55% more in cells treated with silica coated MNPs under induction heating as compared to untreated control.

Chapter 9: Polyphosphate grafted nanomagnet for therapeutic applications

This chapter entails the synthesis of novel polyphosphate grafted Fe_3O_4 nanomagnets (PPNM), for doxorubicin (DOX) delivery through a pH-labile linkage between DOX and polyphosphate. The developed PPNMs showed high colloidal stability, magnetic responsivity

and specific absorption rate. In addition to synthesis and detailed characterization, the drug release profile and *in vitro* biomedical assessment of the PPNM are also addressed in this chapter. As PPNM is water-soluble, it can directly serve as nanotherapeutics for sustained DOX delivery without the assistance of external reagents, it may potentially be more relevant to clinical applications in cancer treatment.

Chapter 10: Luminescent-magnetic materials

Furthermore in this thesis an attempt has been made to synthesise a luminescent-magnetic material. A soft chemical method of preparing fct phased FePt from FCC phased FePt nanoparticles at low temperature has been developed using PVP as a protective agent. The preliminary results suggest that, in addition to unique functional properties, these nanomaterials also show typical nano-bio interactions leading to varied toxicity characteristics. Flower shaped FePt and ZnO coated FePt with core-shell nanostructures are synthesized by a facile solvothermal procedure. Two different compositions (molar ratio) of FePt and ZnO (FePt : ZnO = 1:3 and

FePt : ZnO = 1:6) were synthesized by varying FePt concentration with respect to ZnO, thereby changing the ZnO shell thickness. Core-shell structure with lower FePt concentration (FePt: ZnO = 1:6) exhibited bifunctionality such as near room temperature ferromagnetism and photoluminescence. However, attempts to make FePt coated ZnO core-shells by a similar method resulted in the formation of luminescent and superparamagnetic ZnO nanorods decorated with FePt nanoparticles.

Chapter 11: Summary and future scope

The last chapter of this thesis provides a brief summary of the work done and its significance. Synthesis and characterization of several nanostructures along with their plausible applications in the environmental as well as bio-application were reported.

In the first part of the work, various low cost adsorbent materials were synthesized and evaluated for their sorption efficiencies. Various limitations faced in each step were addressed and circumvented. Design of a highly effective, stable and cost effective nanosorbent is reported in this thesis. Whilst, in later part efforts were made to address concerns like colloidal stability, biocompatibility and surface functionalities of magnetic nanoparticles for therapeutic applications.

Along with the summary of the works done, future scopes have also been listed.

References

1. C. Burda, X. Chen, R. Narayanan and M. A. El-Sayed, *Chem. Rev.*, 2005, 105, 1025- 1102.
2. N. M. Dimitrijevic, Z. V. Saponjic, B. M. Rabatic, O. G. Poluektov and T. Rajh, *J. Phys. Chem. C*, 2007, 111, 14597-14601.
3. T. Vossmeyer, L. Katsikas, M. Giersig, I. G. Popovic, K. Diesner, A.

Chemseddine, A. Eychmuller and H. Weller, *J. Phys. Chem.*, 1994, 98, 7665-7673.

4. F. Lu, W. Cai and Y. Zhang, *Adv. Funct. Mater.*, 2008, 18, 1047-1056.
5. J. Y. Choi, D. S. Kim and J. Y. Lim, *J. Environ. Sci. Health A, Tox./Hazard. Subst. Environ. Eng.*, 2006, 41, 1155-1172.
6. C. E. Harland, *Ion Exchange: Theory and Practice*, Royal Society of Chemistry, 1997.
7. Z. M. Payne, K, M. Lamichhane, R. W. Babcock and S. J. Turnbull, *Environmental Science: Processes & Impacts*, 2013, 11, 2023-2029.
8. M. Hua, S. Zhang, B. Pan, W. Zhang, L. Lv and Q. Zhang, *J. Hazard. Mater.*, 2012, 211–212, 317-331.
9. K. Y. Kumar, H. B. Muralidhara, Y. A. Nayaka, J. Balasubramanyam and H. Hanumanthappa, *Powder Technology*, 246 125-136.
10. M. M. Khin, A. S. Nair, V. J. Babu, R. Murugan and S. Ramakrishna, *Energy Environ. Sci.*, 2012, 5, 8075-8109.
11. P. Wang and M. C. L. Irene, *Water Res.*, 2009, 43, 3727-3734.

LIST OF FIGURES

LIST OF TABLES

LIST OF ABBREVIATIONS

AC	alternating current
AMF	alternating magnetic field
BET	Brunauer-Emmett-Teller
CNT	carbon nano tubes
CS	Chitosan
CV	$CeVO_4$
CVM-4	40% Mo doped $CeVO_4$
DLS	dynamic light scattering
DOX	Doxorubicin
DOX-PPNMS	dox conjugated PPNMs
DTA	differential thermal analysis
ED	eddy current
EG	ethylene glycol
f	Frequency
FC	field cooled
FePt NFs	FePt nanoflowers
FePt NPs	FePt nanoparticle
FePt -ZNRs	FePt decorated ZnO nanorods
FePt-ZNFs	ZnO coated FePt nanoflowers
FT-IR	fourier transform infrared
H	magnetic field
h k l	Planes
Hc	Coercivity
HeLa cells	human cervical cancer cells
HRTEM	high-resolution transmission electron microscopy
ICP-AES	induction coupled plasma -atomic emission spectroscopy
ILP	intrinsic loss power
IPA	iso-propanol
L929	primary fibroblast

M	Magnetization
MB	methylene blue
MFM	magnetic fluid hyperthermia
M-H	magnetization versus applied magnetic field
MNPs	magnetic nanoparticles
MO	methyl orange
Mo-1	1% Mo doped TiO_2
Mo-2	2% Mo doped TiO_2
MRI	magnetic resonance imaging
M-T	magnetization versus temperature
MTT	3-(4,5-dimethyl thiazol-2-yl)-2,5-diphenyl tetrazolium bromide
NMR	nuclear magnetic resonance
NPs	Nanoparticles
OA	oleic acid
PAMP	phosphate anchored magnetic nanoparticle
PBS	phosphate buffered saline
PEG	polyethylene glycol
PEO	polyethylene oxide
PPNMs	polyphosphtate grafted nanomagnets
QD	quantum dots
Rh-B	rhodamine B
SAED	selected-area electron diffraction
SAR	specific absorption rate
SHMP	sodium hexa meta phosphate
SMNPs	silane functionalized magnetic nanoparticles
SPIO	superparamagnetic iron oxide
SQUID	superconducting quantum interference device
SRB	sulforhodamine assay
STTP	sodium tripolyphosphate
S-ZNPs	silica capped ZnO nanoparticles
TFS-ZNPs	thiol functionalized silica capped ZnO nanoparticles
TGA	thermogravimetric analysis

TU-ZNPs	thiourea capped ZnO nanoparticles
VSM	vibrating sample magnetometer
XRD	x-ray diffraction
ZFC	zero field cooled
ZnO-CP	ZnO nanoparticles prepared by precipitation method
ZnO-GC	ZnO nanoparticles prepared by combustion method
ZnO-PY	ZnO nanoparticles prepared by pyrolysis method
ZNPs	ZnO nanoparticles

Chapter 1

Introduction

1.1. Introduction

Nanoscience and technology is a broad and interdisciplinary area of research and development with extensive growth in the past few years. It has the potential to revolutionize the ways in which materials are created as well as to introduce variable range of functionalities. In general, nanotechnology can be understood as a technology of design, fabrication and applications of nanostructures and nanomaterials, in view of their fundamental understanding of physical properties and phenomena [1, 2]. Compared to bulk materials nanomaterials, scale from individual atom or molecule to submicron entity at least with one dimension in the range of 1 to 100 nm and have found significant roles in applications in physical, chemical and biological applications.

1.2. History of nanomaterials

The history of nanomaterials can be traced back to shortly after the big bang when nanostructures were formed in the early meteorites. Many other Nanostructures like seashells, skeletons, etc. were evolved later in nature. The scientific journey of these materials however began much later. One of the first scientific reports is the synthesis of colloidal gold particles by Michael Faraday in as early as 1857 [3]. Nanostructured catalysts have also been investigated for over 70 years. In USA and Germany, precipitated and fumed silica nanoparticles were manufactured and sold as substitutes for ultrafine carbon black for rubber reinforcements from as early as 1940s [4]. The quiet inert gas evaporation technique, for the production of nanocrystals was first reported by Granqvist and Buhrman in 1976 [5]. It is only recently that the Maya blue paint of the ancient Aztec and Maya cultures was found to be a nanostructured hybrid material containing silica and metal oxide nanocrystals [6]. The origin of its color and its resistance to acids and bio corrosion are still not fully understood but fabrication of synthetic samples has shown that the beautiful tone of the blue colour is due to the presence of nanoparticles and superlattice both.

Today, nanophase engineering has expanded on an immense scale of structural and functional materials; both inorganic and organic allowing to finetune desired electric, magnetic, mechanical, catalytic, optical or electronic functions.

1.3. Different from bulk?

The most important query is *why nanostructures are distinguished with superior properties than bulk materials?* The main apparent difference between bulk and nano material lies in the magnitude of dimensionality. This as mentioned earlier can broadly be distinguished as:

- ✓ First the size effect, in particular the quantum size effects, where the classic bulk electronic structure is disintegrated into a series of discrete electronic levels,
- ✓ Second, the surface or interface induced effect, which is important because of the enormously increased surface active sites.

While the size effect is mainly considered to describe physical properties, the surface or interface induced effect plays an eminent role in chemical activity, in particular in connection with catalysis. Experimental evidence of the quantum size effect in smaller particles has been provided by different methods, while the surface induced effect could be confirmed by measuring thermodynamic properties like vapour pressure, specific heat, thermal conductivity and melting point.

1.4. Classification of nanomaterials:

Nanomaterials can be classified into various classes depending upon their morphology as well as dimensionality:

Morphological characteristics considered are flatness, sphericity, and aspect ratio. Nanoparticles can attain diverse morphologies, as a result of templating/directing agent present, and also the solubility product of reactant and products involved in the synthesis. These morphologies sometimes can be guided through the inherent orientation of crystallographic planes, giving faceted morphology. These particles are named after the real world shapes they resemble, like nano-rods, nano-bar, nano-flowers, nano-needles, nano-fibres, nano-reefs, nano-boxes and many more. A general classification exists between high- and low-aspect ratio particles (**Figure 1.1**).

Amorphous particles are usually seen to adopt a sherical shape to satisfy their microstructural isotropy, while the shape of anisotropic microcrystalline particles relates to their particular crystal habit.

Based on dimensionality of materials (**Figure 1.1**), nanomaterials are classified as: Zero-dimensional (0D), One-dimensional (1D), Two-dimensional (2D) and Three-dimensional (3D) nanostructures

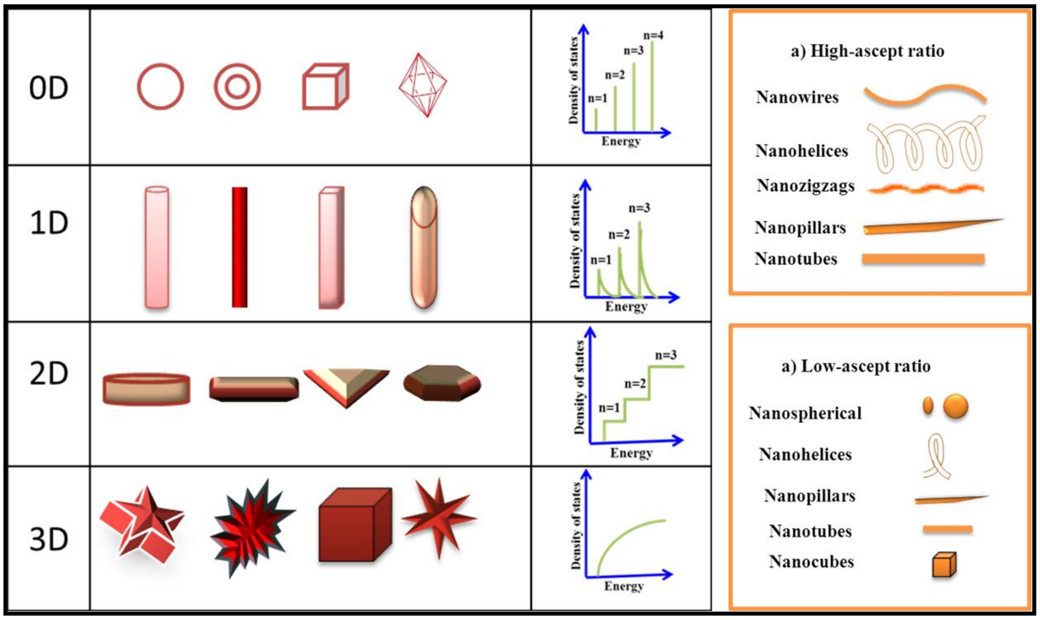

Figure 1.1: Schematics showing the classification of nanostructured materials based on their dimensionality and morphology.

1.5. Availability of nanomaterials

Like bulk materials, they can also be classified as: naturally occurring (metal oxides and metal sulfides commonly found as minerals) and engineered. Synthetically modified nanoparticles are called engineered nanoparticles. Recently, four different types of engineered nanoparticles are being investigated for their excellent properties. They are carbon-based (fullerene, nanotube, and graphene), metal based (nano and quantum dots of both metal and metal oxides), dendrimers (constructed from pieces of different nano molecules called nanopolymers) and composites (mixtures of nanoparticles or nanoparticles linked to larger, bulk-materials).

Many of these metal based nanomaterials such as metal oxides (ZnO, TiO_2), metal vanadate ($CeVO_4$), magnetic nanoparticles (Fe_3O_4, FePt), and composites (ZnO@FePt) are of great significance for different applications. Under the title of the present thesis some of these nanomaterials are discussed in detail.

1.5.1. Metal oxides

Metal oxide nanoparticles are an important class of nanomaterials by virtue of their optical, magnetic, and electronic properties [7, 8]. These properties make them potential candidate for a wide range of applications such as in sorption, catalysts, sensors, optical materials, electrical materials, and magnetic storage [7, 9-19]. Also, over about past half-decade, research in nano metal oxides has attracted considerable attention due to their unique and innovative applications in optical, biomedical as well as environmental and energy related applications. Metal oxides can be semiconductors or insulators depending on their band-gap nature and values. The most widely studied metal oxides are, ZnO and TiO_2 due to their potential wide ranging applications [20-36].

1.5.1.1. Zinc oxide (ZnO)

In addition to being inexpensive, relatively abundant, chemically stable, easy to prepare and non-toxic nature zinc oxide nanoparticle has tremendous scientific and technological interest owing to its multi-functionality. The direct wide band gap energy of 3.37 eV makes it an excellent candidate for short wavelength optoelectronic devices like UV-light-emitting diodes (LEDs), lasers, and transparent transistors [37-41].

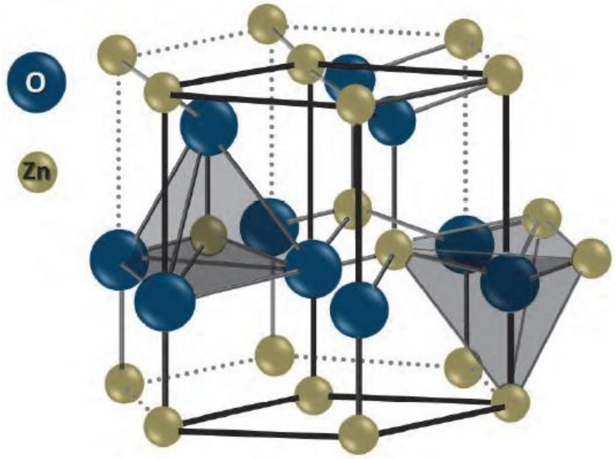

Figure 1.2: The hexagonal structure of ZnO. One unit cell outlined for clarity.

Nano-sized ZnO has been used in electrical [27, 42, 43], optical devices [42-44] and also as catalysts for the photo-catalytic degradation [12, 45]. The most stable crystal structure of ZnO is the hexagonal wurtzite type structure with space group $P6_3mc$ (**Figure 1.2**), in which each Zn^{2+} ion is surrounded by tetrahedra of O^{2-} ions, and vice-versa [46]. Furthermore, ZnO is biocompatible and relatively non-toxic and hence can be used for biomedical and various industrial applications such as adsorption, catalysis and photocatalytic degradation of environmental pollutants from water. Wang et al. [47, 48] demonstrated the higher efficiency of porous ZnO nano-plates and hollow microspheres with exposed porous nanosheets in the removal of Cu (II) from contaminated water. Singh et al. [49] reported on the removal of various toxic metal ions, such as Co^{2+}, Ni^{2+}, Cu^{2+}, Cd^{2+}, Pb^{2+}, Hg^{2+} and As^{3+} from wastewater by porous ZnO nano-assemblies. Ma et al. [50] and Zhai et al. [51] have reported on the photocatalytic activity of ZnO nanorod arrays on arbitrary substrates and ZnO nano-disks for methyl orange (MO) degradation.

Zheng et al. [52] investigated the photocatalytic activity of octahedron and rod-like porous ZnO architectures for the degradation of MO in water under UV light irradiation.

1.5.1.2.Titanium dioxide (TiO_2)

Titanium oxide is another metal oxide with remakably growing interest due to its exceptional electronic properties, combined with the possibility of engineering resulting into high surface area. Similar to ZnO, TiO_2 has band gap energy (3.2 eV) and is a cost effective material [35]. Brookite, rutile, and anatase are the three common crystalline polymorphs of TiO_2, of which rutile and anatase are the most commonly available forms. The structure of rutile and anatase is described in terms of TiO_6 octahedra as follows (**Figure 1.3**).

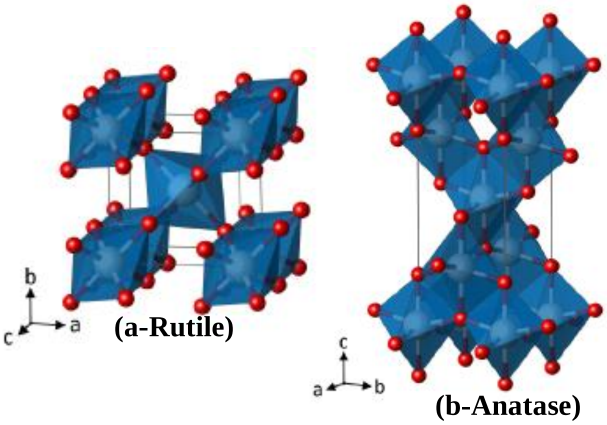

(a-Rutile)

(b-Anatase)

Figure 1.3: TiO_6 polyhedra for the TiO_2 phases rutile (a), and anatase (b) (Ti (white); O (red)) [53].

Each Ti^{4+} ion is surrounded by an octahedron of six O^{2-} ions. In rutile structure, each octahedron is in contact with ten neighboring octahedrons while in anatase structure each octahedron is in contact with eight neighbors. It can be manipulated by a wide spectrum of techniques and tuned into a broad range of morphologies: spherical particles, wires, rods, tubes and ultrathin films. It has various applications such as cosmetic, paper, medical device, coating, and gas sensor [54-62].

Parida et al. [63] have examined the removal of Cr (VI) by TiO_2-immobilized mesoporous MCM-41. Luo et al. [64] have also demonstrated the high absorption capacity, recovery and reuse of TiO_2 nanoparticles for the removal of As (III) from copper smelting wastewater. Pang et al. [65] have demonstrated that Fe-doped TiO_2 nanotubes are an efficient candidate for the purification of real textile wastewater containing a mixture of organic dyes. Yu et al. [66] have reported on the complete photodegradation of MB after 120 min by carbon self-doped TiO_2 sheets under visible light. Ju et al. [67] have also observed a higher catalytic activity of 3% for N- and S-doped TiO_2 nanoparticles in the degradation of MO at pH 4 under sunshine irradiation.

1.5.2. Metal vanadates:

Recently, nanostructured rare-earth orthovanadates (RVO_4), an important class of inorganic materials, have been investigated due to their unusual physical properties. These exhibit two structural types viz. tetragonal zircon-type [68] and monoclinic monazite-type structures [69]. The tetragonal structure belongs to space group $I4_1/amd$ (Z= 4) and consists of alternating edge-sharing AO_8 dodecahedra and VO_4 tetrahedra extending parallel to c-axis. The chains are joined by edge-sharing AO_8 dodecahedra along the a-axis.

Cerium (III) orthovanadate ($CeVO_4$), a common orthovanadate, which according to phase diagrams is located at the boundary of zircon and monazite types. It exhibits three polymorphic forms with the pseudo-octahedral -like structure of tetragonal scheelite in addition to the known zircon (**Figure 1.4**) and monazite forms.

This tetragonal zircon-type structure stabilizes Ce^{3+}cations even in an oxidizing condition [70]. The compound exhibits unique electronic [71-73], optical [71-75], magnetic [71-75], catalytic [74, 75] and luminescent [74, 75] properties. It exhibits wide potential application in various fields, such as oxidative catalyst [70, 74, 76, 77], gas sensors [72, 76, 78], luminescence (LED) [72, 75], electrochromic material [74, 77] and components for Solid Oxide Fuel Cells (SOFCs) [76-78].

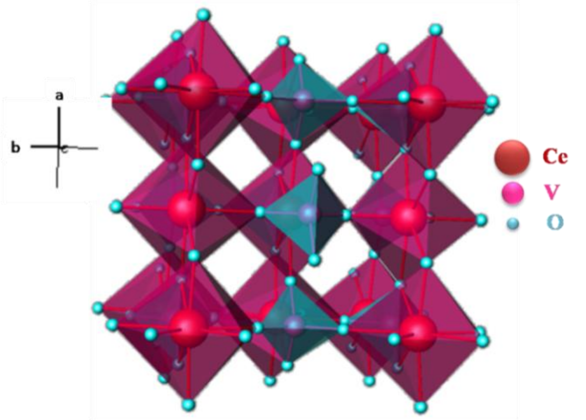

Figure 1.4: Schematic view of the zircon structure with CeO_8 dodecahedra and VO_4 tetrahedra. Red solid spheres correspond to Ce atoms; Blue solid spheres correspond to O atoms, and pink solid spheres correspond to V atoms. The different polyhedra are illustrated.

Mahapatra et.al [74] synthesized $CeVO_4$ under microwave exposure, and their efficiencies for photocatalytic degradation of various dyes and organics were compared. Chen et al., have studied the ethanol sensing properties of hydrothermal synthesized $CeVO_4$ and $CeVO_4$-CeO_2 systems [79]. Tsipis et al. [80] have studied the ionic and p-type electronic transport properties of zircon type $Ce_{1-x}A_xVO_{4\pm\delta}$ systems. Li et al. [81] have studied the selective oxidation of H_2S on rare earth orthovanadates and found that $CeVO_4$ show highest sulphur yield.

1.5.3. Magnetic nanoparticles:

Magnetic materials play an important role in the advancement of industrial and scientific growth due to their unique properties and potential applications in wide range of disciplines, including magnetic fluids [82-85], catalysis [86-90], biotechnology/biomedicine [91, 92], magnetic resonance imaging [93-97], data storage [98], and environmental remediation [99-102]. The magnetic properties of nanostructures are governed by various factors like composition, shape, size, surface morphology, anisotropy and molecular interactions.

In bulk magnetic materials, each particle is composed of multi domains separated by walls and each domain represents a region with a particular direction of magnetization. While in the case of nanomagnetic materials, each particle has a single domain [103].

In larger particles (micrometre size), surrounding thermal energy [kT, where k is Boltzmann constant and T is temperature (Kelvin); and when T=300 K (room temperature), kT=0.026 eV] is much less than particle energy (Kv, where K is anisotropic constant and v is the particle volume) and thus direction of magnetic moment does not change with time (**Figure 1.5 A**).

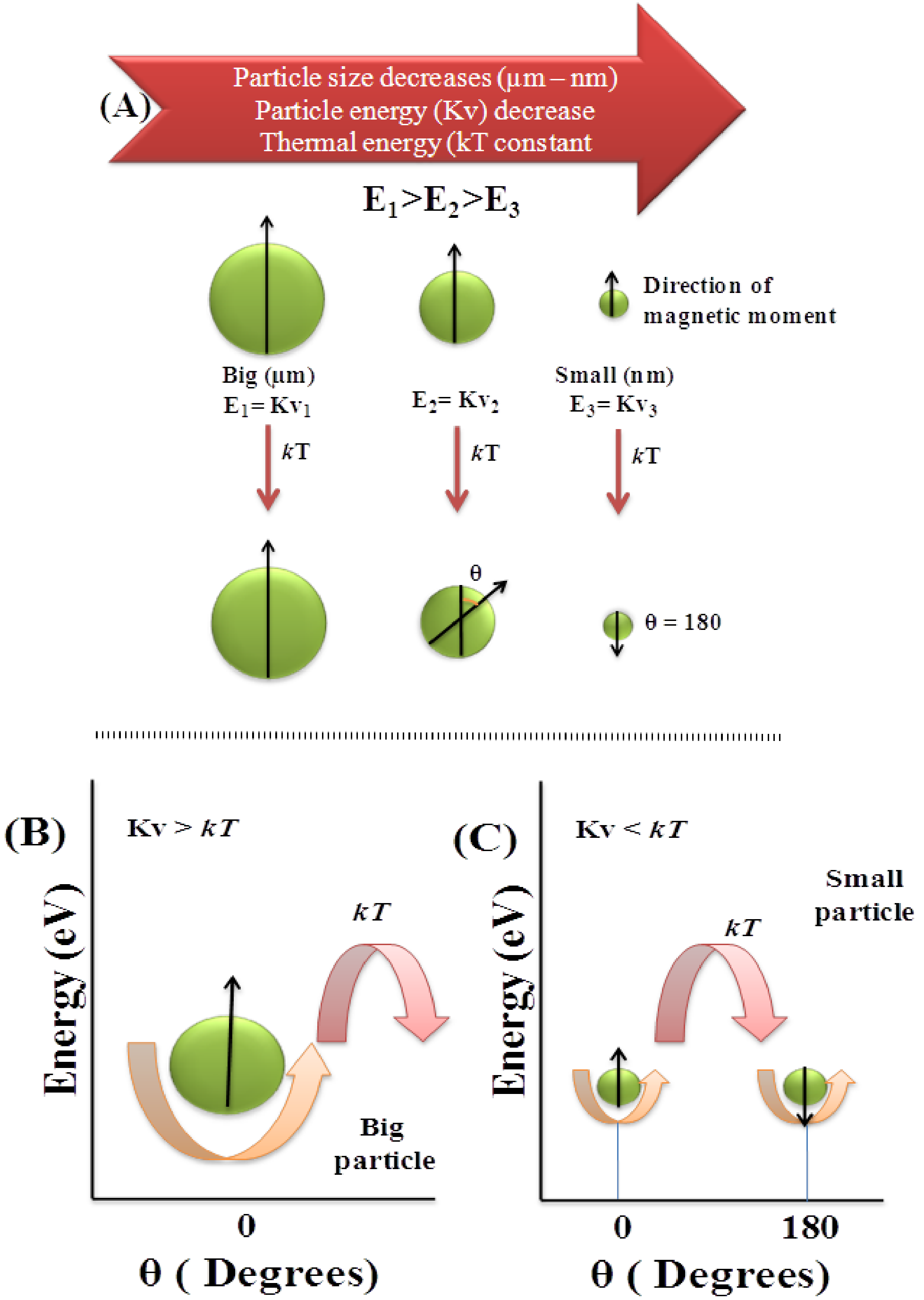

Figure 1.5:(A) Orientation of the magnetic moment of magnetic particles of different sizes under thermal energy (kT). Energy versus θ (degrees) for (B) big and (C) small magnetic nanoparticles under thermal energy (kT) [103].

However, with further decrease of particle size (nano-size), the direction of magnetic moment changes to the opposite direction (θ=180°), which is known as superparamagnetic behaviour of magnetic nanoparticles. Superparamagnetic particles have high magnetic moment of 10^3-10^4 μB [103].

The term 'super' is prefixed to 'paramagnetic' because particles show paramagnetic behaviour in absence of a magnetic field and no magnetization is retained after removal of the magnetic field. Ferromagnetic particles can be changed to superparamagnetic particles when particle size decreases below the critical size (**Figure 1.5**.**B and C**). However, the inter-atomic magnetic interaction in ferromagnetic or superparamagnetic materials gives the net magnetic moment of the particle. On either decreasing temperature or increasing magnetic field, there is a possibility of transition from superparamagnetic to ferromagnetic [104] related to the extent of increment in the alignment of spins of magnetic nanoparticles. The temperature at which the $Kv = kT$ is called Blocking Temperature (T_B) and below that temperature the superparamagnetic particles start to behave ferromagnetically.

In this thesis, Fe_3O_4 and FePt based magnetic nanoparticles are explored for their applications; so further discussions are confined only of these two materials.

1.5.3.1. Fe_3O_4 nanoparticles:

Fe_3O_4 (magnetite) is a renowned material that shows tunable magnetic properties with respect to their particle size. It has a cubic inverse spinel structure (**Figure 1.6**), where Fe^{2+} ions occupy half of the octahedral sites and Fe^{3+} ions occupy the other half and all the tetrahedral positions [105]. Fe_3O_4 nanoparticles (Fe_3O_4 NPs) also exhibit superparamagnetism. In the long term, Fe_3O_4 NPs are chemically unstable under atmospheric oxygen and slowly oxidise to Fe_2O_3 [106].

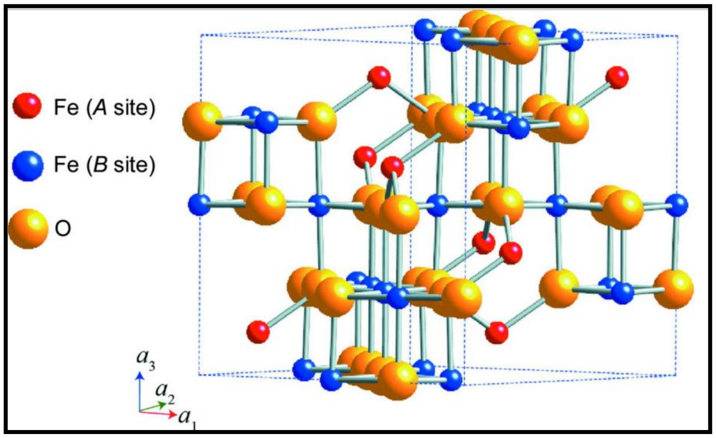

Figure 1.6: Schematic of inverse spinel structure of Fe_3O_4 (The yellow atoms are O, the blue atoms are Fe in a B site, and the red atoms are Fe in the A site) [105].

In bulk Fe_3O_4, spontaneous magnetic domains occur where each individual domain contains its own magnetization direction and is separated from other domains by domain walls and exhibit ferromagnetism. In Fe_3O_4 NPs, each particle behaves as a single domain; constraints are removed, and each single domain can spontaneously switch directions resulting in superparamagnetism behavior. When an alternating magnetic field is applied to these nanoparticles, the particles undergo thermal fluctuations as the spins overcome their blocking energy barrier and flip with the alternating magnetic field [92, 107]. These thermal fluctuations can be utilized for the hyperthermia treatment. Fe_3O_4 nanoparticles have attracted much interest not only in the field of recording media and magnetic separation but also in the areas of medical applications, including drug delivery systems, radio-frequency hyperthermia, and magnetic resonance imaging (MRI) and cancer therapy and applications, catalysis and magnetic sensing [92, 107-116].

1.5.3.2. FePt nanoparticles:

FePt nanoparticles are an important class of magnetic nanomaterials with a near-equal atomic percentage of Fe and Pt. They exist in either a chemically disordered face-centered cubic (fcc) structure or a chemically ordered face-centered tetragonal (fct) structure [98, 117] as shown in **Figure 1.7**. The fcc-structured FePt has a small coercivity and is magnetically soft. The fully ordered fct-structured FePt can be viewed as alternating atomic layers of Fe and Pt stacked along the [001] direction.

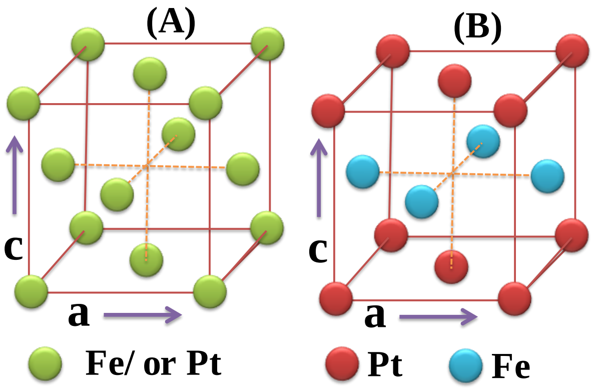

Figure 1.7: Schematic illustration of the unit cell of A) chemically disordered and B) ordered FePt.

The anisotropy constant *K*, of FePt measuring the ease of magnetization reversal along an easy axis, can reach as high as 107 Jm^{-3} [118] a value largest among all known hard magnetic materials. This *K* might be due to Fe and Pt interactions induced by spin-orbit coupling and the hybridization between Fe 3d and Pt 5d states [119, 120]. These interactions further render the FePt nanoparticles chemical stability much more than the typical high-moment nanoparticles of Co and Fe, as well as other significant coercive materials like $CoSm_5$ and $Nd_2Fe_{14}B$, making it exclusively useful for practical applications like solid-state devices, catalysis and biomedicine [121-127].

Self-assembled ferromagnetic FePt nanoparticle arrays being a prospective magnetic-media candidate, preliminary recording experiments on a ferromagnetic $Fe_{48}Pt_{52}$ nanoparticle array with Hc at 1800 Oe carried out by Sun et al. [128] showed that the ferromagnetic FePt nanoparticle assembly can indeed support magnetization reversal transitions. Another set of experiments was performed by Zeng et al. by choosing FePt and Fe_3O_4 nanoparticles as building blocks in binary composite assemblies by reductive annealing, transforming Fe_3O_4 to Fe and converting the fcc FePt to fct FePt [129]. Gu's Group has conjugated vancomycin to FePt, which exhibits selective binding to Gram-negative bacteria with a concentration of 15 cfumL^{-1} (cfu: colony forming units), which is an order of magnitude more sensitive than one of the best assays for bacteria detection based on luminescence (detection limit: 180 cfumL^{-1}) [130, 131]. Zhu et al. prepared magnetic ordered mesoporous carbon with superparamagnetic FePt nanoparticles via a merenano casing route and successfully used them for the phenol adsorption [132].

1.6. Synthesis approaches and techniques

The drive for exploring new synthesis route for nanomaterials has been of great importance recently due to the increasing demand for smaller particle sizes. Microstructural properties like grain size, large number of grain boundary junctions and interfaces, porosity and several lattice defects can be tailored using proper synthesis route and result in unique physical and chemical properties.

Thus, in order to explore the novel physical properties as well as phenomena and to realize potential applications of these nanostructures, the ability to fabricate and process is the first corner stone in nanotechnology. There are two approaches to the synthesis of nanostructures: top-down and bottom-up.

For example, milling a typical top-down method for manufacturing nanoparticles, whereas the colloidal dispersion, an excellent case of bottom-up approach in the synthesis of nanoparticles. Both methods play crucial roles in nanotechnology. In this thesis, the bottom up approach was used for synthesis of nanomaterials. This approach can be further classified into liquid phase assisted growth and solid state assisted growth

1.6.1. Liquid phase growth (Soft chemical method)

Nano-crystalline particles are generally synthesized by soft chemical routes, wherein the homogeneity of the reacting constituents can be achieved at atomic level. These methods employ a solvent medium from which the required product can be obtained by several ways such as precipitation, solvent evaporation, etc. The soft chemical processes include solvent routes such as co-precipitation process, hydrothermal process, sol-gel process, pechini and citrate gel processes, etc.

The basis of all solvent based synthesis procedures involves nucleation and growth, which are the two important steps in the bottom up approach. Nucleation is the step where aggregates of atoms starts forming, the first step in phase transformation. The growth of nuclei results in the formation of large crystalline particles. The major issues for the synthesis of nanoparticles are control of the particle size, thus composition, and homogeneity along with the control of the interfaces within fully formed nanostructured materials.

Generally, three kinds of nucleation processes occur: homogeneous nucleation, heterogeneous nucleation and secondary nucleation. Homogeneous nucleation occurs in the absence of a solid interface [133]. The driving force of thermodynamics results in homogeneous nucleation, as the supersaturated solution is not stable in energy and thus, solute molecules combine to produce embryos. The overall free energy change, ΔG, is the sum of the free energy due to the formation of a new volume and the free energy due to the new surface created, for spherical particles and is given as;

$$\Delta G = -\frac{4}{v}\pi r^3 k_B T ln(S) + 4\pi r^2 \gamma \tag{1.1}$$

Where v is the molecular volume of the precipitated species, r is the radius of the embryo, k_B is the Boltzmann's constant, S is the saturation ratio and γ is the surface free energy per unit surface area. When saturation ratio, $S > 1$, ΔG has a positive maximum at a critical size, r^*. This maximum free energy is the activation energy for nucleation. Embryos larger than the critical size will further decrease their free energy by growth and form stable nuclei that further grow into particles. The critical nuclear size, r^*, can be obtained by setting $d\Delta G/dr = 0$.

$$r^* = \frac{2v\gamma}{3k_B T ln(S)} \tag{1. 2}$$

For a given value of S, all particles with $r > r^*$ will grow and all particles with $r < r^*$ will dissolve.

The short nucleation time model proposed by Lamer [134], originally developed to describe the formation of sulfur sols and has been used to describe the precipitation process for many chemical reactions. In this model, when a solution is supersaturated, a new phase nucleates homogeneously out of this solution. Then particles grow via molecular addition, which acts to decrease the super-saturation.

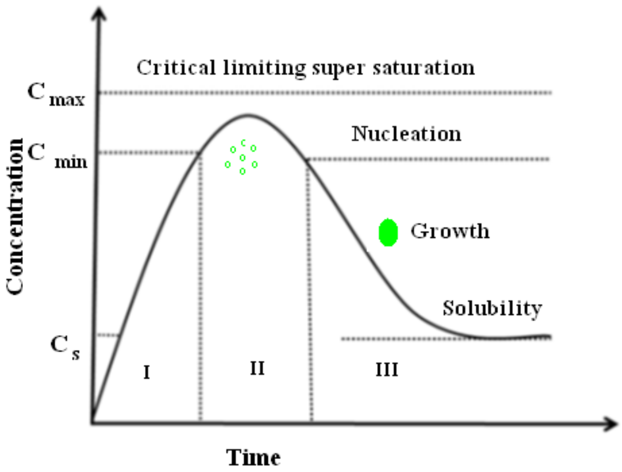

Figure 1.8: Schematic representation of variation of concentration as a function of time during the nucleation and growth.

When the concentration of soluble material drops below the super-saturation, nucleation stops and particles continue to grow by molecular addition until the equilibrium concentration of the precipitating species is reached. Uniformity of size distribution is achieved through a short nucleation period that generates all of the particles seen at the end of the reaction. That is followed by a self-sharpening growth process where smaller particles grow more rapidly than larger ones, as the free energy driving force is larger for smaller particles than larger particles. Narrow particle size distribution can be achieved by either suspending the reaction quickly or by providing reactant source to keep a saturated condition during the reaction course.

On the other hand, when the reactants are depleted, the larger particles continue to grow and smaller one gets further smaller and finally dissolves. This process can schematically represented as shown in the **Figure 1.8**. Because the saturation ratio (S) decreases and corresponding critical nuclei size (r*) increases, the particles smaller than this new critical size will dissolve in the reaction medium/solvent. Formation of particles with a broad size distribution results, if the reaction is quickly stopped at this stage. However, if the reaction is allowed to continue for long enough time, smaller particle will get completely dissolved and bigger particles will grow, as a result uniform particle size distribution with relatively larger particle size will occur.

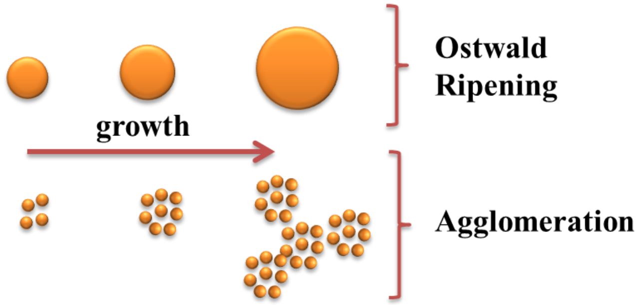

Figure 1.9: Schematic representation of nanoparticles growth by Oswald ripening and agglomeration.

Besides the molecular addition due to diffusion of monomer into the nuclei, particles can grow by aggregation due to collision with other particles and this is called secondary growth (schematically shown in **Figure 1.9**). The growth rate of the particles due aggregation is much higher than that by the molecular addition. The particles grow to a stable size, and it grows further by combining with smaller unstable nuclei. To get mono-disperse particle size distribution, the rate of nucleation must be high enough i.e. high saturation ratio S with slow rate of growth.

1.6.1.1. Precipitation:

Among all of the synthetic strategies, the most popular is the chemical co-precipitation which is widely used in laboratory and industrial applications because of its ease of handling, large scale production and its cheap raw materials. Hydrolysis is attractive because it can produce fine, spherical particles with improved chemical purity, better chemical homogeneity and controlled particle size. Mono-dispersive particles can be prepared by carefully controlling the kinetics either by forced hydrolysis (faster kinetics) or controlled release of anions (slow kinetics).

1.6.1.1.1. Forced hydrolysis

The easiest way to prepare uniform colloidal metal (hydrous) oxides is based on forced hydrolysis of metal salt solutions [135]. It is well known that most polyvalent cations readily hydrolyze, and that de-protonation of coordinated water molecules is greatly accelerated with increasing temperature. Because hydrolysis products are intermediates to precipitation of metal (hydrous) oxides, these complexes can be generated at the proper rate to yield uniform particles eventually by the adjustment of pH and temperature. In addition, anions other than hydroxide ions can affect the homogeneous precipitation of metal ions. These anions can be strongly coordinated to dissolve metal ions or affect the particle morphology without being incorporated in the precipitates.

1.6.1.1.2. Precipitation by controlled release of anions

The kinetics of nucleation and particle growth in homogeneous solutions can be adjusted by the spontaneous release of precipitating anions from organic molecules [136, 137]. It is also essential to fulfill the requirements of homogeneity of solution, slow precipitation and easy control of the final pH for homogeneous precipitation. From these points of view, urea ($(NH_2)_2CO$) is almost an ideal reagent to use in a hydrolytic process to prepare spherical particles. It possesses negligible basic properties and is quite soluble in water and its hydrolysis rate can be easily controlled. Urea hydrolyses easily at about 90°C and hydrolysis can be quickly terminated at a desired pH by cooling the reaction mixture to room temperature. Urea hydrolyses in aqueous media and yields ammonium cyanate as follows [138]:

$$H_2N-CO-NH_2 \leftrightarrow NH_4^+ + NCO^- \qquad \textbf{(1. 3)}$$

This is a rate-determining reaction and its rate constant, *k*, is first order with respect to urea over a wide concentration range after which, the cyanate ion is converted into carbonate and ammonium ions:

$$NCO^- + \ 2H_2O \rightarrow NH_4^+ + CO_3^{2-} \qquad \textbf{(1. 4)}$$

1.6.1.2. Sol-gel processing

Sol–gel technique is also one of the most popular solutions assisted method for producing metal oxide nanoparticles. This process is well described in several books [139, 140] and reviews. In sol–gel processing, a reactive metal precursor, such as metal alkoxide, is hydrolysed with water, and the hydrolysed species are allowed to condense with each other to form precipitates of metal oxide nanoparticles. The precipitate is subsequently washed and dried, which is then calcined at an elevated temperature to form crystalline metal oxide nanoparticles (**Figure 1.10**).

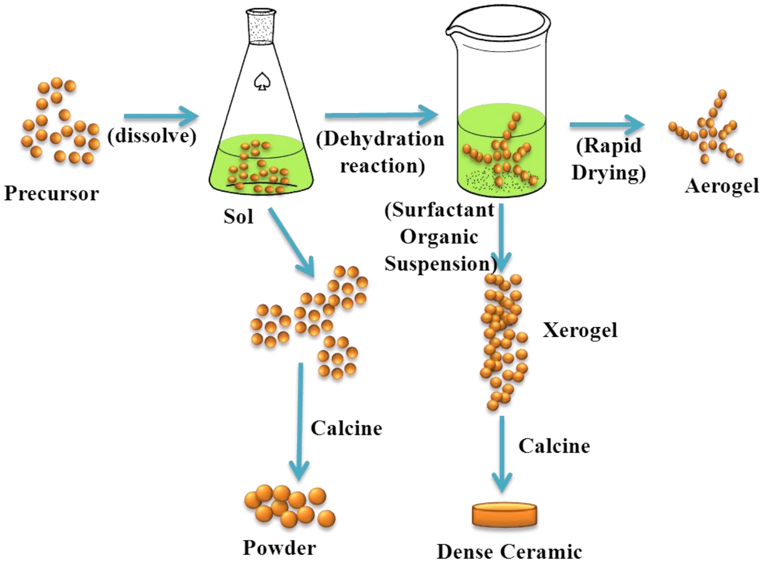

Figure 1.10: Schematic showing the sol-gel process.

The reactions involved in the sol-gel chemistry based on the hydrolysis and condensation of metal alkoxides M(OR) can be described as follows: [139]

$$MOR + H_2O \rightarrow MOH + ROH \text{ (hydrolysis)} \quad \textbf{(1.5)}$$

$$MOH + ROM \rightarrow M\text{-}O\text{-}M + ROH \text{ (condensation)} \quad \textbf{(1.6)}$$

Condensation occurs when either hydrolysed species react with each other and release a water molecule or a hydrolysed species react with an un-hydrolysed species and releases an alcohol molecule. The rates at which hydrolysis and condensation reactions take place are important parameters that affect the properties of the final product. For example, slower and more controlled hydrolysis typically leads to smaller particles and base-catalysed condensation reactions form denser particles.

1.6.1.3. Gel-combustion synthesis

This is a facile synthesis technique that can be employed on both laboratory and industrial scale to prepare nanocrystalline ceramic powders with reproducible characteristics. Combustion is basically a redox reaction between the oxidant and fuel and is controlled by various factors such as the nature and amount of fuel.

First, nitrate/oxynitrate salts of the metals, in the required molar ratio, are mixed together in an aqueous media to produce a transparent mixed metal nitrate solution. A suitable fuel (glycine, citric acid, urea, etc.) is then added in an appropriate amount to this solution. The aqueous solution of fuel and oxidants is thermally dehydrated on a hot plate (at about 80–100°C) to obtain a viscous liquid (hereafter termed as gel). This thermal dehydration and gel formation process is an important step, because any excess water left behind would lead to sluggish combustion, deteriorating the phase purity and powder quality.

The gel, as formed in the first step, is further heated at a relatively higher temperature (200–250 °C) that initiates self-propagating combustion. The exothermic decomposition of the fuel–oxidant precursor is manifested in the form of flame, which rapidly propagates throughout the gel; therefore this step is also termed as auto-ignition. The auto-ignition is a very short-lived phenomenon as the flame persists for only a few (5–10) seconds. It is within this short duration that the product formation takes place. The auto-ignition of the gel results in a large voluminous powder. During auto-ignition, gaseous products are evolved which dissipate the heat and fragment the solid residual products resulting in ultrafine powders of oxide.

1.6.2. Solid phase formation:

1.6.2.1. Pyrolysis

Pyrolysis is a chemical process in which chemical precursors decompose under suitable thermal treatment into one solid compound and unwanted waste evaporates away. Upon completion, the desired new substance is obtained.

The pyrolytic synthesis of compounds leads to powders with a wide size distribution in the micrometre regime. To get a uniform nanosized material, some modifications of the pyrolytic preparation procedure and reaction conditions are added. There are many alterations used to make nanomaterials by pyrolysis, for example: (1) atomize the precursor solution; (2) use stable matrix, i.e., zeolite molecular sieves or glass, to disperse the precursor solution; (3) slow down the reaction rate to obtain nanoparticle film, i.e., the oxide superconducting films formed in a vacuum; (4) allow the reaction to occur in the inert solvent or inert gas; (5) use a decomposable polymer or molecules to disperse and protect precursors and as prepared nanoparticles.

These alterations effectively decrease the critical formation temperature of nanoparticles and protect the nanoparticles from aggregation and agglomeration. These methods usually can be combined to synthesize specific materials for different applications.

1.7. Applications of nanomaterials

Within the last decade, many areas of the industry have witnessed the advent of nanoscience. This section is focused on the technological uses of nanostructured oxides as adsorbents. Other applications involving catalysts, explicitly photocatalysts and magnetic materials for various therapeutic applications are also summarized here.

1.7.1. Environmental remediation

The fast industrialization and its consequential by-products have disturbed the environment by creating hazardous wastes and poisonous gases and smokes being released to the environment. Conventional technologies have been used to treat all types of organic and toxic waste by adsorption, biological oxidation, chemical oxidation and incineration. The treatment of pollutants in water and air is the greatest challenge in the present scenario. Parallely, the potential of nanotechnology has extended a great deal of interest in the environmental remediation as well. Nanomaterial exhibit high surface to volume ratios and high surface energy leading to high reactivity. These exceptional properties can be utilized to capture and degrade the pollutants in water and air. The species adsorbed onto the nanomaterials can be recovered by applying mild (and affordable) gravitational (centrifugal) or magnetic force (in the case of magnetic nanoparticles). Furthermore, several natural and engineered nanomaterials have also been proved to have strong antimicrobial properties, including silver nanoparticles, photocatalytic TiO_2, chitosan and carbon nanotubes (CNT) [141-148]. Nanotechnology is also used for the detection of pesticides and heavy metals (e.g. cadmium, copper, lead, mercury, arsenic, etc.) [149-151]. In addition, nanomaterials have enhanced redox and photocatalytic properties [152-154].

1.7.1.1. Low-cost adsorbents

Heavy metals and organic pollutants are becoming one of the most serious environment problems globally [155-160]. Among that one of the most threating problems for the densely populated countries is the polluted water [161-164]. Even present in low concentration, heavy metals and organic pollutants in various water resources could be harmful to living organisms. The treatment of these pollutants is necessary due to their persistent nature in the environment. In order to detoxify these, various techniques like photocatalytic oxidation [165, 166], chemical coagulants [167], electrochemical [168-170], bioremediation [171], ion-exchange resins [172-174], reverse osmosis [175], and adsorption/adsorbents [176, 177] have been employed. The core issue of such technology is to devise materials that can absorb these ions irreversibly, efficiently, selectively and in large quantities from contaminated bodies. Besides, the sorbent materials should be very stable to chemicals, thermal and mechanical changes so that the ions can be safely separated from the sorbent. Currently, available absorbents such as activated alumina, zeolite, activated carbon and silica gel cannot fulfil the task of safe disposal. New and better absorbents are required to meet these challenges. Nano-based adsorbents are the most convenient technologies for removal of pollutants from the aqueous system [178-181]. Schematic representation of a sorption process is shown in the **Figure 1.11**.

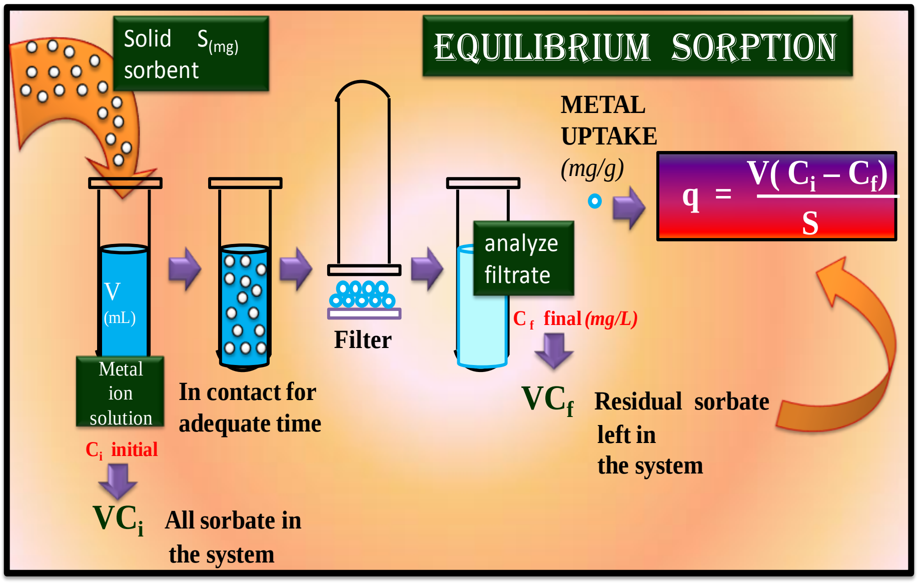

Figure 1.11: Schematic representation of a sorption process.

Nanostructured metal oxides are expected to play a prominent role as effective absorbents for these applications. Great deal of fundamental as well as applied research is yet to be carried out in this very promising and interesting field. The most promising applications being:

- Soil/groundwater remediation by carbo-iron;
- Nano-clays for the adsorption of organic contaminants and phosphorus;
- Nano-aerogels for the removal of heavy metal ion from groundwater;
- Nano-iron oxides to adsorb pharmaceuticals and hormones from wastewater;
- Nano-metal oxides, dendrimers and polymer nanofibres for the removal of arsenic and heavy metals.

Challenges: The technical challenges are still quite fundamental, the development of the nanosorbent on one hand and on the other hand regarding the system setup.

- Novel nanosorbents must fulfill a variety of requirements at the same time to be economically and societally beneficial: specificity, high sorption capacity and cost low;
- Scaling up the production is challenging especially for carbon based materials;
- Since the water industry is very conservative, new nanosorbents systems should ideally be compatible with existing systems implying that it must be possible to integrate the nanosorbents cost effectively into existing systems;
- The system setup must ensure that the nanosorbent is removed entirely (for example by magnetic forces or by filtration) to avoid remnant nanoparticles in the environment and in drinking water as well as to make it cost effective by regenerating the nanosorbents for reuse.

1.7.1.2. Photocatalysts

Heterogeneous photocatalytic oxidation has been used to degrade environmental pollutants resulting in the formation of benign products. Efforts have been made to improve the catalytic performance of nanostructures based on semiconductor oxides, such as TiO_2 and ZnO. The catalytic reaction involves the adsorption of pollutant molecules onto the surface of NPs, chemical bond breaking and formation and the release of product molecules. The unique surface area and the surface activity of NPs play essential roles in these catalytic reactions.The photocatalytic reaction occurs, at least principally, in the adsorbed phase and the overall process can be formally divided into five steps [182]:

1. The transfer of the reactants from the fluid phase to the surface;
2. The adsorption of at least one of the reactants;
3. The reaction in the adsorbed phase;
4. The desorption of the product(s); and
5. The removal of the product(s) from the interfacial region.

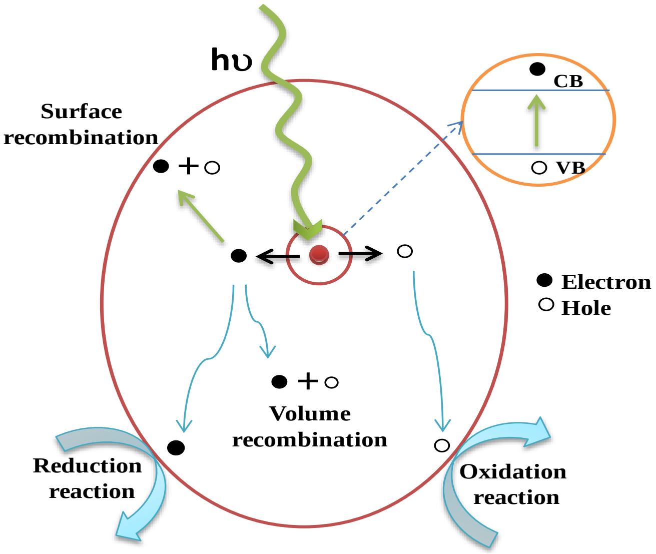

Figure 1.12: Schematic illustration of the charge separation theory of semiconductor upon a photo excitation.

As the adsorption and desorption rates are temperature dependent, temperature can have an effect on the photocatalytic reaction rates. A typical photocatalytic process showing the possibilities of charge separation theory in semiconductor upon a photoexcitation can be depicted as in **Figure 1.12**.

1.7.2. Bio applications

Nanoparticles have numerous applications in the field of Biotechnology and Biomedicine. The major advantage of using nanoparticles in medicine is its small size which allows penetration through blood capillaries which leads to increased accessibility to the target site [91, 123, 183]. This feature enables the nanoparticles to be utilized in different aspects in medicine including (1) Therapeutics/Hyperthermia, (2) *in vitro* diagnostics, (3) *in vivo* imaging, and (4) drug delivery. These topics are briefly discussed below.

1.7.2.1. Drug delivery

The major disadvantage of the chemotherapy is its lack of selectivity toward tumor cells. The therapeutic drugs are administered intravenously resulting in general systemic distribution in the body, which lead to severe side effects because the drugs attack healthy cells simultaneously in addition to the tumour cells. However, it is possible to make the continued use of these potent and efficient agents if such treatments could be localized. In view of these the drug-delivery systems using magnetic nano and microparticles show a definite potential application for cancer treatments [184-186] owing to the following advantages: (1) the ability to reduce the amount of systemic distribution of the cytotoxic drug, thus reducing the associated side effects; (2) the ability to decrease the drug dosage required by more efficient, localized targeting of the drug [184, 187]. The cytotoxic drugs attached biocompatible magnetic nanoparticles (generally superparamagnetic nanoparticles) are carriers in magnetically targeted therapy. When the magnetic nanocompositions have entered the bloodstream after injection, into the patient via the circulatory system, high-gradient magnetic fields are used externally to concentrate the nano-compositions at a specific target site within the body. Once the drug-carried nano-compositions are concentrated at the target, the drugs release from magnetic nano-compositions either *via* enzymatic activity or changes of physiological conditions such as pH, osmotic pressure, and temperature [188].

In recent several years, the drug-delivery systems based on magnetic nanostructures have been widely developed [184-186, 189]. One of the most investigated nanostructures is the mesoporous silica matrix containing magnetic nanoparticles [190-194] because the walls of the silica pores contain free silanol groups can react with appropriate drug functional groups; moreover, silica is non-toxic and highly biocompatible. Lin et al. [195] recently demonstrated that mesoporous silica nanorods capped with superparamagnetic iron oxide nanoparticles (magnet-MSNs) can be used as a stimuli-responsive controlled-release delivery carrier. Guest molecules that are smaller than 3 nm, such as fluorescein, could be encapsulated and released from the magnet-MSN delivery system by using cell-produced antioxidants (e.g. dihydrolipoic acid) as triggers in the presence of an external magnetic field. The magnet-MSNs delivery system may play a significant role in the advancement of new generations of site-selective controlled-release drug delivery devices.

1.7.2.2. Hyperthermia

The potential of hyperthermia therapy (HT) as a treatment for cancers was first predicted following the interpretations that several types of cancer cells are more sensitive to temperatures in excess of 41 °C than their regular counterparts [196, 197]. Magnetic nanoparticles have been probed as potential hyperthermia triggering agents due to their high specific absorption rate (SAR). The HT method relies on the theory that any metallic objects, when placed in an artificial (AC) magnetic field, will induce currents flowing within them. The amount of current is proportional to the size of the magnetic field and the size of the object. As these currents flow within the metal, the metal resists the flow of current and thereby causes heat; a process termed inductive heating. If the metal is magnetic, such as iron, the phenomenon is greatly enhanced. Therefore, when the magnetic nanoparticles are exposed to AC magnetic fields, the particles become powerful heat sources and destroy the targeted tumor cells [91, 92, 198]. The possibility of treating cancer by induced HT has led to the development of many different devices designed to heat malignant cells while sparing surrounding healthy tissue [197, 199]. Whereas the majority of HT devices are restricted in their utility because of unacceptable coincidental heating of healthy tissue, magnetic HT is appealing because it offers a way to ensure that the calefaction only happens in intended target tissue.

Recently, there have been numerous publications and reviews describing a variety of HT schemes using different types of magnetic materials, different field strengths and frequencies and different methods of encapsulation and delivery of the particle [84, 113, 200-210]. In 2005, Gu et al. described the conjugate of porphyrin and Fe_3O_4 magnetic nanoparticles may lead to a bimodal anticancer agent for the combinational treatment of photodynamic therapy (PDT) and HT [211], they have chosen porphyrin derivatives and magnetite as the building blocks because (1) both porphyrin derivatives and iron oxides are biocompatible [212]; (2) biological processes allow both iron oxides and porphyrin derivatives to be biodegradable after treatment; (3) the well-studied pharmacokinetics and low systemic toxicity have already led to some clinical trials and usage of porphyrin derivatives in PDT and iron oxides in HT [211-214]. This bimodal conjugate methodology may provide a great platform for the applications in the emerging field of nanomedicine.

1.7.2.3. Magnetic resonance imaging:

Magnetic resonance imaging (MRI) is an imaging technique used primarily in medical settings to produce high-quality anatomical images of the human body. Based on the principles of nuclear magnetic resonance (NMR), MRI relies on the counterbalance between the exceedingly small magnetic moment on a proton and the exceedingly large number of protons present in biological tissue, which leads to a measurable effect in the presence of large magnetic fields [215, 216]. In clinical practice, MRI is used to distinguish pathologic tissue (e.g., a brain tumor) from normal tissue. One advantage of an MRI scan is that it is non-invasive to the patient. It uses strong magnetic fields and non-ionizing radiation in the radio frequency range. The recent development of molecular and cellular imaging which aims for visualizing the disease-specific biomarkers at the molecular and cellular levels has led to prevalent recognition of the magnetic nanoparticles as MRI contrast agents.

Recently, superparamagnetic iron oxide (SPIO) nanoparticles have been widely investigated and developed as an MRI contrast agent [109, 183, 215-219]. Many other unusual magnetic nanoparticles also have potential application as MRI agents. Dai et al. [220, 221] reported FeCo/graphitic shell nanocrystals synthesized by a scalable chemical vapor deposition method. The FeCo nanocrystals can be used as an advanced MRI agent because of its ultra-high saturation magnetization, $\tau_1$and $\tau_2$relaxivities.

1.8. Scope of the thesis

The main objectives of the present investigations under the title of "Nanostructures for bio-application and toxic species remediation" are:

- To fabricate nanostructures of ZnO with varying surface charge by employing different synthesis procedure and evaluate their sorption efficiencies for several toxic species.
- Surface functionalization of these nanoparticles using various organic and inorganic materials like thiourea, silanol, mercapto-silanol etc. to make them selective as well as stable against aggregation and leaching.
- Synthesis of other low cost possible stable adsorbent materials in both acidic and basic pH using simple co-precipitation method and sorption evaluation for heavy metal ions.
- Synthesis of magnetic –silica nano-composites and evaluation of their various properties and plausible bio-applications.
- Synthesis of FePt and FePt –ZnO nano-composites and detailed investigation of their properties.

Chapter 2

Experimental Techniques

2.1. Methodology

2.1.1. Synthesis of ZnO nanostructures by different routes:

2.1.1.1. By pyrolysis method:

In a typical pyrolytic synthesis, 2.2 g (10 mmol) of $Zn(CH_3COO)_2.2H_2O$ and 2 g (23.8 mmol) of $NaHCO_3$ were mixed thorougly at room temperature and pyrolysed at 160 °C in a tubular furnace to get ZnO nanoparticles and sodium acetate. The acetate salt was removed by washing with deionized water. The washing and centrifugation process was repeated a couple of times to remove the adsorbed acetate group present in the sample. Finally the powder was dried in a oven at 80 °C . Herein, these particles are referred as ZnO-PY.

2.1.1.2. By combustion method

The synthesis of ZnO by combustion route involves the use of zinc nitrate ($Zn(NO_3)_2.6H_2O$) and glycine as the oxidant and fuel, respectively. 3.66 g of zinc salt was dissolved in water and heated on a hot plate and to this 0.8312 g glycine was added and heating was continued till a thick viscous gel was formed. When the gel was further heated, combustion occurred resulting in the formation of white zinc oxide nanoparticles. The obtained oxide powder was further heated in a furnace at 450 °C for 1 h to remove the carbonaceous impurities. Here after these particles are referred as ZnO-GC.

2.1.1.3. By co-precipitation method

ZnO nanoparticles were prepared using the methodology adopted by Imai et al. [222]. In a typical synthesis, 25 mL of zinc nitrate (2 M) taken in a beaker was heated to 70 °C. To this 50 mL of NaOH (2 M) was added with vigorous stirring. The final pH of the mixture was fixed at 13, as highly basic conditions are favourable for the preparation of ZnO nano-crystals. After precipitation, the mixture was further maintained at 70 °C for 2 h. The products obtained by centrifugation were washed with deionized water thrice, finally with methanol and then dried at 500 ºC in air. Henceforth, these particles are referred as ZnO-CP.

2.1.2. Synthesis of surface functionalized ZnO nanoparticles

2.1.2.1. Thiourea capped ZnO nanoparticles (TU-ZNPs)

TU-ZNPs was prepared by simple precipitation of Zn(II) in basic medium followed by in situ coating of thiourea (TU) group on to the surface. In a typical synthesis, desired amount of $Zn(NO_3)_2$ was dissolved in 25 ml methanol in a round bottom flask to get a 2 M solution. The reaction mixture was heated to 70 °C under vigorous stirring. 50 ml of NaOH (2 M) was added drop by drop to the mixture till the pH of the medium became 11-12. Further, the reaction was continued at 70 °C for 2 h. In order to get thiourea coating, 1 g of thiourea was added to the above mixture and reacted for 1 h under the same conditions. The obtained white precipitate was centrifuged and washed with distilled water and acetone to remove the unreacted particles.

2.1.2.2. Silica capped ZnO nanoparticles (S-ZNPs)

In a typical synthesis, desired amount of $Zn(NO_3)_2$ was dissolved in 25 ml methanol in a round bottom flask to get a 2 M solution. The reaction mixture was heated to 70 °C under vigorous stirring. 50 ml of NaOH (2 M) was added drop by drop to the mixture till the pH of the medium turn out to be 11-12. Further, the reaction was continued at 70 °C for 2 h. In order to get silica coating, 1 ml of tetra-ethyl-ortho-silicate (TEOS) was added to the above mixture and reacted for 1 h under the same conditions. The obtained white precipitate was centrifuged and washed with distilled water and acetone to remove the unreacted particles.

2.1.2.3. Thiol functionalized silica capped ZnO nanoparticles (TFS-ZNPs)

To synthesize thiol functionalized silica capped ZnO nanoparticles the as-prepared 2 g S-ZNPs was further dispersed in alcoholic solution and 1 ml of 3- Mercaptopropyl-trimethyl-silane (MPTMS) was added to the above solution under vigorous stirring. It was heated to 70 °C for about 2 h. The white precipitate was centrifuged and washed with distilled water and acetone to remove the unreacted particles.

2.1.3. Preparation of silane functionalized Fe_3O_4 nanoparticles (SMNP)

Fe_3O_4-SiO_2 MNPs was prepared by one pot co-precipitation of Fe(II) and Fe(III) in basic medium followed by *in-situ* coating of SiO_2. In a typical synthesis, 1:2 ratio of $FeCl_2.4H_2O$ and $FeCl_3.6H_2O$ was dissolved in 50 ml double distilled water in a round bottom flask. The reaction mixture was heated to 80 °C under vigorous stirring in argon atmosphere. When the required temperature was attained, 20 ml of NH_4OH was added drop by drop to the mixture till the pH of the medium changed to 11-12. The reaction was continued at this temperature for another 2 h. For SiO_2 coating, 1 ml of TEOS was added to the above mixture and reacted for another 1 h at same conditions. The obtained black coloured precipitate was magnetically separated and washed with distilled water and acetone two to three times to remove the un-reacted particles and excess of ammonia. The sample was left for drying in air overnight. The silica coated particles are henceforth referred as SMNPs.

2.1.4. Synthesis of Mo doped $CeVO_4$ nanoparticles (CVMNPs)

The system $Ce(V_{1-x}Mo_x)O_4$ ($0.0 \leq x \leq 0.5$) was synthesized by a simple co-precipitation. For each nominal composition, the reactants were weighed to achieve ~ 1g of the final product. For a typical co-precipitation synthesis, stoichiometric amounts (1:1) of $Ce(NO_3)_3.6H_2O$, ammonium molybdate and ammonium metavanadate (NH_4VO_3) were weighed and dissolved separately. The anion solutions (ammonium metavanadate and ammonium molybdate) were mixed and stirred at room temperature to achieve homogenisation. The cerium nitrate solution was then slowly added to the ammonium vanadate (or a mixture of ammonium metavanadate and ammonium molybdate solutions) with continuous stirring. The reaction mixture was stirred and heated at 80 ^{o}C for two hours. The precipitate so obtained was centrifuged and washed with de-ionized water followed by washing with acetone and dried in oven at 100 ^{o}C for two hours.

2.1.5. Synthesis of Mo incorporated TiO_2 nanoparticles (Mo-TiO_2)

A new and simple method has been developed for the preparation of the nano TiO_2 and molybdenum doped TiO_2[223]. In this modified sol-gel process, the required stoichiometric amount of molybdic acid (Aldrich Make), is initially dissolved in nano pure water at room temperature at a neutral pH. The solution of molybdic acid was maintained at a temperature of 0 °C by the addition of ice-salt mixture from outside. To this dissolved molybdic acid solution, Ti(IV) iso-propoxide solution in iso-propanol (IPA) was added drop wise in a controlled manner over a period of 1 h, with vigorous stirring until the formation of a uniform gel. This gel was stirred further for 1 h, to ensure incorporation of the molybdenum precursor in the titanium gel phase. The gel was kept for nucleation for 12 h in the dark, and then IPA is removed by keeping the gel in a Petri dish for 12 h. The mass was then dried in an oven at 100 °C for 4 h. The resulting solid mass was crushed and calcined at a temperature of 500 °C for 4 h. The requisite amount of incorporation of (1.0, 2.0, 5.0 and 10 mol %) of Mo was attained by adding stoichiometric amount of molybdic acid solution and Ti(IV) iso-propoxide in order to get the gel. However, though the stoichiometric amount of molybdic acid was added in order to have desired substitution of the Ti^{4+} in the crystal lattice of the TiO_2, yet it was observed (as will be presented subsequently in chapter 7) that the total amount of molybdic acid resulted to a hetero layer of MoO_3 along with partial substitutional doping of Mo in TiO_2 crystal lattice. Therefore, for the sake of simplicity these different samples synthesized in the form of TiO_2 (anatase), and Mo-TiO_2, MoO_3 samples will be called as Mo-0, Mo-1, Mo-2, Mo-5, Mo-10, Mo-100 throughout chapter 7.

2.1.6. Synthesis of Fe_3O_4@SiO_2 core shell magnetic nanosphere (Fe_3O_4@SiO_2)

Fe_3O_4 - MNPs without capping agent were prepared by co-precipitation method. 2 g of ferrous chloride ($FeCl_2.4H_2O$) and 3.25 g ferric chloride ($FeCl_3.6H_2O$) were dissolved separately in 25 mL double distilled water. The above solutions were mixed in a round bottom flask under vigorous stirring in Ar atmosphere and heated at different temperatures (80 and 100 °C). Once the temperature was attained, 20 mL of NH_4OH was added drop by drop with continuous stirring to this solution. When the pH of the reaction medium was retained at 11-12, black precipitate was observed. The reaction was continued under Ar atmosphere for 2 h. In the present study $SiO_2.xH_2O$ obtained from hydrolysis of TEOS was used as coating material for preparation of Fe_3O_4-SiO_2 core – shell nanoparticles (Fe_3O_4 - SiO_2 MNPs). 1 mL of TEOS was added to the above colloidal form of black precipitate (Fe_3O_4 in ammonical solution) followed by stirring for 1 h. After 3 h, the black precipitated powder was isolated by applying an external magnetic field and the supernatant was removed from the precipitate by decantation. The powder was washed three times with 20 mL of double distilled water followed by acetone to remove excess NH_4OH. Fe_3O_4-SiO_2 MNPs prepared at 80 and 100 °C are referred as Fe_3O_4-SiO_2-80 and Fe_3O_4-SiO_2-100, respectively.

2.1.7. Synthesis of Fe_3O_4@STPP magnetic nanomagnets (PPNMs)

A modified co-precipitation method is adopted for synthesis of Fe_3O_4 nano-magnets. In a typical synthesis of polyphosphate grafted Fe_3O_4 nanomagnets (PPNM), 5.406 g of $FeCl_3.6H_2O$ and 1.988 g of $FeCl_2.4H_2O$ were dissolved in 80 ml of Milli Q water in a round bottom flask, flushed with N_2 and temperature was slowly increased to 70 ^{o}C in refluxing condition under nitrogen atmosphere and constant stirring. The temperature was maintained at 70 ^{o}C for 30 min and then 30 ml of 25% ammonia solution was added directly to the reaction mixture, and kept for another 30 min at 70 ^{o}C. Then, 10 ml aqueous solution of excess sodium tri-poly-phosphate (STPP) (2 g) was added and the temperature was slowly raised up to 90 ^{o}C under reflux and reacted for 60 min with continuous stirring for surface functionalization of Fe_3O_4 nano-magnets with polyphosphate moieties. The black colored precipitates obtained were then thoroughly rinsed with water and separated from the supernatant magnetically.

2.1.8. Synthesis of FePt nanoparticles (FePt NPs)

FePt nanoparticles were synthesized by thermal decomposition of iron(III) acetylacetonate and H_2PtCl_6 in tetra-ethylene glycol as solvent and poly vinyl pyrolidone (PVP) as stabilizer. In a typical process to synthesize fcc phased FePt NPs 1:1 molar ratio of the two reactants were refluxed in tetra-ethylene glycol in a round bottom flask at 300 ^{o}C for 2 h. The obtained product dried at room temperature after washing with acetone and ethanol repeatedly several times. Partially ordered fct phased FePt NPs were synthesized in a similar manner by adding different ratios of PVP (1:1, 1:2, 1:3) with respect to Fe and Pt precursor taken during reactions.

2.1.9. Synthesis of FePtnanoflowers (FePt NFs)

Equimolar ratio of iron(III) acetylacetonate and H_2PtCl_6 were weighed and transferred to a round bottom flask containing 10 ml oleylamine. The above solution was sonicated for 5 min and then refluxed at 320 °C for 2 h in argon atmosphere followed by cooling and centrifugation. The obtained precipitate was washed with acetone many times and kept for drying at room temperature.

2.1.10 Synthesis of FePt@ZnOnanoflowers (FePt-ZNFs)

60 mg of the FePtnanoflowers, prepared by the above mentioned method, was dispersed in 10 ml tri-n-octylamine by sonication, taken in a round bottom flask. Zinc acetate dihydrate (162 mg) was added to the FePt dispersion and was dispersed by sonication for 30 min. The above solution was then heated upto 320 °C with a slow heating rate and then refluxed at 320 °C for 2 h in argon atmosphere followed by cooling and centrifugation. The precipitate obtained was washed with acetone 3 to 4 times and kept for drying at room temperature. This particular ratio was for FePt:ZnO = 1:3, while for a 1:6 ratio .the same pocedure was followed by reducing the amount of FePt to half and by keeping ZnO weight constant by taking 162 mg zinc acetate dihydrate as ZnO source. To prepare FePt@ZnOnanoflowers (1:6), 30 mg of FePt nanoparticles were taken instead of 60 mg with 162 mg of zinc acetate dihydrate.

2.1.11. Synthesis of FePt decorated ZnO nanorods (FePt-ZNRs)

ZnO nanorods were prepared by dispersing zinc acetate dihydrate in tri-n-octylamine by sonication and then refluxed at 320 °C for 2 h. The precipitate obtained was washed with acetone several times and kept for drying at room temperature. 150 mg of ZnO nanorods (NR), prepared by above mentioned method, were dispersed in 10 ml oleylamine taken in a round bottom flask with 50 mg of iron(Ill) acetylacetonate and 73 mg of H_2PtCl_6. The above solution was sonicated for 15 min and then refluxed at 320 °C for 2 h in argon atmosphere. The precipitate was centrifuged and washed with acetone 3 to 4 times and kept for drying at room temperature. This ratio was applicable for ZnO:

FePt = 1:0.08 and for 1: 0.2, same procedure was followed by taking 150 mg of ZnO NR, 10 ml oleylamine, 134 mg of iron(III) acetylacetonate and 196 mg of H_2PtCl_6.

2.1. Characterization techniques

2.2.1. X-ray diffraction (XRD)

X-ray diffraction technique is one of the most widely used technique for the characterization of nanomaterial. To understand and explain the properties of nanomaterials, the understanding regarding its crystal structure and coordination environment around the atoms in the lattice is essential. XRD patterns of the samples can give valuable information on these aspects. The technique is briefly described below.

When electromagnetic rays are incident on a crystalline material (which can be also considered as a grating), they are either coherently/in-coherently scattered or absorbed. The coherent scattering of rays can interfere with each other giving rise to bright (constructive interference) and dark (destructive interference) fringes. However, the scattered rays will become constructive (path difference between the two rays, differ by an integral number of wavelength) only at a particular angle when the wavelength is fixed. This phenomenon is broadly termed as X-ray Diffraction. The classical Bragg's law of diffraction that relates the possibility of constructive interference to the inter-planar separations of the lattice is given by the following equation

$$n\lambda = 2dSin\theta \qquad \textbf{(2. 1)}$$

Where, λ is the wavelength of X-rays, θ is the angle of incidence (called as Bragg's angle), d is inter-planar separations, and n is the order of diffraction. Each plane is characterized by miller indices given by (hkl). By knowing the wavelength of radiation and the diffraction angle, the inter-planar spacing can be easily determined from the diffraction pattern.

Powder X-ray diffraction: Experimental set up for X-ray diffraction consists of an X-ray source, sample holder, X-ray slits and a detector to pick up the diffracted X-rays. A sketch of the typical powder X-ray diffractometer is shown in the **Figure 2.1**.

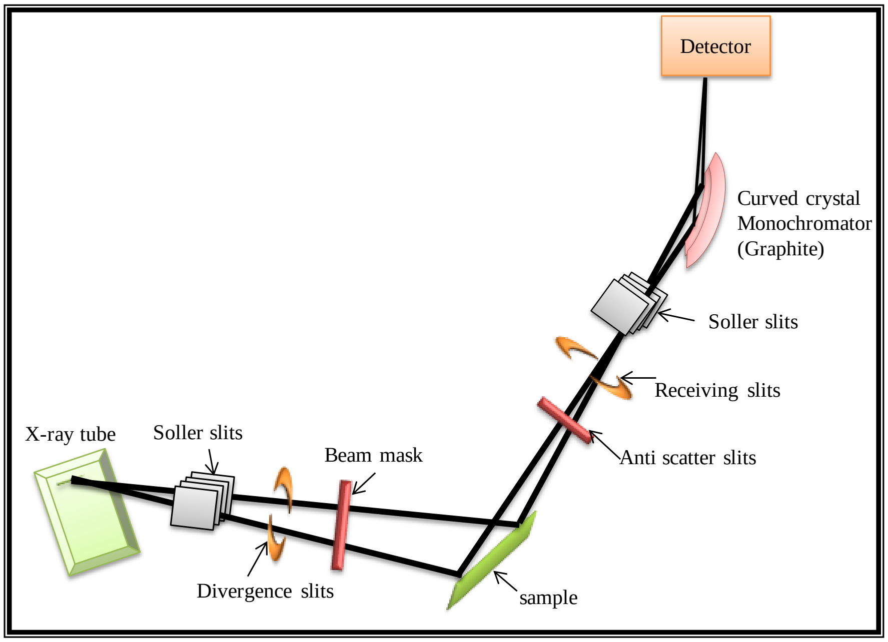

Figure 2.1: Ray diagram of a typical reflection mode diffractometer.

In the present study, the observed diffraction patterns were compared with JCPDS (Joint Committee on Powder Diffraction Standards) files available for reported crystalline samples. The unit cell parameters were refined by a least square method using the computer software “Powderx” method [224]. The average crystallite size of the nano particles was estimated from the full width at half maximum (FWHM) of the intense diffraction peaks in the XRD pattern using the Scherrer's formula, which is given as:

$$t = \frac{0.9\lambda}{BCos\theta_B} \qquad \textbf{(2. 2)}$$

Where t is the average crystallite size of the crystal (in angstroms), λ the X-ray wavelength and θ_B the Bragg angle. The line broadening, B is measured from the extra peak width at half the peak height and is obtained from the Warren formula:

$$B^2 = B_M^2 - B_S^2 \qquad \textbf{(2. 3)}$$

Where, B_M is the measured peak width in radians at half peak height and B_S is the measured peak width of a peak of a standard material (silicon).

In the present study Philips 1710 diffractometer based on the Bragg-Brentano reflection geometry was used for XRD measurements for all the samples. The Cu-Kα line was used as the incident beam with a Ni filter. The diffracted beam was monochromatised with a curved graphite single crystal. For the detection of X-rays, a proportional counter (argon filled) was attached with the diffractometer. The X-ray tube rating was maintained at 30 kV and 20 mA. The goniometer was calibrated for correct zero position using silicon standard. Samples were well ground and made in the form of a thin slide prior to mounting on the diffractometer.

2.2.2. Surface area and porosity measurements

Surface area is a physical characteristic that is important for materials that are to be used as sorbents. High surface areas imply a larger number of adsorption sites, leading to higher total adsorbate loadings as well as faster sorption kinetics. The most common method used to measure surface area of solid materials is the Brunauer-Emmett-Teller (BET) method [225] where the sample is cooled to liquid nitrogen temperatures and exposed to a gas adsorbent (typically nitrogen) and the BET equation is applied:

$$\frac{1}{\mathrm{V}\,[({P_0}/{P})-1]} = \frac{1}{\mathrm{V_m C}} + \frac{C-1}{V_m C}\left(\frac{P_0}{P}\right) \qquad \textbf{2. 4}$$

Where, V is the weight of the gas adsorbed at a relative pressure P/P_o (true equilibrium pressure/equilibrium pressure if no gas were adsorbed), $V_m$is the weight of a monolayer of adsorbate, and the term C (the BET constant) is related to the energy of adsorption of the first adsorbed layer. While using nitrogen as the adsorbate gas, a linear plot is constructed of $1/V\ [(P_o/P) - 1]$ *vs* P/P_o over an appropriate range ($P/P_o = 0.05 - 0.35$). V_m is obtained from the slope and intercept of the plot and the specific surface area is calculated using this number and the molecular cross-sectional area of the adsorbate molecule.

The constant C determines the shape of the isotherm. The higher the value of C, the more the isotherm tends to Type-II, which is desirable for accurate determination of surface area. A plot of $P/(P_o-P)$ against relative pressure P/P_o yields a straight line and from the slope $S = (C-1) / V_mC$ and intercept $I = 1 / V_mC$, V_m can be calculated as follows.

$$\mathrm{V_m} = \frac{1}{\mathrm{S+1}} \qquad \textbf{(2. 5)}$$

For many practical purposes the BET equation (2.4) is generally fitted to the data over a range $P/P_o = 0.05 - 0.3$ as at higher P/P_o values complexity associated with multilayer adsorption and/or pore condensation may arise. In the present study, QuantachomeAutosorb - 1 surface area analyser was employed. Prior to surface area determination, samples were subjected to a pre-treatment at 300 °C for ~ 5 h under vacuum so as to remove impurities such as moisture.

An understanding of the surface area and porosity of an adsorbent can be achieved by the construction of an adsorption isotherm. When the quantity of adsorbate on a surface is measured over a wide range of relative pressures at constant temperature, the result is an adsorption isotherm. The adsorption is obtained point-by-point in the Autosorb-1 by admitting to the adsorbent, successive known volumes of adsorbate, by measuring the equilibrium pressure. Similarly, desorption isotherms can be obtained by measuring the quantities of gas removed from the sample as the relative pressure is lowered. All adsorption isotherms can be grouped into five types (**Figure 2.2**[226])*viz*

Type I or Langmuir isotherms are concave to the P/P_o axis and the amount of adsorbate approaches a limiting value as P/P_o approaches 1. Type I physisorption isotherms are exhibited by microporous solids having relatively small external surfaces, for example, activated carbons and molecular sieve zeolites. The limiting uptake of adsorbate is governed by the accessible micropore volume rather than by the internal surface area.

Type II isotherms are the normal form of isotherm obtained with a nonporous or macroporous adsorbent. This type of isotherm represents unrestricted monolayer-multi layer adsorption. Point B, the start of the linear central section of the isotherm, is usually taken to indicate the relative pressure at which monolayer coverage is complete.

Type III isotherms are convex to the P/Po axis over its entire range. Type III isotherm are rarely encountered. A well-known example is the adsorption of water vapor on nonporous carbon. The absence of a distinct point B on type III isotherm is caused by stronger adsorbate-adsorbate than adsorbate-adsorbent interactions.

Type IV isotherms are associated with capillary condensation in mesopores, indicated by the steep slope at higher relative pressures. The initial part of the type IV isotherm follows the same path as the Type II.

Type V isotherms are uncommon, corresponding to the Type III, except that pores in the mesopore range are present.

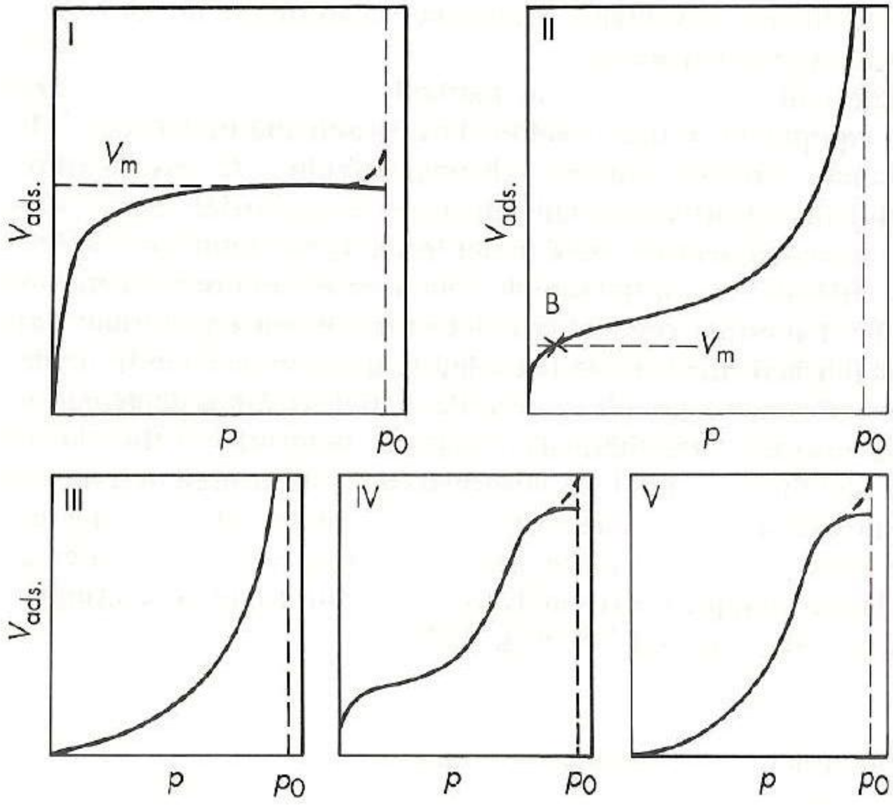

Figure 2.2: Different adsorption Isotherms (TYPE I to V) [226]

2.2.3. Inductive coupled plasma-atomic emission spectroscopy(ICP-AES)

The concentrations of the metal ions in aqueous sample were obtained using ICP-AES (8440 Plasmalab, Labtam, Australia). ICP uses a high-frequency alternating field to transfer energy to a flowing gas of argon to form plasma of ions and electrons. The plasma is propagated when ionization of neutral atoms occurs as a result of collisions with the ions and electrons. Argon is chosen because polarization of its electrons requires less energy than smaller gases.

The ICP sample were prepared by dissolving 10 mg particles in few mL of hydrochloric acid and the solution volume made up 10 mL with MilliQ. The accurate concentration of metal ions in the sample was determined by comparing the intensity of each line with the previously measured intensities of known concentrations of the elements and their concentrations are then computed by interpolation along the calibration lines.

2.2.4. Dynamic light scattering (DLS)

The hydrodynamic diameters of samples were obtained by DLS (Malvern 4800 Autosizer employing 7132 digital correlator). The light source was He-Ne laser operated at 633 nm with a maximum output power of 15 mW. It indicates the diameter including the fluid molecules around the electrostatic double layer. In this technique, random intensity fluctuations arising from the Brownian motion of colloidal particles are analysed by autocorrelation to give either a simple mean size or polydispersity (distribution width) or more complete distribution data even for multimodal distributions. Multiple DLS experiments were performed on the samples to achieve the consistency of the obtained results.

2.2.5. Zeta potential measurement

Zeta Potential analysis is a technique for determining the surface charge of nanoparticles in solution (colloids). Zeta potential is a measure of the magnitude of the electrostatic or charge repulsion or attraction between particles, and is one of the fundamental parameters known to affect stability. The zeta-potential measurements were carried out by Zetasizernano series, Malvern Instruments.

2.2.6. Transmission electron microscopy (TEM)

Transmission electron microscopy is microscopic technique where high energy beam of electron that is transmitted through an ultra-thin specimen and are detected on the other side.

TEM uses a heated pointed filament to thermionically produce electrons which then pass through an anode and into condenser lenses to vary the electron beam spot size. After passing through scan coils, the electron beam will pass through a sample and then an objective lens and aperture that eliminate highly-scattered (> 0.5^o) electrons. Enlargement of the beam is achieved with a projector lens, and the beam strikes a phosphor screen for viewing or a photographic plate for data collection. Electrons interact very strongly with matter, giving rise to the ability to use contrast for detection. Dark areas in the image represent regions where electrons do not transmit through, while lighter areas are those that are more electrons transparent.

The TEM results were analyse by using JSM-7600F JEOL JEM-2100F FEG TEM operating with a 100 kV accelerating voltage. In order to observed diffraction pattern, lattice spacing and particle size, few milligram nanoparticles sample were dispersed in isopropanol, dropped onto a carbon-coated copper grid using a pipette and allowed to air dry.

Selected area electron diffraction (SAED):

Selected area electron diffraction patterns from the sample are obtained when TEM operates in the diffraction mode. Here using an aperture in the image plane, a diffraction region from the specimen is selected. SAED patterns are a projection of the reciprocal lattice, with lattice reflections showing as sharp diffraction spots and can be used to identify crystal structures and measure d-spacing and lattice parameters.

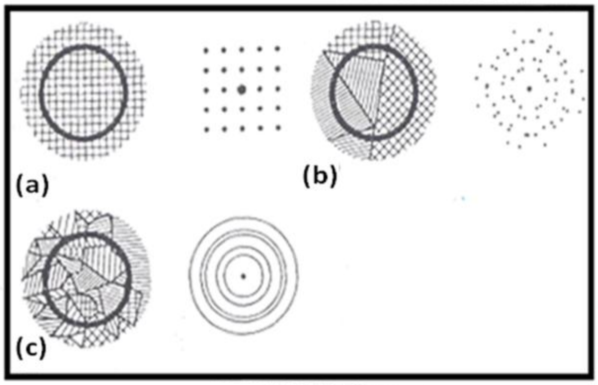

Figure 2.3: Electron diffraction in (a) single crystal, (b) polycrystalline materials and (c) nanocrystalline materials.

Schematic representation of electron diffraction pattern obtained from (a) single crystal, (b) polycrystalline material and (c) nanocrystalline material are shown in **Figure 2.3**. The electron diffraction pattern from a sample can be indexed by using the formula

$Rd = \lambda L$, where R is the radius of diffraction ring, L is camera length, λ is the electron wavelength, d is the spacing corresponding to planes.

2.2.7. Energy dispersive X-ray spectrometry (EDS)

EDS is a useful technique for confirming the chemical composition as well as the degree of chemical homogeneity present in the samples. All the elements from atomic number 4 (Be) to 92 (U) can be detected in principle, though not all instruments are equipped for 'light' elements ($Z < 10$). The X-ray mapping of samples were carried out by using EDS facility of high resolution Hitachi S-3400N scanning electron microscope and their Kα spectral profiles were obtained by using scanning transmission electron microscope (STEM) facility of JEOL JEM-2100F FEG TEM. In these techniques, a finely focused electron beam strikes the surface of a sample and generates X-ray fluorescence from the atoms in its path. The energy of each X-ray photon is characteristic of the element which produces it.

2.2.8. X-ray photoelectron spectrophotometer (XPS)

XPS or electron spectroscopy for chemical analysis (ESCA) is a well-known analytical technique that is used to determine the chemical composition of a surface in addition to the local chemical environment of a given atom. Experiments using XPS require that a sample be under vacuum, where it is bombarded with X-ray photons (200 - 2000 eV) and relies on the photoelectric effect described by Einstein in 1905 where electrons are ejected from a sample after interacting with these high energy photons. X-ray photons will interact with a sample by exchanging enough energy with core-level electrons near the surface of a material to cause electron ejection. Ejected core electrons have a specific kinetic energy (Ek) that is related to the energy of the exciting photon (hν), the binding energy of the electron to the atom (Eb) and the characteristic work function of the material (Φ) by the relation

$$E_{binding} = E_{Photon} - E_{kinetic} - \Phi \qquad \textbf{(2. 6)}$$

Where, $E_{binding}$ is the energy of the electron emitted from one electron configuration within the atom,E_{photon} is the energy of the X-ray photons being used, $E_{kinetic}$ is the kinetic energy of the emitted electrons as measured by the instrument and Φ is the work function of the spectrometer (not the material).

Binding energy is used to determine the oxidation state of elements, and the integrated electron signal can be used to quantitate the elemental composition of a surface.

The XPS study of the samples were carried out on VG model - ESCALAB MK 200X spectrometer equipped with an Al Kα source (1486.6 eV) and calibrated with Au $4f_{7/2}$ line at 84.0 eV from a specimen of Au film on Si substrate. A few milligram of well-ground sample powder was spread uniformly over indium foil and pressed. The foil was attached to a stainless steel stub for mounting to the X-Y-Z translator of the XPS system. The appropriate corrections for charging effect were made with the help of a weak C 1s signal appearing at 285.1 eV.

2.2.9. UV-Visible spectrophotometer

The principle of UV-visible absorption spectroscopy is based on the "Beer-Lambert's Law", which states that "A beam of light passing through a solution of absorbing molecules transfers energy to the molecules, as it proceeds, and, therefore, decreases progressively in intensity". The decrease in the intensity, or irradiance, (dI), over the course of a small volume element is proportional to the irradiance of the light entering the element, the concentration of absorbers (C), and the length of the path through the element, (dl) Mathematically, it can be expressed as:

$$A = \varepsilon \times b \times c \qquad \textbf{(2. 7)}$$

where, ε is the wavelength-dependent molar absorptivity coefficient, *b* is the path length, and *c* is the concentration

When the energy of the incident photon matches with the energy of the excited state of an atom, a molecule, radical or an ion the resonance occurs, and the intensity of the transmitted light is decreased. Depending on the energies of the excited states and the absorbed photons a sorption band is observed. In the present studies, UV-visible optical absorption spectra have been recorded, employing a JASCO Model 605 spectrometer.

2.2.10. Photoluminescence spectroscopy (PL)

Photoluminescence spectroscopy is a non-contact, non-destructive method of probing the electronic structure of materials. In essence, light is directed onto a sample, where it is absorbed and where a process called photo-excitation can occur. The photo-excitation causes the material to jump to a higher electronic state, and will then release energy, (photons) as it relaxes and returns to back to a lower energy level.

In the present study all luminescence measurements were carried out by using an Edinburgh Instruments' FLSP 920 system, having a 450W Xe lamp, 60 W microsecond flash lamp and hydrogen filled nanosecond flash lamp (operated with 6.8 kV voltage and 40 kHz pulse frequency) as excitation sources for steady state and for lifetime measurements. Red sensitive PMT was used as the detector.

2.2.11. Raman spectroscopy

Raman spectroscopy is a very convenient technique for identification of crystalline or molecular phases, for obtaining structural information. Backscattering geometries allow films, coatings and surfaces to be easily analyzed. Ambient atmosphere can be used and no special sample preparation is needed for analyzing samples by this technique. The principle is briefly described below. When an intense beam of monochromatic light is passed through a substance, a small fraction of light is scattered by the molecules in the system. The electron cloud in a molecule can be polarized (deformed) by the electric field of the incident radiation. If we apply an oscillating electric field (the electric field vector of the light wave) to the molecule, the deformation of the electron cloud will also oscillate with the same frequency (V_o) of the incident light beam. This oscillation of the electron cloud produces an oscillating dipole that radiates at the same frequency as the incident light. This process is called Rayleigh scattering. The Rayleigh-scattered radiation is emitted in all directions. Since only about 0.1 % of the light is scattered, we must use as intense a source as possible and a laser fulfills this requirement admirably. There is a small but finite probability that the incident radiation will transfer part of its energy to one of the vibrational or rotational modes of the molecule. As a result, the scattered radiation will have a frequency V_o - V_m, where V_m is the absorbed frequency. Similarly, there is a slight chance that molecules in excited vibrational or rotational states will give up energy to the light beam. In this case the scattered radiation will have a higher frequency (V_o + V_m). Thus, it is possible to observe

The Raman scattering measurement was performed on Lab RAM HR 800 micro-Raman spectroscopy at back scattering geometry using the 519.261 nm line of an Ar^+ laser as an excitation source with a power of 18 meV.

2.2.12. Thermogravimetric analysis and Differential thermal analysis (TG-DTA)

The thermo gravimetric (TG) analysis is based on the principle of monitoring the known mass of a material or a mixture as a function of temperature, using a thermo balance of high sensitivity, during a predetermined heating or cooling cycle. The weight changes can be monitored during heating as well as cooling or as a function of time (isothermal) in a specified atmosphere. In differential thermal analysis (DTA), difference in the temperatures between the sample under study and an inert reference material is recorded as a function of temperature, as both are simultaneously heated or cooled at a predetermined rate. If there is no heat changes associated with the sample during the temperature range of interest, the DTA scan will show a steady base line. On the other hand, if there is any physical or chemical change (any heat change) taking place in the sample, the temperature of the sample will either lag behind or increase with respect to that of the reference and the difference in the temperature is recorded as a peak. The area under the peak represents the total heat change. The peak obtained for endothermic and exothermic reactions are in opposite directions.

The simultaneous TG/DTA experiments were performed using a SETARAM simultaneous TG/DTA instrument, model 92-16.18, with the heating rate of 10 °C/min.

The sample and reference material (alumina) were placed in two identical platinum crucibles. The weight loss of the sample as a function of temperature was monitored with the help of a thermo-balance whereas difference in temperatures between sample and reference material, as well as sample temperature was monitored simultaneously using two different thermocouples. In the present study simultaneous TG/DTA technique was used to determine the decomposition behavior, phase changes, loss of water and thermal stability of different samples

The chemical changes (removal of solvent and organic molecules, occurrence of thermal decomposition) during thermal treatment were analysed by TGA, Model Q50, V6.1 series, TA Instruments, USA under N_2 atmosphere from room temperature to 550 °C with a heating rate of 10 °C/min.

2.2.13. Fourier transforms infrared spectroscopy (FTIR)

Vibrations of bonds and groups which involve a change in the dipole moment results in the absorption of infrared radiation which forms the basis of IR spectroscopy. Modern IR instruments are based on Fourier transformation method to improve the signal to noise ratio. Unlike conventional IR instrument, in FTIR instrument, all the frequencies are used simultaneously to excite all the vibrational modes of different types of bonds/linkages present in the sample. This reduces the experimental time considerably.

In the present study all infrared experiments were carried out using a Bomem MB102 FTIR machine having a range of 200-4000 cm^{-1} and with a resolution of 4 cm^{-1}. IR radiation was generated from globar source (silicon carbide rod). The instrument used CsI single crystal, as the beam splitter and deuteratedtriglycinesulphate (DTGS) as detector. Prior to IR measurements, the samples were ground thoroughly by mixing with dry KBr powder, made in the form of a thin transparent pellet and introduced into the sample chamber of the instrument to record the spectra.

2.2.14. Carbon - Hydrogen - Nitrogen (CHN) analysis

The elemental analysis was carried out by FLASH EA 1112 series CHNS (O) analyser (Thermo Finnigan, Italy). It determines the percentages of carbon, hydrogen and nitrogen of organic compounds coated on the surface of samples, based on the principle of "Dumas method" which involves the complete and instantaneous oxidation of the sample by "flash combustion". The combustion products are separated by a chromatographic column and detected by the thermal conductivity detector, which gives an output signal proportional to the concentration of the individual components of the mixture.

2.2.15. Magnetic measurments

The magnetic properties of the samples were measured by Vibrating Sample Magnetometer (Lakeshore, VSM – 7410) and Physical Property Measurement System (PPMS, Quantum Design). The principle of VSM is the measurement of the electromotive force induced by magnetic sample when it is vibrating at a constant frequency, under the presence of a static and uniform magnetic field. The room temperature field dependent magnetic measurements (M vs. H) were carried out on powder samples mounted tightly in the sample holder by varying the magnetic field. The magnetization vs. temperature (M *vs*.T) was measured by VSM-7410 under a constant applied magnetic field to obtain the Curie temperature (T_c) of the sample. The temperature dependent magnetization under zero-field cooled (ZFC) and field-cooled (FC) conditions in a constant applied field were measured by PPMS. In the ZFC measurements, the samples were cooled from 305 to 5 K without applying an external field. After reaching 5 K, a field was applied and the magnetic moments were recorded as the temperature increased. For FC measurements, the samples were cooled from 305 K under an applied field; then the magnetic moments were recorded as the temperature increased.

2.2.16. Nuclear magnetic resonance (NMR) spectroscopy

Nuclear magnetic resonance spectroscopy is a technique that exploits the nuclear magnetic properties of atomic nuclei and can give valuable information about the structure, dynamics and chemical environment of around a particular nucleus in a molecule/ lattice.

Chemical shift: The chemical shift of any nucleus is defined as the difference between its resonance frequency and the resonance frequency of the same nuclei in a reference sample and can be expressed by the Equation (2. 8.)

$$\delta = \frac{\omega - \omega_0}{\omega} \times 10^6 \qquad \textbf{(2. 8.)}$$

Where, ω, $\omega_O$represent resonance frequencies of nuclei in the sample and in the reference, respectively.

Chemical shielding interaction: Chemical shift arises because of the effective magnetic field experienced by nuclei is brought about by the polarization effect of electron cloud around the nuclei created by the applied magnetic field. Since this is particularly sensitive to the configuration of valance electrons, which is governed by the nature of chemical bonding, this aspect has been labeled as chemical shielding interaction.

2.3. Sorption studies

The sorption experiments were carried out in batch mode where in 10 mL of the solution containing the solute of known concentration, at a particular pH was equilibrated with a fixed amount of sorbent for a definite period of time. Once equilibration is over, the two phases, namely solid and liquid are separated by centrifugation and the liquid phase is analysed for the amount of the solute left behind. The amount taken up by the sorbent, which can be calculated from the difference of initial and final concentrations in solution, can be expressed either as % sorption or mg/g of sorbent. Various experimental factors were optimized at room temperature to get maximum uptake. The concentration variation studies were carried out using 10 mL of solutions containing different concentration of the metal ion, adjusted to a fixed pH and equilibrated with 0.1g of the solute for a period of one hour. The kinetic studies were carried out by fixing the other parameters like concentration, pH, amount of sorbent and equilibrating the solution for different periods of time. The effect of sorbent amount was also varied to get the maximum uptake. The sorption was also studied as a function of varying concentrations of solute solution.The error in the measurements by ICP-AES obtained with replicate measurements was found to be around 5%.

$$\text{Removal efficiency (\%)} = \frac{(C_o - C_t)}{C_o} \times 100 \qquad \textbf{(2. 9)}$$

$$q_e = (C_o - C_t) \times V/M \tag{2. 10}$$

where, C_o and C_t are the initial and residual concentration of metal ions (mg/L) in aqueous solution, V is the total volume of solution (L) and M is the adsorbent mass (g). Further to examine the feasibility of recycling nanoadsorbents, desorption studies were performed at weak acidic medium 50 mg in 10 mL of 0.1 M HCl/ EDTA. The above mixture was further kept for 24 h at room temperature for desorption of metal ions. The desorption ratio of metal ions was determined using the following equation:

$$\text{Desorption ratio (\%)} = \left(\frac{\text{Amount of desorbed metal ion}}{\text{Amount of adsorbed metal ion}}\right) \times 100 \tag{2. 11}$$

2.3.1. Sorption isotherm

2.3.1.1. Langmuir isotherm

Langmuir was the first to propose a coherent theory of sorption onto a flat surface based on a kinetic viewpoint. The Langmuir sorption model is one of the best known and most frequently applied isotherms. The Langmuir equation initially was formulated on the basis of a dynamic equilibrium between the sorbent and the sorbate, that is, the rate of sorption (which is the striking rate at the surface multiplied by a sticking coefficient, sometimes called the accommodation coefficient) is equal to the rate of desorption from the surface. The assumptions of the Langmuir model are:

1. Surface is homogeneous, that is, sorption energy is constant over all the sites

2. Sorption on the surface is localized, that is, atoms or molecules are sorbed at definite, localized sites
3. Each site can accommodate only one molecule, or atom

Langmuir proposed that the rate at which the sorbate molecules (B) strike a surface of a sorbent (A) is proportional to the product of the concentration of the sorbent and the fraction of the surface remaining uncovered by sorbate. Langmuir [227] can be used to compare the sorption efficiency of various sorbents. The assumptions of this model are that adsorption is monolayer and occurs at finite defined localized identical and equivalent sites with no hindrance from each other. The mathematical expression of Langmuir isotherm is given by Equation (2. 12). The main aspect of Langmuir isotherm can be expressed by R_L, [227, 228] a constant known as the constant separation factor or equilibrium parameter which can be used to predict if an adsorption system is "favourable" or "unfavourable". The separation factor, R_L is defined by Equation.(2. 13), where C_o is the initial solute concentration (mg/L) and b is the Langmuir adsorption equilibrium constant (L/ mg). The value of R_L value indicates the adsorption nature; it can be unfavourable ($R_L > 1$), linear ($R_L = 1$), favourable ($0 < R_L < 1$) or irreversible ($R_L = 0$).

$$\frac{C_e}{q_e} = \frac{1}{Q^0 \times b} + \frac{C_e}{Q^0} \qquad \textbf{(2. 12)}$$

$$R_L = \frac{1}{1 + C_e \times b} \qquad \textbf{(2. 13)}$$

2.3.1.2. Freundlich isotherm

The Freundlich isotherm [229] is the earliest known relationship that describes the non-ideal and reversible adsorption and can be applied to multilayer adsorption. The linear form of the equation is given in Equation. (2.16), and the slope gives the value of n which is a measure of sorption intensity or surface heterogeneity and the sorption is termed chemisorption when the value is between 0 and 1. The value of n if within the range of 1-10, indicates favourable sorption.

$$\ln q_e = \ln K_f + \frac{1}{n}\ln C_e \qquad \textbf{(2. 14)}$$

2.3.1.3. Temkin isotherm

Temkin isotherm [230] considers a heterogeneous surface, where no molecular interaction exists. It is based on Langmuir sorption isotherm. However, like Langmuir model, it does not take into account the lateral interaction between the sorbates. Temkin isotherm assumes that the decrease in the heat of sorption as a function of temperature is linear rather than logarithmic. The heat of sorption of all the molecules in the layer would decrease linearly with coverage due to sorbate-sorbent interactions [231]. The linear form of the Temkin model is given as,

$$q_e = \frac{RT}{b}\ln A_T + \frac{RT}{b}\ln C_e \qquad \textbf{(2. 15)}$$

The model is expressed by Equation (2. 15), where A_T (L mg^{-1}) is the Temkin equilibrium binding constant, and b (dimensionless) is the Temkin isotherm constant. R is the gas constant, and T is the absolute temperature. A linear plot of qe*vs*ln (C_e) enables the determination of the isotherm constants KT and b, from the intercept and slope, respectively.

2.3.1.4. Dubinin-Redushkevich isotherm

The Dubinin–Radushkevich isotherm is an empirical model initially conceived for the adsorption of subcritical vapors onto micro porous solids following a pore- filling mechanism. This model is often successful for high and intermediate concentration ranges but deviates at lower concentration. This has been used to distinguish the physical and chemical adsorption of metal ions [232]. The model is expressed by Equation 2.18,

$$\ln q_e = -\beta\varepsilon^2 + \ln Q \tag{2. 16}$$

$$E_s = \frac{1}{\sqrt{2 \times \beta}} \tag{2. 17}$$

Where $\beta$is the degree of heterogeneity ($0 < \beta < 1$) and **ε**is the Polanyi potential= $RT \ln(1+1/C_e)$. The apparent energy of sorption E_s which is the mean free energy of sorption per molecule of sorbate when it is sorbed from infinity in the solution to the surface of the solid and can be computed from the parameters obtained from Dubinin- Radushkevich isotherm model using Equation 2.19.

2.3.2. Kinetic isotherm

Sorption kinetics describes the time-dependent evolution of the sorption process until equilibrium is reached. Such studies yield information about the possible mechanism of the sorption and the different transition states involved on the way to the formation of the final sorbate-sorbent complex. The results of such study help to develop appropriate mathematical models, to describe the interactions. Among the most popular kinetic models/equations are the so-called "pseudo-first-order" and "pseudo-second-order" rate expressions.

2.3.2.1. Pseudo first-order kinetic model

Lagergren equation is probably the earliest known one, describing the rate of sorption in the liquid-phase systems. This equation is called the pseudo first-order equation, or the Lagergren's rate equation, and can be written as [233, 234]

$$\log(q_e - q_t) = \log q_e - \frac{k_{ads} \times t}{2.303} \qquad \textbf{(2. 18)}$$

Where q_t is the amount of sorbatesorbed at time t, and k_{ads} is the rate constant of the first order sorption.

The values of k_{ads} and q_e can be determined from the slope and intercept, respectively, of the straight line plot of log (q_e - q_t) versus t. Determining $q_e$accurately is a difficult task, because, in many sorbate-sorbent interactions, the chemisorption becomes very slow, after the initial fast response, and it is difficult to ascertain whether equilibrium is reached or not. Therefore, it has been reported that, many sorption processes follow Lagergren pseudo first-order model only for the initial 20 to 30 min of interaction. The value of k_{ads}parameter, also called time-scaling parameter, decides how fast the equilibrium in the system can be reached. The experimental studies have confirmed that the value of k_{ads} parameter can be both dependent and independent of the applied operating conditions. Its value depends on the initial concentration of the sorbate. It usually decreases with the increasing initial sorbate concentration in the bulk phase. Since the model does not describe the interactions for the whole range of contact time, in many cases, higher order kinetic models are employed to analyse the experimental results.

2.3.2.2. Pseudo second-order kinetic model

The pseudo second-order kinetics is usually associated with the situation, when the rate of direct sorption/desorption process (seen as a kind of chemical reaction) controls the overall sorption kinetics. The pseudo second-order kinetic model is expressed as [235]:

$$\frac{t}{q_t} = \frac{1}{k_{2ads} \times q_e^2} + \frac{t}{q_e} \qquad \textbf{(2. 19)}$$

Where k_{2ads} is the rate constant of the pseudo second-order sorption. The plot of t/q_tvs t gives a straight line, from the slope and intercept of which, the values of q_e and h, respectively, can be determined. Once the value of $k_{2ads}q_e^2$ is known, the value of k_{2ds} can be determined there from. Many reports are available in literature, indicating that the value of k_{2ads} has strong dependence on the applied operating conditions, such as the initial solute concentration, pH of solution and temperature, etc[236].

2.3.2.3. Intraparticle diffusion model

This model is represented by the following equation [237]

$$q_t = k_d t^{0.5} + I \qquad \textbf{(2. 20)}$$

wherek_d is the intraparticle diffusion rate parameter and I (mg/g) is a constant that gives an idea about the thickness of the boundary layer. The values of k_d and I can be determined from the slope and the intercept, respectively, of the plot of q_t*vs* $t^{1/2}$. Intraparticle diffusion process involves the migration of ions into the internal surface of the sorbent particles through pores of different sizes. Boundary layer diffusion and the rate of surface sorption affect the intraparticle diffusion. These factors, along with the intraparticle diffusion rate, are dependent on surface characteristics of the sorbent [238].

2.3.2.4. Boyd plot

In order to further confirm whether the sorption proceeds via film diffusion or intraparticle diffusion mechanism, the kinetic data can be analyzed, using the kinetic expression given by Boyd et al. [239]

$$B \times t = -\ln(1-F) - 0.4977 \qquad \textbf{(2. 21)}$$

Wherein, $F = q_t/q_e$; q_t and q_e are the amounts of metal ion sorbed on the surface ($\mu g \cdot g^{-1}$) at time t and at equilibrium respectively. These were used to calculate the effective diffusion coefficients D_i ($cm^2 \cdot s^{-1}$) using Equation 2.24, where r is the radius of the particles.

$$B = D_i \times \left(\frac{\pi}{r}\right)^2 \qquad \textbf{(2. 22)}$$

The linearity of B_t*vs*. t plot provides useful information to distinguish between the film diffusion and the intraparticle diffusion rates of sorption [240]. A straight line passing through the origin is indicative of sorption processes only governed by intraparticle-diffusion mechanisms, otherwise, it is governed by film diffusion [241].

2.4. Photo catalytic degradation of dye

The molybdenum doped TiO_2 samples were evaluated as photocatalysts for the degradation of Rhodamine B (Rh-B) dye in the presence of UV light. A 100 ml batch cylindrical pyrex glass reactor (basically a glass beaker) was employed. The irradiation source was a 400W medium pressure Hg lamp (SAIC) located inside a quartz tube, situated perpendicularly in the reactor with 170 mW/cm^2 flux. The white light source simulating the visible spectrum emits in the 350-700 nm range with a peak around 430 nm and a flux of 234 mW/cm^2 range. For each set of experiments, the reaction mixture consisted of 50 mg of catalyst powder suspended in 100 ml of the dye solution ($\sim10^{-5}$ M). The suspension was magnetically stirred for 30 min in the dark to establish adsorption/desorption equilibrium. The dye-catalyst suspension was irradiated under UV light and small aliquots were withdrawn at regular intervals of time (keeping the volume of reaction mixture almost constant) and UV-visible spectra were recorded. A blank consisting of only aqueous Rh-B solution (dye, without the catalyst, was also subjected to same procedure to cancel the effect of self-degradation of the dye). The extent of reaction was monitored by measuring the decrease in absorbance values using a spectrophotometer.

2.5. Induction heating experiments

Induction heating of magnetic nanoparticles (MNPs) was performed in plastic micro-centrifuge tube (1.5 mL) using instrument (Easy Heat 8310, Ambrell, UK) with 6 cm diameter (4 turns) coil. To keep the coil at ambient temperature, water circulation to coils was provided. MN (2-10 mg) dispersed in 1 mL of distilled water were placed at the centre of coil and the applied frequency was 265 kHz. Samples were heated for 10 min. for desired current (200-400 A). For the conducted experiments, magnetic field was calculated from the relationship:

$$H = 1.257ni/L \text{ (in Oe)} \qquad \textbf{(2. 23)}$$

Where, n, i and L denote the number of turns, applied current and the diameter of the turn in centimetres, respectively. Calculated values of magnetic field (*H*) at 200, 300 and 400 A were 168, 251 and 335 Oe (equivalent to 13, 20 and 27 kA/m), respectively. Heat generation from the sample was measured by the temperature probe (Palm Sense based on fibre optics).

Principle: When highly dispersed magnetic nanoparticles are subjected to applied ac magnetic field, the magnetic particles can experience a self-heating due to hysteresis loss, relaxation loss and eddy current (ED) [242].

According to Faraday's and Lenz's law, the heat loss due to ED is due to the interaction between the conductive material and oscillating magnetic field which can be represented as:

$$ED = \frac{\mu\pi d f H_0}{20\rho} \qquad \textbf{(2. 24)}$$

Where μ is the permeability of a material, d the diameter of the particle and ρ the resistivity of the material. These magnetic nanoparticles are semiconductors/insulators, which have significantly high resistivity ($\rho = \sim 10^2$ Ohm cm). Thus the heat generation due to eddy current is negligible.

Hysteresis loss in AC magnetic field is given by:

$$Area = f \int MdH \tag{2. 25}$$

Where f is the frequency of AC magnetic field and it is represented as $f = \omega/2\pi$, M, magnetization, H applied magnetic field. The ratio of magnetization M to the applied magnetic field H is defined as the susceptibility (χ). In AC field the susceptibility (χ) is expressed as real (χ') and imaginary (χ'') terms out of which the imaginary part is related to the heat dissipation of the system. Heat/power dissipation of the total system is expressed as:

$$P = \boldsymbol{\mu_0 \pi \chi'' f H_0^2} \tag{2. 26}$$

Where μ_0 is the permeability of free space. The imaginary term is expressed as:

$$\boldsymbol{\chi'' = \frac{\omega\tau}{1 + (\omega\tau)^2}\chi} \tag{2. 27}$$

Where τ is the total relaxation contributed by Brownian relaxation (τ_B) and Néel's relaxation (τ_N). In former the magnetic moment is aligned with the applied magnetic field (H) where particles rotate in AC field due to which they collide with the surrounding medium and thus cause heating. While later relaxation is due to the magnetic spin domain rotation from 0–180°.The Brownian relaxation occurs in all dispersed nanoparticles, whereas Néel relaxation occurs in superparamagnetic particles [242]. At a particular temperature T, Brownian relaxation is given by:

$$\tau_B = \frac{4\pi\eta r_h^3}{k_B T} \tag{2. 28}$$

Where $\tau_B$the Brownian relaxation time, k_B the Boltzmann constant, T the temperature, η the viscosity andr_h the hydrodynamic radius of the particle.

Whereas Néel relaxation is given by:

$$\tau_N = \tau_0 e^{\Delta E/k_B T} = \tau_0 e^{KV/k_B T} \quad \textbf{(2. 29)}$$

Where τ_0 is of the order of 10^{-9} s and ΔE, the anisotropic energy barrier which can be defined as the product of anisotropic energy constant (K) and volume (V), k_B, Boltzmann’s constant and T, the temperature. Néels relaxation is fast for the small particles. When small particles are dispersed, the particle spin relaxation of the nanoparticles gets accelerated. Thus the combined relaxation is expressed as:

$$\frac{1}{\tau} = \frac{1}{\tau_B} + \frac{1}{\tau_N} \quad \textbf{(2. 30)}$$

For small particles where the particle size is less than that of the critical size (that is a single domain particle in size), the heating caused is mainly due to the contribution of Brownian and Néel’s relaxations and some contribution from frequency, which can give hysteresis loss. Heat-generation is dependent on frequency and applied magnetic field. The density of the particle relates the loss power density P with specific absorption rate (SAR) which can be calculated using following relation:

$$SAR = c\frac{\Delta T}{\Delta t}\frac{1}{m_{magn}} \quad \textbf{(2. 31)}$$

Where, c is the sample specific heat capacity, which is calculated by considering both sample weight and weight of water. Specific heat capacity of sample is neglected as its contribution is very small due to small weight. Thus the specific heat capacity of water is considered to represent the total heat capacity of the sample that is 4.18 J g^{-1} K^{-1}. $\Delta T/\Delta t$ is the slope of the time dependent temperature curve obtained at 400 A for 5 mg of the nanoparticles weight. $m_{magn}$is the amount of magnetite or Fe in the 1 mL system.

As the SAR values Heat-generation/dissipation is dependent on frequency and applied magnetic field So to allow direct comparisons between SLP measurements performed in various laboratories and under different AC field strength and frequency conditions, intrinsic loss power (ILP) has been defined as [243]:

$$ILP = \frac{SAR}{H^2 f} \tag{2. 32}$$

This equation is valid under frequencies of up to several MHz; and also provided the applied field strength H is well below the saturation field of the magnetic nanoparticles.

2.6. Biocompatibility

2.6.1. MTT assay

The biocompatibility of the nanoparticles with MG63 (Osteosarcoma) cells were evaluated using the 3-(4,5-dimethylthiazol-2-yl)-2,5-diphenyltetrazolium bromide (MTT) assay. MG63 cells were obtained from the National Center for Cell Sciences (NCCS), Pune, India and routinely cultured in MEM (Sigma Inc. MO, USA) supplemented with 10 % serum (Invitrogen CA, USA) and antibiotic solution. For biocompatibility study, the cells were first seeded into a 96-well plate at densities of 1×10^3 cells per well for 24 h. Then different concentrations of nanoparticle suspension (0, 1.2, 9.65, 33.45, 50, 100 and 250 μg/ml) were added to each wells and incubated for another 24 h in 5 % CO_2 at 37 ^oC. The cells supernatant was discarded and thereafter, 10 µl of MTT solution (5 mg/ml) was added and incubated for 4 h. Formazan crystal was solubilized by addition of 200 µl of solubilizing buffer (20 % SDS in 50 % DMF). The 96-well plate was centrifuged at 2000 rpm for 5 min and kept on magnetic rack for an hour. Supernatant was transferred into a new 96-well plate and absorbance was measured at 570 nm with reference to 630 nm in BioTek Universal Microplate Reader (BioTek Inc. USA). The percentage of cell proliferation was calculated as ratio of optical density (OD) of treated and control cells multiplied by 100. Further, the cytotoxicity of pure DOX and DOX- loaded particles (0.125 and 1 μM DOX) were also evaluated using the MTT assay. The drug concentrations were chosen based on the 50% inhibitory concentration (IC50) value of DOX for MG63 cells. For IC50 value of DOX, 1×10^3 cells were incubated with different amount of DOX (0.015-5μM) for 24 h and then processed for MTT assay. The experiments were performed in triplicate.

2.6.2. SRB assay

The biocompatibility of the nanoparticles in HeLa cells was done using sulforhodamine-B (SRB) assay The cells were seeded into 96-well plates at densities of $1\text{x}10^5$ cells per well for 24 h. MNPs with 0 – 1 mg/mL dispersed in NaCl solution was added to the cells and incubated for 24 h at 37 ^{o}C in the atmosphere of 5% CO_2. Thereafter, the cells were washed thrice with phosphate buffered saline (PBS) and the cells were processed for SRB assay to determine cell viability. For this, cells were fixed with a solution of 50% cold trichloroacetic acid (25 mL) and stained with 0.4% SRB dissolved in 1% acetic acid. Cell-bound dye was extracted with unbufferedtris buffer solution (100 mL, 10 mM, pH 10.5), and then the optical density (OD) was measured at 550 nm using a microplate spectrophotometer (Model 680, Bio-Rad, Japan). The experiments were performed in triplicate.

Chapter 3

ZnO based nanosorbents

1. *Kinetic modeling: dependence of structural and sorption properties of ZnO—crucial role of synthesis*
   Jerina Majeed, Jayshree Ramkumar, S. Chandramouleeswaran, O. D. Jayakumar and A. K. Tyagi
   RSC Adv., 2013, 3, 3365-3373.

2. *Highly Selective Uptake of Copper (II) Ions from Aqueous media using nanosorbents in batch mode*
   Jerina Majeed, Jayshree Ramkumar, S. Chandramouleeswaran and A. K. Tyagi
   Adv. Porous Mater., 2014, 2, 1-10.

3. *Effect of synthesis protocol on the surface charge of Zinc oxide nanoparticles and its consequence on sorption ability*
   Jerina Majeed, Jayshree Ramkumar, S. Chandramouleeswaran and A. K.Tyagi
   Sep. Sci.Tech., 2015, 50, 404-410.

3.1. Introduction

The importance of water is appreciated as it is the essence of life. There is now a growing awareness of the nature of the water contamination and getting clean and affordable potable water is a global concern. Therefore, the first step in this direction is to minimize the discharge of the toxic species into the water system. The second step, of course, is to treat the contaminated water and remove the various toxic species present in the water system.

The rapid industrial development has resulted in the pollution of the environment and thus making environmental remediation a crucial aspect. Often discharges from various industries contain heavy metals and organic pollutants, which are toxic and cause severe problems ranging from gastroenteritis to more severe ailments like cancer. Because heavy metals are not biodegradable in natural conditions, they tend to accumulate in living organisms causing various diseases and disorders [244]. Furthermore, the presence of heavy metal ions in waste water inhibits biodegradation of organic pollutants, which might be present in the waste water [245].Therefore; their concentrations in water must be reduced to acceptable levels before discharging them into the environment. Removal of these toxic species is being carried out using different procedures like chemical precipitation [246], sorption [179, 247, 248] etc. Sorption using different sorbents with good thermal stability is an efficient and versatile method for removal of heavy metals when combined with appropriate desorption. Sorption also offers an additional advantage of regeneration of used sorbents thus making it possible to use novel materials that possess excellent sorption properties, but are costly. Thus, it is of growing interest to researchers to develop newer sorbents with multi-functional properties. Recently, significant approaches have been made for the development of cheaper and effective adsorbents which are even made commercially available, such as Perlite [249], activated carbon [250], activated alumina [251], silica gel [252], glasses [253] and polymeric porous materials/frameworks [254]. However, these adsorbents suffer from inefficient extraction and almost all of them become problematic about recycling and reuse. In the present scenario, although being strongly desired, a high-performance yet low-cost adsorbent that is easily separable and easily regenerated is still not available.

Nanomaterials play a significant role in shaping of our current environment by providing new materials, remediation/treatment techniques and sensors for monitoring purposes [255]. Chemical reactivity and catalytic activity of nanomaterials also depend on size and it is seen that smaller the nanomaterials, more the surface activity, thus they could be good adsorbents owing to their high specific surface area and surface activity. ZnO NPs are extensively used as a promising candidate for photocatalyst [12, 45, 256, 257], sensor [258-261], solar cell [33, 262, 263]. ZnO is a biodegradable material and its surface can be easily functionalized with many functional groups, such as acetate groups, hydroxyl groups, etc. which can be active sites for adsorption [264-267] making it an excellent candidate as adsorbent for wastewater treatment. However, the reports on the use of nanostructured ZnO as sorbents for environmental remediation are very limited, to the best of our knowledge [34, 47, 268-270].

The present chapter elucidates the possibility of fine tuning the surface charge by changing the synthesis protocol for the nanoparticles and henceforth, its efficiency as sorbents for removal of various cationic and anionic species. ZnO nanoparticles synthesized by different procedures like pyrolysis, gel-combustion and co-precipitation were characterized in-detail and their sorption characteristics with respect to different toxic species were studied. Various factors that affect the sorption have been varied to get a complete insight of the sorption.

3.2. Results and discussion

3.2.1. Characterization of nanomaterials

The XRD patterns shown in **Figure 3.1** for ZnO NPs prepared by different methods, matched well with that of pure ZnO (JCPDS No.36-1451), indicating that the sample has a polycrystalline hexagonal wurtzite structure. Though different synthesis protocols were used, the resulting nanoparticles have the same crystalline structure. Moreover, it was observed that there were no other peaks indicating the absence of any impurities. The ZnO NPs prepared by pyrolytic, combustion and co-precipitation methods were referred to hereafter as ZnO-Py, ZnO-GC and ZnO-CP, respectively.

The average crystallite size of these samples was calculated using Scherrer's equation and represented in **Table 3.1**. To explore the surface of the nanoparticles, surface area measurements and infrared spectroscopic (IR) studies were performed on the as-synthesized nanoparticles (summarized in **Table 3.1**).

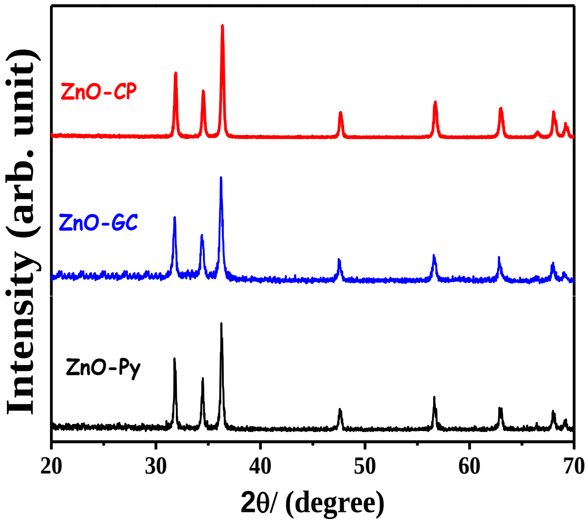

Figure 3.1: XRD patterns of the ZnO NPs prepared by pyrolytic (ZnO-Py), combustion (ZnO-GC) and precipitation (ZnO-CP) methods.

Table 3.1: Various physical characteristics of the ZnO NPs prepared by different methods.

Physical Characteristics	**ZnO-GC**	**ZnO-Py**	**ZnO-CP**
Average crystallite size(nm)	29	46	20
Surface area (m^2/g)	48.1	47.3	20.6
Pore volume (cm^3/g)	0.75	0.11	-

Nitrogen adsorption−desorption isotherms and Barrett−Joyner−Halenda (BJH) pore-size distribution curves were used to determine the specific surface area and pore size and pore volume of the synthesized zinc oxide nanoparticles. It is seen from the results that porous structures are present in the synthesized samples and the method of preparation affects the pore size and co-precipitation procedure results in much smaller nanoparticles with lower surface area (ZnO-GC > ZnO-Py > ZnO-CP) as compared to gel combustion and pyrolysis methods, due to higher calcination temperature.

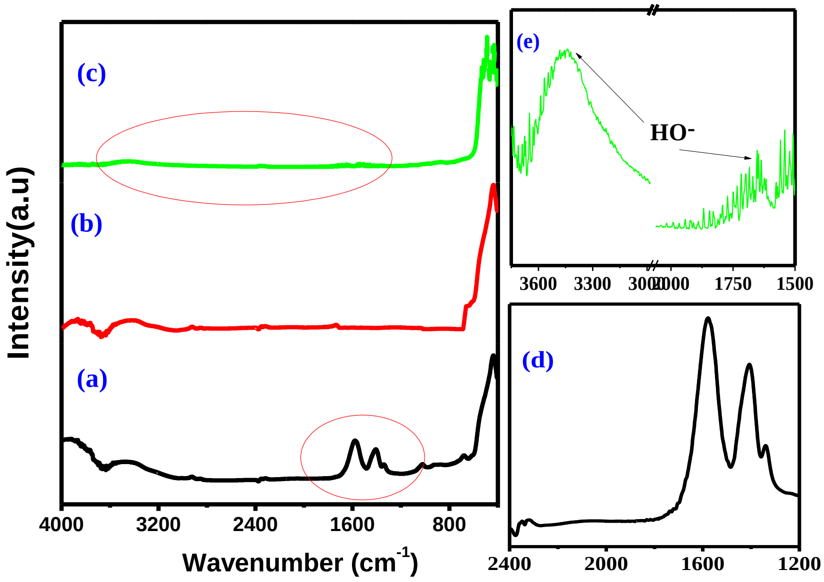

Figure 3.2: IR spectra of (a) ZnO-Py (b) ZnO -GC (c) ZnO- CP (d) and (e) represent the enlarged view of the spectra at selected wavelength for ZnO-Py and ZnO-CP, respectively.

IR spectra of these three samples (**Figure 3.2**) showed peaks at ~440 cm^{-1} corresponding to the stretching vibrations of Zn−O and the broad absorbance peak around 3500 cm^{-1} corresponding to the surface adsorbed OH groups. In the case of ZnO-Py, in addition to those bands, there are three intense bands centered at 1330 cm$^{-1,}$1410 cm^{-1} and 1576 cm^{-1}$_{,}$ attributed to the stretching vibration of C═O (υC ═ O), C-C (υC═C) and C−H (υC−H) groups of acetate species, present on the particle [271]. It suggests the presence of acetate groups as adsorbed species on the surface of nanocrystals. It is reported that the acetate groups bound to the surface of the metal ion, forming three different bonding structures namely unidentate, bidentate (chelate), and bridging.

The schematic representation of possible modes of attachment of the acetate groups to ZnO Np surface is shown in **Scheme 3.1**, which is in accordance with the results obtained by Sakohara et al. [272]. While in the case of ZnO-CP sample, the powder sample show a broad absorbance peak at 3460 cm^{-1} corresponding to surface adsorbed OH group resulting from the surface hydroxyl group as a result of synthesis in highly alkaline medium and the emergence of peak corresponding to bending modes of OH (1600 cm^{-1}) as observed from the enlarged view in **Figure 3.2** also shows the presence of OH groups on the surface. Thus, it is confirmed that the acetate groups present during the synthesis have got adsorbed onto the surface in the case of ZnO-Py while hydroxyl groups get adsorbed onto the surface in the case of ZnO-CP.

Scheme 3.1. Schematic diagram of acetate group on ZnO-Py sample.

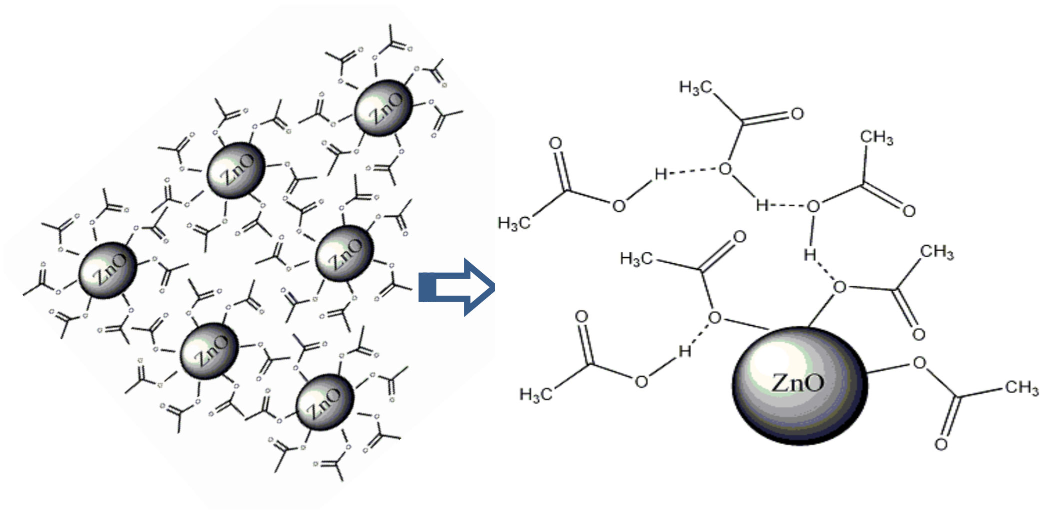

Further, for the application of nanomaterials as sorbents, the surface charge is another most important aspect as it determines the application of these sorbents for a particular type of toxic species. Bearing this in mind, the surface charge was monitored at different pH values using zetapotential measurements (refer to **Section 2.2.5**). The variation of surface charge as a function of pH is given in **Figure 3.3.(a**) and shows that for the three samples, the surface charge at lower pH is positive and with increase in pH value it decreases.

It is seen that pH_{zpc} is 3.93 for ZnO-CP while the values are 9.1 and 9.3 for ZnO-GC and ZnO-Py, respectively. This might be arising due to the synthesis conditions, which is highly alkaline in the former case inducing more of the hydroxyl group on to the surface thus at highly alkaline pH it forms ionic pair with Na^+ (used to adjust the pH), hereby inducing negative surface charge at the near neutral pH. All these measurements give an idea as to the actual application of the three differently surface modified ZnO NPs.

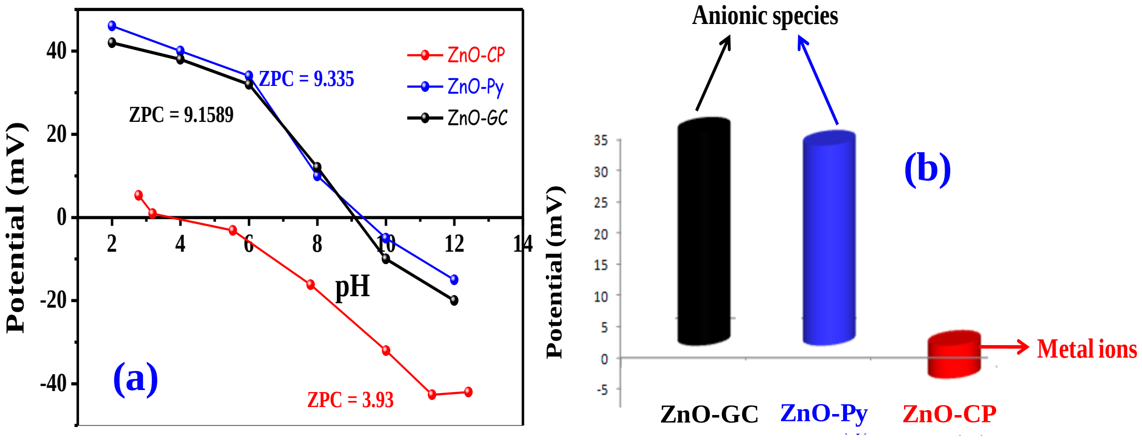

Figure 3.3: (a) Variation of zeta potential with pH of the ZnO NPs prepared by different routes (b) Value of zeta potential of the ZnO NPs at pH ~ 6.

The removal of toxic species from water medium is usually done without much pre-treatment of the samples. Hence the pH of operation typically ranges from 5.5-6.5, indicating the importance of examining the surface property in this pH range. The comparison of the surface charge of the ZnO NPs at pH of 6 is given in **Figure 3.3(a).**It is seen that at pH ~ 6, the ZnO-CP has a negative surface charge and therefore can be used for the sorption of cationic species from solution whereas, ZnO-GC and ZnO-Py exhibit positive surface charge indicating the applicability for anionic species. The synthesized ZnO nanoparticles were then tested for their sorption efficiency with respect to toxic species like dyes, heavy metal ions and chromate depending on their surface charge.

3.2.2. Uptake studies

3.2.2.1. Chromate ions and Dye

The as-synthesized nanoparticles (ZnO-GC and ZnO-Py) were tested for their sorption efficiency with respect to toxic species like dyes and chromate ions. Preliminary studies using the pyrolytic sample showed that there was an uptake of cationic dye like R6G. In order to understand the sorption mechanism, the zeta potential data was used (**Table 3.1**). From the values, it is seen that the surface charge on the zinc oxide nanoparticles was positive, and hence it was not expected to take up cationic species like R6G. Hence to completely understand the mechanism of sorption, the uptake of chromate and Rhodamine-6G (R6G) was carried out, and various experimental factors were optimized to get the maximum uptake.

The pH of the external solution is a major factor in the sorption studies. The effect of pH on the uptake was studied by keeping the other factors like solute concentration, time of equilibration and amount of the sorbent constant. The results of these studies are shown in **Figure 3.4(a)**. It is seen that from a pH of 2, there is uptake of both dye and chromate anion. However, there is a difference in the uptake trend. As can be seen from the fact that uptake of R6G is constant over pH range of 2-6 for ZnO-GC whereas there is a slight decrease in the uptake for ZnO-Py with decreasing pH, with the maximum at pH 2. For chromate, the uptake is lower at lower pH and keeps increasing with an increase in pH till it reaches a maximum at pH of 8 and then decreases for both ZnO-GC and ZnO-Py samples. However, the decrease is rather sharp using ZnO-Py sorbent.

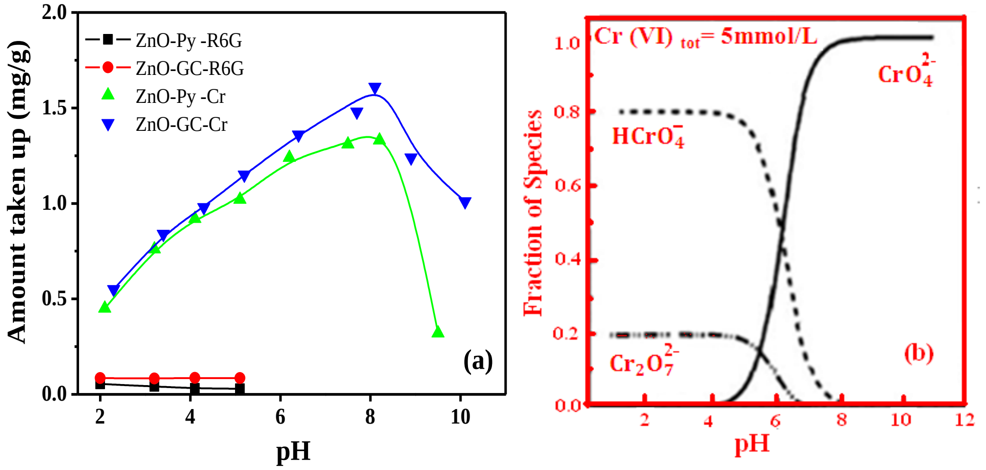

Figure 3.4: Sorption studies (a): Effect of pH on the sorption and (b) Distribution curve of species of chromium as a function of pH [273].

The amount of sorbent needed for maximum uptake was optimized by maintaining the concentration of sorbate and pH constant and varying the sorbent amount in the range of 0.05-0.5 g and it was found that the maximum uptake is achieved with 0.1 g. Hence, further experiments were carried out with 0.1 g. The kinetic studies were carried out by varying the equilibration time while keeping the pH, concentration and the amount sorbent as constant. From these studies, it was seen that the maximum uptake of the dye and chromate was achieved within 1 h and 20 min, respectively. Hence, the further experiments were carried out using this period of equilibration.

All the above results can be explained as follows. From the zeta potential values, it is expected that there should not be any uptake of cationic dye like R6G. Surprisingly our studies showed that the uptake does occur. This could be probably due to the interaction between the protons of the acetate group on the surface of ZnO that tend to coordinate with the nitrogen atom of R6G species thus leading to uptake of R6G. In the case of ZnO-GC, the presence of the porous structure results in the sorption of the dye molecules within the pores along with the surface proton coordination. Thus the combination of the two processes results in higher uptake of the dye molecule using ZnO-GC. At pH greater than 6, the dye gets converted into its neutral form [274] and in turn will not be able to coordinate with the surface protons, but the dye molecules can be incorporated into the pores for the ZnO-GC sample. Hence, there is a sharp decrease in the uptake of increasing pH for ZnO-Py sample as compared to ZnO-GC. For chromate anion, the electrostatic interaction between the positive surface and anions results in the uptake. However, in the pH range in this study, hexavalent chromium exists as various species. **Figure 3.4.(b)** shows various species as a function of concentration and pH [275]. From the figure, it is seen that H_2CrO_4 predominates at pH less than about 1.0, $HCrO_4^-$ at pH between 1.0 - 6.0, and

CrO_4^{2-} at pH above about 6.0 [275]. The dichromate ion $Cr_2O_7^{2-}$, (dimer of $HCrO_4^-$, minus a water molecule) forms only when the concentration of chromium exceeds approximately 1 g/L. In our present study, the possibility of dichromate species existing in solution does not arise. Hence only $HCrO_4^-$ at pH between 1.0 and 6.0, and CrO_4^{2-} are present till pH of 8 and hence there is a competition between the two species with the monovalent ion having less preference compared to the divalent species. Till pH of 8, the monovalent ion is dominant compared to the divalent ion. At pH 8, both the species are equal in concentration. Hence the resulting competition between the two species of chromium results in lowering of uptake. As the concentration of divalent species increases, the uptake increases and is a maximum at pH 9. This is because, only CrO_4^{2-} ion is present, and there is no competition from any other chromium species. The competition from OH^- ions is also not so dominant at this pH. At pH greater than 9, the uptake decreases because in this pH range, the surface of zinc oxide becomes negative and the electrostatic repulsion decreases the chromate uptake. Hence, the optimum pH for maximum uptake is pH 8-9. It is also to be noted that the decrease is rather steep in the case of ZnO-Py as compared to ZnO-GC. This is because the latter sample has got pores into which the chromate would have been sorbed, and this is not greatly affected by the surface charge and hence the decrease in uptake is not very steep.

It is to be noted that the surface of the zinc oxide nanoparticles has a positive charge as seen from the value of zeta potential values. Since the surface charge is positive, only anionic species should be taken up, and cationic dyes like Rhodamine

6G is not expected to be taken up. However from the present studies it is seen that the cationic R6G is taken up. It is to be noted that at lower pH, the dye does not remain as a cation but is converted to its lactam structure [274].

In order to get the maximum capacity of uptake, the amount taken up (represented as mg/g) was studied as a function of initial solute concentration, and the results are shown in**Figure 3.5**. From the plots, it is seen that the amount of dye taken up is much lower than that of chromate. From **Figure 3.5**, it is seen that the maximum uptake capacity obtained experimentally for ZnO-Py and ZnO-GC are 4.66 and 5.06 mg/g of chromate respectively and for the dye sorption the values are 0.55 and 0.84 mg/g of R6G, respectively.

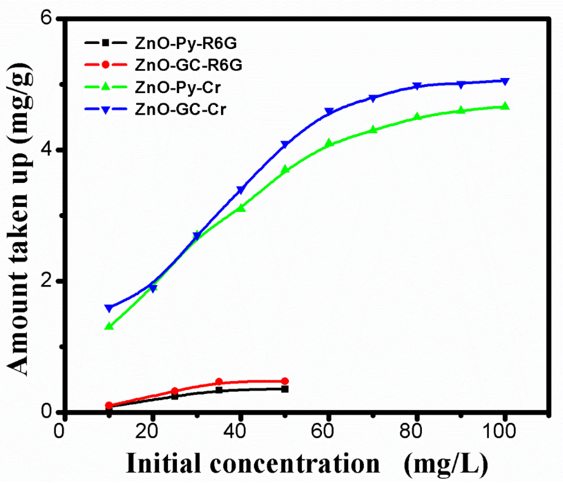

Figure 3.5: Variation of amount taken up as a function of initial solute concentration.

In order to understand the sorption process, the data is fitted to both equilibrium and kinetic modeling. In equilibrium modeling, (refer to Section 2.3.1) the sorption data is fitted to two well-known models, namely Langmuir [227] and

Freundlich [229] as shown in **Figure 3.6(a)-(d)** respectively. The results of the equilibrium modeling of the sorption in the present studies showed that the dye uptake does not follow either Langmuir or Freundlich model suggesting that the sorption is not due to surface phenomena and does not result in a monolayer.

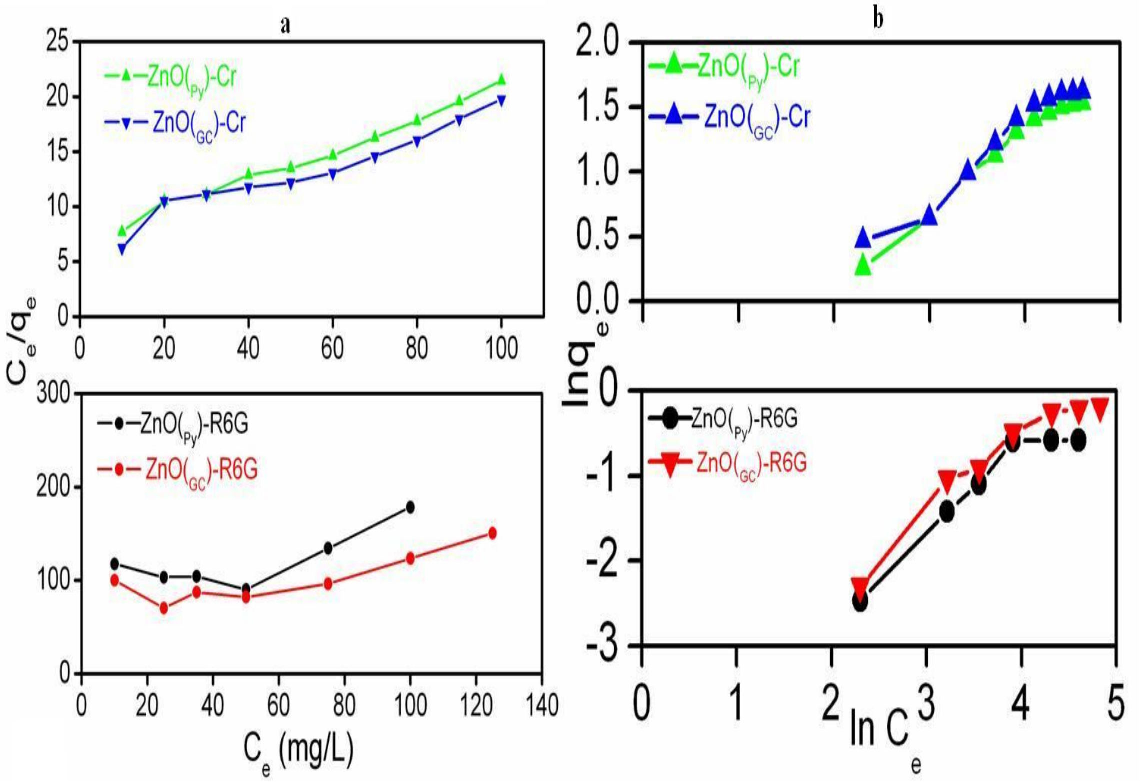

Figure 3.6: Equilibrium modeling using (a) Langmuir equation and (b) Freundlich equation.

Moreover, the values calculated from these curves are not significant and hence not tabulated. This is in confirmation with the earlier expectation that the dye being cationic will not be sorbed onto the surface of zinc oxide. Hence, it is the presence of certain binding sites or pores that results in the uptake of the dye, and thus the uptake is very low. Unlike the dye uptake, the data of sorption of chromate is fitted well to both Langmuir and Freundlich models, given in **Figure 3.6(a) and (b)** respectively and the values calculated from these models are tabulated in **Table 3.2**.

Table 3.2: Calculated values of parameters of chromate sorption by zinc oxide nanoparticles, using different models.

	Equilibrium Modeling				**Kinetic Modeling**			
Sorbent	**Langmuir**		**Freundlich**		**First Order**		**Second Order**	
	$\mathbf{Q^o}$	**B**	$\mathbf{K_f}$	**n**	$\mathbf{K_{ads}}$	$\mathbf{q_e}$	$\mathbf{K_{2ad}}$	$\mathbf{q_e}$
ZnO-Py	7.14	0.02	.015	1.7				1.5
ZnO-GC	8.33	0.01	0.4	1.9				1.8

It is seen that the calculated values of uptake capacity of chromate using ZnO-Py and ZnO-GC are 7.14 and 8.33 mg/g, respectively. The calculated value of n is in the range of 1-10 [229], suggesting that the sorption of chromate is favourable using both the samples. The primary aspect of Langmuir isotherm can be expressed by R_L, a constant known as the constant separation factor or equilibrium parameter which can be used to predict if an adsorption system is "favourable" or "unfavourable". From the values given in Table 3.2 , it is clear that R_L values are in the range of $0 < R_L < 1$, indicating that the sorption of chromate on zinc oxide nanoparticles prepared by both methods is favourable.

The sorption data were also fitted to the kinetic modeling (refer **Section 2.3.2**) using different equations to explain the solid/liquid adsorption. In order to distinguish the kinetics equation based on the adsorption capacity of solid from the concentration of solution, the first order and second rate equations equations proposed by Lagergren [233] and Ho [235] are known as pseudo-first and pseudo-second –order respectively. The results of the kinetic modeling are shown in **Figure 3.7(a)** and values are given in **Table 3.2**.

The mechanism of ion adsorption on porous adsorbents may involve three steps: (i) diffusion of the ions to the external surface of adsorbent; (ii) diffusion of ions into the pores of adsorbents; (iii) adsorption of the ions on the internal surface of adsorbent [276].These mechanisms were further explored by fitting the sorption data in the present studies into the Weber−Morris [237] and Boyd [239] models.

Values of intercept in the plot gives an idea about the thickness of the boundary layer; i.e., the larger the intercept, the greater will be the boundary layer effect. The plot for Weber−Morris modeling (refer to **Section 2.3.2**) of sorption data for chromate ions using ZnO NPs are shown in **Figure 3.7(b)**. Sectionwise linear regression of the data showed that these plots have three distinct regions. The first linear portion included the sorption period of 0−60 min, which represents external mass transfer. The second linear portion included the sorption period of 60−120 min, representing intraparticle diffusion. The third linear portion covered the period of 130−270 min, which indicated adsorption−desorption equilibrium. As the plots do not cross the origin, it is possible that both intraparticle diffusion and external mass transfer occur simultaneously. However, the ratio of the time taken by external mass transfer to intraparticle diffusion was about 1:1.

Therefore, the overall sorption process was controlled by both external mass transfer and intraparticle diffusion [277].

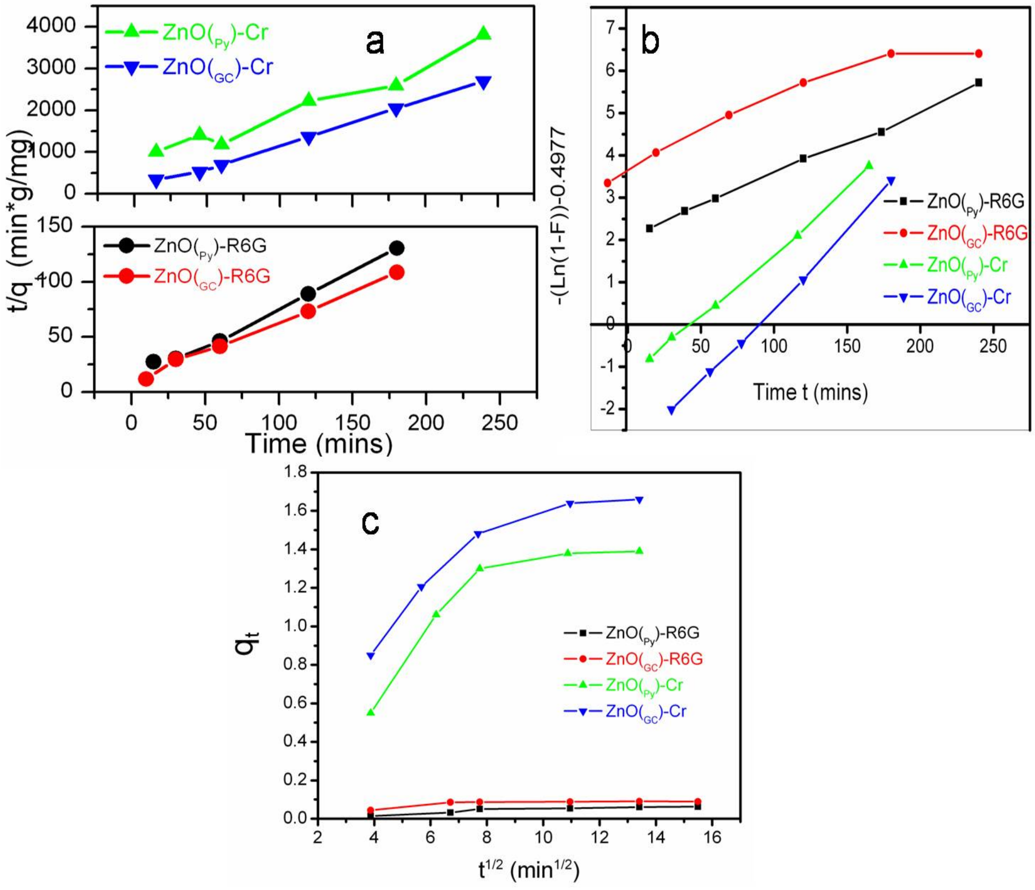

Figure 3.7: Sorption studies: Kinetic modeling using (a) pseudo second order equation (b) Boyd Plot; (c) Weber – Morris Model.

The Boyd plots (**Figure 3.7(c)**) do not pass through the origin, confirming the involvement of external mass transfer in the entire adsorption process. This result again confirmed the rate controlling mechanism of adsorption stated in Weber−Morris kinetic model studies [237]. The average effective diffusion coefficients (D_i) values for chromate sorption on ZnO-Py and ZnO-GC were estimated as 6.63 x 10^{-10} and 7.72 x 10^{-10} cm^2 /

sec, respectively. From literature [278] it is known that if external mass transfer of adsorbate across the liquid film to the adsorbent exterior surface is to be the rate-controlling step, the value of D_i should be in the range of 10^{-6}–10^{-8} cm^2/s, and if intraparticle diffusion is the rate limiting step, the D_i value should be in the range of 10^{-11}–10^{-13} cm^2/s. But in these studies, the calculated values of D_i values were in neither of the two ranges but the range between them (10^{-8}–10^{-11} cm^2/s), so both film and intraparticle diffusion may play a significant role in the present sorption.

a) Comparison of the current sorbent with various other sorbents used

The present study showed that the zinc oxide nanoparticles synthesized can be used as sorbents for removal of toxic chromate ions. The performance of the synthesized zinc oxide nanoparticles are compared with some of the sorbents used for chromate uptake, and the results are tabulated in **Table 3.3**.

It is seen from the table that for most of the adsorbents, the optimum pH was around 2. This could be due to the fact that Cr(VI) is reduced to Cr(III) at pH near 1. Certain sorbents like leather, tyres showed exceptionally high adsorption capacity. This could probably be due to the initial carbon content, activation process and formation of pores due to the fundamental morphology of the raw material.

Table 3.3:Comparison of the various sorbents used for chromate uptake.

Adsorbents	**pH**	**Sorption capacity** (mg/g)	**Reference**
Leather	2.0	459.00	[279]
HSAC	1.0	170.00	[280]
Tyres activated carbon	2.0	58.50	[281]
Leaf mould	2.0	43.10	[282]
Coconut shell carbon	2.0	20.00	[283]
Beech sawdust	1.0	16.10	[284]
Sugarcane bagasse	2.0	13.40	[282]
Coconut shell carbon	4.0	10.88	[285]
Treated sawdust of Indian Rosewood	3.0	10.00	[286]
Coconut tree sawdust	3.0	3.60	[287]
Pohang clinoptilolite	3	3	[288]
Harunachabazite	2	8.6	
Modifiedorgano-kaolinite	5-9	10	[289]
Staphylococcus aureus	2	28	[290]
Iron (III)-impregnated sugarcane bagasse	1-8	10	[291]
Cetylpyridiniumbentonite	7	0.7	[292]
Zinc oxide nanoparticles	6-8	10	Present work

However, the ZnO NPs can be used as sorbents in less acidic and realistic conditions. Furthermore the synthesis of these nanoparticles is very easy and less tedious as compared to the processing of certain raw materials to produce activated carbon.

3.2.2.2. Heavy metal ion uptake

The co-precipitation zinc oxide nanoparticles (ZnO-CP) were then tested for their sorption efficiency with respect to metal ions at pH near neutral. This was studied with the aim of having probable application to removal of metal ions from ground water system.

Various experimental factors were varied and optimized to get maximum uptake. The pH of the external solution is an important factor that usually controls the uptake of most of the metal ions from solution. However, the primary aim of the present study involved in ascertaining the possibility of use of the synthesized nanoparticles in water system and the pH of these solutions need to be near neutral. Also beyond pH of 6, the transition metal ions do have a tendency to get hydrolyzed, and thus the studies carried out at pH greater than 6 will not provide a reproducible and representative idea of sorption. Thus, pH was maintained at 4.5 for the sorption studies. The amount of the nanoparticles was varied in the range of 0.05-0.5 g, and it was found that the maximum uptake was achieved with 0.1 g. Hence, further experiments were carried out with 0.1 g. The kinetic studies were performed by varying the equilibration time while keeping the pH, concentration and the amount sorbent as constant. The results are shown in **Figure 3.8** and it was seen that the maximum uptake was achieved with half-an-hour.

Hence, the further experiments were carried out by equilibrating with metal ion solution with the sorbent for half-an-hour. The same experiments were performed using the ZnO NPs synthesized by pyrolytic and combustion methods. It was seen that the uptake of the metal ions was insignificant as expected from the results of zeta potential measurements.

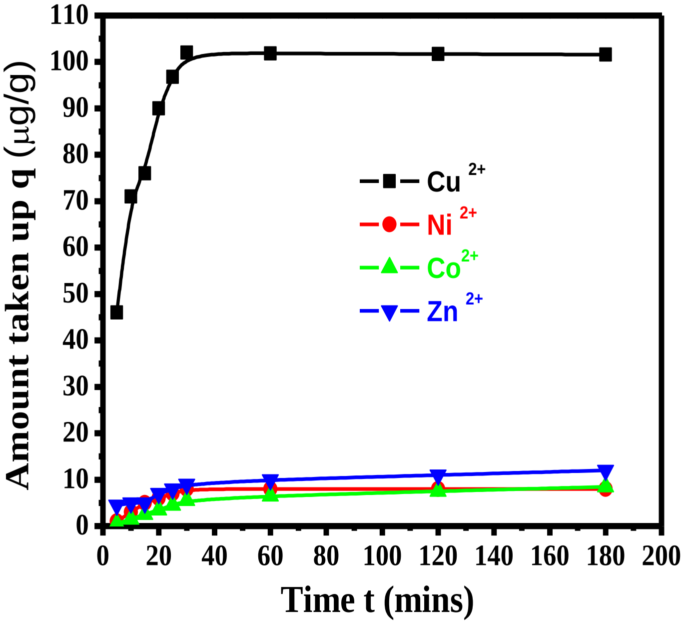

Figure 3.8: Effect of the equilibration period on the amount of metal ion taken up by ZnO-CP.

The effect of initial concentration of the metal ions was studied by equilibrating 0.1 g of the sorbent for half-an-hour with 10 mL of solution containing varying concentrations of the individual metal ions in the range of 10-140 mg/L. From the plot of amount taken up as a function of initial metal ion concentration **(Figure 3.9**), it is seen that the amount taken up for copper does not reach saturation within this initial metal ion concentration range.

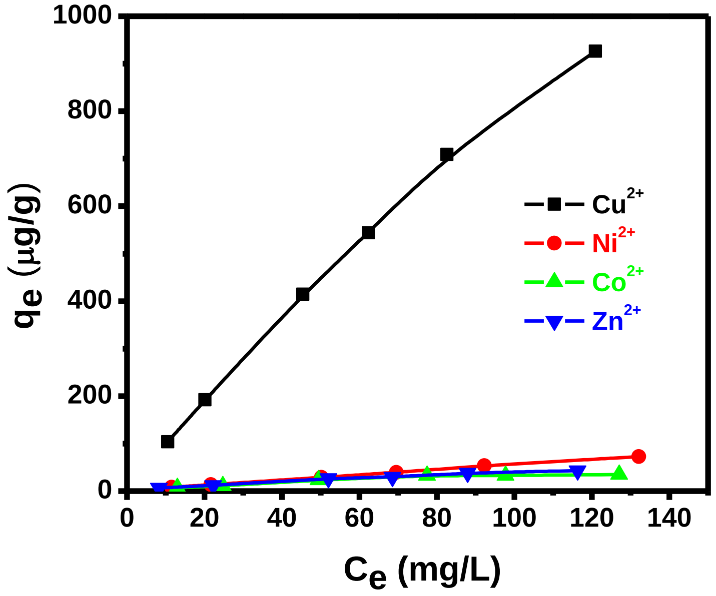

Figure 3.9: Effect of initial concentration of metal ion on the amount taken up.

This shows that the sorbent has a very high uptake capacity for Cu(II) ions. A possible explanation is being offered for the selectivity of Cu(II) ions as compared to the rest of the metal ions. The sorption is affected by amount of the available active sites that are affected by the surface area of the nanoparticles. However, surface area is not the only controlling parameter. There are other factors like porosity, surface charge and surface functionalization that also play a crucial role in governing the efficiency of the nanomaterials in having potential applications as sorbents. From zeta- potential measurements, an idea of the surface charge is obtained, and it is seen that the point of zero charges was 3.7. This meant that at pH less than 3.7, the surface is positively charged and is not suited for the sorption of metal ions as there will be electrostatic repulsion between the metal ions and the positively charged surface. Above pH 3.7, the uptake of metal ions becomes prominent, and the uptake is governed by the electrostatic attraction between the metal ions and surface of the zinc oxide nanoparticles. This electrostatic attraction is governed by the electronegativity of the metal ion that is being studied.

In the present study, the metal ions Co(II), Ni(II), Cu(II) and Zn(II) were considered and the electronegativity values are 1.8, 1.7, 2.1, and 1.8, respectively. Due to the difference in electronegativity values, it is seen that the Cu(II) ions will be preferred compared to other metal ions resulting in a favorable sorption of copper. **Scheme 3.2**also gives a possible mode of attachment of copper ions onto the nanoparticle surface. In the case of ZnO NPs synthesized by combustion and pyrolytic methods, the electrostatic repulsion between the positive surface charge of nanoparticles and the metal ions resulted in the insignificant uptake of these ions.

Scheme 3.2: Schematic representation of Cu(II) sorption on ZnO CP.

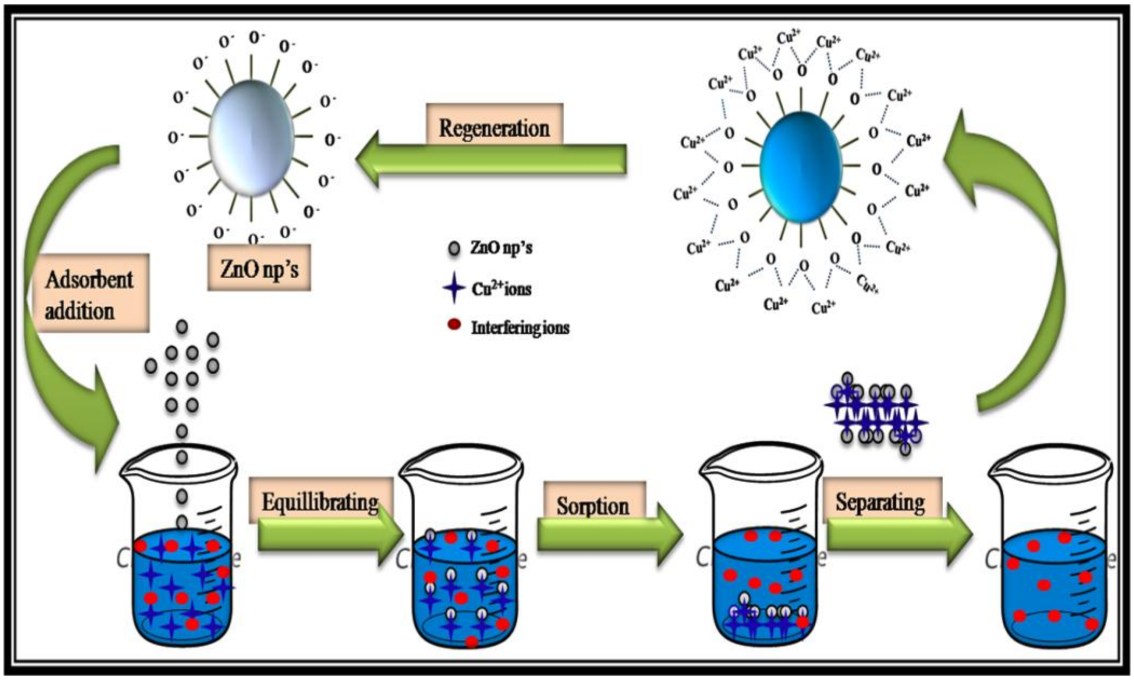

In order to understand the sorption process, the data obtained were subjected to both equilibrium and kinetic modeling using different equations. Langmuir [227], Freundlich [229] and Dubinin–Radushkevich[232]are fitted to know about the mode and energy involved in adsorption. Temkin isotherm model [230] was applied to evaluate the adsorption potentials of adsorbents for adsorbates, i.e., metal ions from aqueous solution. The sorption data were fitted to the equilibrium modelling using different isotherm modelling to explain the solid/liquid adsorption. The values computed from these models are given in **Table 3.4**.

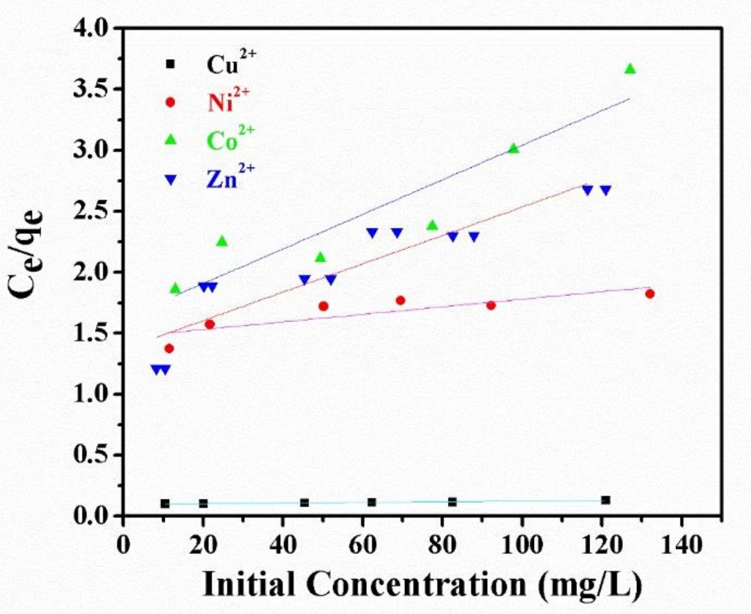

Figure 3.10:Equilibrium modeling using Langmuir isotherm for sorption of different metal ions on ZnO-CP.

The present studies showed that the sorption of only Ni(II) and Co(II) follow Langmuir isotherm (**Figure 3.10**) over the entire concentration range. For Cu(II), it is seen that the values are nearly parallel to that of the x-axis thus indicating the sorption is not monolayer in nature. The R_L values for all the metal ion sorption are below 1 indicating a favorable sorption process that is reversible in nature. This shows that nanosorbent can be regenerated once the sorption is achieved. The fact that copper sorption is not monolayer could attribute to its high uptake in comparison to other metal ions.

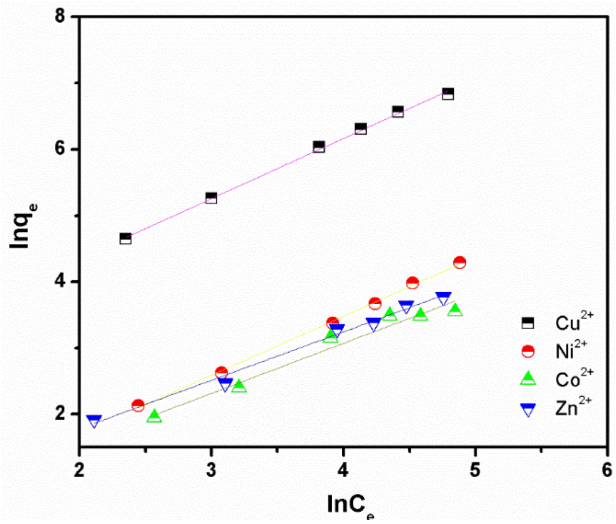

Figure 3.11: Equilibrium modeling using Freundlich isotherm for sorption of different metal ions on ZnO-CP.

It is seen from **Figure 3.11**, that the Freundlich model is applicable at higher concentrations but not at lower concentrations. From the plots, the sorption intensity or the surface heterogeneity as obtained from the value of the slope is found to be between 0 and 1 thus indicating that the sorption is the chemisorption in nature. The value of n lies between 0 and 10 and this indicates that the metal sorption is a favored process. The R^2 value is more favorable for Freundlich model than for Langmuir model as seen from **Figure 3.11**and thus indicating chemisorption.

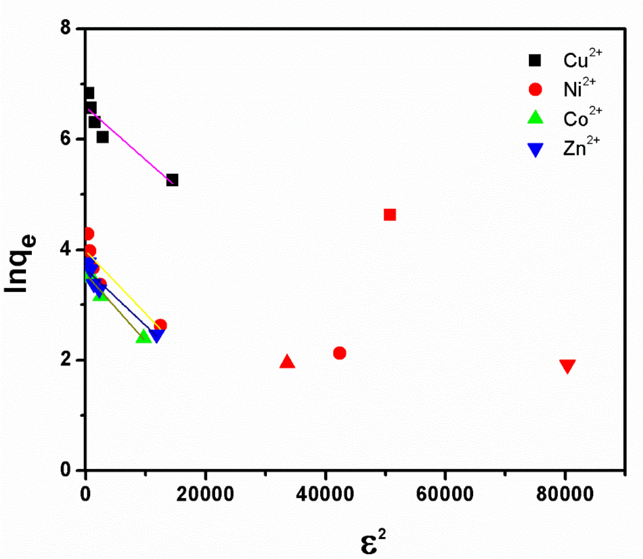

Figure 3.12: Equilibrium modeling using Dubinin–Radushkevich isotherm for sorption of different metal ions on ZnO-CP.

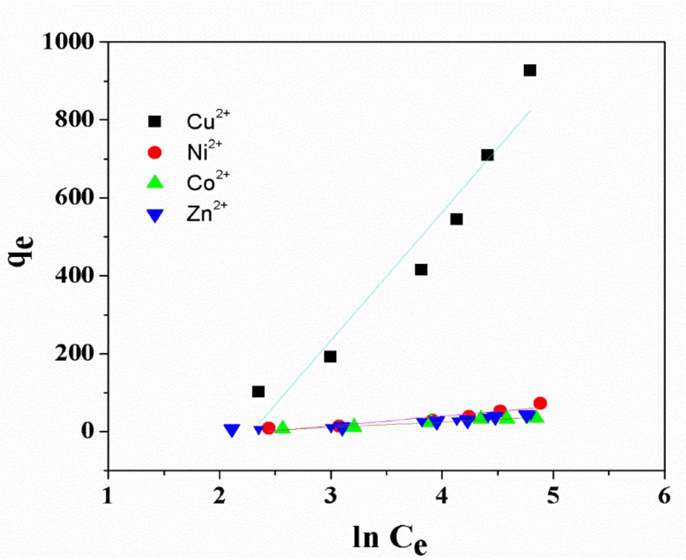

Figure 3.13: Equilibrium modeling using Temkin isotherm for sorption of different metal ions on ZnO-CP.

Table 3.4:Parameters calculated from the linearized equations of different equilibrium models.

Model	**Langmuir**		**Freundlich**				**Temkin**		
	Q^o (mg/g)	**R^2**	**Surface hetero-geneity**	**n**	**K_f**	**R^2**	**A_t** (L/mg)	**b (10^2)**	**R^2**
Cu(II)	400	0.973	0.1	9.9	12.6	0.998	9.873	3.2	0.921
Ni(II)	30	0.647	0.31	3.2	0.9	0.998	11.06	0.24	0.876
Co(II)	10	0.834	0.29	3.4	1.04	0.955	8.695	0.13	0.958
Zn(II)	9	0.834	0.24	4.1	1.3	0.987	6.75	0.14	0.914

The sorption data was fitted to Dubinin–Radushkevich model and the results are given in **Figure 3.12**. The value of mean sorption energy was calculated and was found to be in the range of 8-16 kJ/mol for all the metal ions. This indicates that the sorption is chemisorption as the free energy values are greater than 8 kJ/mol, which otherwise corresponds to physisorption. Thus, the results are in concurrence with that of Freundlich model. The data were further fitted using Temkin isotherm model (**Figure 3.13**) and the values are given in **Table. 3.4**.

The sorption data were further fitted to different kinetic models to get a complete understanding of the sorption process. In order to distinguish the kinetics equation based on the adsorption capacity of solid from the concentration of the solution, the first order and second rate equations proposed by Lagergren[233]and Ho [235] are known as pseudo-first and pseudo second –order, respectively.

The sorption data for only copper were also fitted to the kinetic modeling using different kinetic modelings to explain the rate and process involved in adsorption. The results of the other sorption were so low that it was not considered for the kinetic modeling. The values calculated for the various models are given in **Table 3.5**. Lagergren pseudo-first-order model (**Figure 3.14**) was fitted only in the first 60 min that showed that after 60 min it is not at all following first order kinetics.

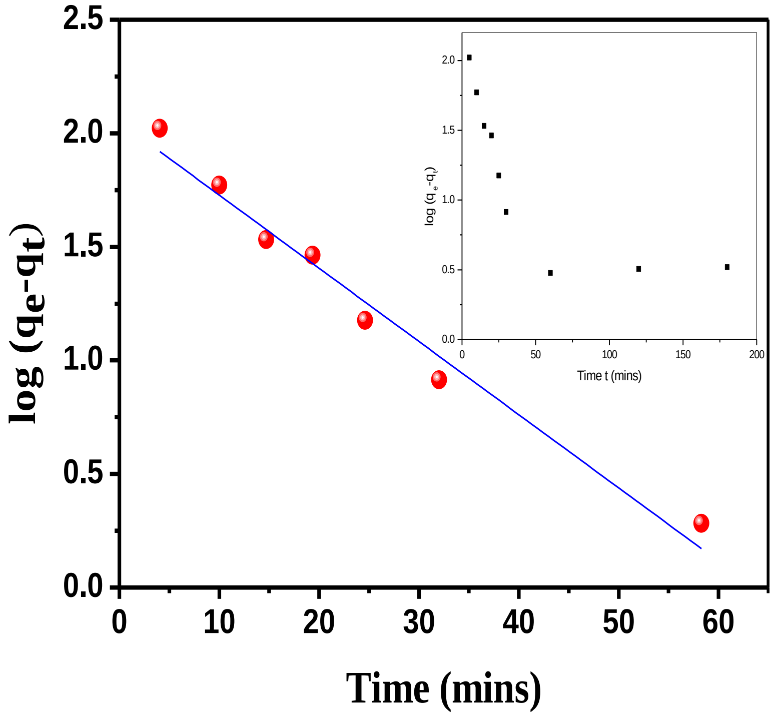

Figure 3.14: Kinetic modeling using First order rate equation for Cu(II) ions uptake using ZnO-CP. (Inset shows the variation over the entire period of equilibration).

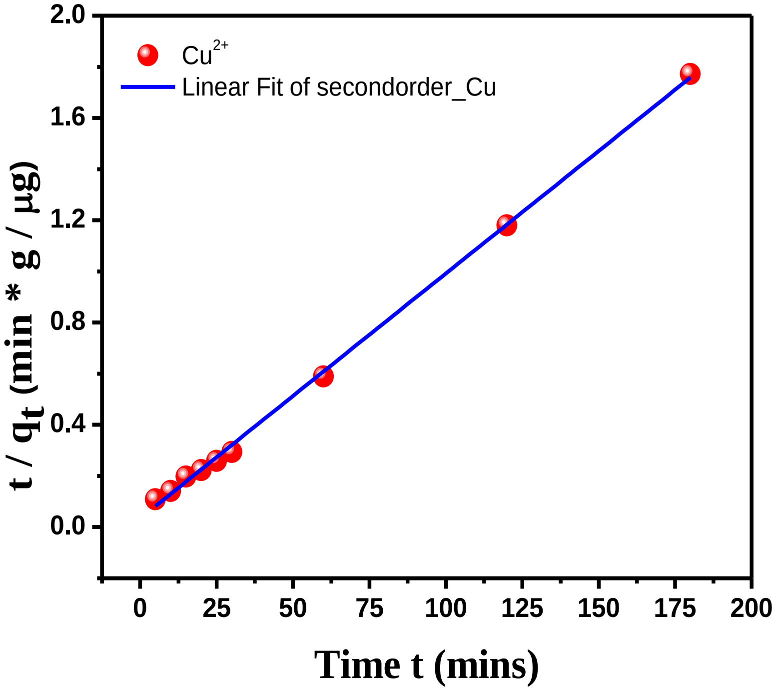

Figure 3.15: Kinetic modelling using Ho and Mackay second order rate equation for Cu(II) ions uptake using ZnO-CP.

Table 3.5: Parameters calculated from the linearized equations of different kinetic models.

First order	**Second order**		
Follows for the first sixty minutes and then does not follow (qe = 112 μg/g)	**Ho and Mackay [293]**		
	q_e	K_{2ads}	R^2
	104	3063	0.9988

However, it was found that the second order model proposed by Ho and Mackay (**Figure 3.15**) was applicable to the entire period of equilibration confirming that the uptake proceeds via a chemisorption mode.

The sorption data in the present studies were also fitted to the Weber–Morris [237] and Boyd [239] models. Weber–Morris Model was used to determining the actual rate- controlling step involved in the sorption. The results of fitting of sorption data to Weber–Morris model is given in **Figure 3.16** and the values of intercept I provides an idea of the thickness of the boundary layer; i.e., the larger the intercept, the greater will be the boundary layer effect.

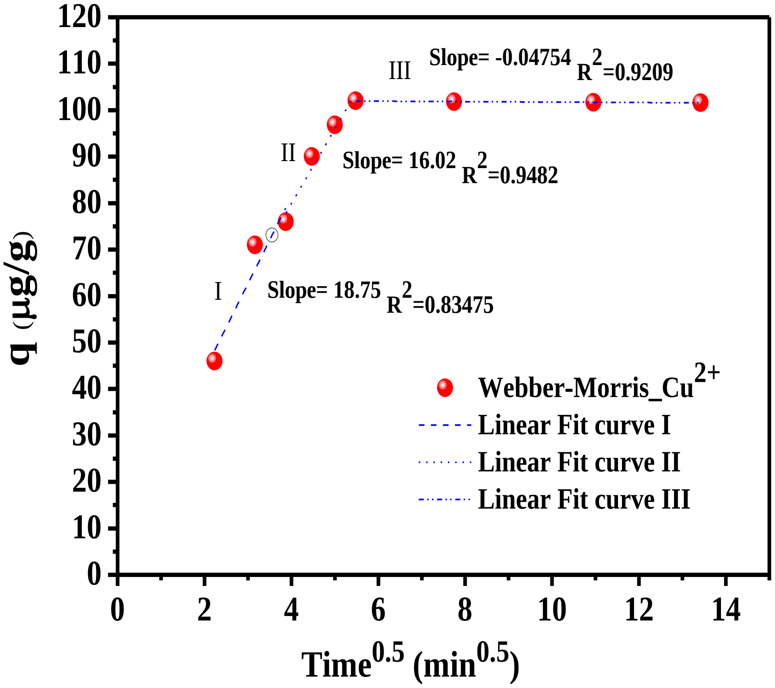

Figure 3.16: Kinetic modeling using Webber Morris model equation for Cu(II) ions uptake.

In the present study, it is seen that the plots of Weber−Morris model can be subjected to linear regression in different regions. It is considered that these plots have three distinct regions. The first linear portion included the sorption period of 0-15 min which represents external mass transfer, i.e., Cu(II) ions transport through the hydrodynamic boundary layer of the adsorbent surface which is affected by the thickness of the layer (obtained by the intercept of the curve). It is mainly facilitated due to molecular diffusion.

The second linear portion in the sorption period of 15-30 min represents the intraparticle (internal/pore) diffusion. It takes place after the Cu (II) ions are transported through the boundary layer and has to reach adsorption sites through the pores. The third linear portion (the period of 30-180 min) indicates adsorption−desorption equilibrium. It is clear that as the plots do not cross the origin, both intraparticle diffusion and external mass transfer occur simultaneously. However, the ratio of the time taken by external mass transfer to intraparticle diffusion was about 1:1. Thus, the overall sorption process was controlled by both external mass transfer and intraparticle diffusion.

From the modeling of the data using Boyd's equation (**Figure 3.17**), the diffusion coefficient was calculated and found to be of the order of 10^{-10} cm^2s^{-1}. From literature it is known that if external mass transfer of sorbate across the liquid film to the sorbent exterior surface is to be the rate-controlling step, the value of Di should be in the range of 10^{-6}–10^{-8} cm^2s^{-1}, and if intraparticle diffusion is the rate limiting step, the Di value should be in the range of 10^{-11}–10^{-13} cm^2s^{-1}. However in these studies, the calculated values of D_i values were in neither of the two ranges but the range between them

(10^{-8}–10^{-11} cm^2s^{-1}), therefore it is proposed that both film and intraparticle diffusion plays a significant role in the present sorption.

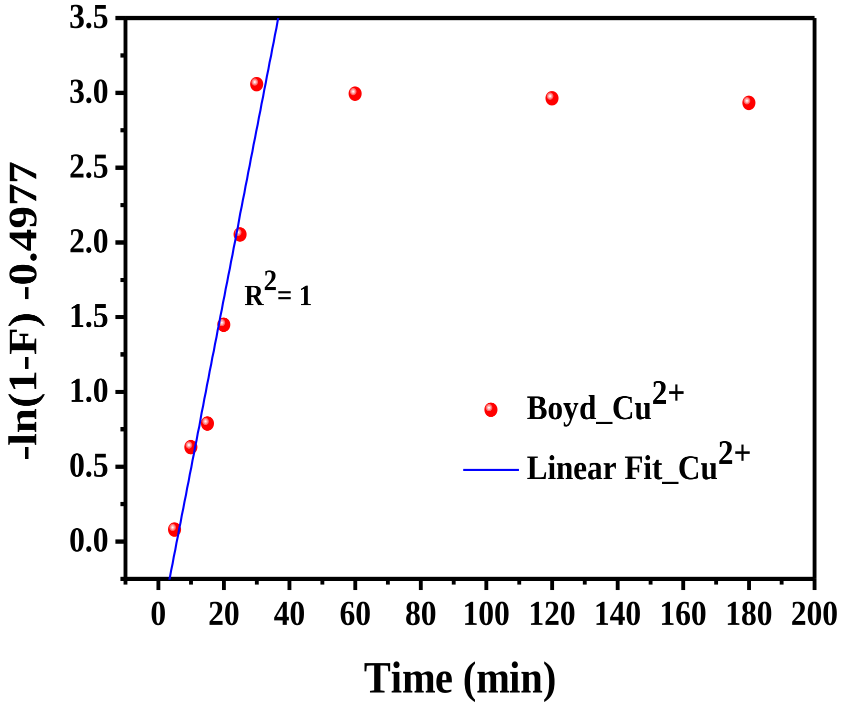

Figure 3.17: Kinetic modeling using Boyd model equation for Cu(II) ions uptake.

The sorption study is explained in **Scheme 3.2**. In order to get a clear insight as to the changes occuring on the surface of nanoparticles during sorption, extensive DLS studies were carried out. The ZnO NPs were equilibrated with pure water and copper ion solution for a period of 30 minutes. This time was taken based on our studies that within half an hour maximum uptake were achieved. The results are given in **Table 3.6 (Figure 3.18 and 3.19).**

Table 3.6: Variation of hydrodynamic diameters of ZnO CP with time in the presence and absence of Cu(II) ions.

Time (min)	Hydrodynamic diameter (nm)	
	In Water	In Cu(II) solution
0	750	550
5	800	575
10	875	580
20	990	590
30	1000	600

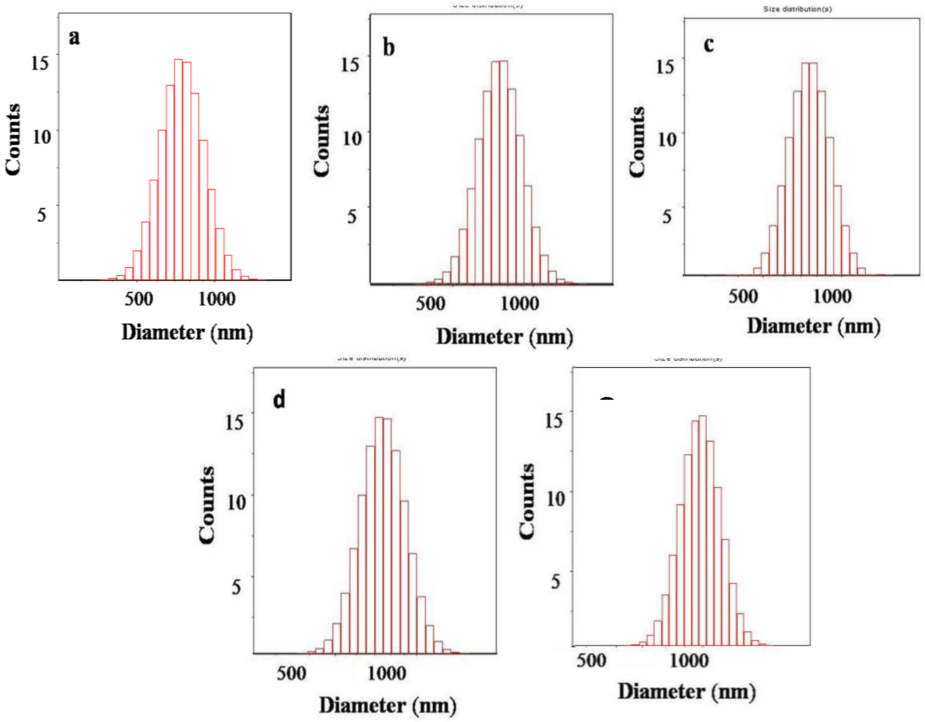

Figure 3.18: Variation of hydrodynamic diameters of ZnO CP with time (a) 0 (b)5 (c) 10 (d) 20 and (e) 30 in in DI water.

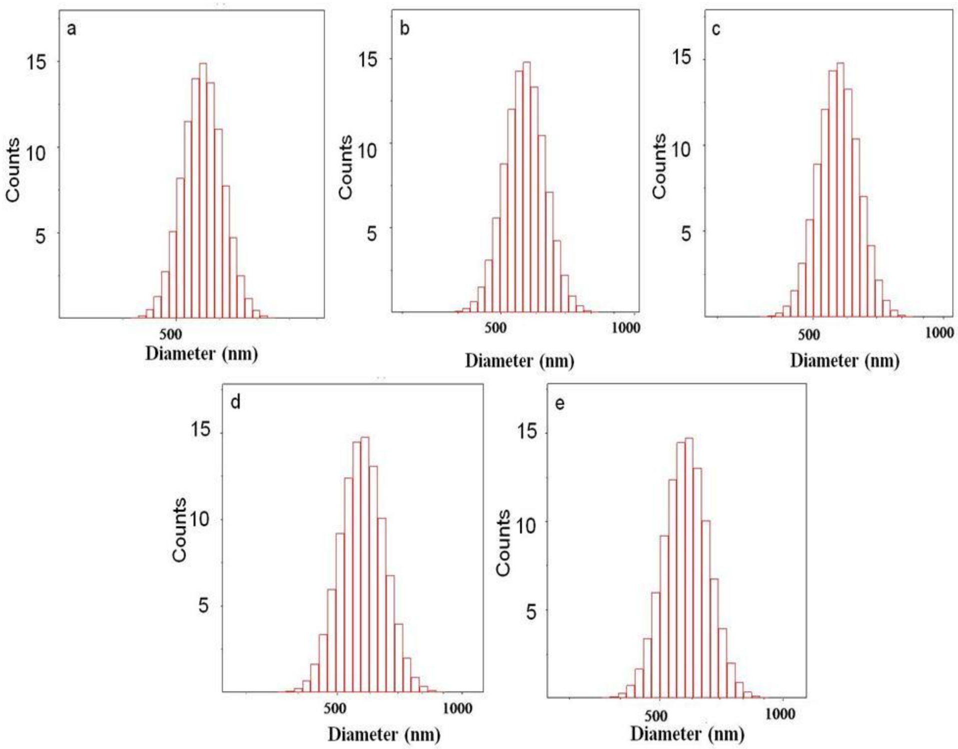

Figure 3.19:Variation of hydrodynamic diameters of ZnO CP with time (a) 0 (b)5 (c) 10 (d) 20 and (e) 30 min in the presence of Cu(II) ions.

b) Regeneration studies:

The regeneration studies shown in Scheme 3.2 were also carried out. Desorption and reusability studies need to be considered for practical applications. It is of great importance that the sorption efficiency is nearly unaffected by a number of cycles. Therefore, the reusability of the present sorbent was evaluated.

To investigate the possibility of restoring the adsorption capacity, at first desorption experiments were conducted under batch experimental conditions. The conditions needed for desorption can be easily understood from the pH variation studies to obtain the maximum pH for sorption. It is seen that at lower pH, the sorption was lower. This suggested that there was a possibility of using this condition for desorption of metal ions from the ZnO CP.

However, this approach did not work in this case as in the lower pH range; the chemical integrity of the ZnO NPs was significantly affected. Therefore, a complexing agent namely EDTA was used as a desorbing solution. The concentration of the EDTA was also an important factor that affected both desorptions as well as the stability of the nano sorbent. Hence, the optimum condition of 0.02 M EDTA was used for the desorption experiments. The reusability of the sorbent for copper sorption was tested by repeating the adsorption-desorption cycle several times using the same adsorbent. The results of this study (**Figure 3.20**) showed that the adsorbent retained about 93% of its initial sorption efficiency even after 5 cycles. This property allows multiple uses of adsorbents for at least 5 times. The results of these studies are shown in **Table 3.7**.

Table 3.7: Regeneration studies: Sorption Desorption Values (%).

No of cycles	% Sorbed	% Regenerated
1	99	97.1
2	98	96.3
3	96.8	95.8
4	95.4	94.2
5	94.1	93.3

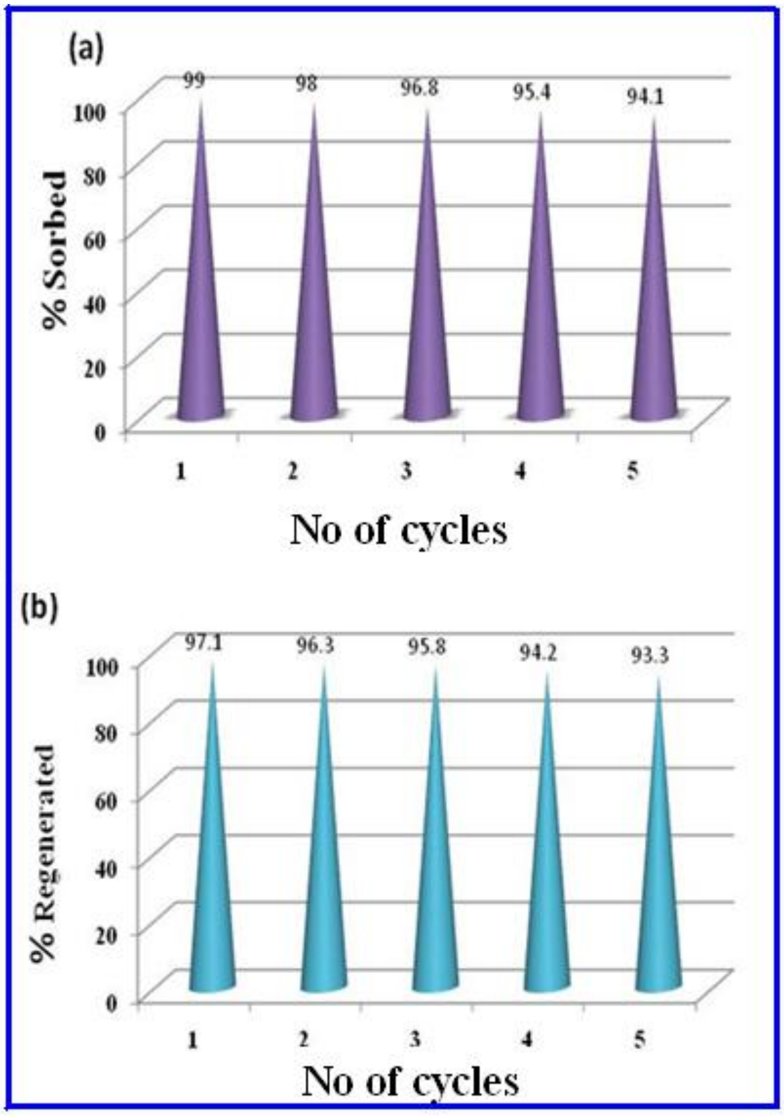

Figure 3.20: Sorption (a)-desorption (b) studies for five successive cycles of ZnO-CP.

c) Comparison of the present study with sorbents used for copper uptake:

The present study showed that the synthesized nanoparticles can be used as sorbents for selective removal of copper ions. The performance is compared with some of the sorbents used for copper uptake, and the results are tabulated in **Table 3.8.**

Table 3.8: Sorption efficiency of various sorbents for copper ion uptake.

Adsorbent	Cu (II) uptake (mg/g)	pH	Reference
Herbaceous peat	4.8	5.5	[294]
Goethite	0.5	6.0	[295]
Modified carbon Xerogels	299.41	5.0–6.0	[296]
Hydrogel of montmorillonite	49.26	6.8	[297]
Ligand modified a new type mesoporous adsorbent	145.98	5.0	[298]
Carbon encapsulated MNPs	3.21	7.0	[299]
Magnetic pectin−iron Oxide	49	5	
Mn- doped Fe (III) oxide implanted in GO	144	5	[300]
ZnO NPs	400	6	Present work

It is seen that the present sorbent has a capacity comparable to some of the sorbents reported in the literature. It is to be noted that in the present study, the high selective uptake was achieved without any functionalization or surface treatment. Thus, the current system has definite advantages like simple synthetic protocol and highly reproducible nanoparticles that behave as selective sorbent for copper ions. One of the further advantages is the faster sorption kinetics which is another important aspect for actual applications.

3.3. Summary:

In the present study, it has been seen that the synthesis protocol plays a significant role in deciding the surface charge of the nanoparticles and by that affecting its applications. The zinc oxide nanoparticles synthesized by two different routes namely pyrolytic and the gel combustion produce particles with various physical characteristics that considerably affect the sorption properties. It was also seen that though the surface of zinc oxide nanoparticles was positive, the sorption of a cationic dye like rhodamine 6G occurs proving that the sorption is not only an electrostatic interaction but can occur due to the presence of pores or some binding surface groups. It is seen from the sorption studies that the nature of the zinc oxide nanoparticle affects the sorption capacity, especially for that of chromate. The co-precipitation method resulted in ZnO NPs possessing a negative charge, and it was tested for the transition ion. The synthesized nanoparticles were found to have selective sorption with respect to copper ions with an uptake capacity of 400 mg/g. Cu(II) adsorption isotherms on ZnO NPs can be well-fitted by the Freundlich model, indicating of a multi-layer adsorption, and the adsorption kinetics follows the pseudo-second-order model. The adsorbent could be recycled up to five cycles without a significant decrease in its adsorption capacity. Considering the simple fabrication procedure, environmental friendliness, high sorption capability and good regeneration performance of ZnO-NPs, it is expected that these ZnO nanoparticles can be a potential candidate for the sorption and pre-concentration of heavy metal ions and chromates from aqueous systems as well as the photocatalytic degradation of organic pollutants. The actual applications are further investigated. However, the primary aim of this work was to bring out the changes in the surface charge of nanoparticles by adopting different synthetic protocols. Apart from all these advantages ZnO NPs has a major disadvantage of dissolution in acidic condition. Further to overcome these drawbacks, in the following chapter attempts were made to stabilize the nanoparticles by coating with various functional groups like thiol and silica.

Chapter 4

Surface functionalized ZnO nanoparticles

1. *Functionalized Nanoparticles as Sorbents for Removal of Toxic Species*,
   Jerina Majeed, Jayshree Ramkumar, S. Chandramouleeswaran and A. K. Tyagi
   Int. J. Chem. Nuc. Metall. Mater. Eng., 2014, 8, 6, 476-478.

2. *Thiol-functionalized ZnO-SiO_2 nanocomposites for highly efficient removal of Hg(II) and Pb(II) from water*
   Jerina Majeed, Jayshree Ramkumar, S. Chandramouleeswaran, and A. K. Tyagi
   (Manuscript under preparation)

4.1. Introduction

Adsorption is an extensively explored technique for the removal of low concentrations of heavy metals from water. The efficiency of various adsorbents has been validated over many years in different water and waste-water applications [48, 172, 176, 301-309]. The most common industrial adsorbent used for heavy metal removal is activated carbon (AC) [285, 310-312], yet studies have shown its practical limitations. A loss of ~ 15% of the original material is expected during regeneration of the carbon even in a well-operated system. While coupling these with complexing agents for improved performance can result in substantial waste generation [176, 313]. Fly ash [314], clay [315], zeolite [316] and peat moss [317] have also been commonly used as adsorbents because their structure provides sufficient surface area for adsorption. In all cases, the presence of a hazy pore structure [318, 319] has a negative effect on diffusion, which may lead to a decrease in the adsorption rate and the uptake capacity [320]. Ideally, the pores of an adsorbent should facilitate the transport of molecules and provide easy access. This can be achieved through interlinked pores with a near uniform size distribution [319].

In the earlier chapter the practicality of using simple ZnO nanoparticles; synthesized using different synthetic routes as sorbents was discussed. The main drawback of those particles was their poor stability in acidic conditions. To overcome these problems and to further improve specific physical, chemical and surface properties that allow the selective attachment of ions, molecules, macromolecules, cells, colloidal particles or liquid phases, ZnO-composite nanoparticles can be designed [321, 322]. Once the target has been attached, the separation by centrifugation provides a very simple and effective method of separating the particles along with their targeted specifics group from the aqueous phase. Later on these specific groups can be eluted back using dilute acids or EDTA solution without affecting the sorbents. The manufacturing of these ZnO-composite particles first requires creation of the nanoparticles and then modification of the surface to match the requirements and constraints of the proposed end use [304, 323]. Of specific interest in current cases are micro and mesoporousnanomaterials, as these have a high surface area and high porosity; this coupled with high reactivity makes them useful as adsorbents in water and wastewater treatment. Functionalizednanoporous adsorbents are therefore now being studied with respect to their possible use in the removal of heavy metals from aqueous media [324-328]. Among the types examined, those with thiol-functionalized as well as silanefunctionalized groups have been found to be most efficient for the removal of Hg(II) [329] and other heavy metal ions.

In an effective treatment systems desorption of adsorbate and regeneration of the adsorbent is an essential requirement, and one of the key factors in this is the ability to maintain adequate performance of the adsorbent in multi-cycle use [330]. Hydrochloric acid is commonly used for elution of metal ions, including Hg(II) and Pb(II), from adsorbents due to their high solubility, its common usage in industry and its relatively low cost [331]. Recovery of the adsorbate may be a secondary objective, and the more concentrated the adsorbate is in the desorption fluid the more likely the success of the process [313, 332].

The current chapter discusses about various functional groups like thiourea (TU-ZNP), silanol (S-ZNP), and thiol-functionalized silica-coated (TFS-ZNP) ZnO nanoparticles prepared by one pot co-precipitation method and their characterization using a variety of physico-chemical techniques. In this chapter Thiourea, Tetra-ethyl-ortho-silicate (TEOS) and (3-Mercaptopropyl)-trimethyl-silane (MPTMS) is used as the coating agents. The composite particles were then used in an adsorption process for Pb(II) and Hg(II) removal, and the Langmuir and Freundlich isotherm models used to process the adsorption isotherm data. Desorption and regeneration were also examined as the next steps in progressing the application of this new type of adsorbent to more complex aqueous mixes containing other ions and dissolved species typical of what might be found in natural and waste waters.

4.2. Results and discussion

4.2.1. Characterization of adsorbent

The XRD diffraction patterns of various functionalized ZnO nanoparticles are shown in Figure 4.1, in which seven diffraction peaks (400, 002, 101, 102, 110, 103 and 112) are seen, which could be indexed to the hexagonal structure of pure ZnO nanoparticles (Figure 4.1), with no other crystalline phases detected. The XRD pattern of S-ZNPs shows that the particles have similar diffraction peaks with much noisier data and presence of a broad peak between 2θ 20-30° suggesting the presence of amorphous silica on the surface. Similarly in the case of TFS-ZNP along with the original peaks, the noise and the broad peak becomes much prominent suggesting the increase in silica content from the mercaptosilane also. While in the case of TU-ZNPs the broad peak at 2θ= 20-30° is absent indicating absence of any amorphous content.

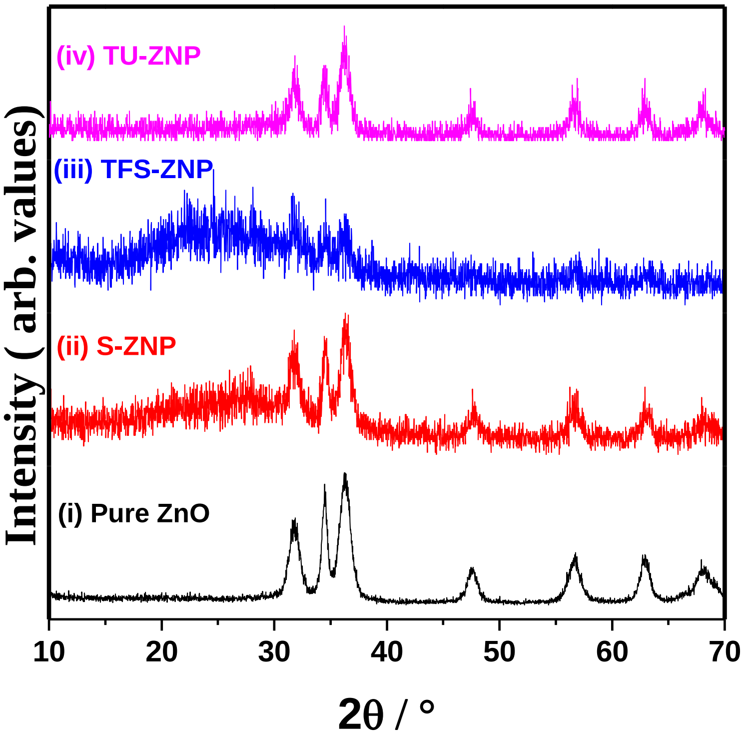

Figure 4.1: Structural properties of pure and functionalized ZnO nanoparticles as shown X-ray diffraction (XRD) (i) ZnO NPs (ii) Silica coated ZnO NPs, (iii) Thiol Functionalized silica coated ZnO NPs and (iv) Thiourea functionalized ZnO NPs.

It can be observed from **Figure 4.1**that coating does not change the peak position but the intensity, particularly the intensity of index [101], decreases with increasing the amount of coating. It means that coating process does not lead to change the ZnO NPs but reduces the crystallinity level. Addition of amorphous materials such as silica and mercapto-silica contributes irregularly arrangement of the material and leads to the crystalline peak intensity lowering. The change of intensity and crystallite size (D_{XRD}) has been calculated and presented in **Table 4.1**, which reveals same crystallite size of coated ZnO in comparison to that of pure one indicating that coating of amorphous silica/

thioureaon the ZnO surface is not affecting the original crystallite size of it, thus proving the amorphous coating layer.

Table 4.1: Intensity of index peak (101) and the crystallite size (D_{XRD}) of coated ZnO.

Material	**2θ**(°)	**Intensity** (%)	D_{XRD} (nm)
Pure-ZnO (ZNPs)	36.28	85	8
ZnO-SiO_2 (S-ZNPs)	36.31	57	9
ZnO-SiO_2-SH (TFS-ZNPs)	36.17	10	9
ZnO-SH (TU-ZNPs)	36.25	65	9

The FTIR spectra of ZnO NPs, S-ZNPs, TFS-ZNPs and TU-ZNPs are shown in **Figure 4.2**. For ZnO NPs, the peak at 470 cm^{-1} is attributed to the Zn-O bond vibration of ZnO. Absorbance bands in coated ZnO IR spectra around 1620-1640 cm^{-1} and 3400-3450 cm^{-1} come from bending and stretching vibrations, respectively, of –OH groups from both Zn-OH and Si-OH. The presence of silica coating on ZnO is shown by characteristic band at 787-802 and 1072-1126 cm^{-1} from asymmetry bending vibrations corresponding to Si-O-Si bonding. Isolated Si-OH groups present on the surface usually show a strong band at 3750 cm^{-1} and stretching vibration of Si-O-H bonding often shows a single broad absorbance band 810-960 cm^{-1} [333]. In IR spectrum of ZnO coated only with silica (S-ZNPs), absorbance of Si-OH vibration does not appear clearly due to overlap with broad band of stretching vibration from Si-O-Si.

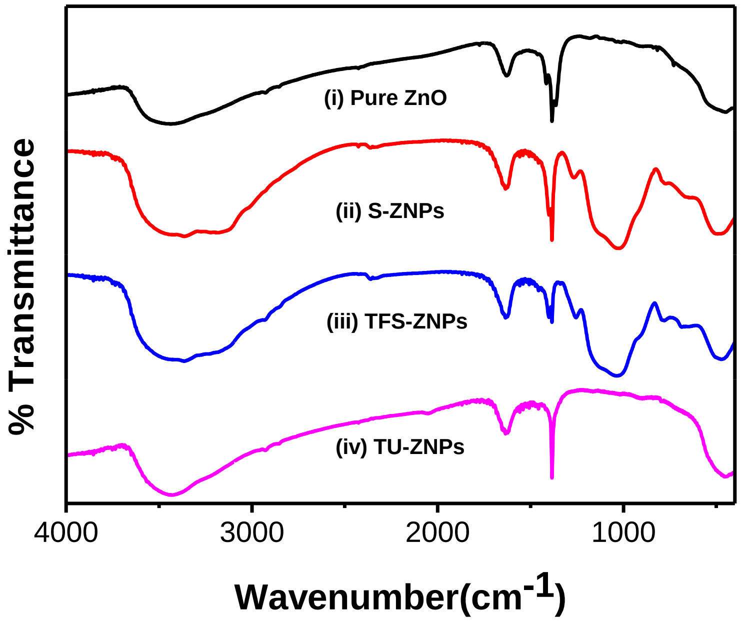

Figure 4.2: FTIR spectra of ((i) ZnO NPs (ii) Silica coated ZnO NPs, (iii) Thiol functionalized silica coated ZnO NPs and (iv) Thiourea functionalized ZnO NPs.

In comparison to ZnO (ZNPs) and silica coated ZnO (S-ZNPs), IR spectra of thiol-silica coated ZnO (TFS-ZNPs) gives characteristic absorbance of propyl and thiol-groups from MPTMS. The presence of propyl groups can be indicated by bands at 1040-1050 cm^{-1} and 1400-1480 cm^{-1} assigned to stretching vibration of –C-C- chain, bending of CH_2-, respectively. Additionally, C-H bonding in propyl groups results in absorbance at 2920-3000 cm^{-1} corresponding to asymmetric vibrations of C-H [334]. The presence of thiol groups is identified by the appearance of bands at 694 cm^{-1} and 890 cm^{-1} that can be assigned to asymmetric stretching of C-S and bending vibration of S-H. Weak bands at 2450-2600 cm^{-1} in IR spectra of thiol coated S-H stretches were found at 2510 cm^{-1}, which are convoluted by contamination of the CO_2 stretching bands from the background.

Generally, the S-H stretching band is characteristically weak and cannot be detected in the spectra of dilute solutions or thin films [335, 336]. The FTIR spectra show, however, that the surface of TFS-ZNPs contains an (-SH) group which results from the modification procedure with 3-MPTMS. While in the case of thiourea capped sample (TU-ZNPs) the presence of a shoulder at 650 cm^{-1}can be assigned to asymmetric stretching of C-S. From the above observations, the hypothetic structure of coated ZnO-NPs can be expressed as in Scheme 4.1

Scheme 4.1: Structural models of (a)ZnO- TU, (b) ZnO- SiO_2 and (c&d) ZnO-SiO_2-SH.

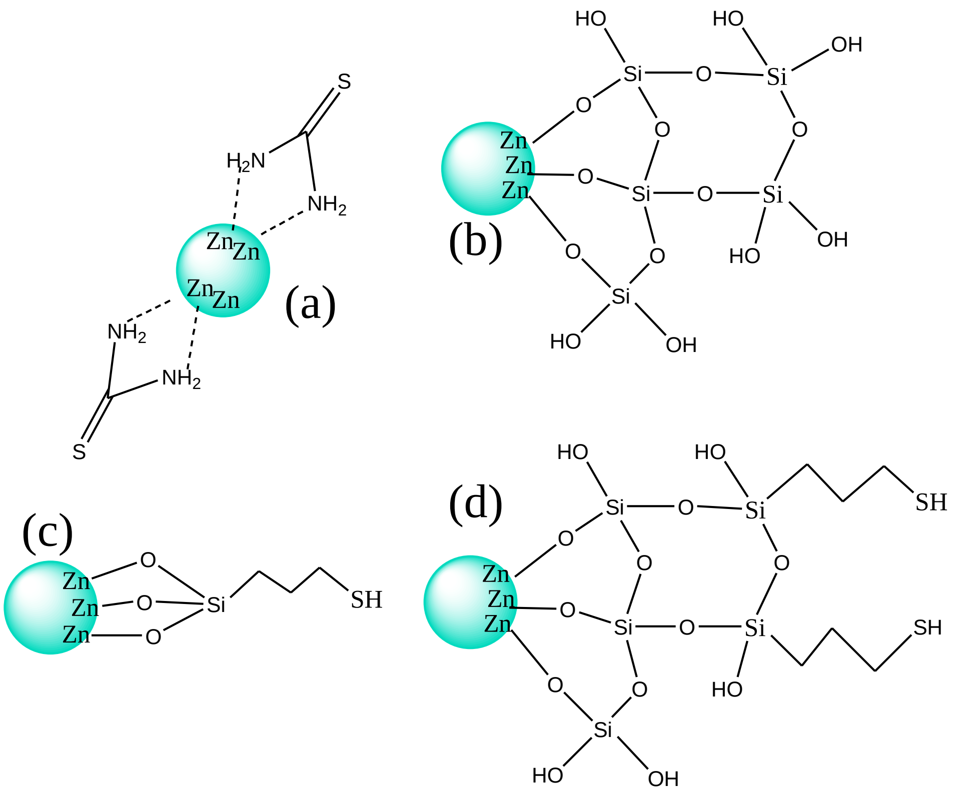

Another important character of ZnO NPs is particle porosity including surface area and pore size that may be measured using BET analysis. The porous nature of the nano-particles was investigated using N_2 adsorption- desorption isotherm. The N_2 isotherm (Figure 4.3) displays the typical Type IV curve with a H_3 type hysteresis loop, a characteristic of the predominant 3D network of mesopores according to IUPAC classification [226]. The Braunauer-Emmett-Teller (BET) surface area measurement and t-plot analysis were also carried out to obtain more information on surface area and porosity (refer to **Section 2.2.2**). It was found that the BET surface area plots of ZNPs (**Figure 4.3**) correspond to the well-known BET equation [225].

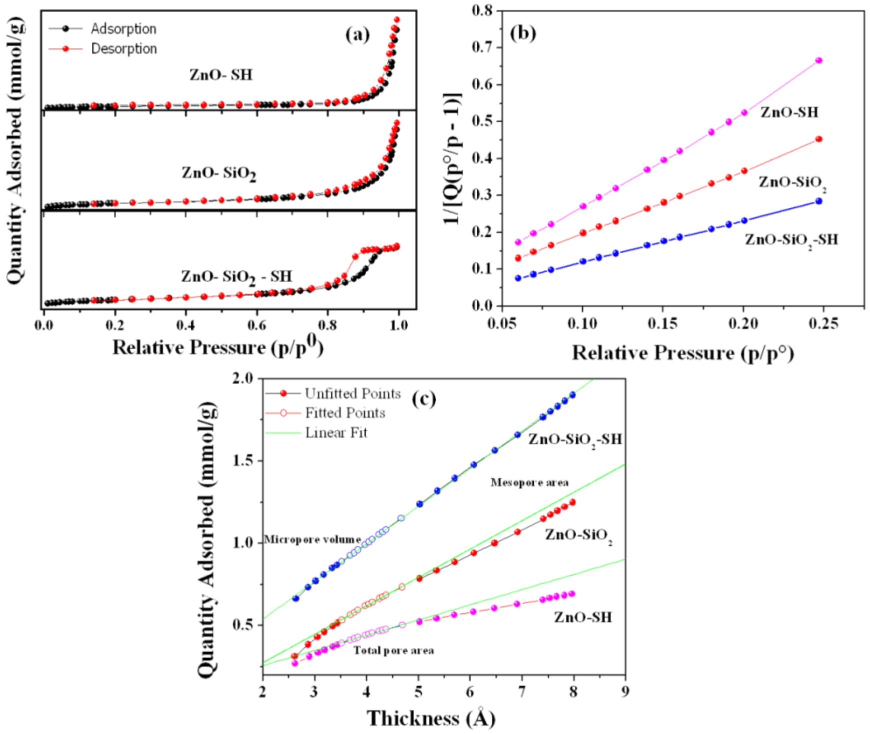

Figure 4.3: (a) N_2 adsorption –desorption isotherm, (b) BET surface area and (c) t-plot analysis of ZnO NPs.

The t-plot where Q (the quantity of nitrogen adsorbed in mmol/g) at different, P/Po values is plotted as a function of thickness of adsorbed gas are shown in**Figure**

4.3.The experimental values are found to be in good agreement with the Harkins and Jura equation [337]. The experimental points of ZnO NPs falls in straight line for thickness, t = 0.36-0.5 nm and does not pass through origin clearly indicating the porous nature of the sample. This can be further confirmed by the positive intercept of the fitted linear line which indicates the presence of micropores and the deviation from linearity at higher t values in the t-plot shows the presence of mesopores.The result of analysis is summarized in **Table 4.2** revealing that surface area of coated ZnO NPs increases with increasing the surface coating of the sample.

Table 4.2: Parameters obtained from BET analysis of functionalized ZnO NPs.

Material	**Surface area** (m^2/g)	**Porous totalvolume** (cm^3/g)	**Average pore diameter** (nm)
ZnO-SiO_2	57	0.29	20.17
ZnO-SiO_2-SH	87	0.25	10.84
ZnO-SH	38	0.40	46.60

As described before in the scheme, silica coated on ZnO may experience oligomerization reaction and exhibit porous layers outside of ZnO seed. In contrary ZnO coated only with thiourea gives smallest surface area plausibly due to only one layer of thiourea formed on the surface of ZnO. While, ZnO coated with silica and MPTMS have the highest surface area. Reaction between silica with MPTMS results in thicker coating on ZnO. Based on **Table 4.2**, the pore diameter average of all coated ZnO is higher 100 Å that can be categorized as mesoporus material.

As seen from **Table 4.3**, in particular for the latter two samples there is an increase in carbon content and also the presence of sulfur after treatment with thiol-silane and thiourea, which in principle corroborates the attachment of thiol groups at the surface of the nanoparticles. Note that due to the chemical nature of these materials, there are practical difficulties in their quantitative elemental analysis and these results should be regarded as indicative of the presence of the analyzed elements.

Table 4.3: Elemental analysis (weight %) for surface modified ZnO nanoparticles.

Material	**C**	**H**	**N**	**S**
ZnO-SiO_2	0.13	1.34	–	–
ZnO-SiO_2-SH	0.61	0.46	0.07	0.09
ZnO-SH	0.59	0.43	0.39	2.49

The thermal behavior of the modified ZnO nanoparticles was monitored from ambient to 800 °C. Thermogravimetric (TG) and Differential Thermogravimetric (DTG) curves of the silica coated and mercaptosilane coated ZnO NPs as well as the TG and Heat flow curve of thiourea coated ZnO NPs and thiourea are shown in **Figure 4.4** for comparison. The weight-loss stage below 150 °C in all the samples can be a result of the evaporation of physically adsorbed water in the samples. The second weight-loss stage in the case of thiourea coated sample in the region of 180–300 °C might result from the decomposition of thiol groups on the surface of material. The similar kind of behavior is observed in the case of TG-curve of pure thiourea with a slight shift in the degradation peaks to higher side indicating the presence of weak linkages on to the surface of ZnO nanoparticles. Thus, functionalization of ZnO nanoparticles with thiourea moieties is further confirmed.

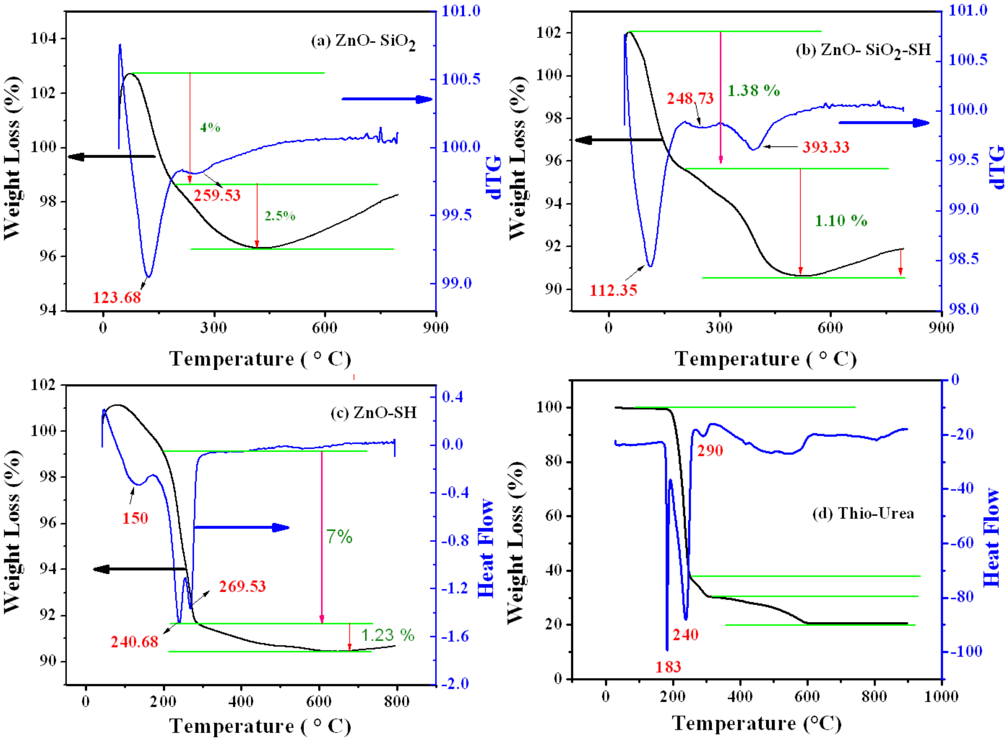

Figure 4.4: TG/DTG analysis of (a) ZnO- SiO_2 (b) ZnO-SiO_2-SH and TG/Heat Flow curve for (c) ZnO- TU and (d) Thiourea.

4.2.2. Adsorption kinetics

The time of equilibration is one of the experimental conditions which were varied in the range of 10-60 min. The rate of Hg(II) and Pb(II) uptake *vs* time for S-ZNPs, TFS-ZNPs and TU-ZNPs, respectively are shown in **Figure 4.5**. The adsorption was enhanced rapidly in the initial time, and then slowed down, and reached equilibrium finally. In the case of TU-ZNPs about 99% of Hg(II) and 93% of Pb(II) removed during the first 10 min. There was then a gradual reduction in rate of removal leading to an equilibrium condition which was achieved within less than 10 min with 100% Hg(II) adsorbed. Similarly in the case of TFS-ZNPs about 99% of Hg(II) and 95% of Pb(II) could be removed during the first 10 min, while in the case of S-ZNPs the uptake values of Hg(II) and of Pb(II) were found to be about 12% and 52%, respectively.

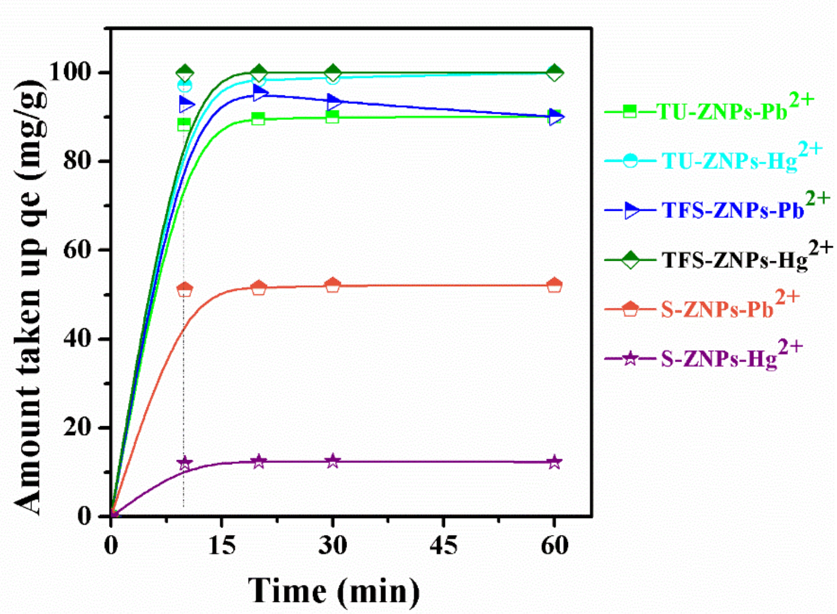

Figure 4.5: Adsorption kinetics of Hg(II) and Pb(II) on ZnONPs. Reaction conditions: ion concentration: 10 mg/L; sorbent concentration: 10 mg; solutionpH: 6.5.

The rapid adsorption in the case of thiol-functionalized nanoparticles might be attributed to two factors: first, there is a chemical binding between Hg(II) ions and the surface functional groups; second, there is electrostatic attraction between the external surface of the adsorbent and the metal ion. The reduced adsorption in the case of S-ZNPs should attribute to the absence of ready accessibility of mercury to the binding ssites (thiol group) which were coated on the exterior surface of sorbents. In the case of S-ZNPs the absence of thiol group results in relatively lower uptake as compared to the thiol functionalized counter parts like TU-ZNPs and TFS-ZNPs.

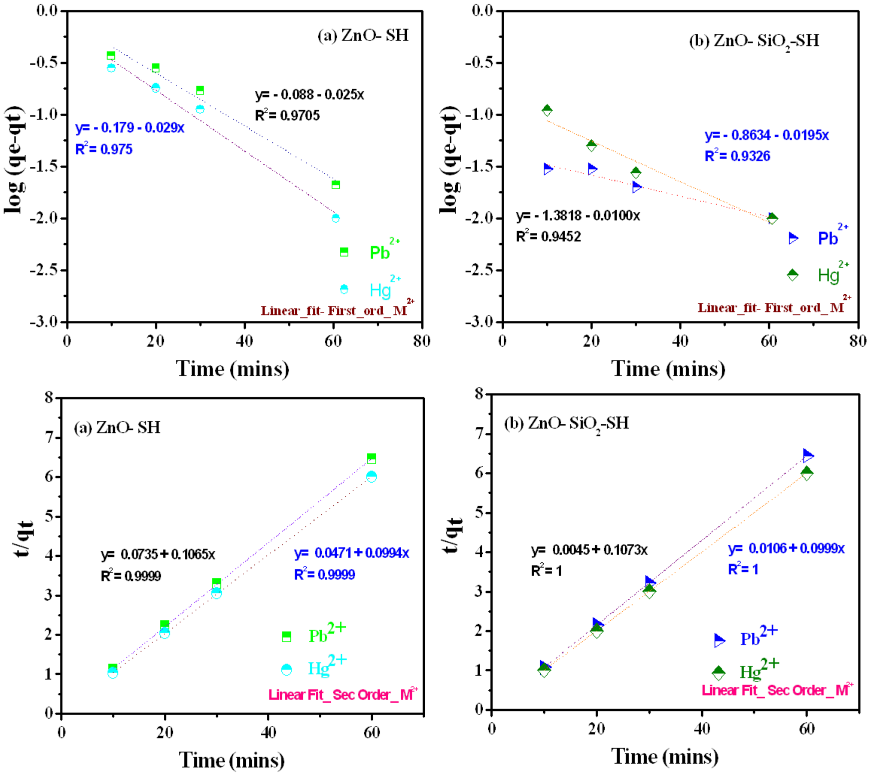

Figure 4.6: Kinetics modeling for the adsorption of Hg(II/ Pb(II) on ZnO NPs pseudo-first order (a) ZnO- TU NPs, (b) ZnO-SiO2-SH NPs and pseudo-second order (c) ZnO- TU NPs and (d) ZnO-SiO_2-SH NPs.

The kinetic sorption data obtained were analyzed using various kinetic models (refer to **Section 2.3.2**) to examine the rate law for sorption of metal ions onto the ZNPs. Herein, pseudo-first-order (refer to **Section 2.3.2.1**) [233], and pseudo-second-order (refer to **Section 2.3.2.2**) [235] models were used to test the experimental data. The plots of the pseudo-first-order (a & b) and pseudo-second-order (c & d) kinetics of Hg(II) or Pb(II), adsorption on ZNPs are shown in**Figure 4.6**. The calculated kinetic parameters are given in **Table 4.4**.

Table 4.4: Adsorption parameters obtained from the kinetics for the adsorption metal ions on ZnO NPs.

		Pseudo-first-order			**Pseudo-second-order**			
Adsorbent	**Metal ion**	**K_1** *(min^{-1})*	**q_e** *($mg\ g^{-1}$)*	**R^2**	**K_2** *($g\ mg^{-1}min^{-1}$)*	**q_{ecalc}** *($mg\ g^{-1}$)*	**q_{eexp}** *($mg\ g^{-1}$)*	**R^2**
TU-ZNPs	Pb(II)	0.06	0.82	0.970	0.14	9.38	9.3	0.999
	Hg(II)	0.07	0.66	0.975	0.21	10.10	10	0.999
TFS-ZNPs	Pb(II)	0.02	0.04	0.945	2.56	9.32	9.32	0.999
	Hg(II)	0.05	0.13	0.932	0.94	10.01	10	0.999

The comparison of correlation coefficients (R^2) of both models indicates that the kinetic data for the sorbent were fitted well to a pseudo-second-order kinetic model. The best fit to the pseudo-second-order kinetics indicates that the adsorption mechanism depends on the nature of adsorbate and adsorbent.

4.2.3. Adsorption isotherm

To derive data for the adsorption isotherm, initial concentrations of 1, 3, 5, and 10 mg Hg(II) or Pb(II) L^{-1} were used with various adsorbents of weight 10 mg .The adsorption isotherms of Hg(II) or Pb(II) onto the various adsorbents at room temperature near neutral pH are shown in **Figure 4.7**. It can be seen from **Figure 4.7** that, as expected, the amount of Hg(II) ions adsorbed per unit mass of the adsorbent increased with the increased concentration of the ions and does not reach saturation and it could further increase with the increase in equilibrium concentration of the respective ions.

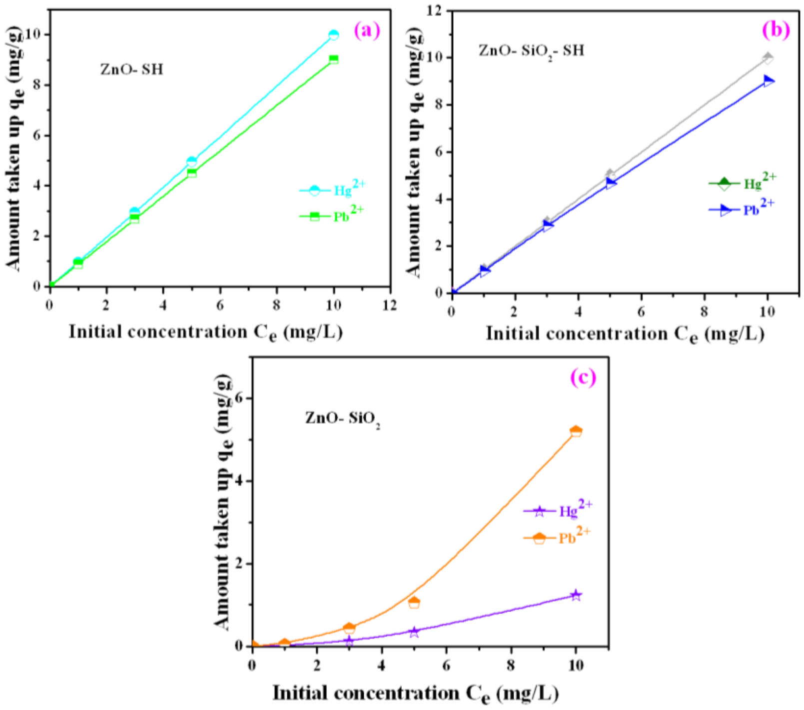

Figure 4.7: Adsorption Isotherms of Hg(II) and Pb(II) on ZnO NPs. (a) ZnO- TU NPs, (b) ZnO-SiO$_2$-SH NPs and (c) ZnO-SiO$_2$ NPs. Reaction conditions:ion concentration: 1-10 mg/L; sorbent concentration: 10 mg; solution pH: 6~5.

From this plot of adsorbed ions (qe) against the equilibrium concentration (Ce) at pH 6.0, the loading capacity of the TU-ZNPs, TF-SCMNPs and S-ZNPS should be larger than 9, 9 and 5.19 mg/g for Pb(II) and 10, 10, 1.23 mg/g for Hg(II), respectively. In all the cases the initial ion concentration of the solution was 10mg L^{-1}.

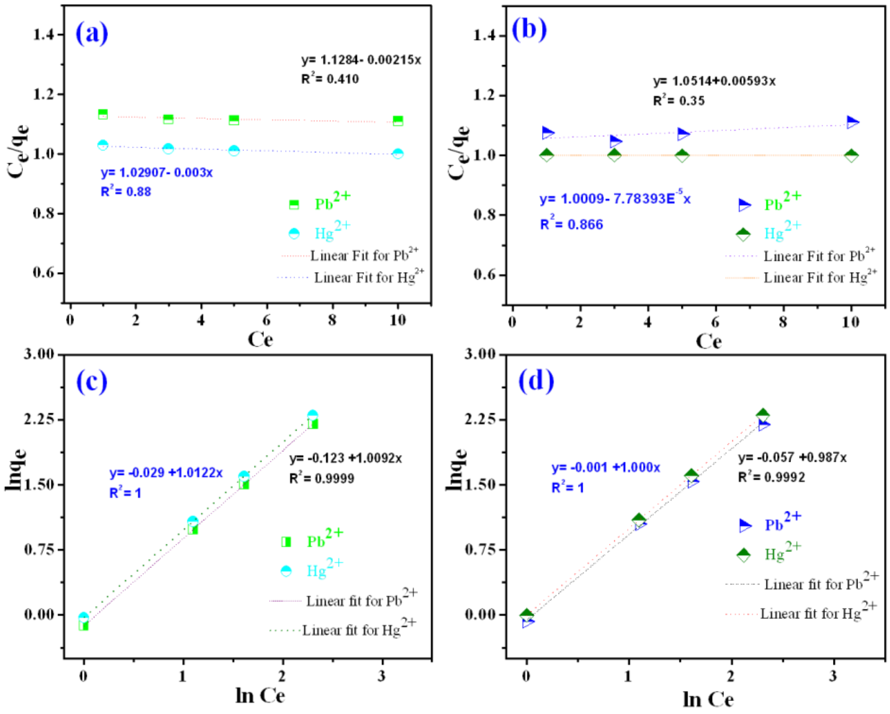

Figure 4.8: Linearized Langmuir (a &b) and Freundlich (c &d) Isotherms of Hg(II) and Pb(II) onto thiol functionalized ZnO NPs (a & c corresponds to that of TU ZNPs and b &d corresponds to TFS ZNPs).

The adsorption data were fitted to both the Langmuir [227] and Freundlich[229] isotherm models (refer to **Section 2.3.1**), which can describe the equilibrium between Hg(II) or Pb(II) adsorbed (qe) and in solution (Ce) at constant temperature. The difference in the models is that Langmuir assumes that adsorption takes place at specific homogenous sites within the adsorbent and is suited to monolayer adsorption processes, whereas Freundlich assumes the uptake of the adsorbates occurs on a heterogeneous surface by multi-layer adsorption. The linearized Langmuir isotherms and Freundlich Isotherms of lead and mercury onto the ZnO NPs are represented in the **Figure 4.8 (a-d).** The plots for C_e/q_eagainstC_e (Langmuir isotherm*)* for both sorbents are shown in **Figure 4.8(a, b)** with a linear regression line fitted. The values of the Langmuir constants $Q^0$and b were calculated from the slope and intercept of this line and are shown in **Table 4.5**. The correlation coefficient $R^2 < 0.9$ for the data to the model indicates monolayer adsorption is not the predominant mode of sorption of these ions on to the surfaces.

Table 4.5:Freundlich and Langmuir isotherm parameters for sorption of metal ions onto the ZnO NPs at 293K.

		Langmuir model				**Freundlich model**		
Adsorbent	**Metal ion**	**q_{max}** *($mg\ g^{-1}$)*	**K_L** *($L\ mg^{-1}$)*	**R^2**	**R_L**	**K_F** *($mg\ g^{-1}$)*	**n**	**R^2**
TU-ZNPs	Pb(II)	465.11	0.0019	0.41	0-1	0.88	0.99	0.999
	Hg(II)	333.33	0.0029	0.88	0-1	0.97	0.98	1
TFS-ZNPs	Pb(II)	168.63	0.0056	0.35	0-1	0.94	1.01	0.999
	Hg(II)	12848.5	-7.8E-05	0.86	0-1	0.999	1	1

The experimental data were also plotted in accordance with the Freundlich model (**Figure 4.8 c, d**) and the constants obtained are shown in **Table 4.5**. The correlation coefficients (R^2) between the experimental data and the model were < 0.9999 for all the cases suggesting that heterogeneous conditions exist. It might therefore be the case that the adsorbents provide heterogeneity by virtue of having different functional groups and a complex porous structure. From the correlation coefficients, it can be seen that the adsorption data fits the Freundlich model better than the Langmuir model in all the cases. The Freundlich parameter $1/n$ gave values of around 1 for all the samples indicating that Hg(II) or Pb(II) can be effectively removed from aqueous solutions

The plausible mechanism for this high uptake efficiency and selectivity of Hg(II) and Pb(II) can be attributed as follows. In case of thiol functionalized nanoparticles, the adsorption mechanism of metal ions may involve two surface reactions namely strong metal–sulfur complexation and weak electrostatic interaction. As anticipated from Pearson’s hard soft acid-base theory (HSAB) [338], the soft Lewis base such as thiol (SH) group is more favorable to undergo remarkable interaction with soft Lewis acids (heavy metal ions) rather than hard Lewis acids (alkali and alkaline earth metal ions). The high selectivity and affinity for Hg(II) by the thiol-functionalized group is a possible explanation for this [339]. The relatively large ionic size, low electronegativity, and high polarisability (highly deformable bonding electron orbital) of Hg are characteristics of a soft acid, and as the thiol group is a soft base they have a high affinity to each other. Thus, the thiol group (containing soft donor atom, sulfur) on the surface of nanoparticles mainly reacts with heavy metal ions directly to form stable metal–sulfur complexes through chelation.

4.2.4. Effect of competing ions

The initial experiments to assess the adsorption properties of the nanoparticles were carried out with Hg(II) dissolved in deionised water. Practical applications would, however, be for the removal of very low concentrations of Hg(II) from water sources or treated waste-water. As a first step in assessing the effect that an interaction between Hg(II) and dissolved ions could have on adsorption, some tests were carried out using a synthetic mixture containing 10 mg/L of each of the metal ion like Zn(II), Co(II), Ni(II), Cu(II), Pb(II) and Hg(II).The results are given in **Figure 4.9 (a-c)**.

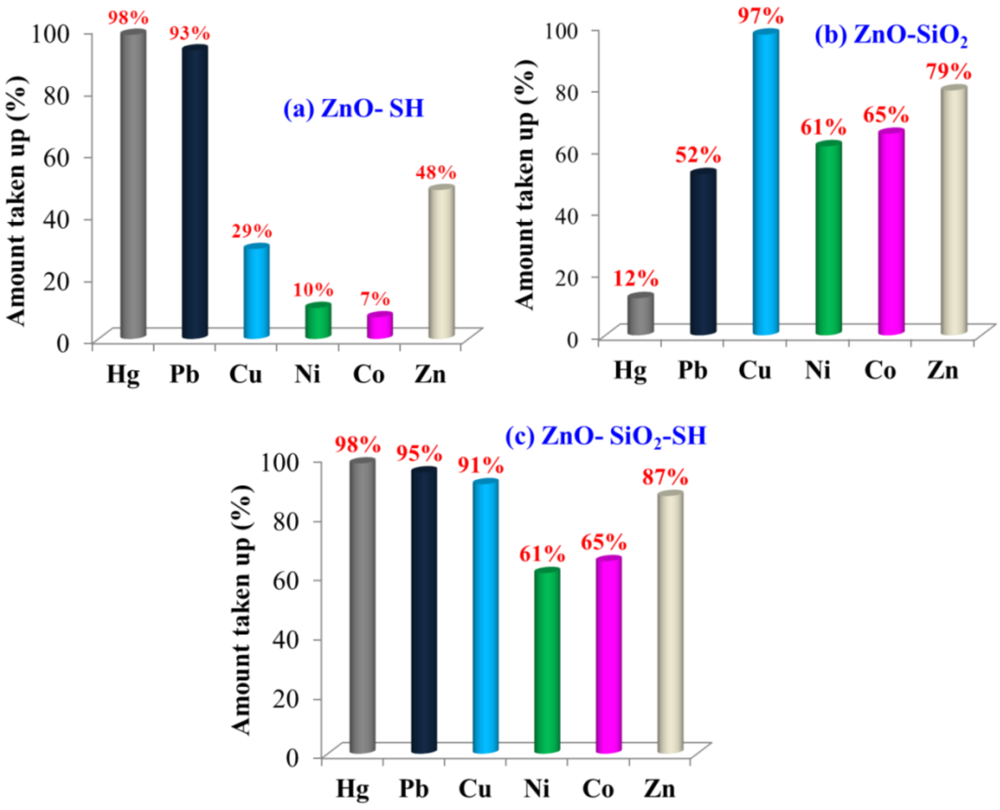

Figure 4.9: Removal efficiency of different toxic metal ions by (a)TU-ZnO NPs, (b) ZnO-SiO$_2$NPs and (c) ZnO-SiO$_2$–SH NPs.

The removal efficiency of metal ions with 10 mg of TU-ZNPs are found to be about 48%, 7%, 9%, 27%, 90% and 99% for Zn(II), Co(II), Ni(II), Cu(II), Pb(II) and Hg(II), respectively. While in the case of TFS-ZNPs 87%, 65%, 61%, 91%, 95% and 99% for Zn(II), Co(II), Ni(II), Cu(II), Pb(II) and Hg(II), respectively indicating that there was no interference with the maximum adsorption capacity for Hg(II) or Pb(II). Initial Hg concentrations of 10 mg L^{-1} were used in the case of all the sorbents.The uptake of the coexisting ions in the case of TFS-ZNPs clearly indicated the role of silica in the uptake of ions.

4.3. Summary

The functionalization of ZnO nanoparticles was done using a straight forward simple one pot co-precipitation method, followed by a facile ligand introduction to bind readily available affinity ligands onto the nanoparticle surface. This technique allows for tailoring of the surface chemistry to impart the specificity and affinity towards the target analytes (heavy metals of environmental concern). The resultant functionalized nanoparticles are easy to synthesize and are excellent sorbents for heavy metal contaminants like lead and mercury depending on the surface ligand installed. Thiol surface chemistry has been imparted on the ZnO nanoparticles and was shown to be highly effective, selective active sorbent materials. The reported synthetic method could be used to impart additional relevant surface chemistry chosen to target other biological and chemical analytes, for example, semipolar organics, radionuclides, proteins, and nucleic acids, of importance to environmental monitoring, decontamination, and remediation. In summary, a simple, flexible method for the preparation of highly effective, high surface area nano-sorbent materials was established and demonstrated their efficacy for the capture of toxic heavy metals from aquatic systems of relevance to the global problem of drinking water decontamination.

Chapter 5

$CeVO_4$ based adsorbents

Mo-substituted $CeVO_4$ oxides: Potential sorbents and Insight into solid solution formation

Jerina Majeed, Vinita Grover, Jayshree Ramkumar, K. Bhattacharyya and A. K. Tyagi

Dalton Transactions (Communicated)

5.1. Introduction:

ABO_4 class of compounds (A: lanthanide ion, including Sc and Y), in particular orthovanadates and orthophosphates, have been the subject of continued research due to the interesting physical properties exhibited by these compounds [74, 81, 340-342]. The $REVO_4$ compounds exhibit three structural types viz. tetragonal scheelite and zircon-type [68] and monoclinic monazite-type [69]. Cerium(III) orthovanadate ($CeVO_4$), which according to phase diagrams is located at the boundary of zircon and monazite types, exhibit three polymorphic forms with the pseudo-octahedral -like structure of tetragonal scheelite (occurring naturally in calcium tungstate) in addition to the known zircon and monazite type forms. The compound exhibits unique electronic [71-73], optical [71-75], magnetic [71-75], catalytic [74, 75], and luminescent [74, 75] properties. They are also used as sensors and electrode in electrochromic devices [74, 77]. Lanthanide ortho-vandates also used as catalyst and exhibit selective oxidative dehydrogenation of propane to propene [343]. Recently, they have been examined as potential photocatalysts for the degradation of dyes and organics [344]. Due to interesting physical features depicted by $REVO_4$, many studies have been dedicated to structural changes observed in this system using various diffraction and spectroscopic techniques [345, 346]. However, most of the studies on cerium vanadate have focused on A-site substitution. Out of few studies performed on B-site substituted $CeVO_4$, one was by Hirano et al. [347] on $Tb(V_{1-x}P_x)O_4$ systems wherein 'V^{5+}' was isovalently substituted by P^{5+}. To the best of the knowledge, there has been no structural study reported on substituted $CeVO_4$ with aliovalent substitution at B-site. It has been reported, that A-site substitution in $CeVO_4$ brings about variation (depending on relative ionic radii of host and guest) in $CeVO_4$ lattice but does not affect the VO_4tetrahedra. With this background, it is worth exploring the effect of substituting V^{5+} with a moiety possessing differently charged anion, on the structure of $CeVO_4$ and the possible solid solution formation mechanism adopted by the lattice to maintain the local charge neutrality.

The presence of lead in water has been a big menace in the present times. Pb(II) has got severe health implications involving immune disorders [348]. In fact, among inventory of priority heavy metal pollutants in ground water system set by most of the Environmental Protection Agencies, lead (Pb) is most challenging with high toxicity and carcinogenicity. There has always been a pressing need to circumvent this problem and various procedures have been implemented for the same. Development of an appropriately efficient sorbent which is also cost effective is hence very significant. There have been several examples wherein nanomaterials have been shown to exhibit superior sorption behavior [349]. From some of the earlier studies done in the group, it has been illustrated that nanomaterials can be employed as efficient sorbents for removal of lead and various toxic species through formation of inner-sphere complex with contaminants [350-352]. Some of the nanomaterials have also been explored for separation of radionuclides also [353].

In view of above information, the present work endeavors to explore the synthesis of Mo- doped $CeVO_4$ system, $Ce(V_{1-x}Mo_x)O_4$ ($0.0 \leq x \leq 0.4$). An exhaustive study which probes the solid solution formation mechanism based on X-ray diffraction (XRD) and spectroscopic techniques like Raman and X-ray photoelectron spectroscopy is presented.

The system has also been subjected to microscopic studies. To the best of our knowledge this is a new system and it has not been explored for its sorption properties. Hence, pure $CeVO_4$ and Mo-substituted $CeVO_4$ were explored as potential sorbents for Pb(II) ions. This entails investigating their sorption capacities and modeling of sorption behavior and kinetics.

5.2. Results and discussions

5.2.1. Characterization of adsorbent

All the nominal compositions synthesized in $Ce(V_{1-x}Mo_x)O_4$ ($0.0 \leq x \leq 0.5$) system were characterized by powder X-ray diffraction (XRD). The XRD patterns observed for the nominal compositions $Ce(V_{1-x}Mo_x)O_4$ ($0.0 \leq x \leq 0.5$) are shown in **Figure 5.1**. The XRD pattern for pure $CeVO_4$ matched well with that reported in the literature (JCPDS-PDF file No. 84-1457) and indicates well crystallized structure. It possesses tetragonal symmetry (SG: $I4_1/amd$) and the lattice parameters were calculated (by Powderx) to be: a= b= 7.336 Å, c= 6.472 Å, which are in good agreement with that reported in the literature for bulk $CeVO_4$. It is observed (**Figure 5.1**) that upto 40 mol% substitution of Mo^{6+} into $CeVO_4$ lattice, similar XRD patterns were obtained and on further increasing the Mo^{6+}-content to 50 mol%, a small and broad impurity peak centered at $2\theta \sim 28°$ could be observed. This implies that 40 mol% is the solubility limit of Mo in $CeVO_4$ under present experimental conditions, retaining the zircon-type crystal structure. Also, the peak broadening decreases on successive Mo-substitution. Hence, the particle size of $CeVO_4$ increases on substituting Mo^{6+} (**Table 5.1**). The XRD patterns of various nominal compositions in $Ce(V_{1-x}Mo_x)O_4$ ($0.0 \leq x \leq 0.4$) are refined and the refined lattice parameters are shown in **Table 5.1**.

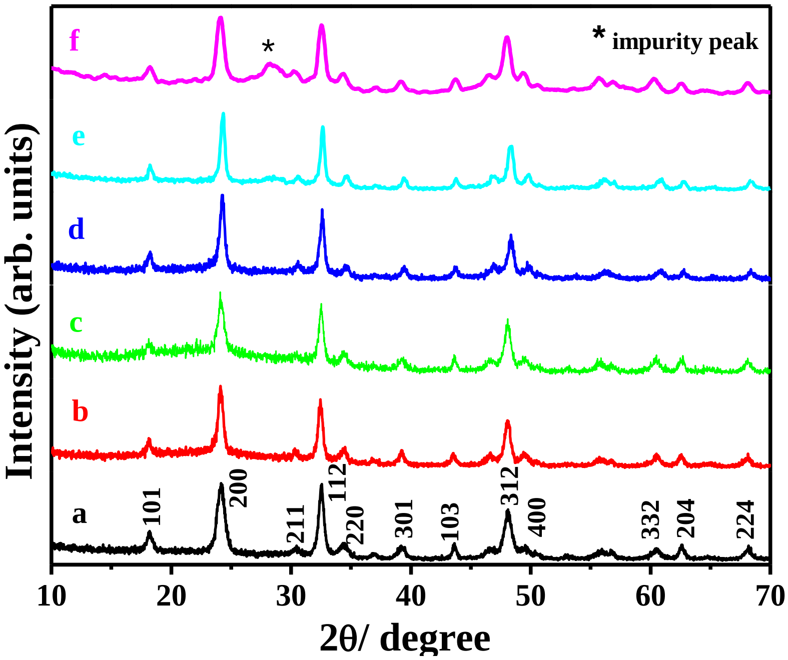

Figure 5.1: XRD pattern as synthesized (a) $CeVO_4$, (b) 5 % Mo-$CeVO_4$, (c) 10 % Mo-$CeVO_4$, (d) 20 % Mo-$CeVO_4$ (e) 40 % Mo-$CeVO_4$ and (f) 50 % Mo-$CeVO_4$ nanoparticles.

It is also interesting to note that initially upon 5 mol% Mo substitution in $CeVO_4$ lattice, there is no shift in peak positions and then there is a slight peak shift to higher angle side in the XRD patterns on subsequent Mo-substitutions up to 40 mol%. This implies that the cell parameters initially do not change and then decrease slightly. The ionic radii of V^{5+} and Mo^{6+} are 0.355 and 0.42 Å, respectively [354]. If it is assumed that Mo is substituting V^{5+} as Mo^{6+}, it predicts an increase in lattice parameter of the solid solution formed by substituting Mo^{6+} in $CeVO_4$.

Table 5.1: Lattice parameters and unit cell volume of as synthesized $Ce(V_{1-x}Mo_x)O_4$ (0.0≤ x ≤0.4) samples.

Sample $Ce(V_{1-x}Mo_x)O_4$	**Structure**	**A** (Å)	**c** (Å)	**Volume**(Å^3)	**Crystallite size from Scherrer equation** (nm)
x=0.0	zircon	7.354	6.483	350.609	10
x=0.05	zircon	7.352	6.482	350.364	15
x=0.1	zircon	7.344	6.464	348.632	12
x=0.2	zircon	7.303	6.470	345.069	16
x=0.4	zircon	7.305	6.455	344.458	20

This is indeed surprising because, 40 mol% substitution is large enough amount to be manifested as the increase in lattice parameters of the solid solutions (**Table 5.1**) if the lattice is same as the parent compound and Mo is getting substituted in the lattice. This result is in contrast to that reported by Porta et al. [355] who could observe an increase in lattice parameters in Mo-doped cerium vanadate solid solutions. Hence, it becomes absolutely essential here to confirm whether the increasing amount of Mo is indeed getting substituted in $CeVO_4$, by an alternate technique.

The X-ray fluorescence studies performed on all the nominal compositions (**Figure 5.2**) show that there is a definite increase in the Mo-content in corroboration with nominal compositions. Hence, this observation along with absence of any other Mo-containing phase in the XRD patterns, upto 40 mol% substitution, confirms, that even though significantly small and opposite shift in peaks of the diffraction patterns (and consequently the lattice parameters) is observed in contrast to that expected, an increasing amount of Mo is indeed getting substituted in these compositions. The Mo doped CeVO$_4$ samples will be denoted as CVM henceforth.

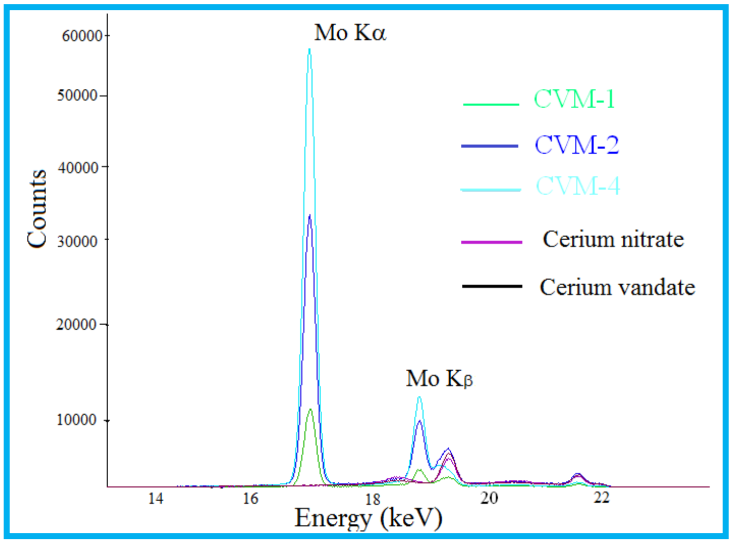

Figure 5.2: Trend in Mo-content observed in variousCe(V$_{1-x}$Mo$_x$)O$_4$(0.0≤ x ≤0.4)samples as obtained by EDXRF analysis.

A series of Raman spectra were recorded on all the nominal compositions (**Figure 5.3(a)**). CeVO$_4$, which exists in zircon structure, is supposed to exhibit 12 active Raman modes. Out of 12 Raman modes expected for this system, 9 modes have been observed. The main modes of CeVO$_4$ which are observed are 118, 142, 218, 260, 370, 446, 771, 784 and 845 cm^{-1}.The spectrum is dominated by the Raman band at 845 cm^{-1} which is assigned to vanadate symmetric stretching (ν_1), and at 771 cm^{-1} to the anti-symmetric stretching of vanadate. The other major bands at 444 and 368 cm^{-1} can be ascribed to bending deformations of the vanadate group. The modes observed at lower wave numbers like 118 cm^{-1}, 220 cm^{-1}are due to external rotations, translations etc. A careful observation of **Figure 5.3(a)** shows that the Raman spectra of all the Mo-substituted $CeVO_4$ are qualitatively similar to pure, undoped $CeVO_4$ which suggests the structural similarities between all the nominal compositions in the present CVM system. The Raman bands are clearly broadened, which can be ascribed to nano-size as well as the randomization introduced by hetero-ion (Mo) substitution in the lattice (**Figure 5.3(a)**). It is noticeable that with increase in Mo-content, there is a progressive red-shift in the frequencies of the symmetric (845 cm^{-1}) and asymmetric stretch (769 cm^{-1}) of BO_4 (B: V, Mo) groups (**Figure 5.3(b), (c)**). The red shift can be explained by increase in average cationic size on substituting V by larger Mo and hence the increased B-O bond length. This leads to decrease in the force constant and hence the observed red shift in the stretching frequencies (symmetric, asymmetric stretch) of B-O bond. In addition to the support provided by XRF for Mo-substitution in $CeVO_4$ lattice, the shift in Raman mode frequencies is also a valid proof of the substitution of Mo into $CeVO_4$ lattice.

However, the bending Raman modes do not show similar and consistent trend. The substitution of Mo in place of V, will lead to irregularities in BO_4tetrahedra which are otherwise regular in zircon structure. The bending of distorted polyhedral groups requires higher energy. In zircon structure, as mentioned earlier, the BO_4 - tetrahedra share edge with AO_8 dodecahedra. The substitution of a higher charged cation (Mo^{6+}) in place of V^{5+} should raise the energy of bending vibrations, for it may bring higher charged positive cations closer (across the edge) and hence require greater energy. Now, there are two competing factors operating here which are (i) decrease in force constant due to higher size of Mo-ion which should lead to red shift and (ii) increase in bending vibrational energies which should result in blue shift. As a consequence of these two opposing factors, the modes ascribed to the bending vibrations (260- 455 cm^{-1}) do not show a consistent trend. The symmetric bending vibration at 368 cm^{-1} is almost constant whereas, the asymmetric bending vibration at 445 cm^{-1} shows blue shift initially and then shows red shift in subsequent compositions with increase in Mo content.

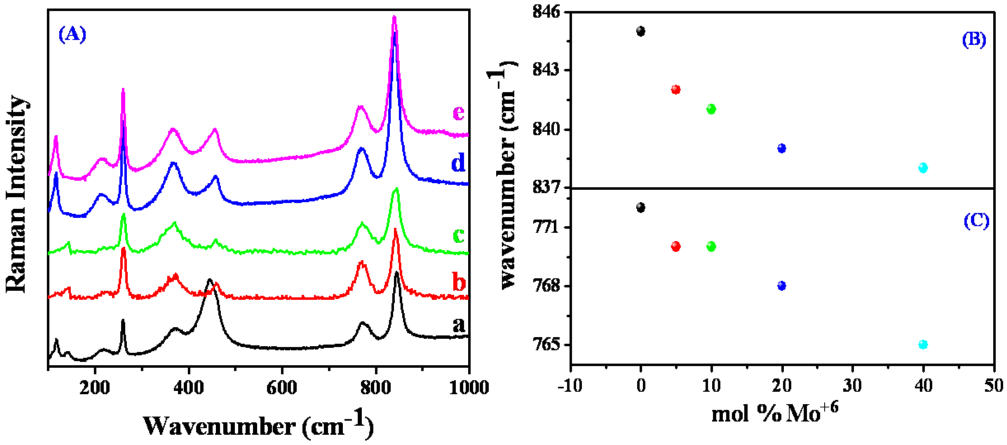

Figure 5.3: (A): Raman spectra of as synthesized (a) $CeVO_4$, (b) 5% Mo-$CeVO_4$,(c) 10 % Mo-$CeVO_4$, (d) 20 % Mo-$CeVO_4$ and (e) 40 % Mo-$CeVO_4$ nanoparticles, (B): Shift in symmetric (845 cm^{-1}) stretch and (C) asymmetric stretch (769 cm^{-1}) of VO_4 groups in all the $Ce(V_{1-x}Mo_x)O_4$ samples.

According to the general principle of preservation of local charge neutrality in case of substitutional solid solutions, the aliovalent substitution of V^{5+} by higher charged Mo^{6+} should either create an anion excess or cation vacancies for maintaining local charge neutrality. A similar study on $Bi(Mo_{1-x}V)O_4$ has shown, that among these two options, cation vacancies at Bi^{3+}-site are preferred over anion excess [356]. In this present system, the electro-neutrality can also be maintained by change in oxidation states of cations. This is possible at B-site, wherein both Mo and V (which are known to exist in variable oxidation states) can adopt lower oxidation states to maintain charge neutrality. However, the reduction of V^{5+} and Mo^{6+} to lower oxidation states should again lead to increase in the average cationic size because lower valent states are known to have larger ionic radii than higher valent in the similar co-ordination. This should also then result in increase in the lattice parameters in contrast to what is actually observed.

Thus, X-ray diffraction, X-ray fluorescence and Raman studies, quite evidently support the formation of substitutional solid solutions by replacement of V by Mo in $CeVO_4$. However, the lattice parameter trend is indeed intriguing. Also, there is no signature of any secondary phase $Ce(V_{1-x}Mo_x)O_4$ ($0.0\leq x \leq0.4$) system and the major phase appears to be same.

The XPS studies were performed on the representative nominal compositions in $Ce(V_{1-x}Mo_x)O_4$ ($0.0\leq x \leq0.4$). The Ce^{4+} 3d spectra of $Ce(V_{1-x}Mo_x)O_4$ ($0.0\leq x \leq0.4$) system are shown in **Figure 5.4**. The Ce- XPS spectra shows, the splitting due to R-S [357] coupling (**Figure 5.4**) and the peaks Ce $3d_{5/2}$ and Ce $3d_{3/2}$ can be identified. The individual 3d peaks also show splitting which indicates the presence of both Ce^{4+} and Ce^{3+} in pure $CeVO_4$[68] Certain satellite peaks at (884.1–884.6 eV), (887.6–888.1 eV) and (896.4–897.1 eV) and at (902.9–903.4 eV), (906.0–906.3 eV), (915.1–915.3 eV) are also observed which have been attributed to interaction between Ce-4f and O-2p states [358].

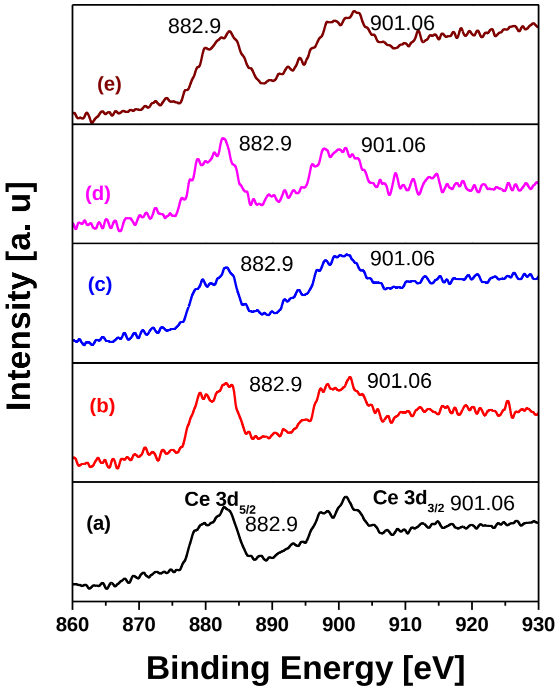

Figure 5.4: Ce-3d XPS spectra for (a) $CeVO_4$, (b) 5% Mo-$CeVO_4$,(c) 10 % Mo-$CeVO_4$, (d) 20 % Mo-$CeVO_4$ and (e) 40 % Mo-$CeVO_4$ nanoparticles.

On substituting Mo^{6+}, it is observed that both the splitting of 3d peaks as well as intensity of satellite peaks decrease and the trend is continued with subsequent Mo-substitutions. The decrease in splitting of individual 3d peaks with increase in Mo-substitution can be taken as the signature of decrease in amount of Ce^{4+} on increasing Mo^{4+}content (**Figure 5.4**). This can be explained, since addition of higher charged Mo will tend to decrease the positive charge in the parent lattice in order to maintain the charge neutrality. Further, the decrease in the satellite peaks attributed to interaction between Ce-4f and O-2p states [73], with the subsequent Mo-substitution, suggests *a decreased overlap between the Ce and O.*

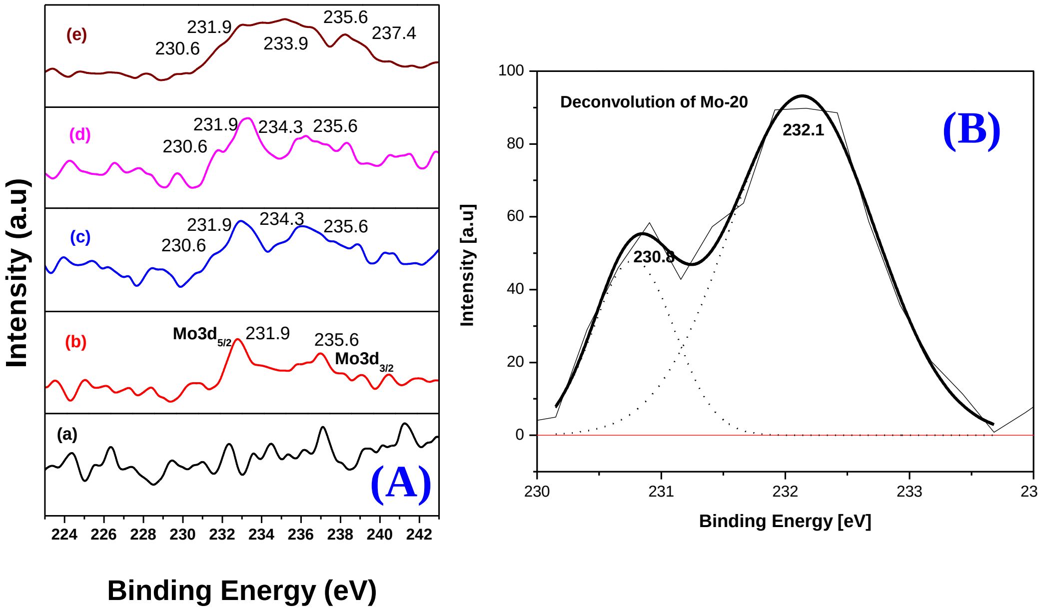

Figure 5.5: (A): Mo-3d XPS spectra for (a) $CeVO_4$, (b) 5% Mo-$CeVO_4$,(c) 10 % Mo-$CeVO_4$, (d) 20 % Mo-$CeVO_4$ and (e) 40 % Mo-$CeVO_4$ nanoparticles(B): Mo-$3d_{5/2}$ de-convoluted XPS spectra for the sample 10 % Mo-$CeVO_4$.

The XPS patterns of the Mo-3d for the various nominal compositions are depicted in **Figure 5.5(A)**. The Mo-XPS peaks are not expected in the parent compound. The 5% Mo-substituted sample shows the presence of the XPS peaks at 231.9 and 235.6 eV respectively attributed to $3d_{5/2}$ and $3d_{3/2}$ of Mo^{6+} [359]. Interestingly, the 10 mol% Mo-substituted sample shows a shoulder at 230.6 eV along with the peak at 231.9 eV which corresponds to Mo^{5+} species [359] and this is found to increases with increase in Mo-substitution.

The deconvolution of the shoulder peak corresponding to Mo^{5+} and the main peak belonging to Mo^{6+} in all the compositions was performed (**Figure 5.5)** and Mo^{5+}-contents present in the system as a function of the Mo doping, are tabulated in **Table 5.2**. Thus, the presence of both Mo^{5+} and Mo^{6+} peaks,with increase in amount of Mo^{5+} on subsequent Mo-substitutions indicate that the reduction of some amount of Mo^{6+} to Mo^{5+} is playing a major role in maintaining local charge neutrality in the CVM system.

Table 5.2: Qualitative estimate of the Mo^{5+} in the Mo-substituted $CeVO_4$ systems.

Sample $Ce(V_{1-x}Mo_xO_4)$	Mo^{5+} (Area under the curve) of 230.8 eV*	Mo^{6+} (Area under the curve) of 232.1eV*	Mo^{5+} (%)
x=0.0	-	-	-
x=0.05	-	552	0
x=0.1	53	188.5	21
x=0.2	39	137.21	22
x=0.4	145	381	27.5

*The area under the curve is found by deconvolution of the Mo $3d_{5/2}$ peaks using the Origin Software and the area under the curve is calculated after fitting (*The chi ^{2} values for each fitting are observed to be greater than 0.989*)

There have been reports in literature wherein Mo^{5+} has been observed to occur in 4-fold co-ordination and detected by esr spectroscopy. The XPS spectra of the V in these systems are relatively simpler. The XPS peaks for $V2p_{3/2}$ and $2p_{1/2}$ are observed at 517.1 and 521.2 eV, respectively (**Figure 5.6**),consistent with that reported in the literature for V^{5+} [223]. However, the oxidation state of V (i.e. $V^{5+/}V^{4+}$ reduction) is not significantly disturbed by Mo-doping unless the substitution is performed at higher concentrations. A small peak at 515.7 eV, corresponding to V^{4+} [359] appears only at 40 mol% Mo-substitution and this shows that the reduction of V is not a significant pathway in the solid solution formation.

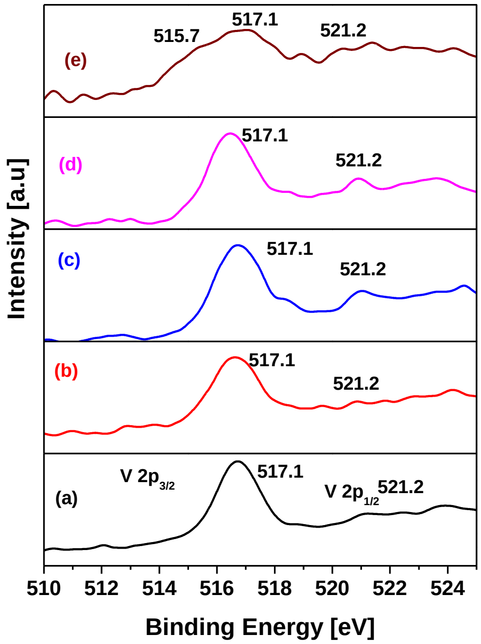

Figure 5.6: V-2p XPS spectra for (a) $CeVO_4$, (b) 5% Mo-$CeVO_4$,(c) 10 % Mo-$CeVO_4$, (d) 20 % Mo-$CeVO_4$ and (e) 40 % Mo-$CeVO_4$ nanoparticles.

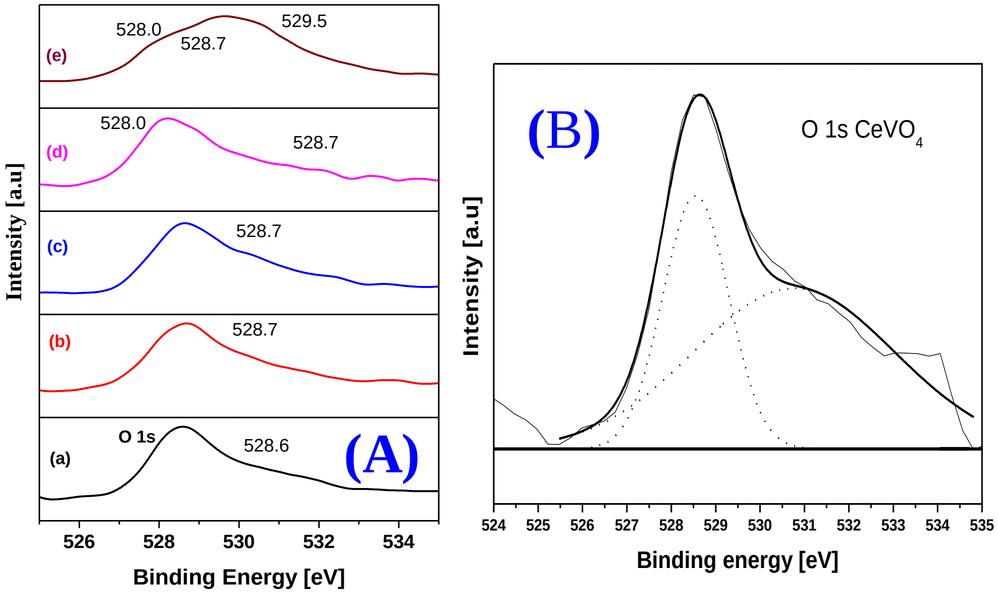

Figure 5.7(A): O-1s XPS spectra for (a) $CeVO_4$, (b) 5% Mo-$CeVO_4$,(c) 10 % Mo-$CeVO_4$, (d) 20 % Mo-$CeVO_4$ and (e) 40 % Mo-$CeVO_4$ nanoparticles,(B): O1s de-convoluted XPS spectra for the $CeVO_4$sample.

The O-1s XPS spectra for this system are depicted in **Figure 5.7(a)**. In $CeVO_4$, the O-1s peak is found at 528.7eV. This O 1s peak is observed to be asymmetric in nature and on deconvolution, (**Figure 5.7(b)**) it shows two peaks centered at 528.5 eV and 531eV. The peak at 528.5 can be attributed to the oxygen attached to CeO_8 and VO_4 since these polyhedral share edges. The peak at 531 eV is generally ascribed to O corresponding to that of surface –OH groups [360]. Also, the asymmetry in O 1s peak increases with increase in Mo-substitution. This may be attributed to the O attached to $Mo^{5+}$and Mo^{6+} in the system.

The collective assessment of results obtained from all the characterizations gives an insight into the mechanism of solid solution formation in CVM system. All the nominal compositions crystallize in tetragonal zircon phase. The charge compensation subsequent to aliovalent substitution of V^{5+} by Mo^{6+} is primarily obtained by reduction of some of the Mo^{6+} to Mo^{5+}. However, similar reduction of V^{5+} to V^{4+} occurs only at higher Mo substitution levels. But since all the Mo^{6+} is not converted to Mo^{5+} as shown by XPS (**Figure 5.5(a)**), and the presence of anion excess could not be confirmed using above mentioned techniques, shows that some Ce^{3+} vacancies should occur. Such A-site vacancies were also shown in $BiVO_4$ based system [356]. The presence of Ce vacancies will not only explain charge neutrality but also the near constancy (slight decrease) of lattice parameters (**Table 5.1**) despite the substitution of smaller V^{5+} by larger Mo^{6+} (or Mo^{5+} and V^{5+}) cation. The presence of vacancies is known to cause contraction of the lattice [361] and hence, the dilation of lattice due to increase in average cationic size is probably compensated resulting in observed trend. The Ce-XPS spectra also indicated decreased interaction between Ce and O on subsequent Mo-substitution which can also be explained on assuming Ce^{3+} vacancies. Anion excess as the charge compensating mechanism will also lead to lattice expansion due inter-anionic repulsion. It must be mentioned however, that the presence Ce^{3+} vacancies could not be directly evidenced.

The presence of variable oxidation states of same ion (Mo) in the same structure without causing the disruption of $CeVO_4$ lattice may applications for such materials in redox catalysis.

5.2.2. Exploring CVM system as Pb(II) ion sorbents

The framework compounds like vanadates and phosphates are known to show good sorption capacities [353, 362]. There has been report about feasibility of $CeVO_4$ and Cemolybdate as sorbents [353], however not much detailed work is reported. Also, to the best of the knowledge, this cerium vanado-molybdate system has not been explored as sorbents. Hence, it was attempted to explore the sorption of unwanted, highly toxic Pb(II) ions from aqueous solutions and examine the effect of Mo-substitution on the sorption efficiency. For the sake of clarity, in this section, $CeVO_4$, $CeVO_4$ -10 mol % Mo and $CeVO_4$ -40 mol % Mo will be represented as CV, CVM-1 and CVM-4, respectively.

The sorption behavior of the nanoparticle has tremendous dependence on their morphology. Thus, in order to reveal whether the powder properties and morphology of the pure and Mo substituted CV nanopowders are conducive to sorption, the samples were subjected to electron microscopic studies. The representative transmission electron micrograph of the as-prepared CeVO4 nanopowders is shown in **Figure 5.8(a)**. The formation of spherical particles of dimension 60-70 nm is easily discernible from the micrographs.

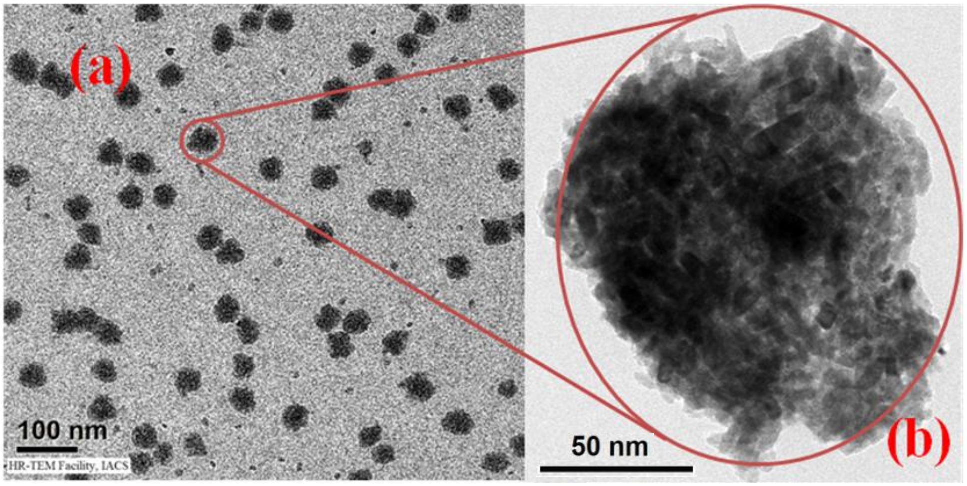

Figure 5.8: (a) TEM image of as synthesized $CeVO_4$ nanoparticle, (b) enlarged view of HR-TEM image of $CeVO_4$ nanoparticle.

Interestingly, a detailed HR-TEM (**Figure 5.8(b)**) reveals that each nano-sphere is composed of numerous nanocrystals (average size ~ 10-20nm) self-aggregated to form highly porous 3D spherical structures. This is also consistent with the particle size obtained from X-ray line broadening. The particles are fairly homogeneous and not very agglomerated. The pore shapes are observed to be irregular and the pore sizes are also not uniform.

In order to investigate the specific area and the porosity behavior of CV and Mo-substituted CV nano-assemblies, the N_2 adsorption- desorption isotherm were measured. The N_2 isotherm (**Figure 5.9(A)**) displays the typical Type IV curve with a H_3 type hysteresis loop.

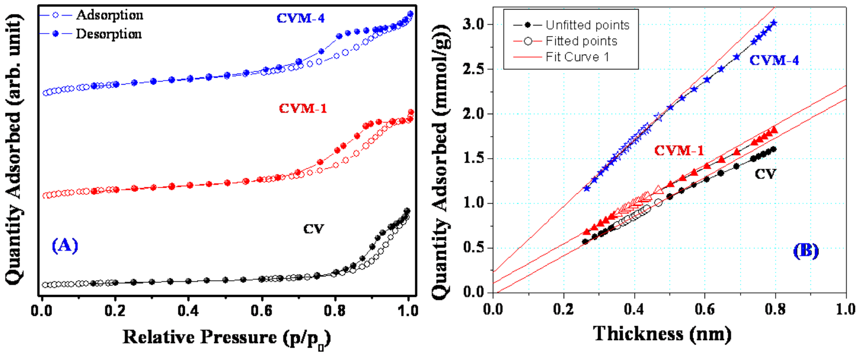

Figure 5.9(A): N$_2$ adsorption-desorption isotherm and (B): t- plot analysis of CV, CVM-1 and CVM-4 nanoparticles.

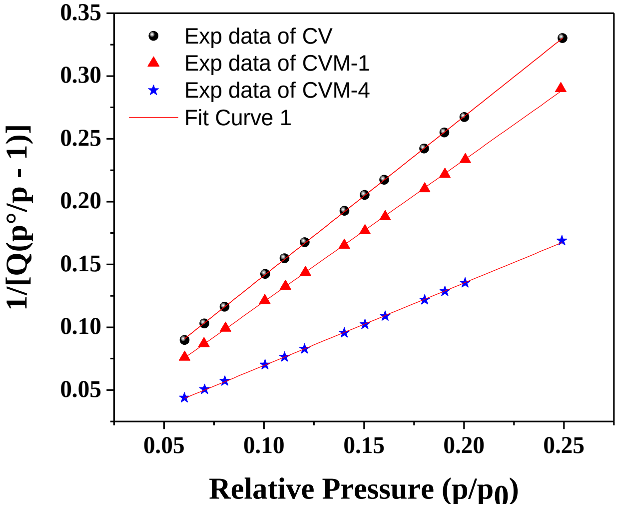

Figure 5.10: BET surface area analysis of pure and doped CeVO$_4$

In order to obtain more information on surface area and porosity, the Braunauer-Emmett-Teller (BET) surface area measurement and t-plot analysis were also carried out [363]. The t-plots showing the quantity of nitrogen adsorbed Q (mmol/g) at different P/Po values as a function of thickness of adsorbed gas, for pure and Mo substituted CV are shown in **Figure 5.9(B)**. The experimental values are found to be in good agreement with the Harkins and Jura equation [337]. It must be noted that in the t-plot, the straight line passing through the data points corresponding to the thickness of 0.35-0.46 nm does not pass through origin for any of these samples. This signifies the porous natures of the samples [364]. Also, the positive intercepts (on y-axis) in these t-plots suggest the presence of micropores for the Mo-substituted $CeVO_4$ samples. This peculiar behavior, attributable to micropores, was however found to be absent in the case of pure $CeVO_4$.

The deviation from linearity in the region of higher t values in the t-plot signifies the mesoporous nature of the materials. The BET surface area plots of pure and doped $CeVO_4$ are shown in **Figure 5.10**. The specific surface areas of CV, CVM-1 and CVM-4 were determined as 76, 86 and 147 m^2/g, respectively, and the corresponding pore volumes (at P/Po = 0.9960) are 0.42, 0.20 and 0.25 cm^3/g, respectively.

The sorption efficiencies of cerium vanadate and 40mol% molybdenum substituted cerium vanadate (CVM-4) with respect to lead ions were investigated. For a Pb(II) sorbent, to be used for potable water, it is much more relevant to evaluate its sorption efficiency in near neutral solution. Hence, the entire investigation was carried out at pH ~ 6-7. The studies were performed by equilibrating a known concentration of lead solution (10 or 100 ppm) maintained at pH 6-7 with 0.1 g of the sorbent for a period of 1 h. It was shown that both CV and CVM-4 are efficient sorbents and more than 99% uptake was exhibited for the initial concentrations of Pb(II) as 10 and 100 ppm.(**Figure 5.11(A), inset**). In order to investigate the effect of initial concentration of Pb(II) ions on the uptake behavior, different initial concentrations of Pb(II) varying from 10-100 mg/L were used at room temperature with vigorous stirring for 1 h. The equilibrium sorption capacity sharply reached the saturation point, showing ~100% uptake, regardless of the initial concentration (**Figure 5.11(A)**). Thus, Mo-substituted $CeVO_4$ is an efficient sorbent in all concentrations ranging from 10-100 mg/L.

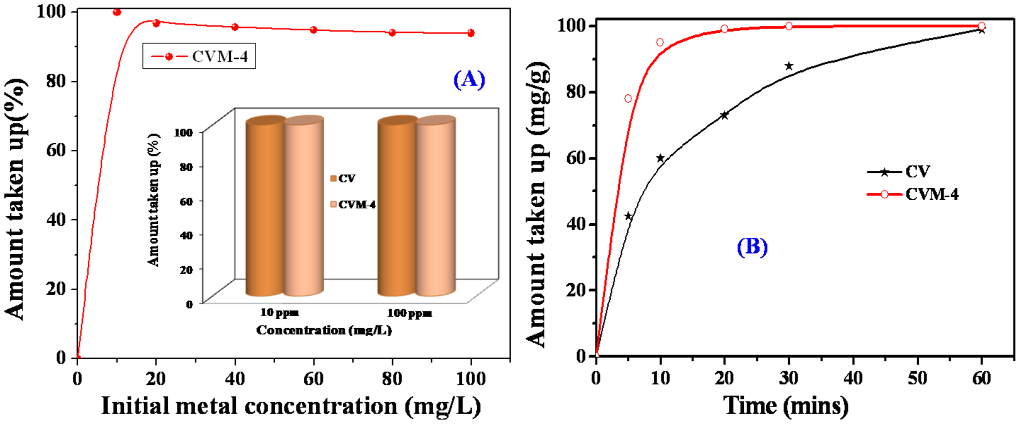

Figure 5.11(A): Effect of initial concentration of Pb (10-100 mg/L) metal ion on sorption behavior of CVM-4, (B): equilibration period on the amount of lead ion taken up and inset of (A):shows uptake by both the nanosorbents (pure CV and CVM-4).

However, since the BET analysis indicated the presence of micro and mesopores in Mo-substituted systems, it was considered worthwhile to analyse the effect of introduction of such features brought about by Mo-substitution on the sorption behavior of $CeVO_4$. Hence, the kinetics of sorption of Pb(II) ions by both pure and substituted $CeVO_4$ was investigated. The results of kinetic studies are shown in **Figure 5.11(B)** wherein it was found that $CeVO_4$ could show fast uptake of Pb(II), with 100% uptake achieved in 1 h. However, in comparison, the Mo-substituted $CeVO_4$ could depict the same uptake in less than 10 min. Thus, even though both CV and CVM-4 exhibited complete uptake of Pb(II) ions, CVM-4 demonstrated exceptionally fast kinetics in comparison to pure CV. This shows that the presence of molybdate anion framework has an immensely favorable effect on sorption kinetics of cerium vanadate lattice.

Since, CVM-4 exhibited better kinetics, so in order to further investigate the mechanism of sorption process on the samples; the data obtained were fitted to both equilibrium and kinetic modelling using different models. One of the most important characteristics of an adsorbent is the amount of adsorbate it can accumulate, which can be calculated from the adsorption isotherms. Adsorption isotherms are constant–temperature equilibrium relationship between the amount of adsorbate per unit of adsorbent (q_e) and its equilibrium solution concentration (C_e).

Herein, the sorption data for Pb(II) uptake on CVM-4 were fitted with the fundamental models of Langmuir [227], Freundlich [229] using the linearized equations for these isotherms and the fittings are shown in **Figure 5.12** and **Figure 5.13**, respectively. The Langmuir model considers that the sorption occurs only at specific homogeneous sites i.e. it takes the monolayer adsorption. On the other Freundlich adsorption isotherm, works on the consideration of multilayer adsorption on a non-homogeneous surface. It further assumes that the adsorption sites are having an exponential distribution with respect to heat of adsorption.

The fitted results of these isotherms are presented in **Table 5.3**. On the basis of correlation coefficient values, the sorption of Pb(II) can be best described by Freundlich isotherm model which implies that adsorption of Pb(II) on CVM-4 is a multilayer sorption process. The high capacity can be explained by the fact that sorption is not restricted to monolayer. The value of 1/n which reveals information about the nature of sorption taking place (physisorption/chemisorption) is found to lie between 0-1 thus indicating the chemisorption process.

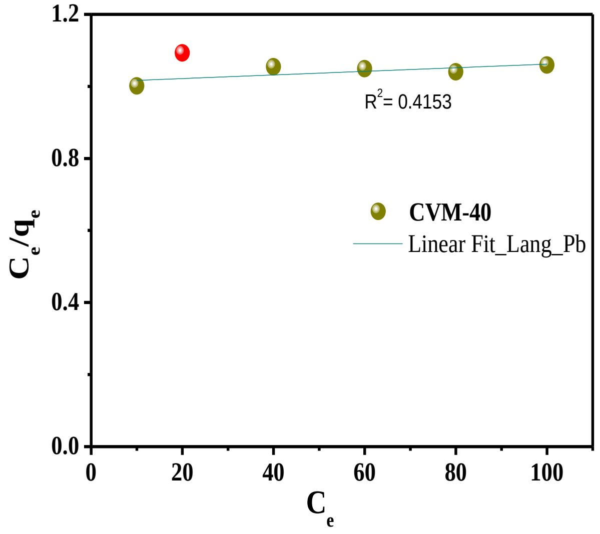

Figure 5.12: Equilibrium modeling using Langmuir isotherm for sorption of Pb(II) ions on CVM-4.

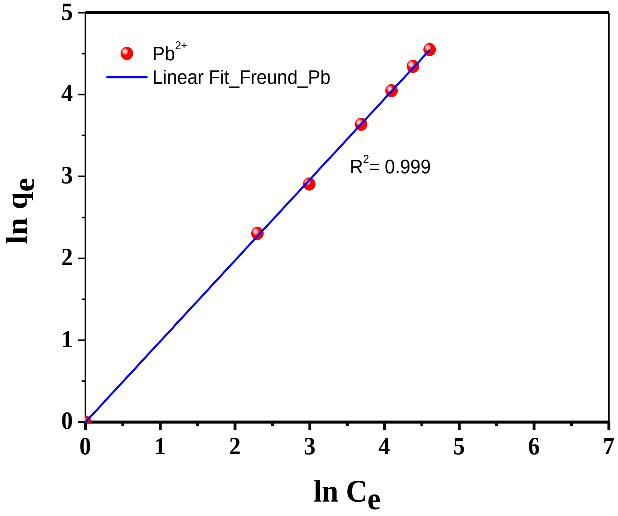

Figure 5.13: Equilibrium modeling using Freundlich isotherm for sorption of Pb(II) ions on CVM-4 nanoparticles.

Table 5.3: Parameters calculated from the linearized equations of different equilibrium models.

Parameters from linearized equation							
Model	**Langmuir**			**Freundlich**			
	Q_o*(mg/g)*	b	R^2	Surface heterogeneity	n	K_f	R^2
Pb(II)	1995.2	0.0005	0.4153	0.98	1.0	0.99	0.998

The sorption data was also fitted to Dubinin–Radushkevich model [232], from which the energy of sorption was found to be > 8 kJ/mol which lies in the range required for chemisorption process [365]. Using Freundlich model, it can also be confirmed that the process is a favourable given by the value of n which lies between 1 to 10. The Langmuir model, even though not the best fit here, showed the sorption capacity to be quite high.

Two types of kinetic modeling were performed to throw light on the kinetics and the order of Pb(II) adsorption process on CVM-4, the pseudo-first-order [233] (k_1, min^{-1}) model and the pseudo-second-order model [235] (k_2, g mg^{-1} min^{-1}).

q_t is the adsorption amount (mg g^{-1}) at time t and q_e is the adsorption capacity at equilibrium (mg g^{-1}), the $k_1$can be calculated from the plot of log (q_e*vs*q_t) against t, the k_2 can be calculated from the slope and intercept of the plots of t/q_t against t. The results of kinetic modeling are summarized in **Table 5.4**. The sorption data was found to fit well to the pseudo-second-order kinetic model. This suggests a chemisorption process as the rate limiting step (**Figure 5.14**). The equilibrium amount taken up, q_e, was calculated to be ~100 mg/g for both cerium vanadate and CVM-4, from the model fitting. The q_e is very high for CVM-4.

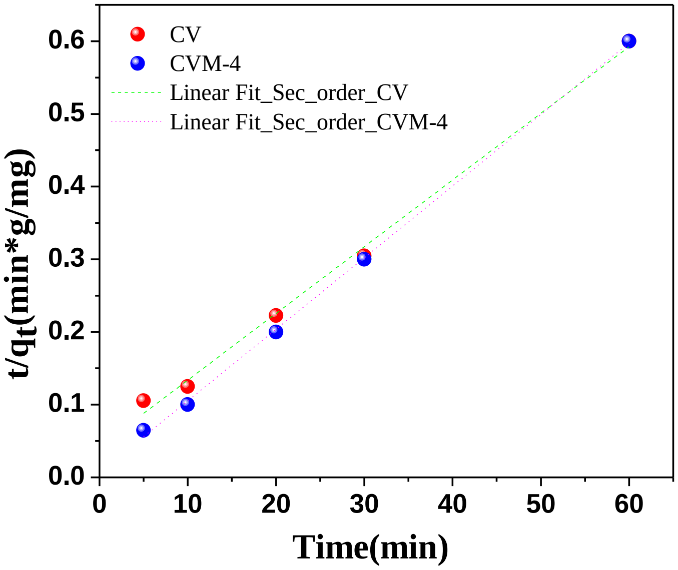

Figure 5.14: Kinetic modeling using Ho and Mackay Pseudo-second order rate equation for both CV and CVM-4 nanoparticles.

Table 5.4: Parameters calculated from the linearized equation of second order kinetic model.

Ho and Mackay (Second order)				
Sample	q_e (experimental)	q_e (calculated)	K_{2ads} $*10^{-2}$	R^2
CV	100	109.4	0.196	0.9949
CVM-4	100	102.5	1.4	0.9991

The q_e values for Pb(II) sorption observed in the present study are compared with those reported for some reported systems in **Table 5.5**[366-370]. It should also be noted that this is very much in agreement with experimentally determined capacity. In order to gain an insight into the rate determining step of the sorption process, Weber–Morris model was employed [237] and the fitted data is shown in **Figure 5.15**.

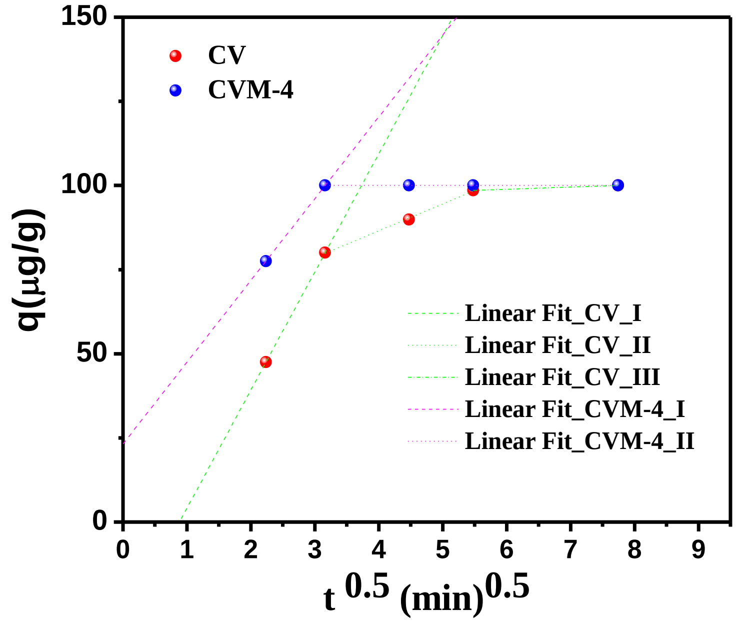

Figure 5.15: Kinetic modeling using Webber Morris model for CV and CVM-4.

The sorption, in general, can be defined by three steps, the mass transfer to surface of sorbent, diffusion of the sorbate through the boundary and finally the adsorption-desorption equilibrium. This corresponds to linear regression in three regions in the Weber Morris fitted plot as shown in **Figure 5.15**. The ratio of the slopes of these regions gives information about the rate determining step. Thus, it shows that external mass transfer to the surface of the sorbent (here CVM-4) that controls the rate of the sorption process. This, even in the chemisorption, that is taking place here, it is the mass transfer to sorbent sites which is the rate determining step.

Table 5.5: Comparison of Pb(II) uptake with that reported for different materials.

Adsorbents	**Pb(II)** (mg/g)	**Reference**
Iron oxide nanoparticles	36.0	[366]
Al_2O_3-supportediron oxide	28.98	[367]
Manganese oxide–carbon nanotube	26.24	[368]
Urchin like Ni−P microstructure	39	[369]
Flower-like titanium phosphate	550	[370]
Hierarchical cerium molybdo-vanadate (40 mol% Mo)	100	Present study

5.3. Summary

In summary, zircon-type Mo-substituted $CeVO_4$ solid solutions were synthesized by co-precipitation method. The system was extensively characterized using X-ray diffraction, X-ray fluorescence, Raman spectroscopy and X-ray photoelectron spectroscopy. The solid solution formation mechanism is proposed which involves reduction of Mo^{6+} to Mo^{5+} accompanied by Ce^{3+} vacancies. The particle size increased on Mo-substitution with concomitant increase in surface area as well which can be attributed to the presence of mesopores as shown by the N_2-adsorption-desorption isotherms. The hierarchical morphology coupled with the mesoporous structure showed efficient uptake of Pb(II) ions by $CeVO_4$. Introduction of hetero-Mo network improved the uptake kinetics by five times wherein 100 mg/L of Pb(II) uptake was exhibited in 10 min. The adsorption equilibrium isotherm showed best fit to Freundlich model. The isotherm analysis and kinetic modeling revealed the process to be a favorable chemisorption phenomenon following pseudo-second order kinetics. The study brings forth highly promising Pb(II) ion sorbents in a hitherto unexplored cerium molydovanadate system.

Further to ease the use of nanosorbents and ease of separation, it was felt worthwhile to use magnetic nanosorbents which will be discussed in the next chapter.

Chapter 6

Magnetic nanosorbents

1. *Fe_3O_4 @SiO_2 core-shell nanoparticles: Synthesis, characterization and application in environmental remediation*
   Jerina Majeed, Jayshree Ramkumar, S. Chandramouleeswaran, and A. K. Tyagi
   AIP Conf. Proc., 2014,1591, 605-609.

2. *Nano-Composites of Magnetite: A promising sorbent for removal of organic dyes and heavy metal ions*
   Jerina Majeed, Jayshree Ramkumar, S. Chandramouleeswaran, and A. K. Tyagi
   (*Manuscript under preparation)*

6.1. Introduction

Environmental remediation is of great importance in the present scenario of escalating development due to the continuous changes of environmental media (ground water) due to the presence of pollutants like heavy metal ions, organic dyes etc. The toxicity of the various pollutants is well understood and therefore regulatory bodies like World Health Organization (WHO) [371] and Environmental Protection Agency (EPA) [372] have given the specifications for water systems in which the maximum permissible concentration of these ions are given. The maximum allowable limit for zinc in discharged water was set by EPA as 5 mg L^{-1}. Dyes are not only toxic but also change the aesthetic characteristics of the ground water system [246, 373]. Therefore it is always of great importance to remove these pollutants from the water system either prior to discharge into the water body or prior to the consumption by mankind. There are number of procedures adopted for removal of these contaminants, including chemical precipitation [246, 374-376], ion exchange [377, 378], membrane filtration [379] and sorption [316, 325, 328]. Usually it is observed that no one particular procedure can completely remove the toxic species and in practice a combination of two or more procedures needed for complete treatment of waste water. Sorption is an attractive and efficient remediation procedure due to the use of substances that are inexpensive, readily available, environmental friendly or can be synthesized easily [176, 380, 381] as sorbents. Numerous sorbents based on metal oxides like as ZnO [269], Fe_2O_3 [382, 383] and FeOOH microspheres [384, 385], silica materials like mesoporous silica [386-388], carbon materials like graphene[389, 390], and silicates like magnesium silicate [391]have been reported successively as adsorbents with excellent performance for purification of waste-water. In recent times, nanomaterials (due to their high surface area) have shown potential as a high performance sorbents. Hence, there is an on-going quest for new nano-sorbents with facile separation properties for removal of organic as well as inorganic pollutants in water effluent from industries.

The main problem associated with nano-sorbents is its recyclability from the aqueous solution due to their smaller particle size and superior dispersive properties. Comparing, usual separation methods, including filtration and centrifugation which are time taking and may lead to loss of the sorbent, magnetic sorbents can be easily and rapidly separated from aqueous solutions using an external magnetic field and regenerated to be used for multiple cycles. Thus it makes sorption a cost effective method.

Composite nanomaterials also have great attraction as it gives rise to the combination of the properties of the two individual nanomaterials and these can enhance the application in waste water treatment. Another important aspect of using such sorbents is the fact that selectivity can be improved by surface functionalization with suitable groups that can selectively remove the metal ion of interest. Silica is a well-known material for its sorption properties both in bulk and nano form, as well as high surface area and porosity, and its high stability in acidic conditions. Therefore modification of magnetic nanoparticles surface with silica is expected to increase the removal efficiency of toxic ions by simultaneously taking advantage of the magnetic properties of the core as well as the properties of shell like high surface area, porosity and stability in the lower pH range.

This chapter deals with the synthesis, characterization and sorption property evaluation of nano-composites of Fe_3O_4 with SiO_2 (SMNPs) with respect to transition metal ions and cationic dyes like methylene blue and rhodamine 6G. The performance of SMNPs was determined in terms of sorption isotherm and kinetics. Taking into account the practical applicability, the regeneration and reusability of the SMNPs were also evaluated.

6.2. Results and Discussion

6.2.1. Characterization of nano-composites

The nano-composites synthesized were characterized using different techniques like XRD, IR, and TEM and magnetic measurements in order to characterize the synthesized nano-composites as well as to get an insight of the sorption mechanism. XRD patterns of the magnetic iron oxide nanoparticles (FMNPs) and magnetic naocomposites of iron oxide with silica (SMNPs) are given in **Figure 6.1(a) and (b)** respectively. The peaks could be indexed to the cubic structure corresponding to magnetite phase ((JCPDS Card No. 88-0315, a = 8.375 Å). The presence of a small broad peak at 2θ in the range of 20–30° and a noisy XRD pattern confirm the presence of amorphous silica on the surface of the magnetic iron nanoparticles.

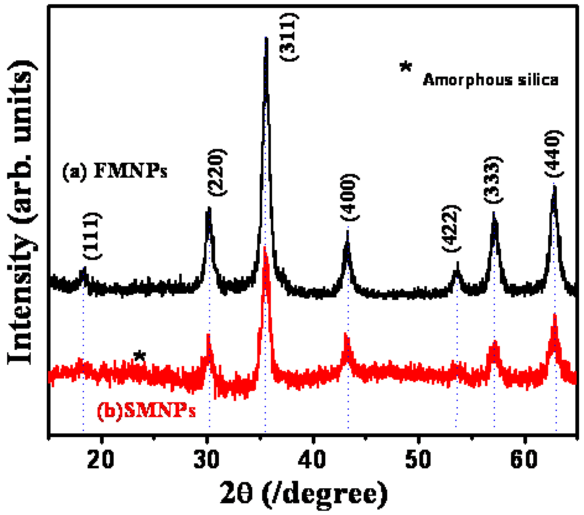

Figure 6.1: XRD patterns of pure (FMNPs) and SiO_2 coated Fe_3O_4 (SMNPs) nano-composites.

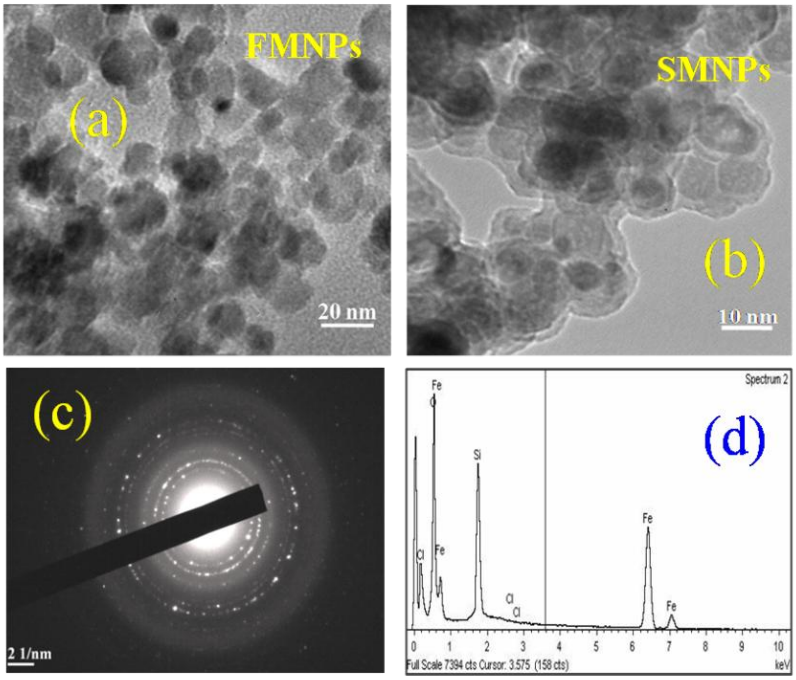

Figure 6.2: TEM images of (a) pure Fe_3O_4, (b) SiO_2 coated Fe_3O_4 and the corresponding (c) SAED and (d) EDS pattern of SiO_2 coated Fe_3O_4.

The TEM image of the pure Fe_3O_4 nanoparticles (FMNPs) (**Figure 6.2(a)**) shows aggregated particles with size of 10 nm, while **Figure 6.2(b)** showed clearly the formation of shell of 2-6 nm thickness around the particles of size in the range of 10 – 20 nm. The corresponding SAED pattern (**Figure 6.2 (c)**) shows that it is a well crystalline structure and further confirmation of the presence of silica in SMNPs was obtained from the EDS spectrum (**Figure 6.2(d)**). IR spectrum (**Figure 6.3(a)**) corroborates the findings of TEM and confirms the coating of SiO_2 particles on to the surface of FMNPs.

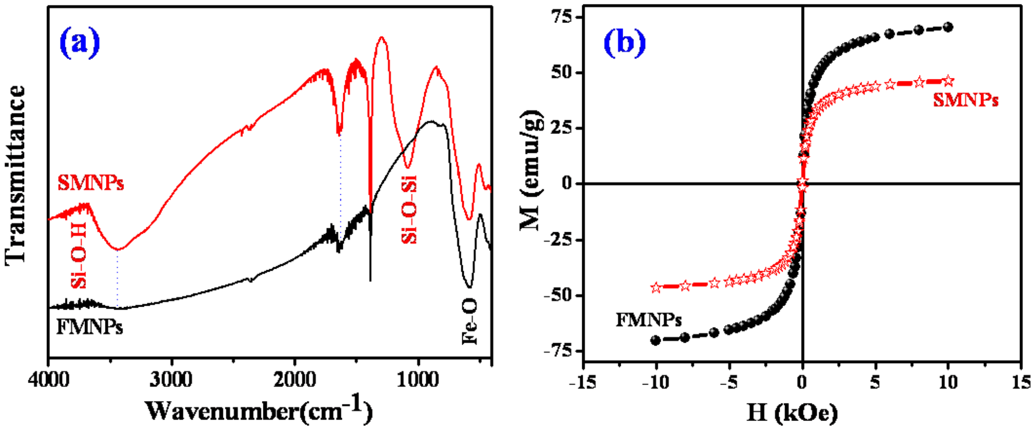

Figure 6.3: (a)FTIR spectra and (b) the magnetization curve for pureFe_3O_4 and SiO_2 coated Fe_3O_4 nanoparticles.

IR spectrum of FMNPs showed an absorption peak centered around 590 cm^{-1}, which corresponds to Fe–O stretching vibration, and a band centered around 3422 and 1650 cm^{-1} corresponding to the H–O–H stretching mode and bending vibration of water adsorbed on the surface of nanoparticles. Increase in intensity of these peaks (3422 and 1650 cm^{-1}) implies the presence of surface hydroxyl groups on silica layer. The broad band at 1092 cm^{-1} is characteristic peaks of the symmetrical vibrations of Si–O–Si in SiO_4

tetrahedron and the band at 3749 cm^{-1} is an indication of the presence of Si–O–H bond [392].

The magnetization *vs* applied magnetic field (M-H) curve at room temperature for FMNPS and SMNPS are shown in **Figure 6.3(b),** which clearly indicates the super-paramagnetic nature of the samples as no coercivity is present.

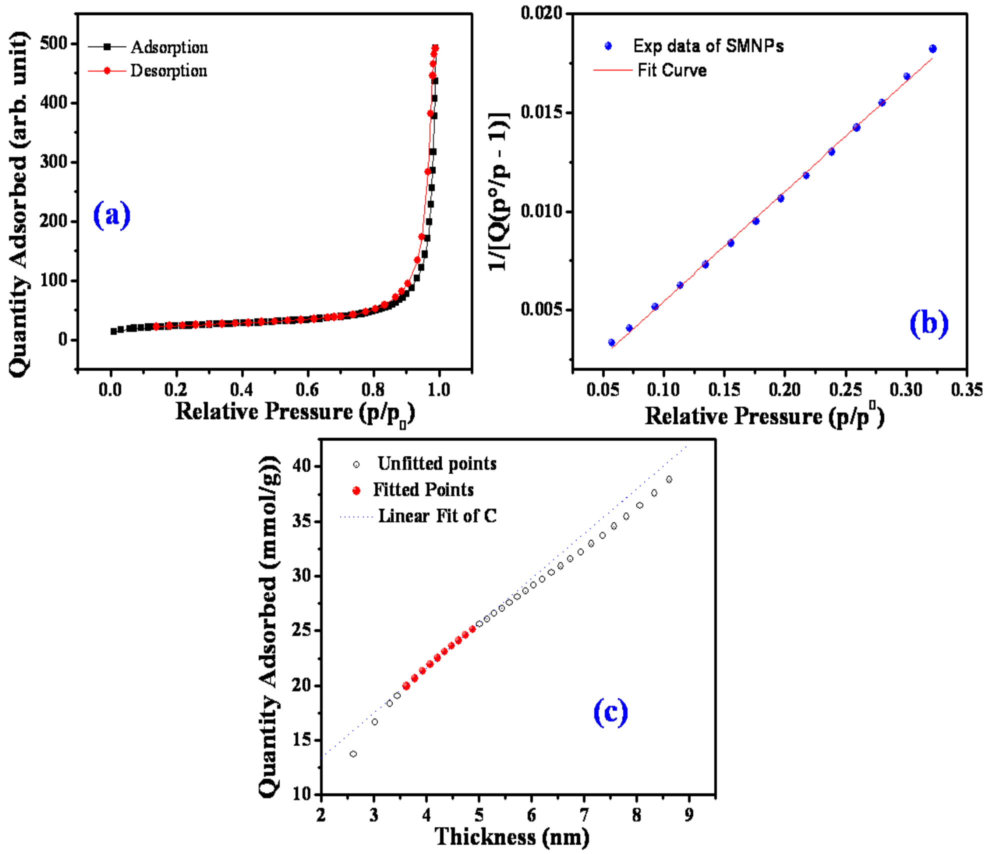

Figure 6.4: (a) N_2 adsorption –desorption isotherm, (b) BET surface area and (c) t-plot analysis of SiO_2 coated Fe_3O_4 nanoparticles.

The porous nature of the nano-particles was investigated using N_2 adsorption-desorption isotherm. The N_2 isotherm (**Figure 6.4(a)**) displays the typical Type IV curve with a H_3 hysteresis loop, a characteristic of the predominant 3D network of mesopores according to IUPAC classification[226]. The Braunauer-Emmett-Teller (BET) surface area measurement and t-plot analysis were also carried out to obtain more information on surface area and porosity, and it was found that the BET surface area plots of SMNPs (**Figure 6.4(b)**) correspond to the well-known BET equation [225]. From the N_2 adsorption-desorption measurements it was observed that SMNPs have a surface area of 125 m^2/g and the corresponding single point adsorption total pore volume of pores at P/Po = 0.9891 was 0.7603 cm^3/g. shows The t-plot, where Q (the quantity of nitrogen adsorbed in mmol/g) at different, P/Po values is plotted as a function of thickness of adsorbed gas are shown in **Figure 6.4(c)**. The experimental values are found to be in good agreement with the Harkins and Jura equation [337]. The experimental points of SMNPs falls in straight line for thickness, t= 0.36-0.5 nm and doesn't pass through origin clearly indicating the porous nature of the sample. This can be further confirmed by the positive intercept of the fitted linear line which indicates the presence of micropores and the deviation from linearity at higher t values in the t-plot shows the presence of mesopores.

6.2.2. Sorption studies

The uptake of both metal ions and cationic dyes were carried out. The main aim of this work was to evaluate whether the synthesized nano-composites could be used for ground water system without any prior pre-treatment of the water sample including adjustment of the pH. The present study can have a probable application of removal of pollutants from these samples. In order to get the maximum sorption efficiency and to understand the sorption behavior, different experimental conditions were varied and the effect of these variations has been studied in detail. The results have been discussed under different sections.

6.2.2.1. Sorption of metal ions

The most important solution parameter that is expected to affect the sorption is the pH of solution. This is because the pH affects the nature of both the solute and the sorbent. In the present study, the main aim was to use the system for near neutral pH water samples. Moreover, from our earlier work it was found that the optimum uptake of transition metal ions is around pH 5 [393]. This is because that the metal ions have a tendency to hydrolyse beyond pH 6. At lower pH the high concentration of protons in solution compete with the surface sites with the metal ions thereby reducing the uptake. Moreover the main aim of this study is to see the potential application of the sorbent for ground water system wherein the pH is around 5 to 6. Therefore the maximum uptake occurring at pH~5 is of advantage for ground water treatment.

The effect of weight of sorbent on the amount taken up was also studied. It is expected that there will be some variation in the amount taken up. For this the 10 mL of the solution containing 10 ppm of the metal ion was maintained at pH ~5-6 and equilibrated with for a period of one hour with different weights of sorbent. These studies showed that maximum uptake of metal ions could be achieved with 0.01 g.The kinetic studies were carried out by equilibrating 10 mL of 10 ppm of metal ion solution maintained at pH between ~ 5 to 6 with 0.01g of the sorbent for different periods of equilibration and the results are shown in **Figure 6.5 (a)**.It is seen that maximum uptake was achieved within half-an-hour.

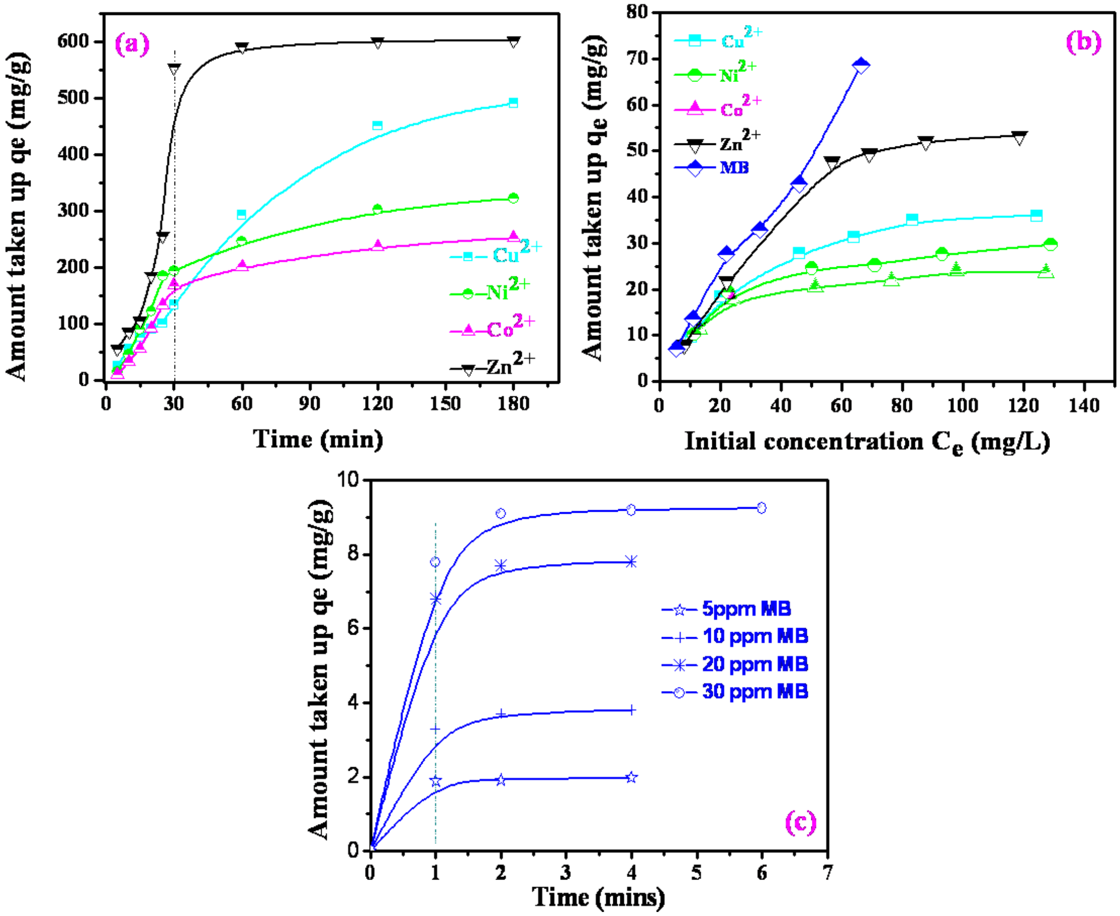

Figure 6.5: Effect of (a) time (b) initial concentration on amount taken up for metal ion sorption and (c) time on amount taken up of methylene blue (MB) sorption on SiO_2 coated Fe_3O_4 nanoparticles.

The effect of initial metal ion concentration on sorption efficiency was studied by equilibrating 10 mL solution of metal ion with varying concentrations maintained at pH ~ 5 to 6 with 0.01 g of sorbent for half an hour and are given in **Figure 6.5(b)**. It was seen that the experimental value reached saturation at a concentration of 125 ppm. The experimentally obtained values of maximum uptake capacity for the different transition metal ions Cu(II), Co(II), Ni(II) and Zn(II) ions were found to be 36, 23,28 and 53 mg/g, respectively.

6.2.2.2. Sorption of cationic dyes

Initial studies showed that the nano-composites did not show any uptake of Rhodamine B (Rh B) whereas the uptake of methylene blue (MB) was significant. Therefore further studies were carried out using methylene blue.

The pH effect was understood from our earlier studies on the uptake of dyes by different sorbents. It is seen that the optimum pH is around 5-6 [351]. This is because the dyes have tendency to get converted into neutral species at pH beyond 6. Once the formation of hydrolyzed or neutral species occurred, the sorption on the surface is expected to decrease. The studies at lower pH indicated that there is a competition between the protons and the cationic species for the sorption sites and this competition reduces the amount taken up. Hence based on all these observations, further experiments were carried out at pH of 6.

The sorption was studied as a function of initial solute concentration and the results of these studies are plotted in **Figure 6.5(b)**. It is seen from the figure that the maximum uptake capacity obtained experimentally for methylene blue is around 68 mg/g and it has not reached saturation in the concentration range of 5-60 mg/L. This showed that the sorbent has got a high uptake capacity for methylene blue also.

The effect of time of equilibration on the amount taken up is important study to understand the kinetics of the sorption. For the sorption of dye, equilibration was carried out with varying concentrations of the dye solution (5-60 mg/L) using 0.007g of sorbent for different periods of time (**Figure 6.5 (c)**), which showed that complete uptake of dyes in this concentration range was achieved within 6 minutes.

6.2.3. Mechanism of sorption

The sorption processes depends extensively on the sites on the surface of the nanomaterials and therefore surface area becomes an important factor in deciding the sorption capacity. However this is always not the only controlling factor. There are various other aspects like surface charge and surface functionalization and complexation capability of metal ions in addition to the porosity of the materials, which can alter the sorption property. Zeta potential measurements give an idea of the surface charge and thus it is seen that the present nanomaterial can take up cationic species. Therefore, metal ions and cationic dyes like Rh B and MB are expected to be taken up. In the study of transition metal ions, it is seen that Zn(II) is the most favoured as compared to others. If the sorption was affected by only electrostatic attraction between the surface negative charges and cations, then Cu(II) should have shown higher uptake capacity as seen from chapter 4 were electronegativity played a major role in sorption process. Thus it is assumed that the complexation of Zn metal ions with silica is much stronger than the other metal ions leading to a faster and higher uptake of Zn ions as compared to the other ions. Similarly if electrostatic attraction was the only governing process, then the highly selective uptake of methylene blue with respect to Rhodamine B cannot be explained.

The main reason associated with the difference in the uptake pattern could be understood from the size of pores obtained from the N_2 adsorption-desorption measurements. It is concluded that the bulkier Rh B (1.44x1.09x0.64 nm) has less access to the active sites of the nano-sorbents (pore size of 1.483 nm), while the size of the MB (1.43 nm × 0.61 nm × 0.4 nm) molecule is within the pore size and can be easily sorbed. The structures of MB and Rh B are depicted in **Scheme 1**. Therefore it is important to understand that though the silanol groups of the silica are involved in the uptake, the access of the molecules to the site is also an important deciding factor. Possible modes of attachment of cations on the nanoparticle surface are given in **Scheme 2**.

Scheme 6.1. Structures of Methylene Blue and Rhodamine B.

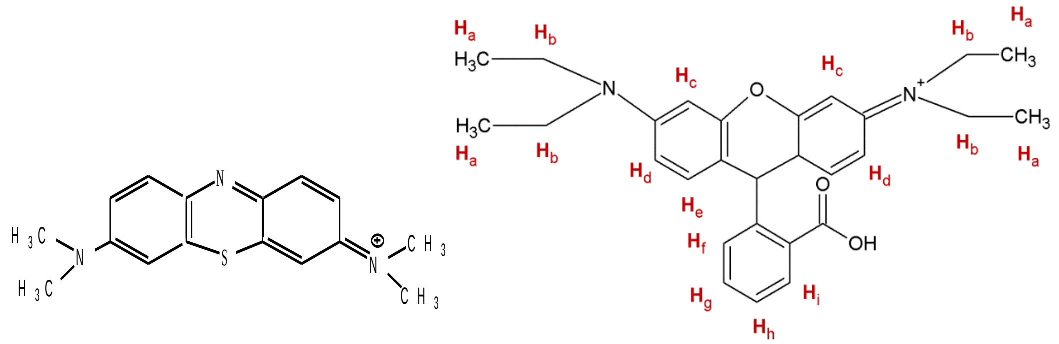

Methylene Blue **Rhodamine -B**

6.2.4. Modeling of sorption data

In order to understand the sorption process, the data obtained were subjected to both equilibrium and kinetic modeling using different equations. Langmuir [227] model is used to find out the sorption efficiency of the synthesized sorbent. According to this model, the monolayer sorption occurs at the identical sites on sorbent surface. Another model that is extensively used is the Freundlich isotherm model [229]. It is the earliest known relationship used to describe the non-ideal and reversible sorption, and can be applied to multilayer adsorption. The value of n if within the range of 1-10, indicates favorable sorption.

The Dubinin–Radushkevich isotherm [232] model was initially used for the adsorption of subcritical vapors onto micro porous solids following a pore-filling mechanism. Usually this model deviates at lower concentration and can explain whether the adsorption is physical or chemical in nature. The data of sorption of transition metal ions and methylene blue were fitted to the different equilibrium models to explain the solid/liquid sorption. The results of these are given in **Figure 6.6 (a-c)**.

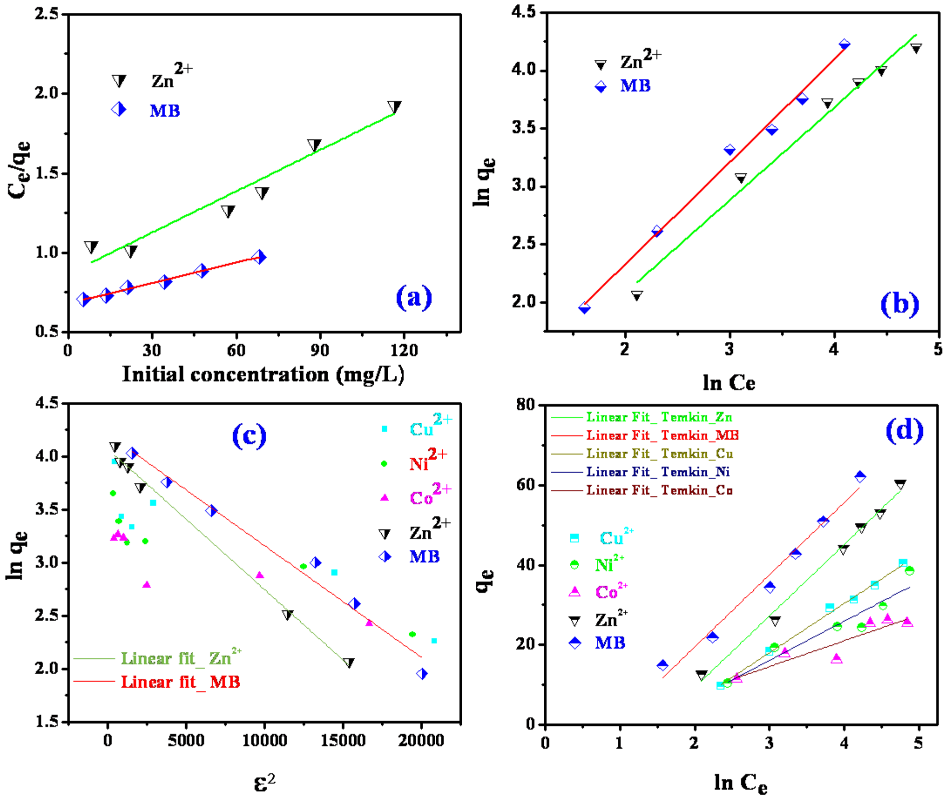

Figure 6.6: Linearized (a) Langmuir, (b) Freundlich, (c) D-R and (d) Temkin isotherms of sorption (Zn(II) and MB) on SiO_2 coated Fe_3O_4 nanoparticles.

From the **Figure 6.6 (a**), it is seen that only the sorption of Zn(II) and MB follow the Langmuir model over the entire concentration range and the maximum monolayer adsorption was found to be 115.48 and 233 mg/g, respectively, whereas the sorption of copper, nickel and cobalt show deviation from the model at higher concentrations. The R_L values are below 1 indicating a favorable sorption process that is reversible in nature. This shows that nanosorbent can be regenerated once the sorption is achieved.

The Freundlich Isotherm which shows that both MB and Zn(II) followed Freundlich model and the sorption intensity (given by the value of slope) was between 0 and 1 indicating the favorable chemisorption as depicted from **Figure 6.6(b)**.The sorption data was fitted to Dubinin–Radushkevich model (**Figure 6.6(c)**) and from the calculations, the process was correlated to be chemisorptions in nature. Thus the results are in concurrence with that of Freundlich model. The results of Temkin modeling (**Figure 6.6(d)**) also conclude that the constant related to heat of sorption (obtained from the slope) correspond to a chemisorption process.

The sorption data were also fitted to different kinetic models to get a complete understanding of the sorption process. Sobkowsk and Czerwi´nski[394] developed an **Equation (6. 1)**, wherein where θ = Γ /Γ∞ denotes the surface coverage, Γ and Γ∞ the surface concentrations at time t and after completion of the reaction, respectively, k the rate constant, and n is the order of the reaction.

$$\frac{d\theta}{dt} = (-\theta)^{n} \tag{6. 1}$$

Thus similar to the above equation when n=1, Lagergren's pseudo-first-order rate equation [233] is obtained and the slope of the straight line plots of log(q_e −q_t) vs t gives the values of the first order rate constant K_{ads}.

Ho and McKay developed a pseudo-second-order rate expression [235] and wherein q_e and q_t are the amount of solute on the surface of the sorbent (mg/g) at equilibrium and at time t respectively. From the plot of t/qt versus time t, the value of K_{2ads} can be calculated.

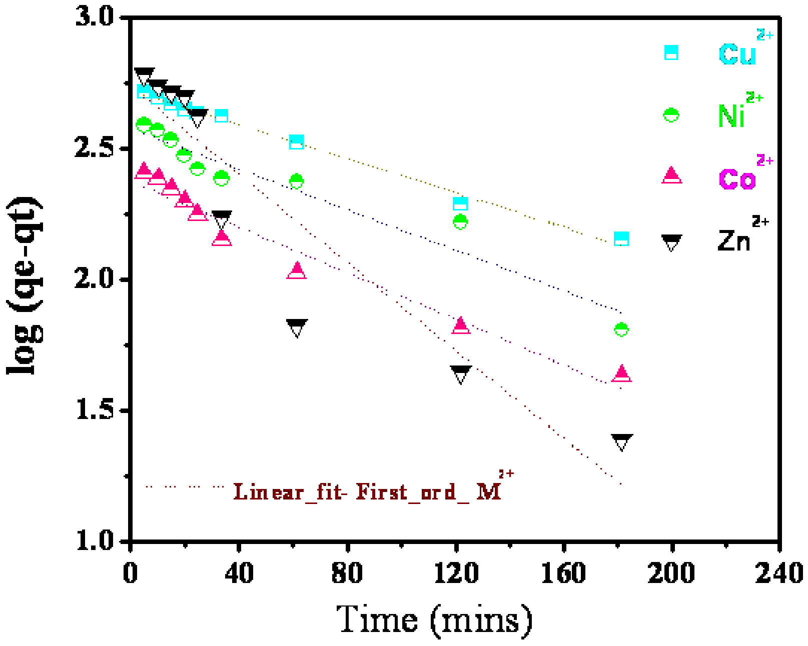

Figure 6.7: Pseudo first order kinetic plot for the sorption of metal ions by SiO_2 coated Fe_3O_4 nanoparticles.

The results of the data fitted to both pseudo first order (**Figure 6.7**) and second order models (**Figure 6.8 (a-b)**). It was seen that for the both the metal ions and dyes, the processes were initially following physisorption followed by chemisorption. For metal ions, the first 10-15 minutes, the process is physisorption and beyond this the sorption follows the chemisorption mode. For the dyes, the kinetics is so fast that it is not possible to get a different time period for both the modes of sorption. From the kinetic models, it was seen that the equilibrium concentration for the metal ions was 142, 64, 52, 42 µg/g for Zn(II), Cu(II), Co(II) and Ni(II) ions of initial concentration of 10 ppm whereas for methylene blue it was around 3.7 mg/g for an initial concentration of 10 ppm of dyes. The values obtained from both the pseudo first and second order models were nearly similar.

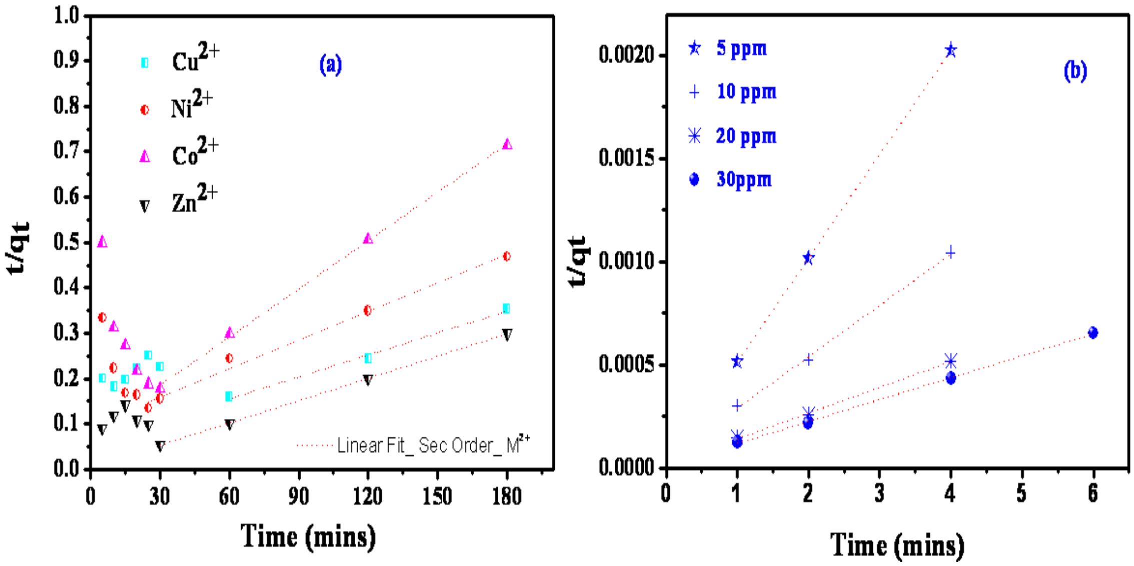

Figure 6.8: Pseudo second order kinetic plot for the adsorption of (a) Metal ions and (b) MB by SiO_2 coated Fe_3O_4 nanoparticles.

The sorption data fitted to the kinetic modeling to explain the solid/liquid adsorption. In order to understand the sorption mechanism the data were fitted to the Weber–Morris [237] and Boyd [239] models. The results of fitting of sorption data to Weber–Morris model is given in **Figure 6.9 (a)** and the values of intercept I gives an idea of the thickness of the boundary layer; i.e. the larger the intercept, the greater the boundary layer effect will be. In the present study, it is seen that the plot of Weber–Morris model for zinc ion sorption can be subjected to linear regression in different regions. It is seen that these plots have three distinct regions. The first linear portion included the sorption period of 0-20 min which represents external mass transfer. The second linear portion included the sorption period of 20-30 min representing intraparticle diffusion. The third linear portion included the time period of 30-180 min, which indicated adsorption–desorption equilibrium.

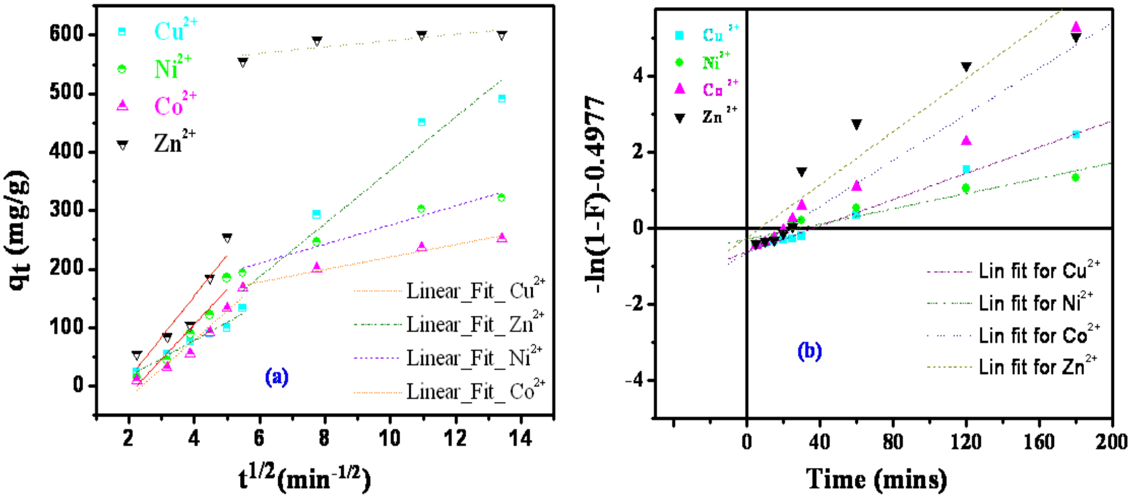

Figure 6.9: Kinetic studies using (a) Webber Morris intra particle diffusion model and (b) Boyd Model for metal ions onto SiO_2 coated Fe_3O_4 nanoparticles.

It is clear that as the plots do not cross the origin, both intraparticle diffusion and external mass transfer occur simultaneously. However, the ratio of the time taken by external mass transfer to intraparticle diffusion was about 1:1. Thus, the overall sorption process was controlled by both external mass transfer and intraparticle diffusion. However for the sorption of methylene blue, the first two portions are not very clearly separated. This indicates that the kinetics is so fast that the external mass transfer does not play a major role in the sorption mechanism.

Adsorption kinetic data analyzed by the linearized form of the Boyd model using Boyd's equation (**Figure 6.9(b)**), the diffusion coefficient was calculated and found to be of the order of 10^{-10} cm^2s^{-1}. From literature it is known that if external mass transfer of sorbate across the liquid film to the sorbent exterior surface is to be the rate-controlling step, the value of Di should be in the range of 10^{-6}–10^{-8} cm^2s^{-1}, and if intraparticle diffusion is the rate limiting step, the Di value should be in the value should be in the range of 10^{-11}–10^{-13} cm^2s^{-1}. But in these studies, the calculated values of Di value for zinc ion sorption was neither in the two ranges but the in the range between them (10^{-8}–10^{-11} cm^2s^{-1}), therefore it is proposed that both film and intraparticle diffusion plays an important role in the zinc ion sorption. However for the dye sorption, the value of Di was in the order of 10^{-12} cm^2 s^{-1} indicating that the intraparticle diffusion played an important role in the sorption. This is in concurrence with the results obtained from Webber Morris modeling.

6.2.5. Regeneration studies

The regeneration studies (shown in **Scheme 2)** were also carried out. Desorption and reusability studies need to be studied for practical applications. It is of great importance that the sorption efficiency is nearly unaffected for a number of cycles. Therefore, the reusability of the present sorbent was evaluated. To investigate the possibility of restoring the adsorption capacity, at first desorption experiments were conducted under batch experimental conditions.

Scheme 6.2: Adsorption –Desorption experiments.

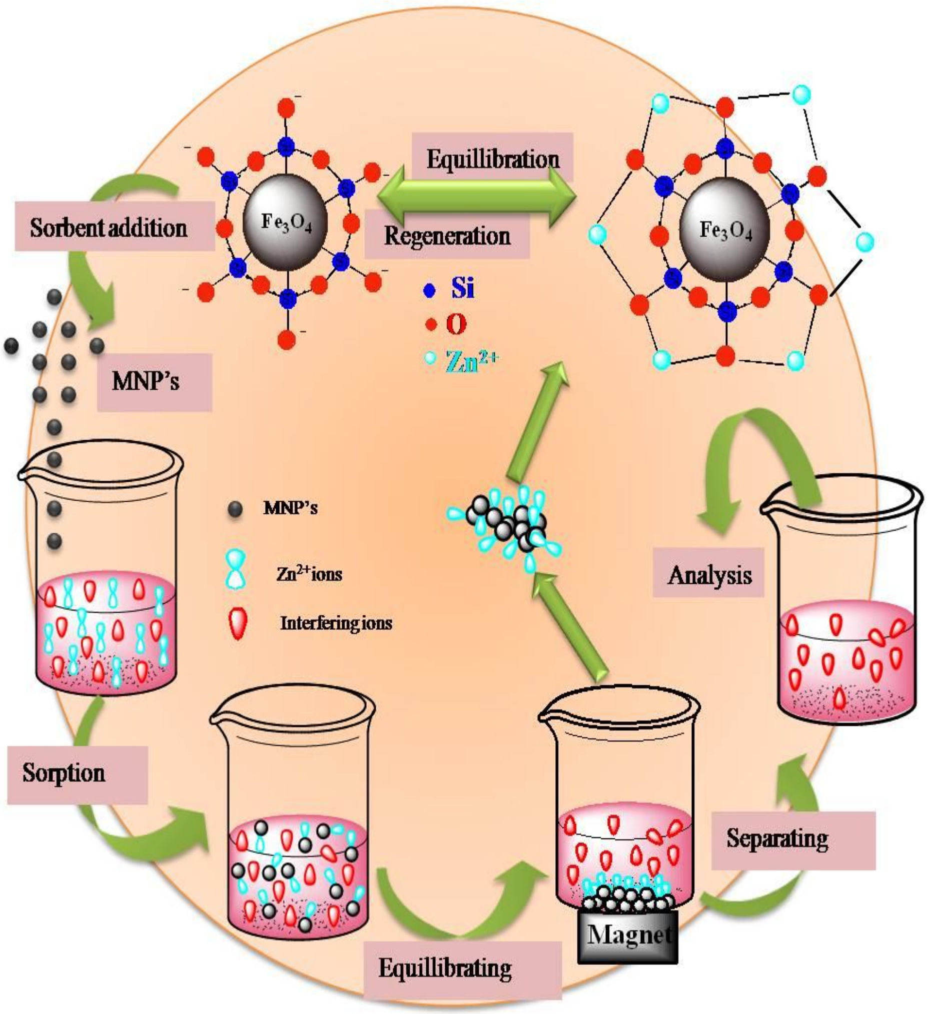

The conditions needed for desorption can be easily understood from the pH variation studies to obtain the maximum pH for sorption. Zeta potential measurements revealed that at lower pH, the surface charge of the nanoparticles becomes less of negative and thus reduced sorption occurs. This suggested that there was a possibility of using this condition for desorption of metal ions and therefore dilute acid (0.1 M HCl) could be used to regenerate the sorbent. It was seen that the sorbent retained about 93% of its initial sorption efficiency even after 5 cycles thus allowing the use of the same sorbent for multiple times.

6.3. Summary

From the foregoing discussion, it can be inferred that porous nanocomposite of Fe_3O_4-SiO_2 could be synthesized by one-pot co-precipitation process. These spherical porous structures comprise of a crystalline magnetic core of size ~ 10nm and an amorphous silica shell as confirmed by detailed characterization techniques. This helps to have a composite with the combination of both the magnetic property of the Fe_3O_4 core and high surface area of silica shell (due to amorphous nature), thus can enhance the application in waste water treatment. This magnetic property of the Fe_3O_4 core, aids in easier and faster removal of the sorbent from its aqueous solution by external magnet as compared to the non-magnetic sorbents. Such nanostructures shall be highly beneficial for the removal of toxic and carcinogenic species from the textiles, pulp mills, leather, printing, food, plastics and dye industrial effluents. The uptake process was found to be thermodynamically as well as kinetically favorable, and the extensive modeling of data showed that maximum adsorption capacity (115 mg/g (Zn(II)ions) and 233 mg/g (MB)) which is in agreement with experimental values and the chemisorption nature of uptake.

Chapter 7

Photocatalytic materials

Effect of Mo Incorporation in the TiO_2 Lattice: A Mechanistic Basis for Photocatalytic Dye Degradation
K. Bhattacharyya, **Jerina Majeed**, K. K. Dey, P. Ayyub, A. K. Tyagi and S. R. Bharadwaj
J. Phys. Chem. C, 2014, 118, 15946-15962.

7.1. Introduction

Anatase, one of the many polymorphs of the TiO_2 family, is regarded as one of the most efficient photocatalysts for the redox reactions in both the gas-solid and liquid-solid interphases. The detoxification of organically polluted wastewater primarily involves liquid-solid interphase reactions. Since anatase TiO_2 possesses an indirect bandgap of ~3.2 eV, it acts as a photocatalyst that primarily absorbs in the UV region. One of the common routes employed to shift its absorbance towards the visible range is to dope the cationic site with different transition metal ions. Doping not only alters the band gap of the material but often also leads to changes in the oxidation state as well as structural parameters. It induces alterations in the redox potential, which plays a primary role in the photocatalytic activity of these doped materials [395-397]. An effective increase in lifetime of the e^-/h^+ may augment the rate kinetics of the photo-chemical reactions. The dopants assist this strategy either by quenching one of the charge carriers of e^-/h^+pair, thus effectively increasing the lifetime of the other or by creating requisite defect sites that effectively facilitates the photochemical activity [398]. On the other hand, dopants can lead to the formation of surface defect sites that trigger certain adsorption/reaction centers effective in catalysis [399-401]. Molybdenum can assume multiple oxidation states and the ionic radius of Mo^{6+} (0.62 Å) makes it favorable to substitute for Ti^{4+} in TiO_2 (0.68 Å). The Mo and W impart stability to the anatase TiO_2 phase [402].

Earlier reports of the Mo-doped TiO_2 system include: a) structure-activity link of anatase- V, Mo, Nb, and W-TiO_2 mixed oxides for toluene photooxidation under sunlight-type excitation [403]; b) probable role of Mo catalyst in quenching Rh-B excited state leading to extended degradation of the dye, through a secondary photochemical process beyond simple de-ethylation[404]; c) Mo^{6+} incorporation in the anatase structure produces a red shift in the absorption edge and lowers the interfacial charge transfer dynamics [405]; d) simultaneous cationic and anionic doping in TiO_2 with Mo and N, respectively [406]; e) Mo-doped anatase prepared by thermal hydrolysis of peroxo-titanium complex showing presence of Mo^{5+}/Mo^{6+} ions doping in the TiO_2 nanostructure, f) substantial enhancement of the photocatalytic activity in the visible region for Mo concentration of about 1.38% [407]; g) characterization and effect, of Mo^{6+} dopants on the phase transformations of TiO_2 lattice and its photocatalytic activity dependence on the dye structure [408-410].

In the present investigation, the growth of TiO_2-MoO_3 nano-heterostructures was explored. TiO_2-MoO_3 nanocomposite photocatalysts have been synthesized by several methods [411]. The presence of a small amount of nano-dispersed MoO_3 along with TiO_2 effectively lowers the band gap and also plays a role in altering the redox potential and promoting the oxidation reactions. However, the simultaneous effect of both these factors has not been studied systematically.

Rhodamine B (Rh-B) is a dye belonging to the triphenylmethane family, containing four N-ethyl groups at either side of the xanthene ring. The long-term presence or accumulation of these dyes in wastewater discharged from these industries is detrimental to the aquatic environment [412, 413]. There has been a comprehensive investigation of the mechanism of TiO_2 photo-catalyzed reactions under UV irradiation. The photocatalytic degradation mechanisms of the triphenylmethane dye pollutants follow the usual N-dealkylation mechanism, generally involving the initial step of abstraction of one or all or several alkyl groups by the hydroxyl radicals. This results in the formation of corresponding aldehyde as a by-product. Once dealkylationis complete, fragmentation of the molecule occurs, resulting in the formation of substituted benzene compounds [414-416]. However, one does not commonly observe routes involving only fragmentation and not de-alkylation. In particular, the nature of the intermediates and the reaction pathways has not yet been clarified. The present study reveals the nature of the initial fragmentation and almost no dealkylationis observed.

In this work, it is shown that the photocatalytic properties of anatase TiO_2 are enhanced by substitutional doping of Mo in the TiO_2 lattice, simultaneously with the presence of a nano-dispersed MoO_3. Attempts were made to delineate structural factors that alter the photochemical behavior of Mo-TiO_2.The photocatalytic activity was correlated with several parameters such as the oxidation state, band gap, surface species,*etc*. The photocatalysis experiments were conducted using a model Rh-B dye and a mechanistic understanding of the photocatalytic degradation of the Rh-B dye with its adsorption properties is reported. The de-alkylation step is completely absent in this case, and photo-degradation occurs through other routes. The different molecular intermediates that are involved in the Rh-B photodegradation are reported and the structural attributions leading to such a mechanism are discussed.

7.2. Result and Discussion

7.2.1. Characterization of photocatalyst

The characteristic powder-XRD patterns of the following typical samples studied in the present investigation: bulk anatase, nano TiO_2 and the Mo-TiO_2 samples (Mo-1, Mo-2, Mo-5, Mo-10 and Mo-100) are shown in **Figure 7.1.** The XRD pattern corresponding to nano-titania is found to match with that of the bulk, tetragonal anatase phase (JCPDS 21-1272). It can be inferred that this process of synthesis forms TiO_2 in the anatase phase. The XRD pattern of the other end member, MoO_3, matches with orthorhombic MoO_3 (JCPDS 05-0508).

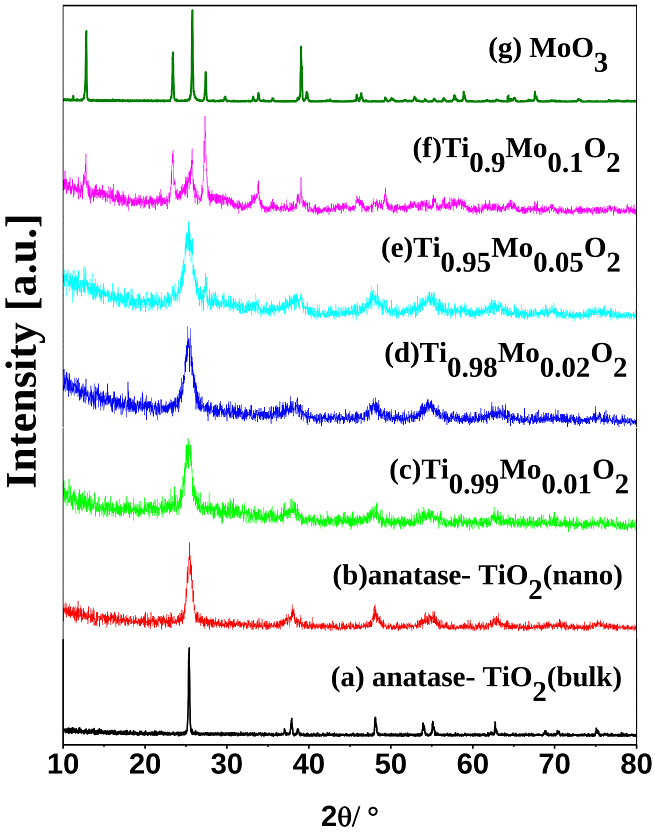

Figure 7.1: The XRD patterns of the Mo-TiO_2 and TiO_2 materials (a) TiO_2 – Anatase-bulk (b) TiO_2- nano (anatase) (c) Mo-1 (d) Mo-2 (e) Mo-5 (f) Mo-10 (g) Mo-100 (MoO_3).

The effect of the doping of Mo in the TiO_2anatase lattice is quite interesting. The XRD patterns of 1 and 2 atom % Mo-doped samples do not show any of the characteristic MoO_3 diffraction lines and match very well with the TiO_2 anatase phase. Therefore within the detection limit of XRD, these samples are primarily Mo-doped anatase. However, with higher amount of Mo-doping (≥ 5 atom %) the MoO_3 phase was observed in the XRD pattern along with anatase. A probability of the XRD not detecting the MO_x phase [for the Mo-presence (≤ 5 atom %)] is that, MoO_x phase might be present in a non-crystalline or poorly crystalline form.

The XRD response for non-detecting the MoO_x phase in the ≤ 5% Mo-TiO_2 samples may also be formed due the quantum confinement of these materials; the nano-form usually is poorly crystalline in nature and the limiting factor may also be the fraction of this phase present which will further broaden the peak. Equivalently if the MoO_x phase is only present on the surface and is not formed in the bulk it will be difficult to detect it completely by XRD. With higher fraction of MoO_xphase, it becomes easily detectable and the more crystalline in nature and also the component of this phase in the bulk increases. However in order to understand it better a spectroscopic tool is needed that can visualize the situation better and is present in the subsequent section. Consequently, it can be visualized as the overall symmetry pattern of this doped heterostructure will not be reduced from the tetragonal symmetry. However, the crystal lattice will experience a certain amount of strain. It is predicted qualitatively, and this is not quantified here. The XRD results further show that with a higher percentage of Mo in the TiO_2 matrix MoO_3 exists as a nano-heterostructure. However, any shift in the (101) line of anataseTiO_2 is not observed. This is expected as the ionic radius of dopant (Mo^{6+}) is almost comparable to that of the host Ti^{4+}. This observation, therefore, could be explained in two ways. Either there is a small amount of doping of Mo^{6+} in the TiO_2 lattice as the ionic radii of Mo matches very closely with that of Ti^{4+}, along with the presence of a surface MoO_3 phase which is quite poorly-crystalline in nature or there is no doping and only MoO_3 nano-heterostructure is present with the presence of a surface MoOx phase. Compared to the parent TiO_2 phase, the XRD peaks of all synthesized samples, nano-titania and Mo-titania, exhibit significant line broadening indicating the presence of smaller particle size. The coherently diffracting domain sizes, calculated using the Scherrer equation from the broadening of the FWHM of the (101) peak, as represented in **Table 7.1**. The crystallite size of the different Mo-TiO_2 nano-composites are as follows: (Mo-1) -30 nm; (Mo-2) -34 nm; (Mo-5) – 32 nm; (Mo-10) – 48 nm.

The Raman spectra of the bulk anatase, the Mo-TiO_2 samples (Mo-1, Mo-2, Mo-5 and Mo-10), and MoO_3 are shown in **Figure 7.2**.

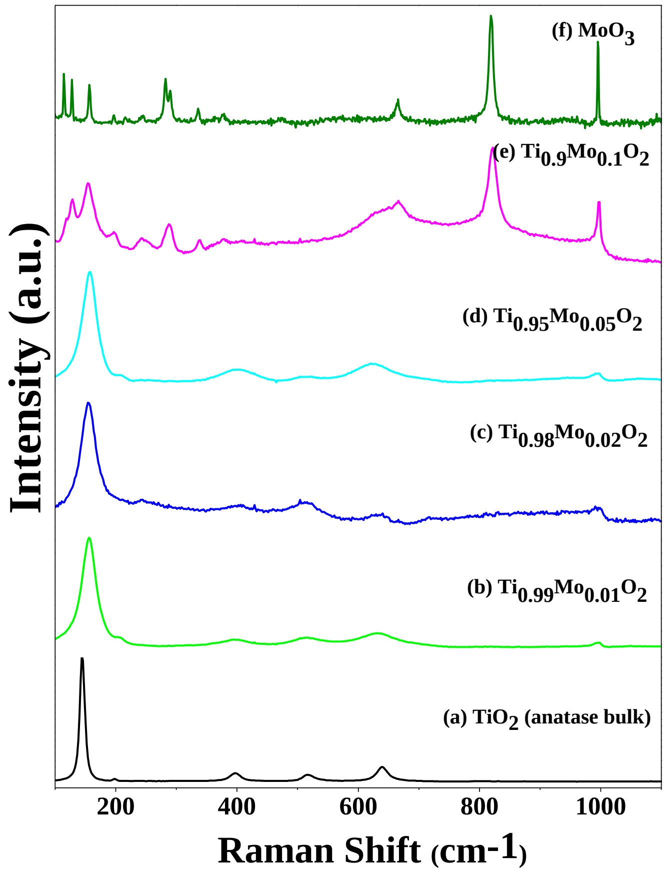

Figure 7.2: The Raman spectra of the Mo-TiO_2 and TiO_2 materials (a) TiO_2– Anatase-bulk (b) TiO_2- nano (anatase) (c) Mo-1 (d) Mo-2 (e) Mo-5 (f) Mo-10 (g) Mo-100.

Orthorhombic MoO_3 belongs to the D_{2h}^{16}(Pbnm) space group [417, 418]. The Raman spectrum of MoO_3 is shown in **Figure 7.2(f)**. The mode frequencies (in cm^{-1}) along with their irreducible representations are as follows: 995 (A_g, B_{1g}), 819 (A_g, B_{1g}), 665 (B_{2g}, B_{3g}), 380 (B_{1g}), 336 (B_{1g}, A_g), 289 (B_{1g}), 281 (B_{2g}), 243 (B_{3g}), 215 (A_g) 198 (B_{2g}), 156 (A_g, B_{1g}), 127 (B_{2g}), 114 (B_{1g}), 96 (A_g) and 81(A_g). The bands at 474 (A_g, B_{1g}), 365 (A_g) and 338 (B_{1g}) are not observed in this sample.

TiO_2, have a tetragonal unit cell and belongs to the space group D_{4h}^{19}(I41/amd) [419, 420]. The primitive unit cell contains two TiO_2 chemical units. The Raman band frequencies (in cm^{-1}) of TiO_2 anatase bulk as observed in **Figure 7.2 (a)** and their respective irreducible representations are as follows: 144 cm^{-1} (E_g), 198 cm^{-1} (E_g), 397 cm^{-1} (B_{1g}), 515 cm^{-1} (A_{1g}), 520 cm^{-1} (B_{1g}), 640 cm^{-1} (E_g). The Raman spectrum of Mo-doped TiO_2/heterostructure samples (**Figure 7.2 (b-e)**) shows peaks from both anatase TiO_2 and MoO_3 phases with a substantial shift in the intermediate regions. The Mo-1 sample (**Figure 7.2(b)**) shows Raman modes at 156, 205, 404, 512, 634 and 995 cm^{-1}, as compared to the bulk anatase TiO_2 peaks found at 144, 198 and 397 cm^{-1}. The full-width at half-maximum (FWHM) increases when the crystallite size decreases, or the structure becomes more disordered when size decreases [421, 422]. It is generally seen that the Raman bands show peak shift towards higher frequencies if the lattice is under some stress [421, 422]. There is a definite change in the FWHM values of bulk anatase compared to that of the Mo-doped samples. It changes from 8.79 to 26.18 cm^{-1} [for the 144 cm^{-1} peak]. However, the peaks at 515 and 634 cm^{-1} are almost at the same position as that of TiO_2anatase bulk, though there is a definite increment in their FWHM values. Therefore the shift of the peak at 144 cm^{-1} to 156 cm^{-1} points towards of the lattice strain. It substantiates our XRD information also.

An additional band at 995 cm^{-1} is also obtained, which is representative of the MoO_3 phase. The Raman spectra in **Figure 7.2 (c, d)**, representing the Mo-2 and Mo-5 samples exhibits a similar trend, with the 995cm^{-1} band increasing in intensity. The other Raman bands at 156, 208, 515 and 624 cm^{-1} indicate the presence of TiO_2anatase phase. The presence of a band at 995 cm^{-1}usually shows the presence of small surface aggregates of MoO_3. This is demonstrated through the Mo=O (995 cm^{-1}) bond and Mo–O–Mo (broad contribution 700–940 cm^{-1}) as shown in the earlier literature [420]. This signifies that for each Mo-TiO_2 samples, starting from Mo-1 upto Mo-5, there is a distinct MoO_3 surface phase [423]. This part is quite evident as in these samples the MoO_3 is not in the bulk phase as in the Mo-10. The FWHM for the Mo-2 and Mo-5samples [peak at 156 cm^{-1}], are 25.5 and 25.6 cm^{-1}, respectively. The Mo-10 sample (**Figure 7.2 (e)**) has almost all the bands of the MoO_3 bulk phase along with those for anatase. Thus, the Raman studies substantiate that the Mo-TiO_2 samples have a composite nature. This is true even for Mo-1 and Mo-2, as also suggested by the XRD data. Further, the MoO_3 phase is nano dispersed in the TiO_2 matrix. This reveals the fact that along with Mo- TiO_2 there is an amount of the MoO_3 as nano-composite heterostructures. However, it is quite clear from the Raman data that in the Mo-10 along with the surface phase of MoO_3 there is a definite growth of the bulk MoO_3 also. The surface phase of MoO_3 is prevalent in the Mo-1 to Mo-5.

The diffuse reflectance spectra (DRS) of the bulk anatase (TiO_2), nano-anatase (TiO_2), the Mo-TiO_2 samples (Mo-1, Mo-2, Mo-5, Mo-10) and $MoO_3$are shown in **Figure 7.3(A)**. Curves ‘a’ and ‘b’ represent, respectively, the spectra of bulk anatasetitania and nano-titania prepared in the present investigation. There is a distinct blue shift of ~13 nm in the synthesized nano-titania as compared to the bulk titania, which can be attributed to quantum confinement effects [424-426]. The absorption edge for MoO_3 is generally seen at 400 nm. The intrinsic strong absorption below 400 nm in MoO_3 is due to interband (VB to CB) and excitonic transitions [427]. A very broad asymmetric absorption band also appears with λ_{max} between 780 and 900 nm in MoO_3 as well as in the other mixed-phase samples. This asymmetric band probably arises from a superposition of many discrete bands [427-429] which is consistent with the presence of localized centers.

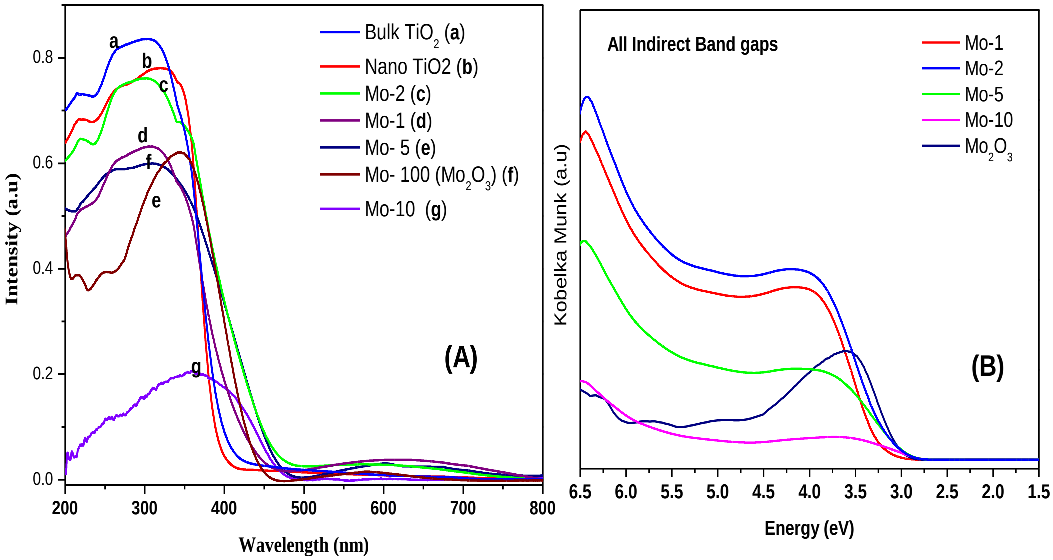

Figure 7.3: (A) The UV-Visible spectra of the Mo-TiO_2 and TiO_2 materials (a) TiO_2 –Anatase-bulk, (b) TiO_2- nano (anatase), (c) Mo-2, (d) Mo-1, (e) Mo-5, (f) Mo-100 and (g) Mo-10. (B) The Kubelka-Munk plots of Mo-TiO_2 materials (a) Mo-1, (b) Mo-2, (c) Mo-5, (d) Mo-1.

The Kubelka-Munk plots of these materials are depicted in **Figure 7.3(B)**. Consistent with the earlier results, MoO_3, TiO_2 (anatase) and Mo-TiO_2 systems, possess an indirect band gap [430]. In the present set of samples, the calculated band gap from Kubelka-Munk plots, range from 3.24 – 2.65 eV. Bulk anatase TiO_2 has a band gap of 3.24 eV, and nano TiO_2 shows a value of 3.30 eV. The Mo-100 has a band gap 2.78eV. In case of Mo-TiO_2 system there is a definite red shift in the band edges and the band gap lowers as a function of the Mo- content: E_g= 2.87 eV for Mo-1, 2.76 eV for Mo-2 and decreases consistently in Mo-5 (2.71 eV) and Mo-10 (2.65eV), as given in **Table 7.1**.

However in this present chapter we do not have a quantitative picture of the percentage of doped Mo in TiO_2 and the nanoheterophase of MoO_3 in/on TiO_2/Mo-doped TiO_2 bulk and surface. Therefore, a qualitative estimate of this environment is presented, and a quantitative correlation of the band gap properties due to nanoheterostructure and/or doping is still an open question. Even a low-level Mo-dopant would lead to better redox properties of the Mo-TiO_2photo-catalyst. In the model shown below in **Scheme 7.1**, the effects of the mid-band gap states areneglected, and that of nanoheterostructure is only considered.

The representation in the **Scheme 7.1**basically represents the sum total of the band gap representation of the fully developed orthorhombic MoO_3 and anatase TiO_2 heterophase both present in the bulk form [431]. However, there will be a strong polydispersity in both the surface MO_x particle size and that of the MO_x particle size. Along with that, there will an added response from the Mo-doped TiO_2, a metal anatase interface. Therefore,the presence of several electronic junctions for the same sample in the Mo-1 to Mo-5 forms is anticipated. However, the Mo-10 will be more of like the representation in the **Scheme 7.1**. We can in some fashion treat this system as a ternary system of MoO_x-TiO_2 (anatase) heterojunction with the Mo-doped in the system.

Scheme 7.1: Band gap representation of MoO_3 and TiO_2 nano-composites.

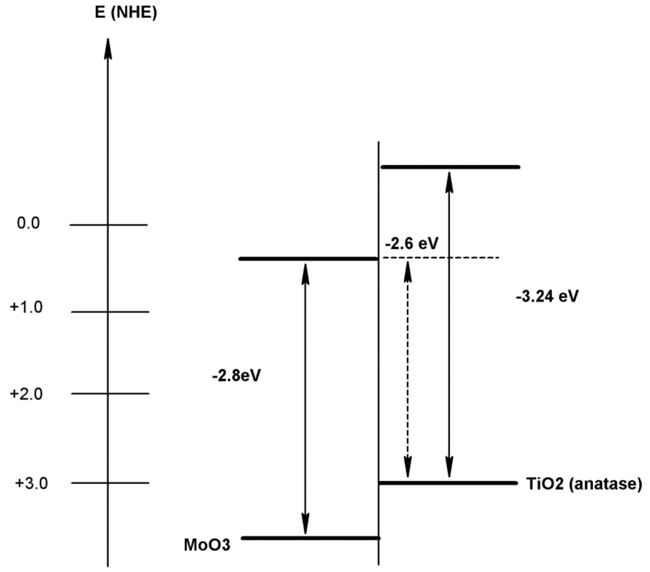

Table 7.1: (a) Zeta potential values at ~neutral pH (6-7); (b) Zeta potential values with Rh-B (c) Crystallite size using Scherer equation (d) Bandgap values using KobelkaMunk plot (e) $t_{1/2}$ values for the visible irradiation reaction with the different photo-catalyst.

Sample	**Zetapotential value** (~pH 6-7)	**Zetapotential value**(mV) (after adding Rh-B)	**Crystallite size** (nm)	**Calculated bandgap Values** (eV)	**t ½ values for photo-degradation of Rh-B visible source** (min)
Mo-0	-22.1	-18.9	25	3.30	66
Mo-1	-25.2	-31.03	30	2.87	26
Mo-2	-30.6	-33.6	34	2.76	13
Mo-5	-34.0	-38.4	32	2.71	9
Mo-10	-38.0	-30.6	48	2.65	90

The core level Ti 2p spectra of MoO_3-TiO_2 nano-composites along with synthesized nanotitania are shown in **Figure 7.4**. For the nanotitania, Ti $2p_{3/2}$ and Ti $2p_{1/2}$ peaks are observed at 458.5 and 464.06 eV, respectively (**Figure 7.4(a)**) [432]. In the MoO_3-TiO_2 nanocomposite samples, a progressive shift is observed toward lower binding energies as compared to that of nanotitania. In the case of Mo-1, the Ti $2p_{3/2}$ peak appears at 458.5 eV, which is the same as in TiO_2. However in case of Mo-2 sample, Ti 2p peak is observed at a lower binding energy (458.1 eV). The other two samples - Mo-5 and Mo-10 –also show the Ti 2p peaks at same position of 458.1 eV. As compared to Mo-1 sample Ti $2p_{3/2}$ peaks for other samples (Mo-2, 5 and10) are broader, probably reflecting the multiple oxidation states in the Ti.

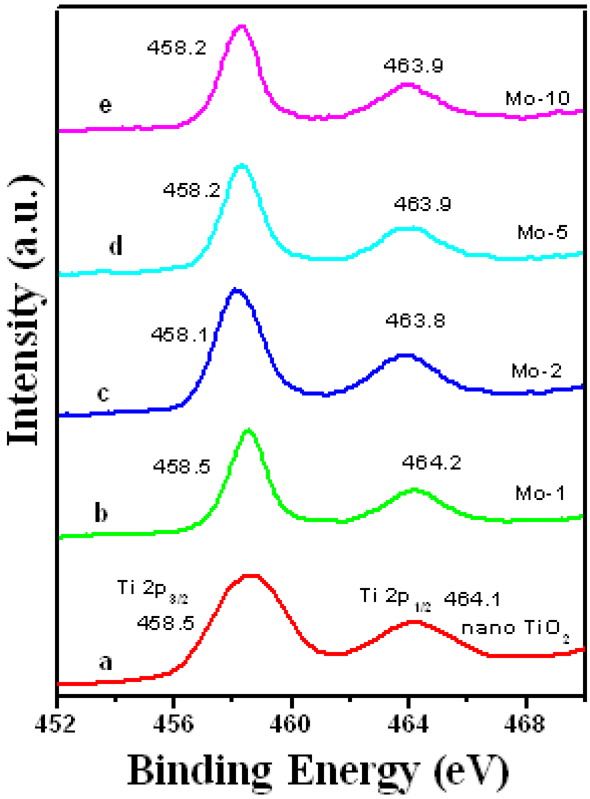

Figure 7.4: The Ti 2p XPS spectra of Mo-TiO_2 and nano-TiO_2 samples viz. a) nano-TiO_2; b) Mo -1; c) Mo-2; d) Mo-5 and e) Mo-10.

The substitutional doping of a higher valent Mo^{6+} in the TiO_2 anatase lattice should result either in oxygen excess, or in Ti^{4+} vacancies, or disproportionation of the oxidation states of Ti in order to maintain the total charge neutrality in the lattice. However, the formation of the lower valent Ti^{3+} or Ti^{2+} is not unequivocally observed in this system apart from the broadening of the Ti peak. Therefore, consistent with the earlier literature, the lowering of the binding energy suggests the formation of Ti^{4+} vacancies [433-435].

The Mo 2d XPS spectrum for different samples are shown in **Figure 7.5(A)**. The Mo-1 sample shows the Mo $2d_{3/2}$ at 233eV and the $2d_{5/2}$ at 236.28eV, respectively. The Mo-2 sample shows the Mo $2d_{3/2}$ at 231.9 eV, with a negative shift of 1.1 eV. The Mo $2d_{5/2}$ peak comes at 235.03eV. The Mo-5 sample shows the Mo $2d_{3/2}$ and Mo $2d_{5/2}$ peaks at 232.16 and 235.29 eV, respectively, which shows a negative shift of 0.84 eV. Mo-10 sample shows the respective XPS peaks for Mo $2d_{3/2}$ and Mo $2d_{5/2}$ at the same position of that of Mo-5 i.e. at 232.16 and 235.29 eV. Thus, these samples also show a negative shift of 0.84 eV. Upon de-convolution (**Figure 7.5(B)**) of the Mo $2d_{3/2}$ peak, two peaks at 230.9 eV and that at 232.2 eV are found. Consistent with the earlier literature, the specific peak for Mo^{5+} is at 231 eV and that due to Mo^{6+} is at 232.6 eV[359]. Further analysis of the Mo peaks for the MoO_3, reveals the presence of the Mo^{5+} and Mo^{6+} states inherently in the MoO_3 itself is found (**Figure 7.5(A)**) [423]. The presence Mo^{5+} in the Mo-TiO_2sample, therefore, may be due to two reasons. One being the presence of Mo^{5+} on the surface MoO_3 states that are inherently formed. The other possibility is that of the Mo^{6+} being doped reduces itself partly to Mo^{5+} in order to maintain the charge neutrality in the TiO_2 lattice. In this system, it may be presumed that both these processes are simultaneously taking place. There is some amount of Mo^{5+} inherently in the MoO_3 states along with that it also indicates that Mo is doped partially in TiO_2. The later statement can be better understood in the light of the O 1s and Ti^{4+} XPS peaks. Therefore, the above results strongly suggest that an increase in the effective Mo percentage in the system definitely leads to the existence of the Mo^{5+} and Mo^{6+} states. The shift of the Mo peak to the lower binding energy is also a result of the presence of Mo^{5+} along with Mo^{6+}.

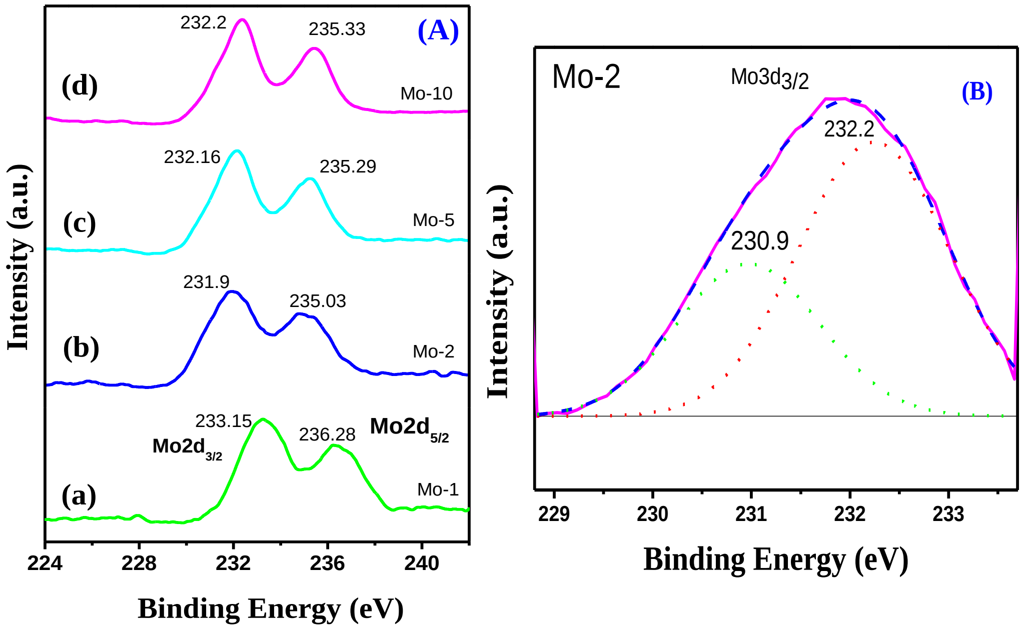

Figure 7.5: (A)The Mo 3d XPS spectra of the photocatalytic samples of (a) Mo-1, (b) Mo-2, (c) Mo-5, (d) Mo-10, (e) MoO_3. (B) Deconvoluted spectrum of Mo $3d_{3/2}$ for Mo-2 sample.

Another interesting observation comes from the O1s XPS spectra of these materials. The O1s peak for nano-TiO_2(**Figure 7.6**) is found at 532.2 eV. The corresponding O1s peaks for MoO_3 sample is found at 530.8 eV.O1s of Mo-1 and Mo-2 samples are found respectively at 531eV showing a negative shift in the binding energy by ~1.2 eV. The Mo-5 and Mo-10 show O1s XPS peak at 529.6 eV. They have further negative shift in the binding energy by ~2.6 eV as compared to the O1s of TiO_2.

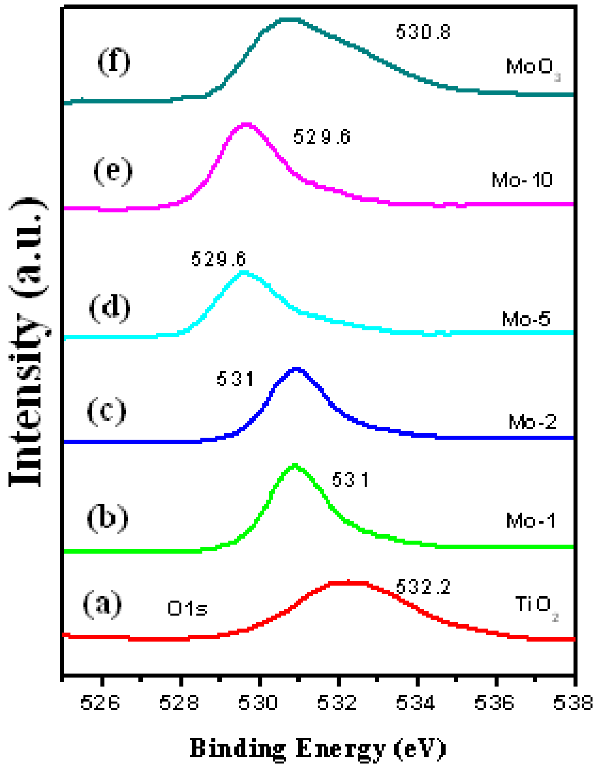

Figure 7.6: O 1s XPS spectra for all the photocatalytic samples (a)TiO_2; (b) Mo-1, (c) Mo-2, (d) Mo-5, and (e) Mo-10, (f) MoO_3.

Deconvolution of the O 1s peak is represented in the **Figure 7.7**. The Mo-2 sample yield speaks at 532, 531 and 529 eV. The intensity of the deconvoluted peak at 529 eV is very low and hence can be neglected. The deconvolution of the O1s peaks of Mo-5 and Mo-10 shows two peaks at 531 and 530 eV. The O of the TiO_2 is not present in any other chemical environment except that Ti-O and –OH. Therefore presumably O1s XPS spectra of nano-TiO_2, shows the presence of O corresponding to Ti-O and O for surface –OH. The O1s of TiO_2 is present at 532.2 eV and that of O for –OH at 535 e V as depicted by the **Figure 7.7**. The O1s of MoO_3sample, three deconvoluted peaks are obtained and the peak representing the 533.5 eV represents the O of –OH.

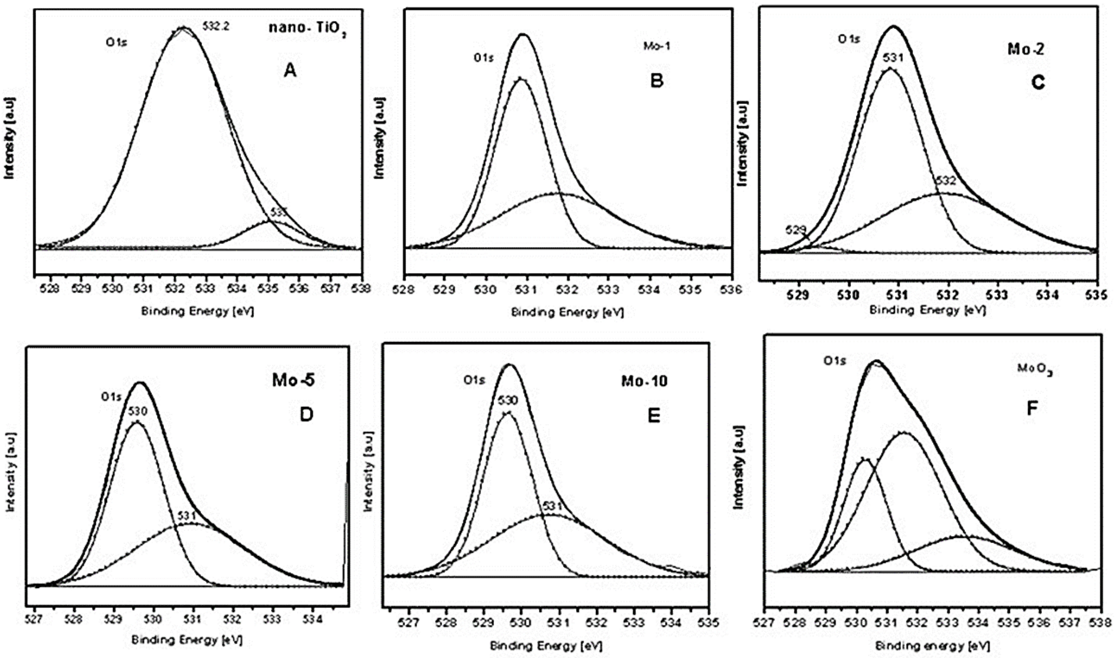

Figure 7.7:Deconvoluted spectra of O 1s (A) nano TiO_2, (B) Mo-1, (C) Mo-2, (D) Mo-5, (E) Mo-10, and (F) MoO_3.

The other two different O's at 530 and 531 eV respectively must be representing the O‘s attached to Mo with various oxidation states (Mo^{6+} and Mo^{5+}). The sample of Mo-2/Mo-1 gave the representative O for the TiO_2 at 531 eVthat shows lower Binding Energy as compared to that of O-(Ti-O) at by 1eV. Therefore, the O for the –OH is also expected to be at lower binding energy than 535 eV. The other peak found on deconvolution of O spectra peaks is perhaps for the –OH consistent with the previous literature [423]. So upon deconvolution of the O peaks we found the O present there for Ti-O and that of –O-H.

However, this does not hint in any way for the Mo-doping in the TiO_2 lattice. Nevertheless, it is found that there is a systematic lowering of the binding enegy of the

O 1s representing the Ti-O. Mostly this is happening due to the presence of non-stoichiometry at the O site, probably due to the presence of excess oxygen anions to balance the charge of Mo^{6+} doped in the TiO_2 lattice [436-441]. Raman studies indicate the presence of MoO_3 in the Mo–doped TiO_2 lattice. The two O peaks (found on deconvolution of the O1s spectra) therefore may represent the oxygen differentially attached with Mo and that of Ti. The O attached to the Mo could result from the MoO_3 or Mo-doped in TiO_2 and the O attached to the Ti is that for the anatase TiO_2.

Therefore from XPS study, it can be probably inferred is that there is a partial doping in the Mo-TiO_2 system along with the predominant presence of the nano-heterostructure of MoO_3 and TiO_2. If only the nano-heterostructures of MoO_3 and TiO_2 existed there would not be any shift present progressively in the XPS patterns of Ti and O respectively, as observed. Then the estimated changes in the XPS spectra of Mo only due to the differential presence of Mo^{6+}/Mo^{5+} inherently even in MoO_3 structure.However, any negative shift in O 1s or in Ti 3p spectra is least expected in that scenario. The systematic difference observed in the electronic environment as reflected in their XPS spectral features definitely proves the fact that there is an electronic interaction of the Mo^{6+}/Mo^{5+} with the TiO_2 lattice and that could only be understood if there is some partial substitutional doping of Mo in the TiO_2 anatase lattice. The XPS studies show that there is a negative shift in the binding energy of the XPS peaks for Ti, Mo and O due to the presence of Mo in the TiO_2 lattice. This leads to think that with a higher oxidation state of Mo^{6+} being incorporated in the lattice, in order to maintain the charge neutrality of the system, there is formation of non-stoichiometry in the Ti and the O sites and disproportionation in Mo site. The Mo has multiple oxidation states of 5+ and 6+, and the O signal can also be deconvoluted into two peaks. This leads to the conclusion that TiO_2 lattice has certain Ti sites substituted by Mo while particular Ti sites are vacant. However, Mo itself disproportionates to Mo^{5+} and Mo^{6+} with some amount of O excess. In addition to this there is also a definite quantity of nano dispersed MoO_3 as a minority phase within the doped TiO_2anatase lattice. From these observations, a qualitative insight of Mo-doping in the TiO_2lattice could be provided. However, an accurate quantitative estimate of the doping level remains to be investigated.

The transmission electron microscopy (TEM) of Mo-1 and Mo-5 samples along with the respective selected area electron diffraction (SAED) and EDS patterns are shown in **Figure 7.8(A) and (B)**. The micrographs suggest that the samples consist of nanoparticles in the range of 7-10 nm, which are mostly spheroidal in shape. A close examination of the SAED patterns confirms the co-existence of both TiO_2 and the MoO_3 in the Mo-5 sample. The lattice fringes of the system reveal d-values representing both the TiO_2 lattice (and Mo-doped TiO_2 lattice) and the MoO_3 lattice. Corroborating our Raman data, the TEM data also provides an evidence for the presence for nano-composites of Mo-doped TiO_2 and MoO_3. In the Mo-1 samples both the SAED pattern and the lattice fringes suggest mostly the presence of anatase TiO_2 rather than the biphasic Mo-TiO_2 and MoO_3. This is evident as the SAED pattern shows mostly the d- values representing the anatase TiO_2. However the EDS pattern shows the presence of the Mo. Therefore it strongly suggests the partial substitutional incorporation of Mo^{6+}/Mo^{5+}-ion in the anatase TiO_2 lattice via doping. This observation also corroborates the XRD patterns. However from the Mo-2 sample onwards, lattice fringes representing two different d-values are found, showing the presence of the nano composite phases.

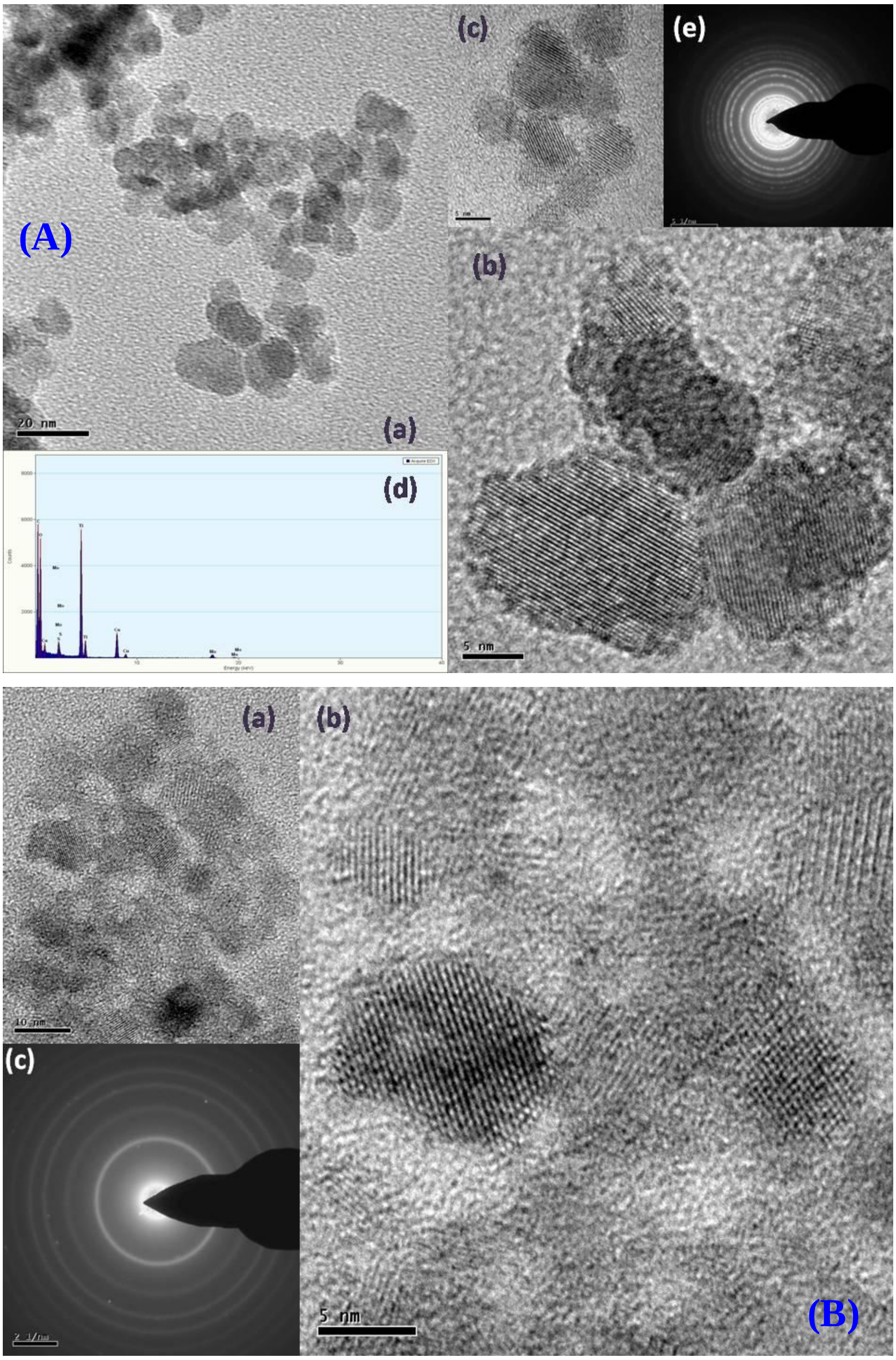

Figure 7.8: (A) TEM image for the Mo-1 on the scale of (a) 20 nm, (b) 5 nm, (c) 5 nm, (e) SAED pattern for the Mo-1 sample, (d) EDS profile for Mo-1 sample.(B) TEM pattern for the Mo-5 on the scale of (a) 20 nm, (b) 5 nm, and (c) SAED pattern of Mo-5 sample.

The presence of a small amount of the MoO_3 phase along with anatase TiO_2 is quite obvious from the SAED patterns of these samples. The EDS results confirm that in addition to the Mo-doped in the anatase TiO_2 lattice, there must also exist some MoO_3 phase for the stoichiometry to be consistent. Therefore in corroboration with the Raman results, the TEM also shows the definite presence of the MoO_3 phase along with the Mo-doped TiO_2anatase sample.

7.2.2. Photocatalytic activity

The photocatalytic activity of these materials was studied under ambient conditions using a photo-irradiative source as described earlier in the experimental section. The absorbance was recorded in the blank experiment at different time intervals for pure Rh- B excluding any photo-catalyst. This shows peak maximum at 554 nm along with two smaller peaks at 354 nm and 260 nm. However, no significant decrease was observed signifying, negligible self-degradation of the dye (**Figure 7.9 (A)**). The adsorption profile of samples was tested by equilibrating the samples with the dye solution in dark for 30 min followed by recording the UV-Visible spectra. There was no decrease in the intensity of the UV-Visible spectra, after adsorption, in any of the samples, except for Mo-2 sample. In the case of Mo-2 sample the intensity of the 554 nm peak decreased almost 50 % within the first 30 min indicating the strong adsorption of the dye on the surface of the catalyst. The photo-irradiation studies for each catalyst were carried out using UV source as mentioned in experimental section. Differential decrease in intensity of adsorption peak maxima of Rh-B (554nm) along with time was monitored. However adsorption of the Rh-B dye over Mo-2 surface shows that the first monolayer of these photo-catalysts is not completely covered/saturated by the –OH and H_2O only. Certain amount of dye is also adsorbed directly on the first monolayer of the photocatalytic surface. Therefore the mechanism of the dye degradation will not be guided by only the free radicals produced in the process of the photo-irradiation. The morphological and the electronic transformations owing to the structural changes created by doping or the formation of nano hetero-structures will have a direct impact of the photocatalytic efficiency of these materials. This data can be further strengthened by Zeta potential studies (**Table 7.1**). An attempt is made to understand further the ways the adsorption may be affected on the surface of these photo-catalysts.

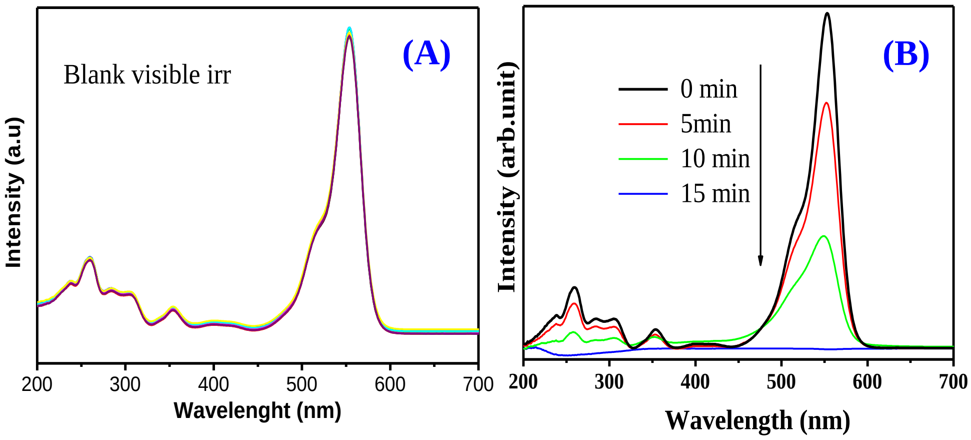

Figure 7.9: Temporal profile for the UV-Vis spectra of Rh-B Dye using (A) Blank –without any photocatalyst and (B) TiO_2 (nano) photo-catalyst irradiated under visible irradiation.

In the case of pure TiO_2 which is UV active, the complete degradation of dye occurred within 30 min as observed from **Figure 7.9 (B)**. The intensity of all the peaks (554, 354 and 260 nm) decreases gradually during the photo-irradiation and completely disappears after 30 min. New peaks were not observed during the course of the photo-irradiation and all the initial peaks diminished in intensity gradually with time. However the shift in peak intensity was also not observed to any extent, indicating the complete degradation of the dye molecule.

In the case of Mo-1 sample, complete photo-degradation of the Rh-B was demonstrated in 120 min photo-irradiated with a UV (**Figure 7.10**). Any shift in the major peaks was not observed in this process. In the case of Mo-2 sample the complete degradation of the dye is shown in 150 min. However, for the Mo-2 sample a prior adsorption effect of the dye is discerned. Within 30 min of equilibration of the dye and the catalyst, almost 50% adsorption of the dye on the catalyst surface was observed. Therefore this extrapolates to an electronic interaction between the dye and the catalytic surface. Similarly, Mo-5 sample also degraded the Rh-B dye completely with a slower kinetics of 180 min to give a clear solution. However, in the case of Mo-10 sample the degradation followed further slower kinetics and did not even degrade up to 80 % in 240 min. Therefore the trend with the photo-degradation of the Rh-B utilizing a UV-source is followed by the given descending trend **(Figure 7.9**): TiO_2> Mo-1 > Mo-2 > Mo-5 > Mo-10. The above descending trend is in accordance with the presence of the lowering percentage TiO_2 in the Mo-TiO_2nano hetero-structures. The anatase having a band gap of 3.2 eV primarily absorbs in the UV region. The nanoanatase TiO_2 structure owing to the quantum confinement effect [424-426] will further absorb in the UV regime only. The MoO_3 on the other hand has a bandgap of 2.78 eV which primarily absorbs in the visible region. The introduction of the Mo in the Mo-TiO_2 system, in effect provides a continuous lowering of the band gap as a function of Mo-loading in the Mo-TiO_2 -system [as was observed in the DRS studies]. Therefore, effectively lower absorption of the UV–source is expected for this series of catalysts with increasing concentration of the Mo. The same effect with the photo-catalysts was observed and therefore it can be easily inferred that under the UV irradiative source it's the TiO_2 band gap absorption that plays a major role.

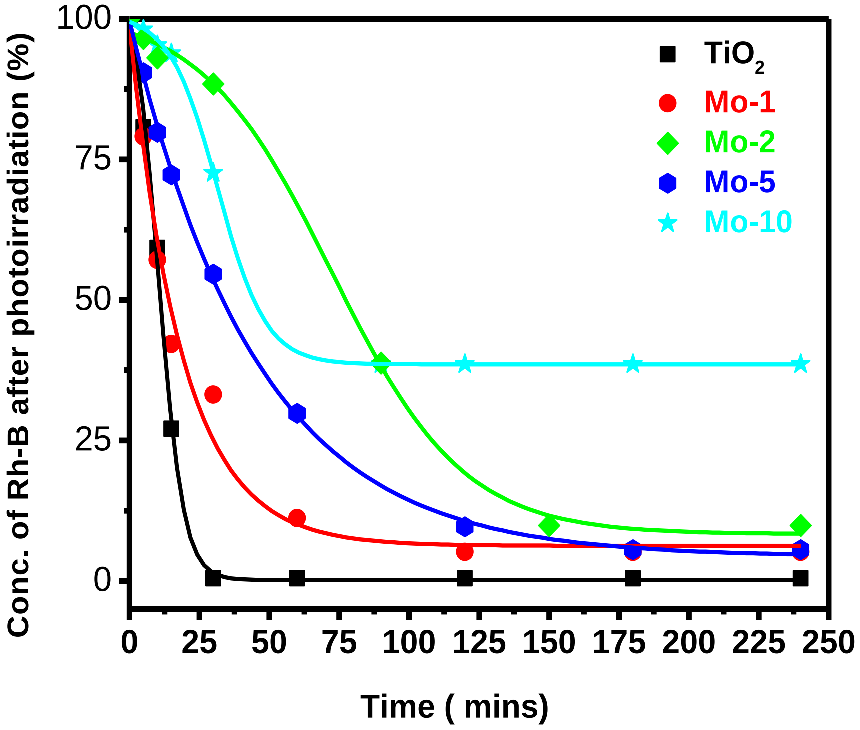

Figure 7.10: Plot of the time dependent photo-degradation of Rh-B using all the photo-catalysts under UV- irradiation. The Y-axis represents the percentage of Rh-B that is left after the photo-degradation of the dye by the individual photo-catalyst.

The photo-irradiation of these samples under visible irradiative source however deciphers a different account altogether. The UV–Vis spectra of Rh- B solution differentially irradiated with respect to time with the nano-TiO_2 particles are shown in **Figure 7.10 (B)**. The intensity of all the peaks (554, 354 and 260 nm) decreases gradually and completely disappears after 240 min.

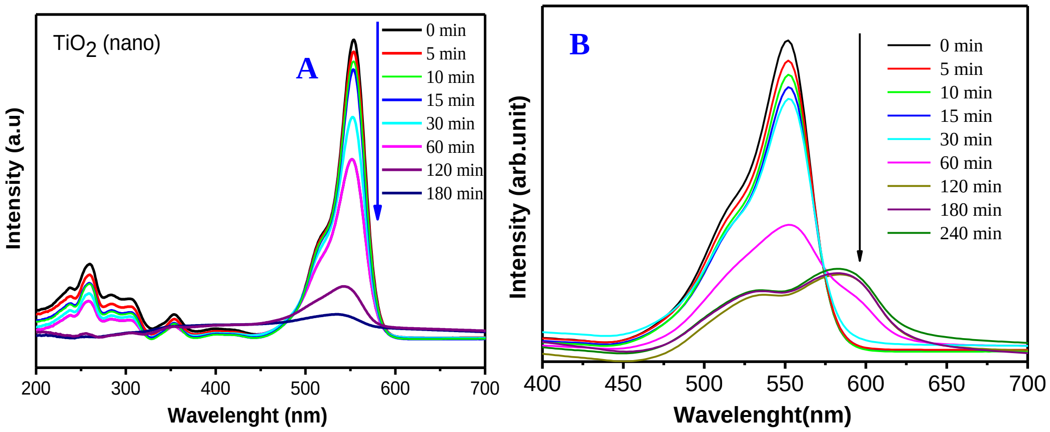

Figure 7.11: Temporal profile for the UV-Vis spectra of Rh-B Dye using (A) TiO_2 and (B) MoO_3 photo-catalyst irradiated under visible irradiation. For all these reactions the above blank given Figure 7.10 (A) is utilized.

There are no additional peaks in the UV–Vis spectra in the course of the experiment using titanianano-particles. This suggests that the dye is completely degraded and not just photo-bleached. According to Watanabe *et al.*[442] the blue-shift in the absorption maximum is related to the N-de-ethylation of Rh-B to Rh, the major intermediate in the degradation of Rh- B. The absence of any hypsochromic shift in dye degradation profile using nano TiO_2 probably disseminate the absence of de-ethylation channel as a major pathway for complete degradation of the Rh-B dye. MoO_3 has a band gap of 2.78eV. However photo-degradation of Rh-B dye by MoO_3 (**Figure 7.11(B)**) did not complete in 240 min. The intensity of 552 nm peak lowers slowly to 50% within 1 h as seen from **Figure 7.11(B)**. Thereafter the 552 nm peak splits into two peaks, with maxima at 526 nm and 582nm, respectively. The photo-degradation of the Rh-B does not propagate further. The Rh-B is probably transformed to different organic moiety which itself is quite stable and therefore has the final ground state.

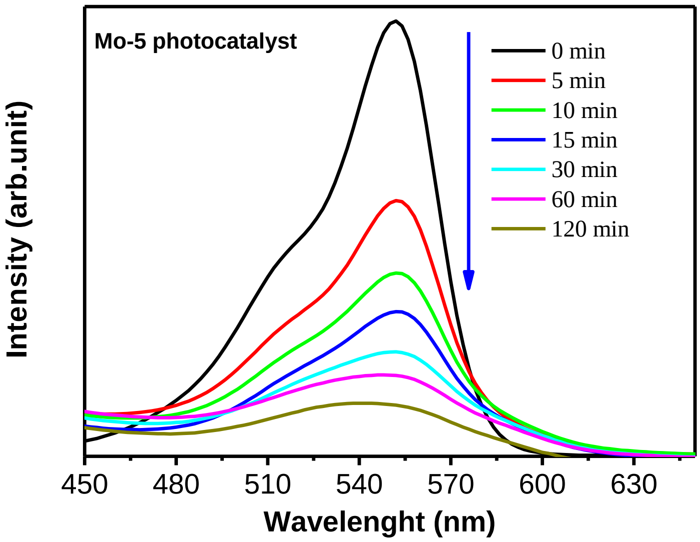

Figure 7.12: Temporal profile for the UV-Vis spectra of Rh-B Dye using Mo-5 photo-catalyst irradiated under visible irradiation.

The Rh-B photo degradation was subsequently undertaken using visible irradiated source with the different Mo-TiO_2 samples. Amongst them Mo-1 sample, took ~ 240 min to completely degrade the Rh-B dye. Utilizing the visible light irradiation Mo-5 sample showed the best (**Figure 7.12**) photocatalytic activity among the undoped TiO_2 and other Mo containing samples, with complete degradation within 120 min, without any shift in peak intensity.

In case of Mo-10 sample the photo-activity is sharply lowered. The Mo-10 sample does not completely degrade the Rh-B dye in ~240 min. Therefore with the visible irradiation the trend for the Mo-TiO_2 (**Figure 7.13**) samples signifying the increasing quantity of Mo present is as follows: Mo-1 < Mo-2 < Mo-5 >> Mo-10. The kinetics of the different photo-catalysts are shown in **Figure 7.13**. It can be stated that under the visible irradiation, as a function of Mo concentration in Mo-TiO_2 system, photocatalytic activity increases up to Mo-5. However after Mo-5 the photocatalyticactivity of the materials decreases sharply as a function of Mo-content in the Mo-TiO_2 system (**Figure 7.14**).

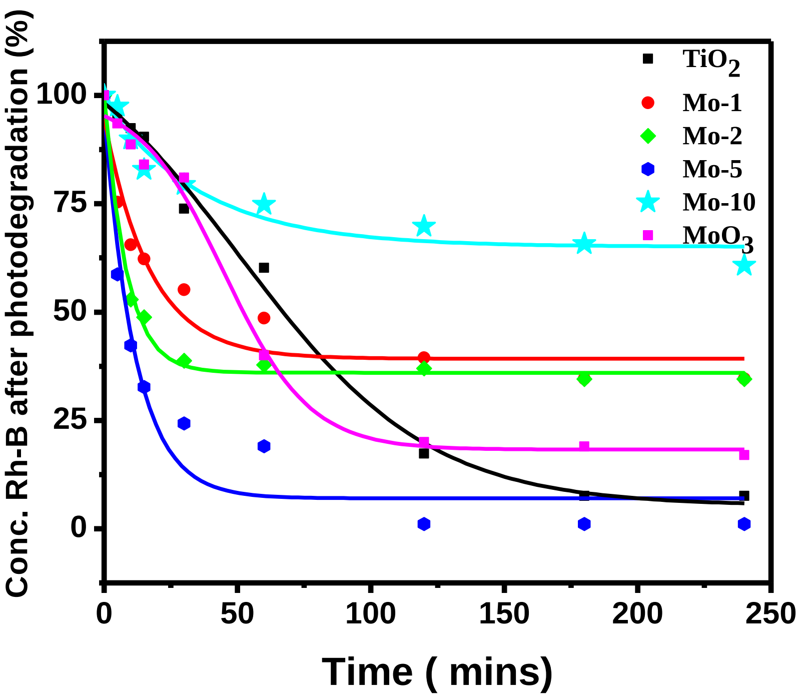

Figure 7.13: Plot of the time dependent photo-degradation of Rh-B using all the photo-catalysts under visible- irradiation. The Y-axis represents the percentage of Rh-B that is left after the photo-degradation of the dye by the individual photo-catalyst.

The Rh-B is adsorbed on the photocatalytic surface and the probable routes for these are enumerated in the later section of the mechanism in the **Scheme 7.4**. The TEM, Raman spectra indicates the presence of a separate phase of MoO_3 in the Mo-10 photo-catalyst. The Raman data however shows the presence of the nano-composite phase starting from Mo-2. Consequently the XRD data also provides certain evidences of Mo being doped in the TiO_2anatase lattice. As a function of the Mo percentage in the nano-composite or the lattice structure the band gap values are also lowered. However with the visible irradiative source. Photocatalytic activity of these materials follows the trend as Mo-1 < Mo-2 < Mo-5 >> Mo-10 (**Figure 7.13**) which shows a peculiar picture. The kinetics of the photo-degradation of Rh-B for all the catalysts are fast for the initial few minutes. After that it becomes quite slow in the rate kinetics. That is reflected in the effect that the complete degradation of the dye in longer time whereas the $t_{1/2}$ is quite low. However the $t_{1/2}$ (represented in the **Table 7.1**) as the representative time for the kinetic effect of the Rh-B degradation. Therefore as a function of the Mo-content in the system the photocatalytic activity increases until Mo-5 and then decreases suddenly. The prevalence of the effect due to the change in the band gap due to the Mo-dopant or the MoO_3 –TiO_2 interface conducts a role of importance to a certain degree as can be seen from the **Figure 7.14**. However, this is not the only effect as this could not explain the decline of photo-activity for the Mo-10 sample so sharply from the Mo-5 sample.

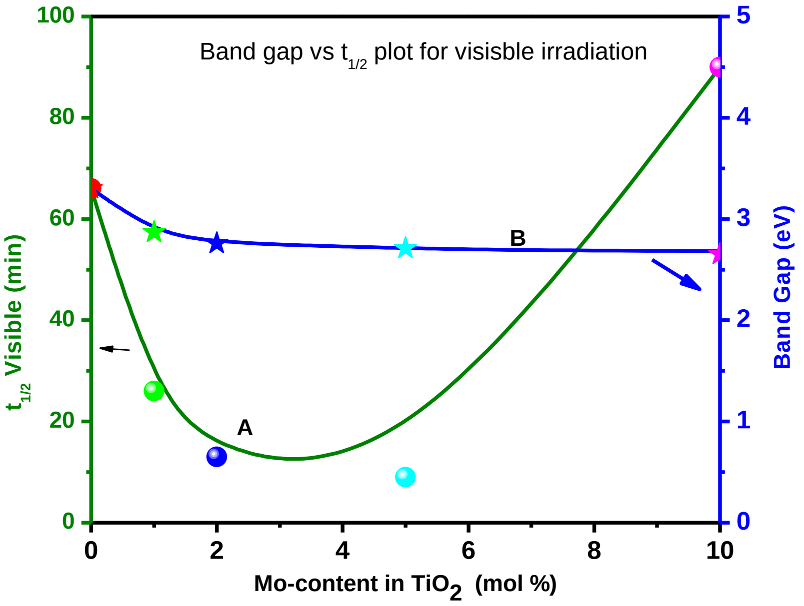

Figure 7.14: A) Plot of the $t_{1/2}$ value (representing the left Y-axis) *vs* Mo-content in the MoO_3-TiO_2 and, B) Plot of bandgap*vs* the Mo-content in the MoO_3-TiO_2 system (representing the right Y-axis).

It is found in the **Figure 7.14** the bandgap and $t_{1/2}$ representing the photo catalytic rate of these samples are comparable. The XPS data definitely show the presence of non-stoichiometry in the Ti sites as a result of the presence of the Mo in the TiO_2 system. However this non-stoichiometry supposedly created by the cationic deficiencies may also play a role in the promoted photocatalytic activity of these materials with the visible irradiation. Effectively the Mo^{6+} also shows a disproportionation to maintain the charge balance in the lattice structure. Perceivably the effect of the non-stoichiometry and the disproportionation could be a result of the Mo being substitutionally doped in the TiO_2 lattice system. This could also result in the change of the resulting oxidation potential of the system which could play a definite role in augmenting their photocatalyticbehavior. However there emerges a clear picture of the presence of a separate phase of MoO_3 along with the TiO_2 –Mo-doped lattice. The resulting inter-phase would also play a significant part in the photocatalytic feature of these catalysts. Even the defect sites present in the MoO_3 could be utilized by these catalytic systems. Conceptually the Mo-O will be more covalent in nature as compared to that of the Ti-O bond. In the MoO_3 structure Mo being in 6+ state and O being in 2- state, will probably be having more covalency in the Mo-O bond as compared to the TiO_2 or Mo-doped TiO_2 system [443-448]. The TiO_2 or Mo-doped TiO_2 system should in principle be more ionic in nature. The ionic radius of Mo^{6+} is 0.62Å whereas the Ti^{4+} is 0.65 Å, which are comparable. The anion (O^{2-}) being the same for both of the them Mo having a stronger charge will be therefore able to polarize the Mo-O bond more than that of Ti-O bond leading to its greater covalent character [This can be understood in the light of the Fajan's Rule] [449-451]. Therefore the presence of the MoO_3 separate phase in the nano-composite system would definitely alter the Redox potential of the system along with the change in the band gap of nanocomposite material. Consequently this can provide a positive effect for the photocatalytic performance of the nanocomposite.

7.2.3. Mechanism

The proton NMR spectra for the Rh-B dye and the temporal changes observed in the course of the photo-degradation of the Rh-B dye are deciphered henceforth. The ^{1}H NMR spectra for pure RhB is shown in **Figure 7.15(a**), consistent with the previous literature [416, 452, 453] the NMR signals of the aromatic hydrogen atoms Hc, Hd, He, Hf, Hg, Hh and Hi (c, d, e, f, g, h, and i are the element H position in RhB structure in (**Scheme 7.2)** are located at δ = 6.53, 6.70–6.73, 6.99–7.02, 7.28–7.30, 7.60–7.65, 7.90–7.93 ppm, respectively. The Ha represents those of the aliphatic hydrogen in the N-diethyl amine group for $–CH_3$ with chemical shifts present ~ δ (1.10- 1.2) ppm. Equivalently the Hb represents the - Methylene group ($>CH_2$) of NN diethyl amine and is shown in the range of ~δ (3.3-3.4) ppm chemical shift [416, 452, 453].

7.2.3.1. Visible irradiation

The sequential changes in the proton NMR spectra with time were observed using visible irradiation for Rh-B dye with Mo-5 photo-catalyst. The **Figure 7.15(c&e)** shows the temporal variation in the ^{1}H NMR spectra after 30 and 120 min of irradiation respectively.

Whilst observing the temporal variation in the ^{1}H NMR spectra after 120 min several interesting features arise. Initially disappearances of several peaks were found for the pure Rh-B without any irradiation. The disappearance of the ^{1}H NMR peaks are induced at the chemical shift values of δ (6.6-7.8) ppm. This region preferably is dominated by the protons for the aromatic moieties. Their disappearance indicates the absence of the aromatic moieties that were present with the Rh-B structure. Therefore this may lead to preferable paths through which the photocatalytic cleavage of Rh-B could possibly occur.

Simultaneously there is advent of several new peaks in the ^{1}H NMR spectra having chemical shift values of δ (0-4.0) ppm. The disappearance of the H_f to H_i (as per the **Scheme 7.2** showing the structure of the Rh-B indicating the different protons present) and presence of the only one aromatic proton post irradiation shows the possibility of the cleavage path 1 (as shown in the **Scheme 7.3**) and the formation of the benzoic acid may occur through this path. The formation of the benzoic acid as a visible photo-degradation product of Rh-B corroborates with the previous literature using other spectroscopic tools like Mass/SIMS [416, 452-454]. However loss of the H_c and H_d NMR signal after photocatalytic irradiation study indicates the cleavage Route 2 (as per **Scheme 7.3**) with the visible irradiation. This may lead to the formation of the amides and subsequent amines and diols. However there could be a cleavage simultaneously through the Route -2 at the same time, as shown in the (2+2) (Refer **Scheme 7.3)**. This would lead to products of diols and primary acids and benzoic acid along with certain amines. These products can be further cleaved to form smaller molecules like acetic acid and formic acid and further to CO_2.

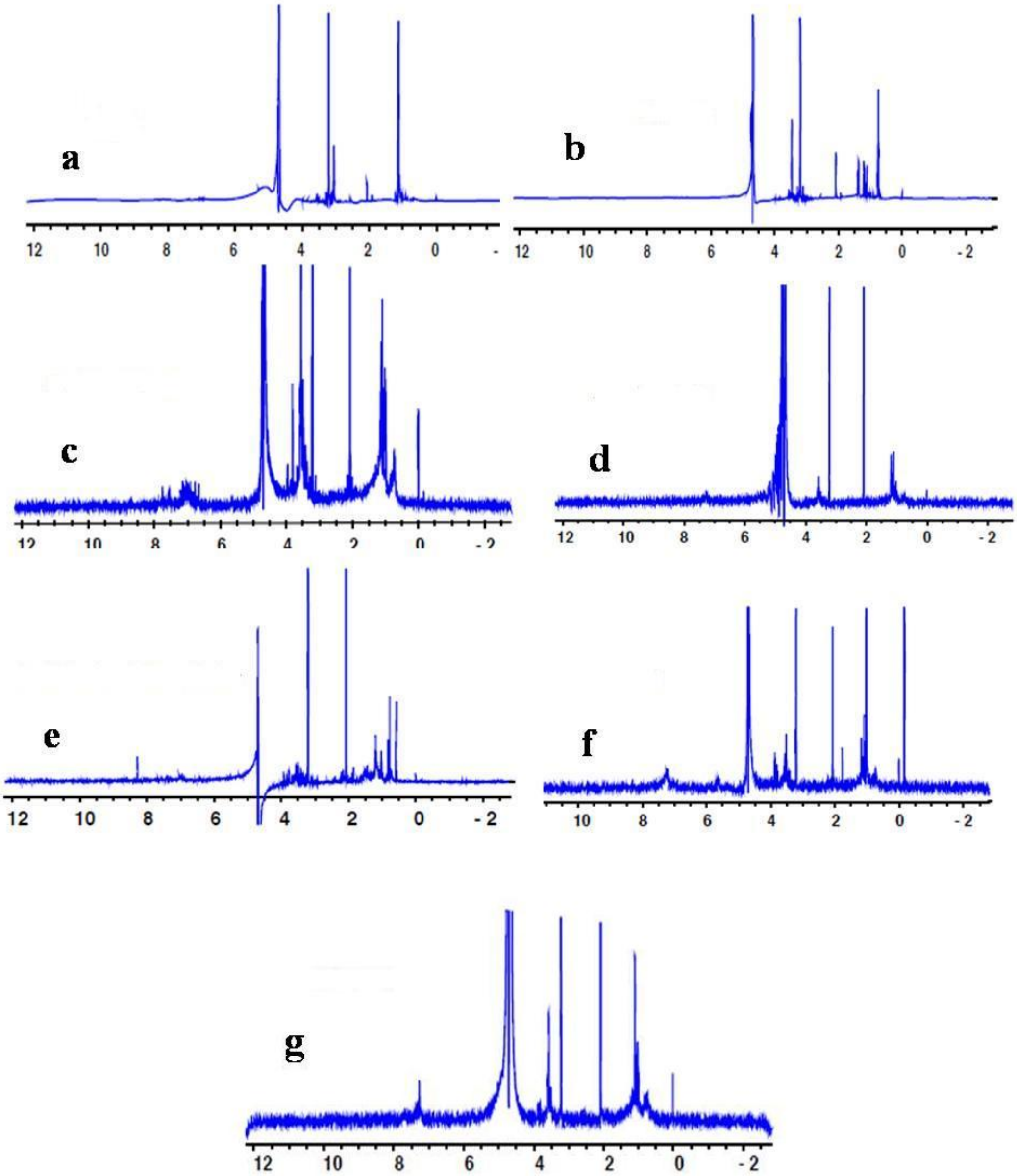

Figure 7.15: Temporal profile for the proton NMR for a) Rh-B pure without any photocatalyst or any irradiation, Rh-B which is photodegraded using visible light with the Mo-5 photocatalyst for b) 0 min, c) 30 min, d) 60 min and (e) 120 min of irradiation respectively. (f) Rh−B photodegraded using UV irradiation by Mo-1 photocatalyst for 120 min and (g) Rh−B photodegraded using visible light using MoO_3 photocatalyst.

The formation of these products as enumerated above is further supplemented by the formation of certain new peaks during the process of the photo-degradation of Rh-B. The proton NMR peak at chemical shift value of δ (0.58) ppm is a sharp high intensity peak which is generally due to a primary alcohol or acetoyl group [416, 452-454].There is small broad peak at δ (0.68) ppm which suggests the formation of –H of an amide or probably a alkyl -CH_3[336, 416, 454, 455]. Presence of two sharp peaks at δ (0.78) ppm indicates -H of –CH_3 group, δ (1-1.2) ppm doublet –H of a primary alcohol. The new peak at δ (2-2.2) ppm indicates the presence of the acetic acid. The secondary amine may be represented by the peak formed at δ (3.15) ppm. There are several peaks between δ (3.2-3.8) ppm representing different alcohols and phenolic groups. There is strong peak between δ (3.8-4.0) ppm suggesting an amide or an ester. The presence of peaks at δ (1-1.2) ppm and δ (3.3-3.4) ppm even after 120 min of photo-degradation suggests the complete absence of the de-ethylation [as in previous literature] [336, 416] pathway for the photo-dissociation by this photo-catalyst.

Scheme 7.2: Rhodamine-B with different protons.

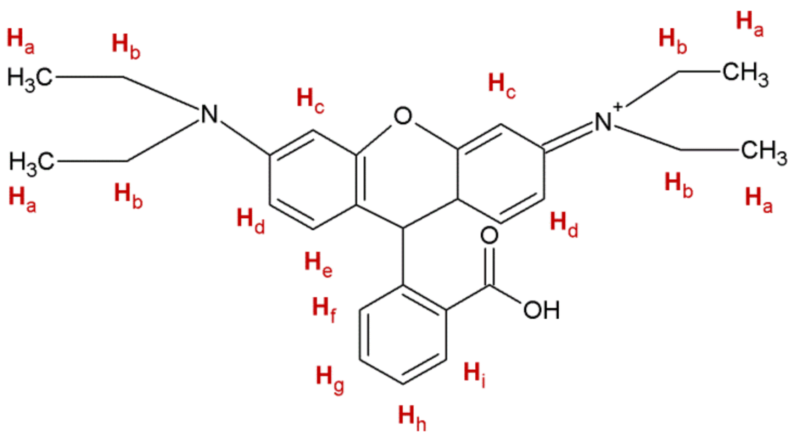

Rhodamine -B

Scheme 7.3: The probable routes for the Rh-B photo-degradation via visible irradiation. The structures are mere representatives of the intermediate products and do not signify essentially the main final products.

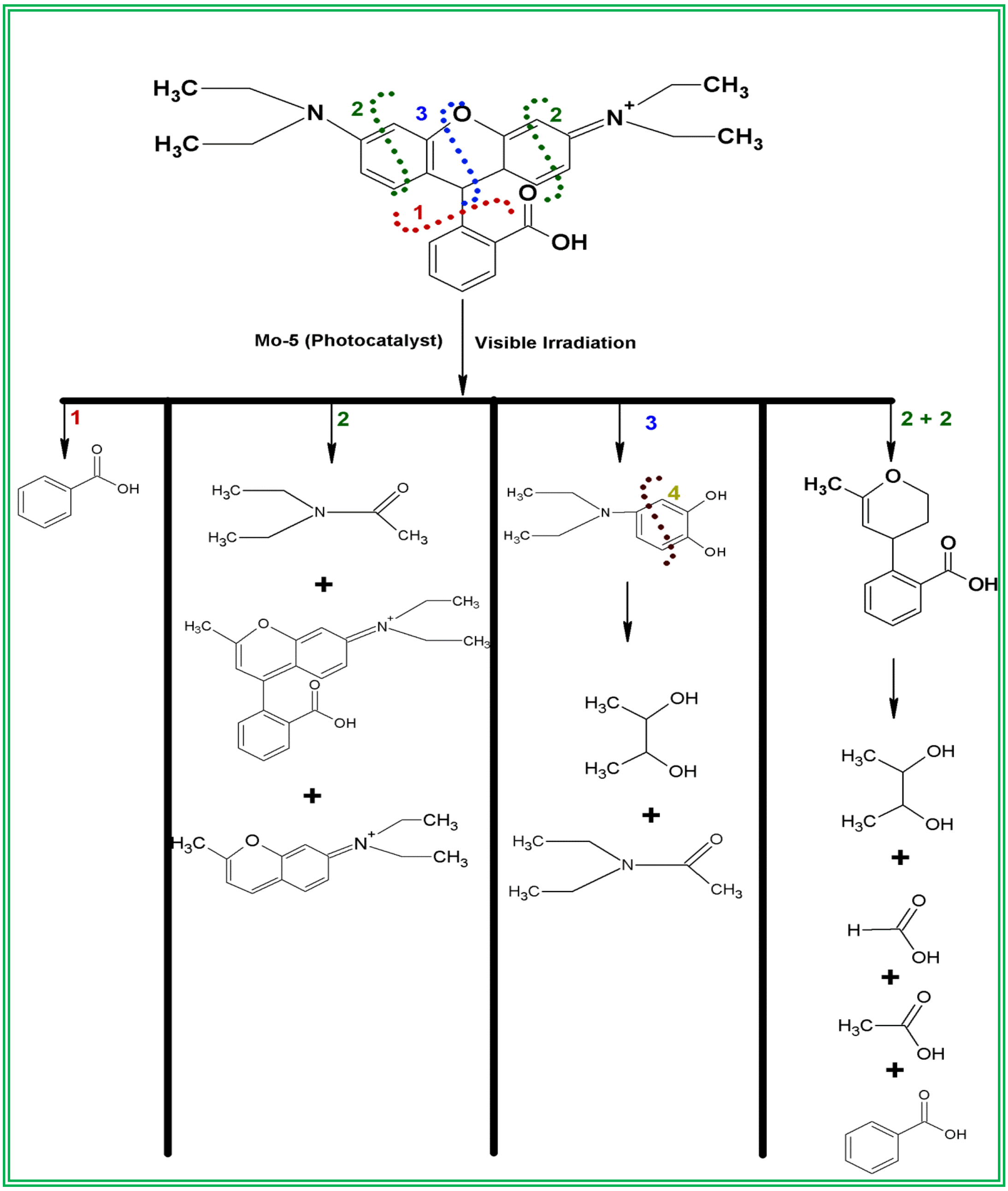

The photo-degradation events after 30 min of photo-irradiation are portrayed in **Figure 7.15(c)**. The ensemble of the events is almost same as that observed in the case of 120 min photo-irradiation with the exception of certain features. After 30 min of the photo-irradiation of all the ^{1}H NMR peaks representing the Rh-B molecule above have lowered down in intensity considerably. However there was no complete disappearance of any of the above ^{1}H NMR peaks. Nevertheless several new peaks were found between chemical shifts of δ (0-4) ppm and a new broad peak was found at ~δ (7.5) ppm and other as described in the previous section of 120 min. This indicates that the time dependent temporal event of photo-dissociation of Rh-B is not a singular / stochastic event and follows a kinetic route too. With 30 min of irradiation the intermediates formed are quite scanty and the Rh-B moiety is still present along with the other intermediate which is reflected in its UV-Vis spectral features of the photo-degradation experiments with the visible irradiation.

7.2.3.2. UV irradiation

The Mo-2 photo-catalyst so used is the representative form for the UV – irradiation route. The Rh-B dye with the UV-Irradiation shows lower amount of intermediate products as formed during the photo-degradation process. The intensity of the intermediates as compared to the visible irradiation is lower and there are fewer peaks observed by the UV irradiation. However in general speaking the disappearance of the aromatic proton NMR peaks are comparable with that of the visible analogue suggesting almost same route of cleavage occurs in the Rh-B moiety with these two irradiations. Occurrence of the new proton NMR peak is again equivalent to that of the visible analogue. Lower intensity of intermediate peaks generally proclaims the faster kinetics for the UV–irradiated process which is also corroborated from the dye degradation experiments. Therefore probably the **Scheme 7.3** can be considered as a unified route for the cleavage of the Rh-B molecule photocatalytically by these series of photo-catalysts.

7.2.3.3. Visible irradiation with MoO_3

The ^1H NMR results using MoO_3 itself as a photo-catalyst provides us certain further insights about the Rh-B photo-degradation by this photo-catalyst. The MoO_3 is having a band gap in the region of 2.8eV. Therefore it is appropriate to check the mechanistic activity of this material under the visible irradiation rather than the UV irradiation. The different temporal features via photo-oxidation of Rh-B shows after even 120 min there is complete loss of the Hc-Hi peaks as reported previously in the Section 7.2.7.1. However there is a prominent appearance of triplet of triplet corresponding to three different aromatic –H in the benzoic acid. This is amply in this system and appears in the range of the chemical shift value of δ (6.9-7.05) ppm. Therefore the cleavage Route 1 (as per **Scheme 7.3**) is always happening. This is further supported with the -H of the benzoic acid found at chemical shift value of δ (8.3) ppm. The lowering/disappearance of the H_a and H_b far lower as compared to the nano composite system of Mo-5. This suggests these species are relatively stable and are present as additionally stable intermediates. Another interesting observation is that the amines and the amides are formed to very lower extent in this system. The absence of the peaks in chemical shift value range of δ (1.6-1.8) ppm & (3.5-4.0) ppm corroborates this data. There is broad peak found for the amines at chemical shift value of δ (1.4-1.6) ppm with very less intensity. The diols equivalently are also formed to a very lower extent suggesting Route-3 (as represented in the **Scheme 7.3**) is quite poor in the photo degradation of Rh-B using MoO_3 as the photocatalyst. The acetic acid peak is present in stronger intensity with chemical shift value referring to δ (3.3) ppm [454]. This perhaps indicates that the diols either are formed in lower quantity or are further photo-oxidised to acetic and benzoic acids. However the absence of the amides could be due to two reasons. The amides can also further oxidise to produce stable acids or are effectively adsorbed on the MoO_3 surface very strongly and are not in the final solution.

The photo-oxidation studied via the UV-Vis in the above Section 7.2.2 indicates clearly that after 120 min there is formation of a very stable intermediate which does not further photo-degrade and is quite stable on the MoO_3 surface. The Zeta potential values show that with excess amount of Mo in the surface the negativity of the surface charge is enhanced (**Table 7.1**). However on adsorption of the Rh-B the negativity is lowered. This phenomenon is observed for the Mo-10 sample also. Therefore identifying this fact rationally suggests that the amides and the amines will be strongly attracted by MoO_3 surface and owing to the electrostatic attraction between them would stabilize these intermediates further. The presence of the excess amount of MoO_3 (as a separate phase) on the surface rather than the doped Mo will lead to formation of certain stable intermediates. The highly stable intermediates will be strongly detrimental to the photo-oxidation of Rh-B on these photocatalytic surfaces. Consequently the presence of the MoO_3 as a nano-composite phase along with the Mo-doped TiO_2 can be detrimental for the Rh-B photo-degradation effect as the dye can be adsorbed very strongly on the surface of the MoO_3 as observed for pure MoO_3. However the most plausible reason for the lowering of the photo activity of the Mo-10 photocatalyst as compared to that of Mo-5 and ever TiO_2 may be due to the concurrence of the events as defined above. Equivalently if we observe the kinetics of the photo-catalysts degrading the Rh-B this also becomes quite apparent. The initial kinetics is quite fast. However after some time the kinetics slows down considerably. This could be correlated between the two effects. The adsorption of certain stable intermediates will happen on MoO_3 surface. This should in turn lower the photo-activity of these photo-catalysts. Qualitatively this could be understood by the fact that presence of the MoO_3 as a different phase with a separate entity from the Mo-doped TiO_2 does change the overall ionicity/covalency of the bonding order for these nanocomposite. As a result the overall redox-potential of the nanocomposite photo-catalyst will also be altered with the differential amount of separate phase of MoO_3 being present in the nanocomposite. As discussed earlier in the above section, MoO_3 structure Mo being in 6+ state and O being in 2- state, will probably be having more covalence in the Mo-O bond as compared to the TiO_2 or Mo-doped TiO_2 system [446-451, 456]. Therefore the presence of the MoO_3 separate phase in the nanocomposite systems would alter the Redox potential of the system along with the change in the band gap of nanocomposite material. Consequently, this can provide a favorable effect for the photocatalytic performance of the nanocomposite. However as the presence MoO_3 can also perceivably play an adverse role due to the stronger electrostatic attraction between the surface and the amine or the amide based intermediates. Strong adsorption of the higher electrophilic N-based intermediates over its surface can lead to a very stable intermediate thereby lowering its photocatalytic activity. The visible irradiation trend for the Mo-TiO_2 samples signifying the increasing quantity of Mo present is as follows. Mo-1 < Mo-2 < Mo-5 >> Mo-10.The Mo-10 being less active than the nano $TiO_{2.}$ In order to explain the process that up to Mo-5 increment in the Mo-content augmented the photocatalyticbehaviour of Mo-TiO_2, however once Mo-10 is reached there is a sharp decline with the Mo- content. Another point worth mentioning from the Raman features is that up to Mo-5 the MoO_3 phase is present on surface whereas in the Mo-10 there is strong presence of the bulk phase. In the bulk phase MoO_3 as per the above discussion, according to the mechanistic determination, plays a detrimental role for photoactivity as certain intermediates get strongly adsorbed on it. The surface MoO_3 along with certain Mo-doping alters the redox potential and positively augments the photocatalytic process. This factor plays a strong role in the Mo-1 to 5 where Mo is doped to an optimum amount and the MoO_3 is present as a surface phase. However the second factor where the intermediates get very strongly adsorbed on the MoO_3 surface which drastically reduces its photocatalytic property becomes very dominant for the Mo-10 where the MoO_3 is present even in the bulk form. Therefore there should be an optimum amount of MoO_3 in the nano-composite of Mo-TiO_2. Perceivably this is observed in almost all the present photo-catalyst as with time the rate lowers down considerably in almost all of them. However the point due to which its effect becomes detrimental still possess to be an open question and requires further detailed investigation.

The zeta potential values as shown in the **Table 7.1** show that almost all of these surfaces are negatively charged. The surfaces of the catalysts being negative in nature under all probability the dye will be guided by the electrostatic attraction on being adsorbed on the surface. The Rh-B being a cationic dye there is a definite possibility of strong electronic interaction for the adsorption effect. Therefore in all probabilities the Rh-B can be adsorbed on the surface of the photocatalytic materials via the following routes as given below in the **Scheme 7.4**.

Either the nucleophilic N-group can be directly adsorbed on the surface via a strong electrostatic interaction as in I or they can be adsorbed over surface –OH of the photo-catalyst. The Rh-B dye degradation is occurring over a solid liquid interface the first monolayer of the photocatalytic surface would be saturated with the hydroxyl groups or the H_2O molecule itself. As found in the photocatalytic data's any de-ethylation step are seldom found for these set of photo-catalyst. The Route –III as shown in the **Scheme 7.4** will have initially the de-ethylation step as the major step for the intermediate formation. Therefore accordingly this would be the least probabilistic step for the adsorption process. Henceforth the Route II in the **Scheme 7.4** could be the most likely route for the adsorption process.

Scheme 7.4: Probable structures after adsorption of Rh-B on the photocatalytic surface.

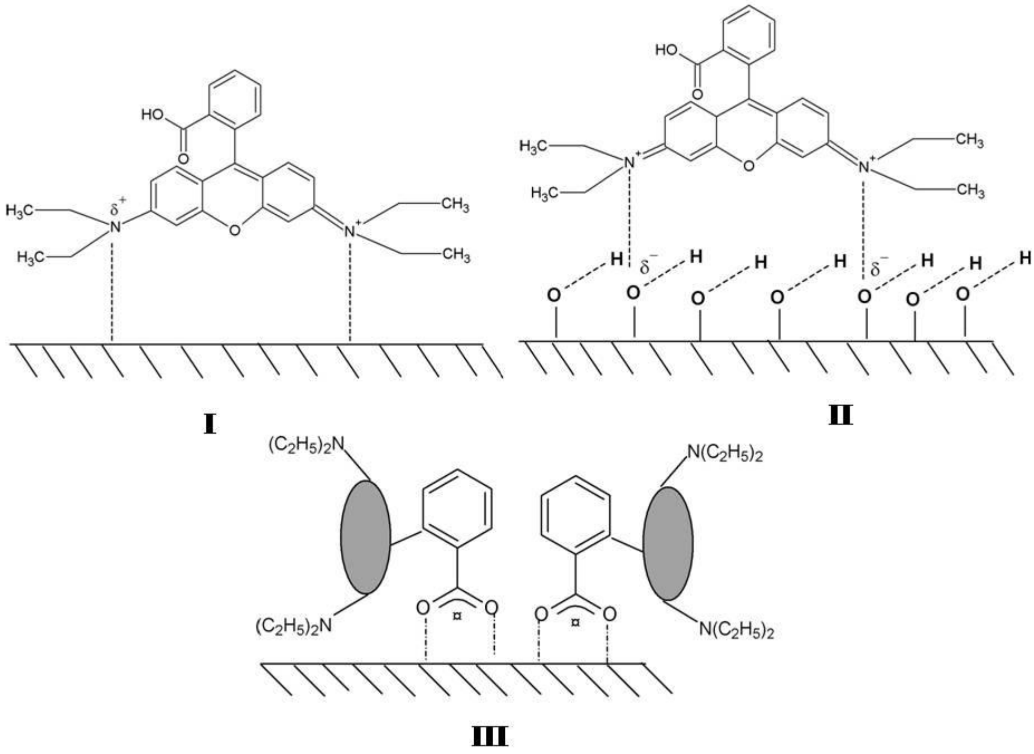

The Route 1, 2, 3 and 2+2 as referred in the **Scheme 7.3** may follow subsequently post this adsorption step. The other prospective route of adsorption for the Rh-B dye on the photocatalytic surface could be a π- Anionic interaction between them [416]. The surface (negatively charged therefore conceivably anionic in nature) and the delocalised π-electrons of the Rh-B. Generally the π-anionic interaction possesses energetically quite low values [455]. Consequently if the system possesses hetero-atoms the π-anionic interaction will show further lower energy values [457]. Therefore this would therefore least perturb a hydrated surface as in that of the present scenario. Therefore this route of adsorption could be neglected.

Therefore overall the mechanistic studies by the *ex situ* NMR hints to the facts that UV and visible irradiation does not have different routes for the photo-oxidation process by these photo-catalyst. This could suggest that the electron and the hole produced by them in this process with the differential UV or the Visible irradiated sources are by some means having equiergic electrons and the holes resulting in the similar intermediate routes. However the process leading to the equiergic production of this e^- /h^+ pair by the differential source is still an open question to be addressed. It could also be result of the intermediate surface resulting in the typically equivalent defect sites.

7.3. Summary

The photo-degradation study of Rh-B dye was performed utilizing a TiO_2-based photocatalyst which shows the effects of both the Mo-doping and incorporation of nano dispersed MoO_3. The primary characterization techniques confirm such a structure. XRD shows the formation of the MoO_3 starting from the Mo-5 sample onwards. The Raman spectroscopic data along with TEM studies however shows the signature of MoO_3 in all the samples (Mo-1 to Mo-10). The DRS studies indicate that the samples are indirect band gap semiconductors. The calculated band gap, from the KubelkaMunk plots, range from 3.24 to 2.65 eV, decreasing as a function of the Mo-content. The XPS study appears to indicate the presence of cationic deficient sites in the TiO_2anatase lattice along with a disproportionation in the oxidation state of Mo.

There are also positive evidences for the presence of excess oxygen in the nano-composites. The XPS also shows the partial Mo-doping in the TiO_2 lattice. The UV-excited photocatalytic degradation of Rh-B is primarily dictated by the quantitative presence of anatase TiO_2 in the Mo-TiO_2 system. However, the photocatalytic degradation of Rh-B, with the visible light is clearly correlated with the Mo-content, increasing from Mo-1 to Mo-5. However, there is a sharp decrease in the photoactivity from Mo-5 to Mo-10, the latter being even less active than undoped TiO_2. Thus, the trend in the activity of these photo-catalysts can be summarized as: Mo-1<Mo-2<M0-5>> Mo-10 for irradiation with visible light. This trend in the photocatalytic activity of these materials could be qualitatively understood in terms of structure-activity correlation. The presence of the nano dispersed MoO_3 phase in the nano-composite system would definitely alter the redox potential of the system as well as the band gap of nanocomposite material and thereby affect the photocatalytic performance. Similarly, the Mo^{6+}/Mo^{5+} dopants could also affect the redox potential of the nano-composite and in turn improve the photo-oxidation process. The MoO_3 in Mo-1 to Mo-5 is present as surface phase which clearly augments the photoactivity of these materials by altering its redox potential. However at Mo-10 the excess amount of MoO_3 (as a separate bulk phase) is present as the bulk phase rather than the surface phase and doped Mo in TiO_2. This leads to formation of certain very stable intermediates, which are strongly detrimental to the photo-oxidation of Rh-B thereby drastically lowering the photo-activity of Mo-10 as compared to the other Mo-5 etc. *Ex-situ* NMR studies shows different intermediates and different probable routes of the Rh-B dye degradation. The stable intermediates were formed by a direct oxidative fragmentation route, without any evidences for the de-ethylation route. The intermediates obtained were benzoic acid, different amines, diols and acids (mostly pertaining towards formic and acetic acid). The adsorption of the Rh-B dye on the catalytic surface via the N-charge centers of the Rh-B also appears to take place. The photo-oxidation can be expected to lead to the complete mineralization of the Rh-B to give CO_2.

Chapter 8

Silica coated nanoparticles for hyperthermia based treatment

Enhanced Specific Absorption Rate in Silanol Functionalized Fe_3O_4 Core-Shell Nanoparticles: Study of Fe Leaching in Fe_3O_4 and Hyperthermia in L929 and HeLa Cells
Jerina Majeed , Lina Pradhan, R. S. Ningthoujam, R. K. Vatsa, D. Bahadur and A. K. Tyagi
Colloids and Surfaces B: Biointerface*, 2014, 122, 396-403.*

8.1. Introduction

Magnetic nanoparticles (MNPs), especially magnetite (Fe_3O_4) and maghemite (γ-Fe_2O_3), are of great interest because of their fascinating properties including superparamagnetism, biocompatibility and low toxicity. Their prospective applications cover various fields, especially in biotechnology and biomedicine, such as drug delivery, magnetic thermotherapy of cancer cells (hyperthermia), enzyme immobilization, bio-sensing, separation and purification, and magnetic resonance imaging [219, 458-462].

Under the influence of external alternating magnetic field (AMF), magnetic nanoparticles evoke magnetization reversal, and create thermal energy which can be measured in terms of the specific absorption rate (SAR) as the nanoparticles return to their relaxed states [463-465]. Conversion of this electromagnetic energy into heat by magnetic nanoparticles has significant application as a non-invasive and potential therapy technique for biomedical applications. Magnetic fluid hyperthermia (MFH) can be used to create localized heating for killing tumor cells. The surface functionalization of magnetic nanoparticles enables such therapeutic treatments to kill cancer cells selectively by localized heating, without affecting the neighboring healthy cells. Thus, the therapeutic efficacy is significantly enhanced compared to conventional chemotherapy and radiotherapy. Magnetic nanoparticles can also be utilized for controlled delivery of drugs as well as combination with magnetic resonance imaging (MRI) at the cellular and molecular level, making them promising materials for multimodal diagnosis and treatment of a number of diseases [466-468]. However, pure Fe_3O_4 MNPs, according to literature exhibits low SAR values, and thus it needs higher concentration of MNPs to achieve the required hyperthermia temperature, which is undesirable for the clinical purpose. This is due to either low saturation magnetization from smaller particle size or agglomeration and leaching of Fe from the MNPs into the medium as a result of inappropriate surface coating. In this context, development of a novel material with both high biocompatibility and high heat transfer efficiency is of utmost importance for the application of magnetic nanoparticles based hyperthermia.

In this chapter, improvement in the efficacy by changing the coating agent and optimizing the surface coating thickness using silica (SiO_2) has been envisaged, which on encapsulating the magnetite crystal yields an unique magnetic responsivity [469, 470]. Silica coating is being used due to its inert nature, low cytotoxicity, biocompatibility, longer stability in both acidic and alkaline pH range and having hydrophilic surface to enable functionalization with other molecules (drug or protein) that makes them suitable for bioconjugation with cell targeting agents [191, 471-473]. Silica-coated MNPs not only can be homogeneously dispersed in aqueous solutions with a wide range of pH values, but also prevent Fe leaching from the MNPs in cancerous cells where the pH is slightly acidic (~ pH 5) than the normal cells (~ pH 7.3). Usually, bare Fe_3O_4 starts to leach out in pH lower than 5. The chemical stability of the MNPs in different pH (2-7) for a fixed period was also evaluated using induction heating experiments. The biocompatibility of the MNPs in HeLa cells is done using sulforhodamine-B (SRB) assay and efficacy of MNPs on the cells under induction heating is carried out. All the experiments were performed in triplicate.

8.2. Results and discussion

8.2.1. Characterization of nanoparticles

The XRD patterns for uncoated Fe_3O_4 and $Fe_3O_4@SiO_2$MNPs prepared at 60, 80 and 100 °C are shown in **Figure 8.1**. All the peaks could be indexed with the cubic structure corresponding to the magnetite phase ((JCPDS Card No. 88-0315, a = 8.375 Å).

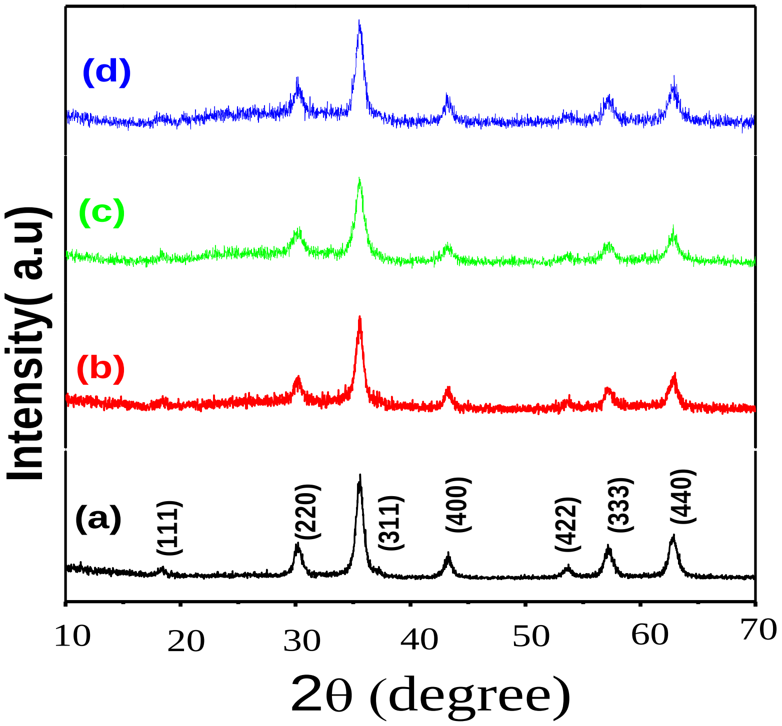

Figure 8.1: XRD patterns of (a) Fe_3O_4, (b) Fe_3O_4-SiO_2 MNPs prepared at 60, (c) 80 and (d) 100 °C.

With the incorporation of SiO_2 into the Fe_3O_4samples, the XRD patterns were found to be noisier which might be due to the presence of amorphous silica on the surface of the nanoparticles. As-prepared particles were further tested for its induction heating efficacy. Since MNPs prepared at 60 °C showed poor heating efficacy, further characterization was done only in MNPs prepared at 80 and 100 °C.

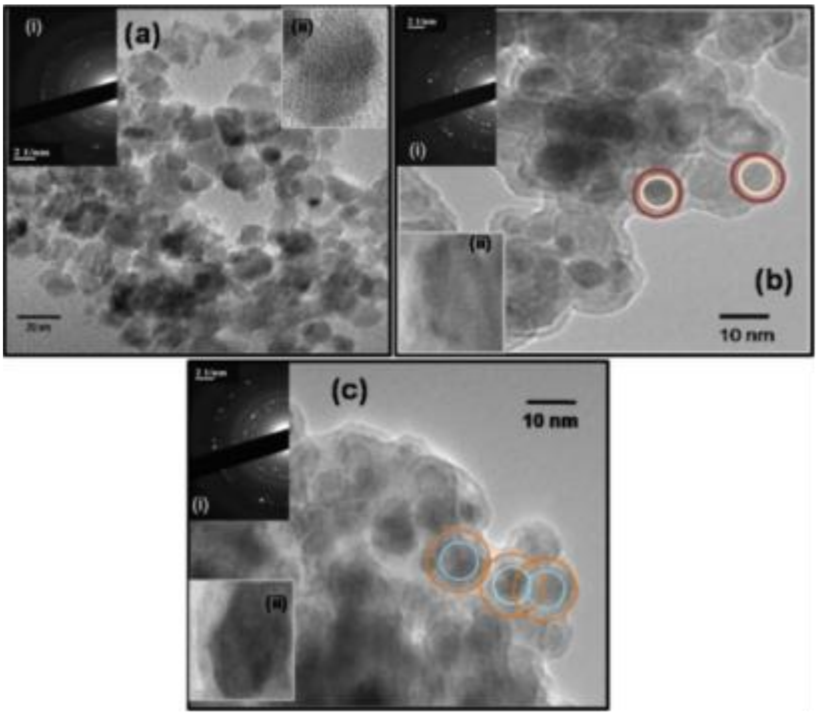

Figure 8.2: TEM images of (a) Fe_3O_4, (b) Fe_3O_4-SiO_2-80 and (c) Fe_3O_4-SiO_2-100 MNPs. Their respective SAED patterns (i) and HRTEM image (ii) are shown as inset.

The TEM images of as-prepared Fe_3O_4 and silica coated samples are shown in **Figure 8.2**. As prepared Fe_3O_4 shows aggregated particles (size 10 – 20 nm) while the silica coated samples show nearly monodispersed spherical shaped particles in the size range of 10 – 20 nm with a shell thickness of 2-6 nm. In the case of MNPs synthesized at lower temperature (~ 80 °C) Fe_3O_4-SiO_2 80, the particles are of the size 10 nm with a shell thickness of 2-3 nm, while in the case of higher temperature (100 °C) Fe_3O_4-SiO_2 100 synthesized samples the shell thickness increases. The increase in shell thickness at higher temperature might be due to the enhanced hydrolysis of TEOS on the surface of the core as compared to the lower temperature, leading to faster growth of $SiO_2.xH_2O$ particle.

The FTIR spectra of Fe_3O_4 and Fe_3O_4-SiO_2 MNPs are depicted in **Figure 8.3(A)**. One main absorption peak centred around 591 cm^{-1} was observed in the case of Fe_3O_4 MNPs, which corresponds to Fe–O stretching vibration. The broad bandcentred around 3422 cm^{-1} is assigned to the H–O–H stretching mode vibration of the adsorbed water. The band at 1650 cm^{-1}is also observed in all samples due to the bending vibration of water [474]. The characteristic absorption for the silica network in Fe_3O_4-SiO_2 MNPs is assigned as follows [475]:

Broad high-intensity band at 1092 and 838 cm^{-1} are characteristic peaks of the symmetrical and asymmetrical vibrations of Si–O–Si in SiO_4 tetrahedron. The band at 3749 cm^{-1} is an indication of the presence of Si–O–H bond [476], which helps in the dispersion of particles in water (Scheme 8.1). The band at 446 cm^{-1} is an indication of the presence of Si–O–Fe. Based on this information, it is inferred that the surface of Fe_3O_4 has chemical bonding with $SiO_2.xH_2O$ that exhibits characteristic IR vibration bands.

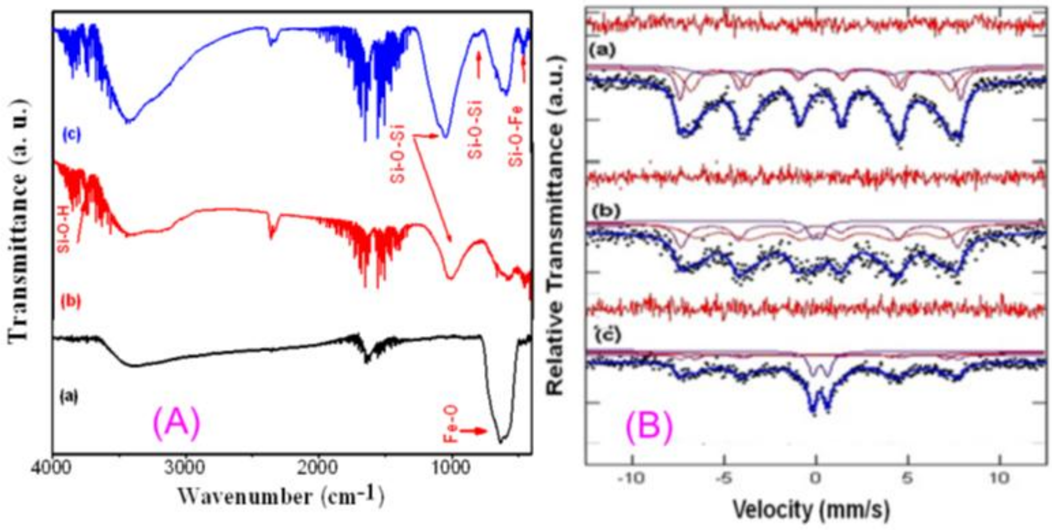

Figure 8.3: (A) FT-IR spectra and (B) Mössbauer spectra of (a) Fe_3O_4, (b) Fe_3O_4-SiO_2-80 and (c) Fe_3O_4-SiO_2-100 MNPs.

Mössbauer spectra of Fe_3O_4 and Fe_3O_4-SiO_2 MNPs are shown in **Figure 8.3(B)**. Uncapped Fe_3O_4 MNPs prepared by co-precipitation show ferromagnetic sextets only. Fe_3O_4 MNPs show two sextets (Zeeman patterns) with hyperfine fields (Hf) of 47 and 43 Tesla [477]. Isomer shift values are found to be 0.23 and 0.27 mm/s. Since isomer shift values are close to Fe^{3+}, this may be due to fitting errors in smaller particles. Similar behaviour was reported earlier in Fe_3O_4 NPs [478]. The quadruple splitting is found to be almost zero. When Fe_3O_4 MNPs interacted with SiO_2, it is found that the magnetic sextet patterns collapse. Instead, a significant evolution of the super-paramagnetic doublet is observed with increasing the reaction temperature from 80 to 100 °C. At 100 °C reaction temperature, the super-paramagnetic doublet is high. With the decrease of reaction temperature up to 80 °C, the super-paramagnetic doublet decreases with respect to the ferromagnetic sextet. This can be explained by fluctuation of small magnetic moments. The nano-sized magnetic particles are single-domain particles and become super-paramagnetic below a critical size (d_c) and above a temperature (T_B) called the blocking temperature. In super-paramagnetic particles, the particle energy (KV, where K is the anisotropic constant of the particle with volume V) is so small and the room temperature thermal energy (kT, where k is the Boltzmann constant) can dominate over the particle energy. In such situation, the magnetization direction of the particle or domain reverses from easy direction to the other directions spontaneously. Relaxation of magnetization is very fast ($\sim 10^{-9}$ sec) and this is known as Néels spin relaxation (τ_N). With increasing the reaction temperature, more of SiO_2 is present as observed by TEM and ICP-MS and these results in lowering of agglomeration of particles. In addition, the number of smaller sized particles increases due to the extent of the decrease of agglomeration of smaller particles and thus enhances the super-paramagnetic doublet.

In Mössbauer experiment, the relaxation of spin/ magnetization $\tau \leq 10^{-8}$ sec could not be determined. Thus, it appears as a doublet. Doublet peaks are related to paramagnetic or superparamagnetic contribution. When $\tau » 10^{-8}$ sec (slow relaxation), it could determine the spin state, and thus sextet spectrum will be observed. Sextet spectrum appears which is related to the ferromagnetic contribution.

Two sextets with hyperfine splitting values 49 and 47 Tesla are related to A and B sites of Fe (tetrahedral and octahedral sites of cubic closed packed structure). Third sextet with hyperfine 38 Tesla will be related to the Fe present as smaller size particles. It is to be noted that superparamagnetic to ferromagnetic transition temperature called the blocking temperature (T_B) is dependent on the measurement time. Generally, SQUID instrument takes 0.1 – 1 sec time to measure the magnetic moment, but Mössbauer instrument takes ~10^{-7} sec. Thus Mössbauer measurement can see some moment in the case of relaxation of smaller particles, but this cannot be seen by SQUID. Thus, sextets are seen in Mössbauer spectra due to ferromagnetic contribution but the same particles can show superparamagnetic behaviour in SQUID measurement.

The iron estimation of the sample was done using ICP-MS. Uncapped MNPs has a value very close to the theoretically calculated value 72% of Fe in Fe_3O_4. Fe content of samples follows Fe_3O_4 (72 %) > Fe_3O_4-SiO_2 80 (61 %) > Fe_3O_4-SiO_2 100 (43 %). Decrease in Fe content is related to increasing SiO_2 per gram of the sample. These results are further supported by the TEM images where the shell thickness is increased by increasing the temperature. Thereby, amount of Fe per unit mass of the sample decreases with an increase in shell thickness.

The magnetization versus applied magnetic field at room temperature for samples (Fe_3O_4, Fe_3O_4- SiO_2-80 and Fe_3O_4- SiO_2 -100) is shown in **Figure 8.4**. The samples show superparamagnetic properties. The coercivity values (H_c) of 10-15 Oeare obtained. It is expected to be zero in super-paramagnetic particles at room temperature but due to particle size distribution it has some H_c values.

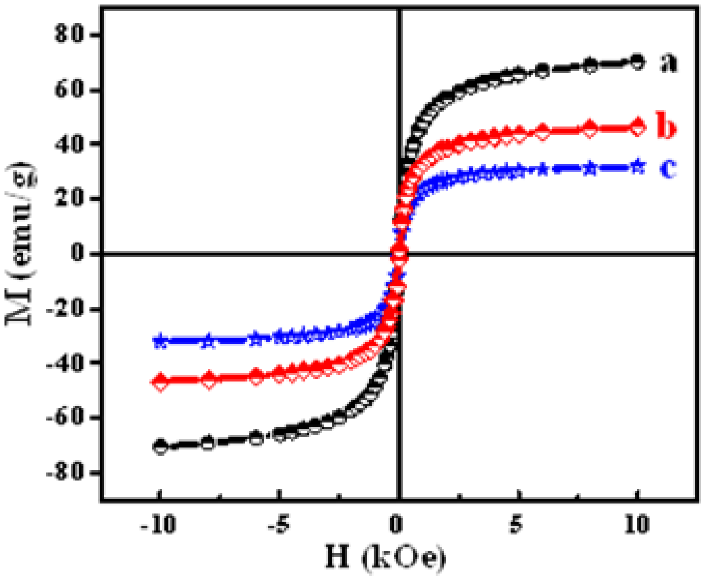

Figure 8.4: Magnetization vs. Applied field of (a) uncoated Fe_3O_4, (b) Fe_3O_4-SiO_2-80 and (c) Fe_3O_4-SiO_2-100 NPs.

Magnetization value is still unsaturated up to 10 kOe. Saturation magnetization (M_s) is calculated when 1/H → 0, M_s values are found to be 59, 40, and 28 emu/g for pure Fe_3O_4, Fe_3O_4- SiO_2-80 and Fe_3O_4 -SiO_2-100, respectively. The M_s of Fe_3O_4 MNPs is lower than of bulk Fe_3O_4 (92 emu/g) due to smaller particle size [479]. Whilst decrease in magnetization in the case of Fe_3O_4- SiO_2-80 and Fe_3O_4- SiO_2-100 is due to two reasons: primarily, due to the presence of silica associated per gram of the weighed sample which, accounts for the gradual decrease in M_s as the amount of silica increases and secondly due to decreased agglomeration or smaller particle size.

8.2.2. Induction heating study

The heating ability of different MNPs was evaluated under increasing magnetic field environment (200-400 A) for 10 min. MNPs show heating ability depending on current applied and their concentration. The temperature achieved by 5 mg of samples (Fe_3O_4 and Fe_3O_4 -SiO_2 MNPs) versus time up to 10 minutes at 400 A current and 265 kHz frequency is shown in **Figure 8.5**. Heating ability of each sample increases with time and rise of temperature is high below 5-6 minutes.

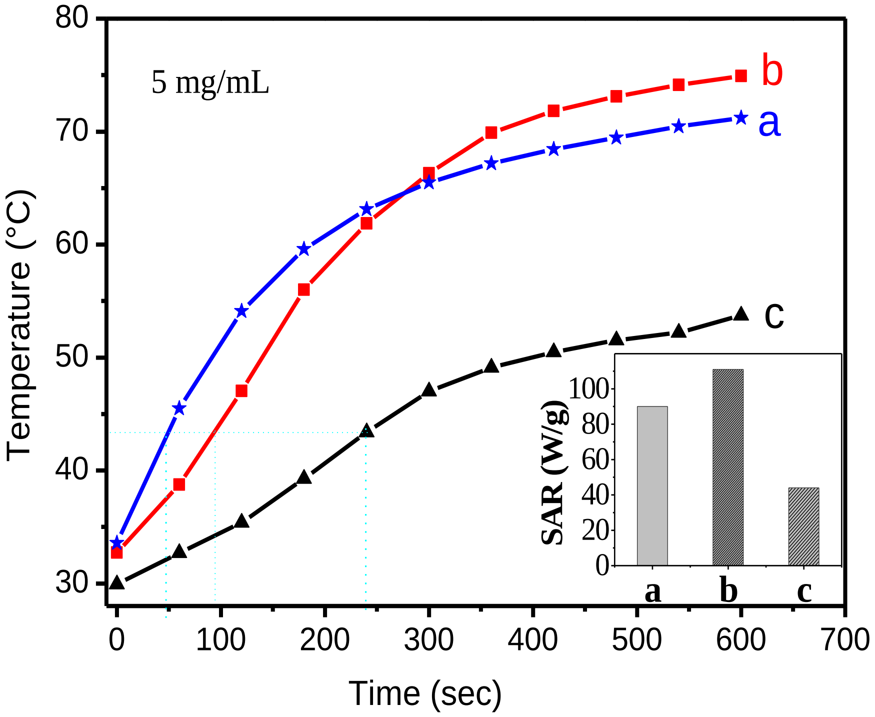

Figure 8.5: Temperature achieved by (a) Fe_3O_4, (b) Fe_3O_4-SiO_2 -80 and (c) Fe_3O_4-SiO_2 -100 MNPs. Here 5 mg of MNPs is dispersed in 1 mL of water (Applied field = 400 A, *f* = 265 kHz). Inset shows the SAR values.

Temperature attained by Fe_3O_4 MNPs, Fe_3O_4 -SiO_2-80 and Fe_3O_4 -SiO_2-100 are 71, 75 and 53 °C respectively in 10 minutes. Magnetic field (H) is fixed at 400 A (335 Oe). At the beginning of the experiment, the Fe_3O_4 MNPs show a fast rise of temperature, but after 5 min the dispersed particles start to aggregate and settle down and thus tend to saturate the temperature achieved till 10 min. In the case of Fe_3O_4 -SiO_2-80 there is a steady increase of temperature, slightly lower than that of Fe_3O_4 MNPs (in less than 5 min) due to the decrease in amount of Fe content per 1 mL of solution. However after 5 min, Fe_3O_4 -SiO_2-80 particles still continue to heat up since the SiO_2 coating helps in preventing agglomeration and Brownian motion of particles is still continuing, as a consequence, Brownian motion is helping in the heat generation.

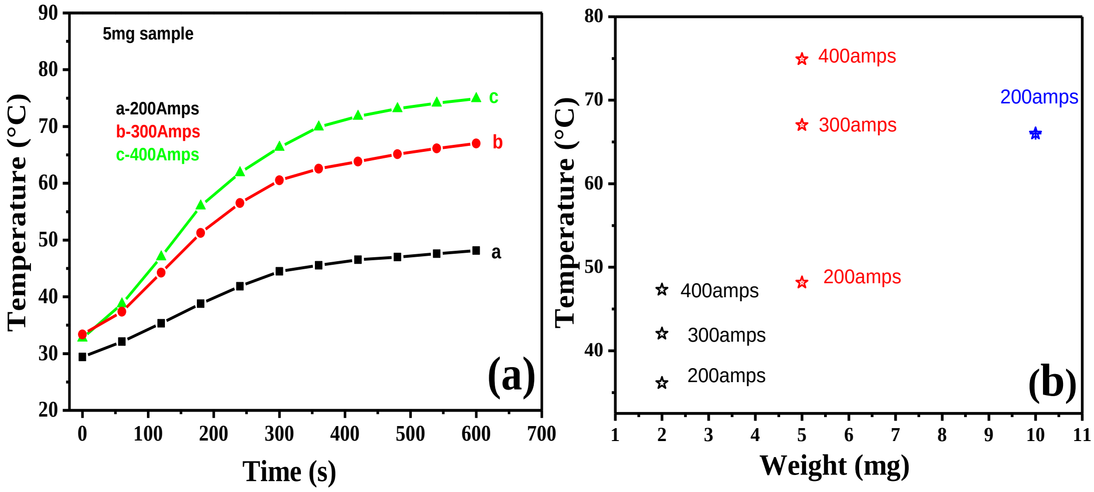

Figure 8.6: Temperature achieved by (a) 5 mg of Fe_3O_4-SiO_2-80 in 1 mL of water at different applied currents (200-400 A) with time and (b) that by 2-10 mg of sample in 10 minutes at different applied currents (*f* = 265 kHz).

The temperatures achieved by 5 mg of Fe_3O_4 -SiO_2 MNPs prepared at 80 °C versus time at different currents of 200, 300 and 400 A are shown in **Figure 8.6(a)**. With increase of current from 200 to 400 A, the temperature increases from 47 to 75

°C.The temperatures achieved by Fe_3O_4 -SiO_2 -80 versus concentration at different currents of 200, 300 and 400 A for 10 min are shown in **Figure 8.6(b)**. Even 2 mg of the sample could achieve the hyperthermia temperature (i.e., 47 °C) at 400 A; 5 and 10 mg of the samples can achieve the temperature of 48 and 67 °C respectively even at 200 A, which is more than hyperthermia temperature. On increasing the concentration, the hyperthermia temperature of 43°C was attained much faster.

In an earlier work by Runa et al., [480] the temperature achieved by oleic acid coated Fe_3O_4 MNPs was around 37 °C and that of polyethylene glycol (PEG) coated Fe_3O_4 MNPs was 36 °C (when a current of 400 A was applied to 5 mg of the sample for 10 min) which was below the hyperthermia temperature required, and to achieve the required temperature they needed an applied current of 550 A and 10 mg of the sample. Increase in temperature indicates that the magnetic field experienced by the Fe_3O_4 MNPs increases. Another work by Neena et.al., [201] when they used 10 mg of the oleic acid capped sample (MN-OA) (current of 400 A, 265 kHz) could achieve hyperthermia temperature in 3 min.

While in the present work, the Fe_3O_4 -SiO_2-80 sample achieves the required temperature of 43 °C within 2 min with 5 mg of the sample under the same conditions of 400 A current, and AC frequency of 265 kHz. Even Fe_3O_4-SiO_2-100 sample achieved the required temperature within 5 min showing that silica coating enhances the heating efficacy (**Figure 8.6**).

Table 8.1: SAR values obtained from Figure 8.5 for Fe_3O_4-SiO_2-80 and Fe_3O_4-SiO_2-100 MNPs and their comparison with the reported values.

Sl No:	Sample Name	Applied field	Frequency	SAR (W/g)	References
1	Fe_3O_4–OA-MN	335 Oe	265 kHz	33.5	[116]
2	Fe_3O_4-PEG-MN	335 Oe	265 kHz	28.3	[116]
3	MN-OA (0.5)	335 Oe	265 kHz	45	[201]
4	Glycine coated MNPs	385 Oe	250 kHz	77	[481]
5	Peptide coated MNPs	335 Oe	265 kHz	146.7	[482]
5	Fe_3O_4-SiO_2 -80	335 Oe	265 kHz	111	Present work
6	Fe_3O_4-SiO_2 -100	335 Oe	265kHz	44	Present work

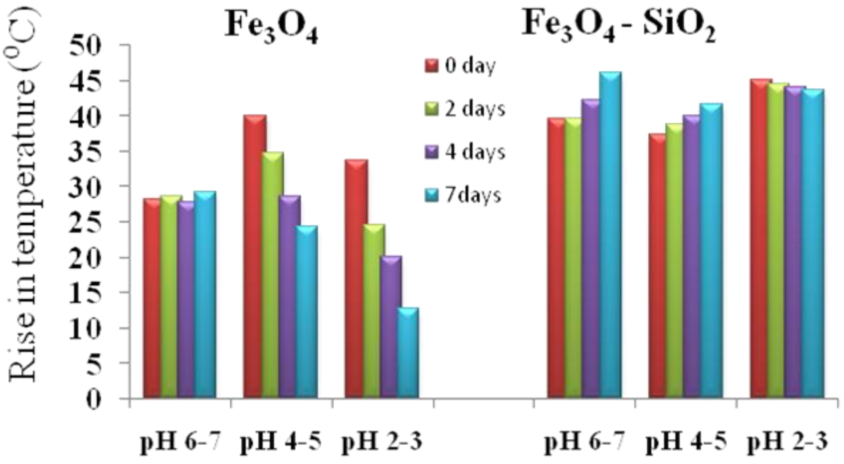

Figure 8.7: Rise in temperature achieved by Fe_3O_4 and Fe_3O_4-SiO_2 at different pH (2 – 7) over a period of 7 days. Increase in temperature above room temperature is observed for 2 mg of sample for a period of 10 min at 400 A and 265 kHz.

Leaching experiments were performed on Fe_3O_4 and Fe_3O_4 -SiO_2-80 at varying pH from 2 to 7. Uncoated Fe_3O_4 samples showed leaching behavior at acidic pH (2-4) over a period of time, while in the case of Fe_3O_4 -SiO_2-80 no leaching of Fe ions is found even at pH 2 over a period of 168 h. Thus leaching experiments showed the stability of the coated particles over the uncoated ones making it more useful over a wide range of pH (**Figure 8.7**). The hyperthermia temperature is observed for 10 min at 400 A and 265 kHz.

When highly dispersed magnetic nanoparticles are subjected to applied AC magnetic field AMF, the magnetic particles can experience a self-heating due to hysteresis loss, relaxation loss and eddy current [225, 242]. Theory of heat generation is given in the experimental section of hyperthermia (Section 2.4).

The specific absorption rate (SAR) per Fe_3O_4 content is calculated from slope in **Figure 8.5** (values are given in **Table 8.1**) and the values for Fe_3O_4 -MNPs, Fe_3O_4-SiO_2-80 and Fe_3O_4-SiO_2-100 are 90, 111 and 44 W/g, respectively calculated at 400 A (335 Oe or 27 kA/m). The inset of **Figure 8.6** shows the bar diagram of SAR values of samples. The SAR value (111 W/g) obtained from Fe_3O_4-SiO_2-80 is comparatively higher than the reported ones (**Table 8.**1). The increase in SAR value of the Fe_3O_4-SiO_2 MNPs prepared at 80 °C as compared to the uncoated sample may be due to the increase in Brownian contribution to hyperthermia. In addition to the applied magnetic field, SAR is also dependent on magnitude of frequency and physical properties of magnetic particles (magnetization, particles size, size distribution and hydrodynamic radius of particles) [483, 484].

8.2.3. Cyto-combatibility studies

The cyto-compatibility is investigated using sulfo-rhodamine (SRB) assay to evaluate whether these samples have any deleterious biological properties, for further in-vivo use. SRB assay shows that more than 90 % of primary fibroblasts (L929) and cancer cells (HeLa) were viable even after 24 h incubation with 0.015-1 mg/mL of coated and bare magnetic nanoparticles (**Figure 8.8**).

Thus, the viability of cells is not affected by the mere presence of Fe_3O_4 -SiO_2 MNPs, registering normal growth in the cells, suggesting that these samples are biocompatible and do not have toxic effect for further in-vivo use. In addition, the quantitative estimation of heat generation of nanoparticles within the cell lines has been evaluated to understand the specific details of thermal therapy for real applications.

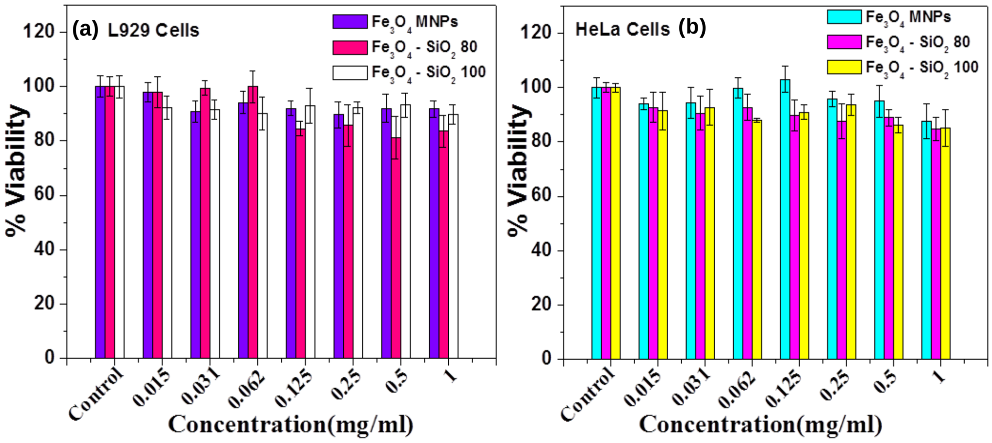

Figure 8.8: The percentage viability of (a) L929 and (b) HeLa cells treated with different types of nanoparticles (Fe_3O_4 MNPs, Fe_3O_4-SiO_2-80 and Fe_3O_4-SiO_2-100) at concentration range 0.015 – 1 mg/mL. Error bar indicates standard deviation (n = 3).

The heating efficiency of the particles is estimated by treating HeLa cells under the exposure of AMF, in the presence of 2 mg of the coated and uncoated particles. It is shown that the heating efficacy of the Fe_3O_4 -SiO_2 synthesized at 80 °C is highest as compared to the 100 °C prepared and uncoated particle (**Figure 8.9**, **Figure 8.10**). No alteration of cellular morphology (i.e., morphology of treated cells is similar to control cells) is observed in the presence of Fe_3O_4-SiO_2 MNPs (typical photographs of HeLa cells for control (untreated), Fe_3O_4 MNPs and Fe_3O_4-SiO_2 treated HeLa cells after 24 h incubation at 2 mg/mL of nanoparticles are shown in **Figure 8.10 (a-f)**.

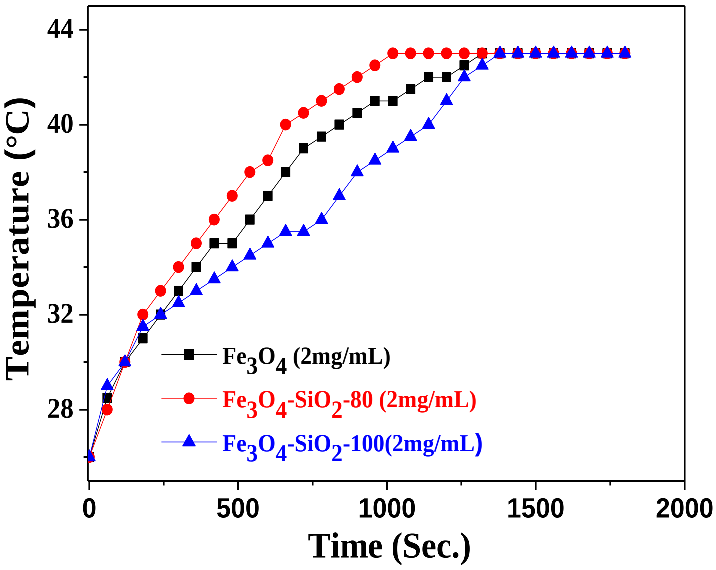

Figure 8.9: The heating efficiency of 2 mg/mL of different MNPs treatment on Hela cells with induction heating. Cells are treated with Fe_3O_4 MNPs, Fe_3O_4-SiO_2-80 and Fe_3O_4-SiO_2-100 (Applied current = 400 A, *f* = 250 kHz, .t = 10 min).

The temperatures achieved by the uncoated Fe_3O_4 MNPs, Fe_3O_4 -SiO_2-80 and Fe_3O_4 -SiO_2-100 at t = 1000 sec as shown in **Figure 8.9**are 41, 43 and 39 °C, respectively.. The uncoated magnetic particles in the presence of AMF showed 15% decrease in cell viability whereas decrease of 42% and 22% viability are found in the case of Fe_3O_4 -SiO_2.80 and Fe_3O_4 -SiO_2-100, respectively as compared to those in the absence of AMF (**Figure 8.11**).These results were further supported by a decrease in cell number as visualized by optical microscopic images (**Figure 8.10**)

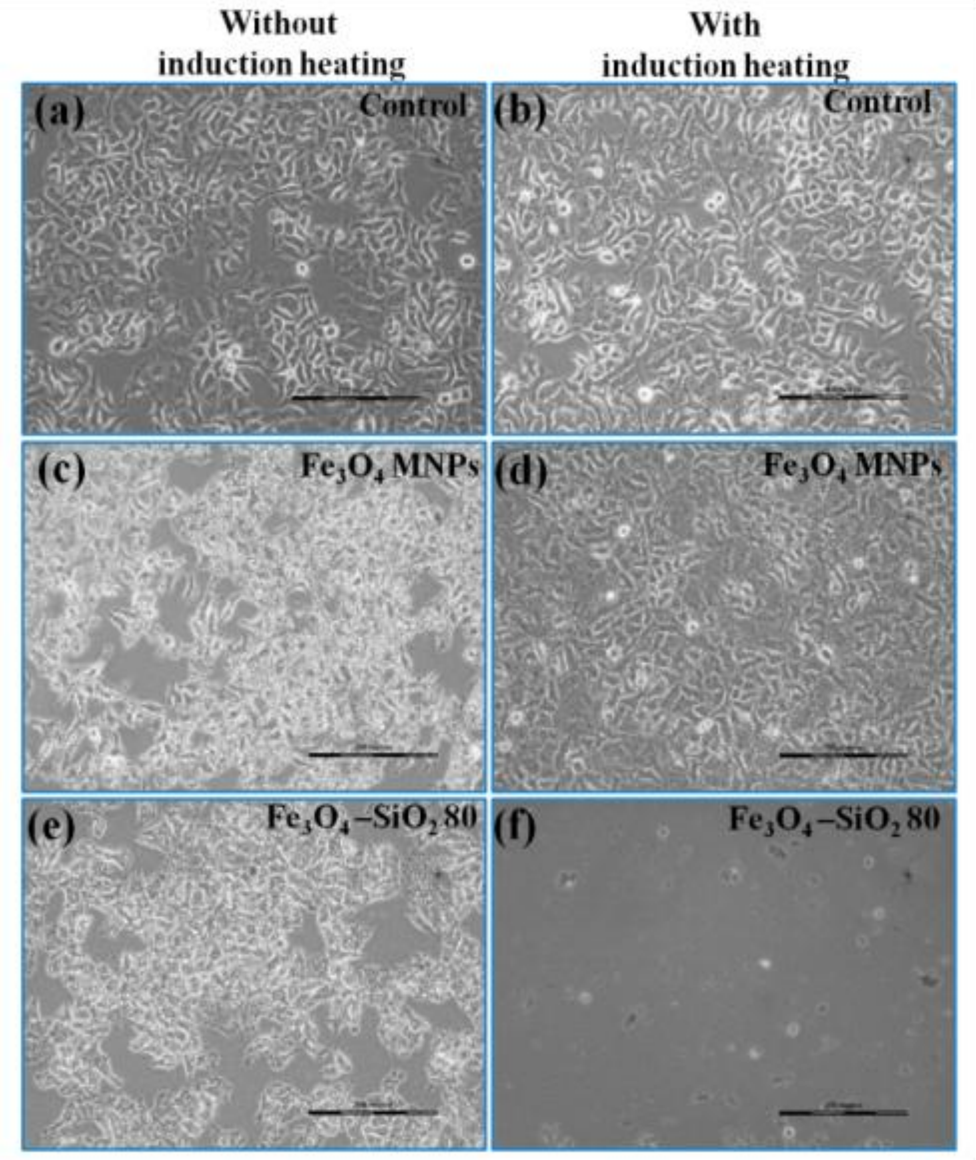

Figure 8.10: The effect of different MNPs treatment on morphological alterations in HeLa cells with or without induction heating. Untreated control (a-b), cells treated with Fe_3O_4 MNPs (c-d), Fe_3O_4-SiO_2-80°C (e-f) were observed under optical microscope. (2 mg/mL of sample at applied current = 400 A, *f* = 250 kHz, t = 10 min, Scale bar = 200 µm).

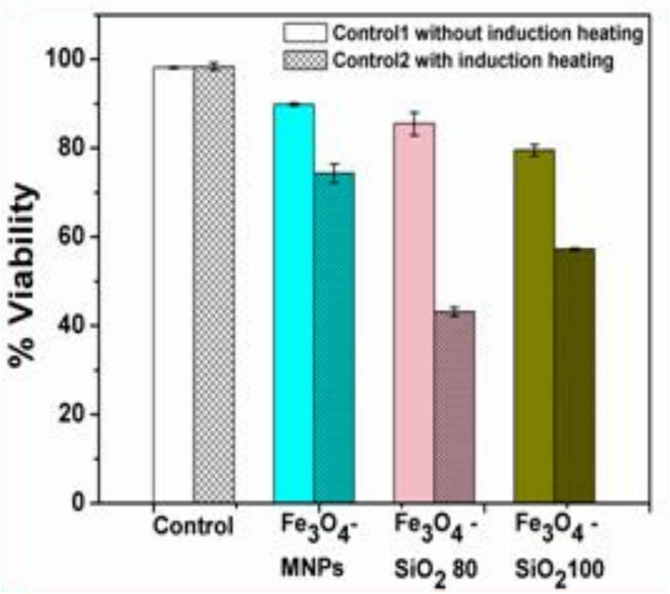

Figure 8.11: The percentage viability of HeLa cells treated with 2mg/mL of different types of MN for 2 h followed with and without induction heating. (Applied current = 400 A, *f* = 250 kHz, t = 20 min).

From these images of cancer cells treated with 2 mg of MNP and AMF (MN + Heat), it is clearly evident that significant death of cells might have occurred via apoptosis. However, further investigations are required to understand the exact mechanism of cell death by MNP under exposure of AMF. From the above results it is clear that Fe_3O_4-SiO_2 synthesized at 80 °C is a potential material in terms of good colloidal stability, high crystallinity, biocompatibility, and high heating efficiency under the exposure of alternating magnetic field.

8.3. Summary

The present work investigates the effect of surface coating on specific absorption rate (SAR) under alternating magnetic field. Core- shell Fe_3O_4-SiO_2 magnetic nanoparticles have been synthesized using one pot synthesis procedure. The optimization of shell thickness is done by varying the preparation temperature, and the products were evaluated for their heating efficiency in water and with cells. The sample prepared at optimized temperature of 80 °C showed highest SAR values of 111 W/g. Fe_3O_4-SiO_2 MNPs has better chemical stability over bare Fe_3O_4-SiO_2 MNPs in pH 2-7. Biocompatibility of the Fe_3O_4-SiO_2 MNPs is evaluated in in-vitro by assessing their cytotoxicity in human cervical cancer cells (HeLa cells) using sulforhodamine B assay. These results show an optimized synthesis procedure for magnetic nanoparticles coated with silica for high-performance hyperthermia applications.

Chapter 9

Polyphosphate grafted nano-magnets for therapeutic applications

Water-dispersible polyphosphate-grafted Fe_3O_4 nanomagnets for cancer therapy
Jerina Majeed, K. C. Barick, Neena G. Shetake, B. N. Pandey, P. A. Hassan and A. K. Tyagi
RSC Adv., 2015, 5, 86754-86762.

9.1. Introduction

Over the last few decades, significant attention is focused on magnetic nanoparticles as potential tool for biomedical applications such as drug delivery, thermal treatment (magnetic hyperthermia) or as a contrast agent for magnetic resonance imaging (MRI) [485, 486]. In particular, iron oxide nanoparticles (IONPs) have received extensive attention due to their unique properties like superparamagnetism and low toxicity. Practical in vivo usage of these particles requires size below 100 nm as well as colloidal stability and biocompatibility in the physiological media. However, the IONPs prepared by conventional co-precipitation method even though have an average size of 10 nm, they are polydispersed and tend to aggregate and adsorb proteins quickly in water or physiological media [487]. In addition, for most biomedical applications, the first significant challenge is to avoid unwanted uptake of iron oxide nanoparticles by the reticuloendothelial system (RES). To overcome the above drawbacks iron oxide nanoparticles are surface engineered often by coating with various bioactive organic and inorganic functional groups like siloxanes [488, 489], phosphonates [490, 491], phosphates [492] and long chain hydrophilic polymers such as polyethylene glycol (PEG) [493], polyethylene oxide (PEO) [494], proteins [495], and dextran [496]. These bioactive layers not only stabilize MNPs but can also provide them with functional terminal groups that can be used for attaching targeting agents, as well as drug molecules.

The main drawback of the surface engineered MNPs currently in use is that the polymer coatings are not covalently bound to the MNP surface and will easily be detached. Moreover, the polymer coatings further cause a significant increase in the overall hydrodynamic diameter of the particles and thus affecting their bio-distribution as well as clearance. Thus further functionalization with targeting ligands increases the complexity. The polymer shell around the MNP core also has been reported to influence the magnetic relaxivity dramatically [497]. Thus, covalent attachment of nonpolymeric layers that would improve the stability of MNPs under physiological conditions without affecting particle size or undermining magnetic properties (e.g., relaxivity and saturation magnetization) while still providing sites for attaching targeting ligands (e.g., antibodies) would be useful. Recent work with organosilanes, carboxylate- and phosphonate-anchored layers grafted on MNPs are proven to be better anchoring groups without adversely affecting their properties The literature on the use of bioactive phosphonates and phosphates on nanoparticle surfaces is limited. Various groups report a strong interaction between the inorganic core and the phosphonic moiety [498, 499], and the most interesting moiety seems to be triphosphonate a class of polyphosphates. In a review article Rao et al. [500] have demonstrated the essential roles of poly phosphates in the virulence of major diseases, such as dysentery, tuberculosis, and anthrax, as well as in apoptosis, in the proliferative aspects of cancer, in osteoporosis, and in aging. Sodium tri Polyphosphate (STPP) is also used as a preservative for food and also as a polyanioncross-linker in polysaccharide based drug delivery [501]. Chitosan/tripolyphosphate nanoparticles (CS/TPP) have been used as an alternative to chitosan to encapsulate peptides, proteins, pDNA and siRNA[502-504]. Recently, Yee *et al.* revealed the adsorption of alkane phosphonic acids on the surface of amorphous ferric oxide particles through two possible bonding schemes, i.e. either by one O or by both O atoms of the phosphonate group binding onto the surface [505]. Similarly, Sahoo*et al.* reported the formation of substantial P-O-Fe bonding on the surface of alkyl phosphonates and phosphate coated Fe_3O_4 nanoparticles [492]. Lamanna et al. [506] developed dendrons having phosphonate head groups and grafted them to the surface of iron oxide nanoparticles, which were shown to have enhanced MRI contrast properties compared to polymer-coated iron oxides nanoparticles. In addition, these functionalized phosphonate and phosphate seems to have an acceptable biocompatibility and thus, they can serve as potential substitutesfor fatty acids as coating agents for metal oxide surface [492, 507]. The oral toxicity limit of STPP is > 1000 mg $kg^{-1}$and, for this reason, its use as a stabilizer in the generation of nanoparticles is safe. However, the use of STPP as a stabilizer in preparation of aqueous-stable Fe_3O_4 nanoparticles is scantily reported.

Traditional chemotherapeutic agents developed over the past 50 years have contributed significantly to reductions in cancer mortality, but these drugs cause adverse reactions such as liver and kidney damage [508], hair loss [509], nausea, and cardiac toxicity [510, 511]. Many of these side effects stem from the systemic nature of standard drug administration and the lack of drug specificity toward tumorigenic cells [512]. Ultimately, a system that is capable of simultaneously lowering effective dose while increasing cytotoxic efficacy would alleviate some of these side effects. The combination of both thermal and chemotherapeutic agents is an especially encouraging approach to optimizing cancer therapy [190, 202, 513-515]. Hyperthermia combined with certain chemotherapeutic drugs, such as alkylating agents, often results in super-additive or synergistic effects that are greater than the projected sum of the two treatments alone [516]. This permits the design of novel combinatorial therapy in which the partnership between the nanoparticle hyperthermia and chemotherapeutic agents can provide effective treatment with minimal side effects. Thus, there is a emergent interest in developing biocompatible magnetic nanocarriers with suitable surface functionality for intracellular drug delivery and hyperthermia.

Recently, Sharma et al. explored the SHMP anchored magnetic nanoparticle (PAMP) for their high loading affinity for DOX as well as self-heating capacity [517]. These nanoparticles exhibited acid-triggered DOX release behavior and significant therapeutic efficacy towards cancer cells. Herein, a novel polyphosphate grafted Fe_3O_4nanomagnets (PPNM), for DOX delivery through a pH-labile linkage between DOX and polyphosphate is investigated. The developed PPNMs showed high colloidal stability, magnetic responsivity, and specific absorption rate. Besides synthesis and detailed characterization, the drug release profile and in vitro biomedical assessment of the PPNM are also addressed in this chapter. Because the PPNM is water-soluble and can directly serve as nanotherapeutics for sustained DOX delivery without the assistance of external reagents, it may potentially be more relevant to clinical applications in cancer treatment.

9.2. Results and discussion

9.2.1. Characterization of nanoparticles

Polyphosphate grafted Fe_3O_4 nanomagnets (PPNM) were synthesized by one pot co-precipitation method of Fe^{2+} and Fe^{3+} ions in basic medium, and their nanocrystalline features are investigated in detail by XRD, TGA, TEM and FTIR analysis. The crystal structure of the iron oxide core has been characterized by X-ray diffraction. The XRD patterns of pure and polyphosphate grafted nano-magnets are shown in **Figure 9.1**. As-prepared samples are well crystalline exhibiting face centered cubic structure with space group Fd3m, and all peaks are matched with JCPDS Card No. 19-0629, a = 8.396 Å. No additional impurity phases are identified. The diffraction pattern peaks are indexed to data with corresponding (hkl) planes between 10–70°. The average crystallite sizes calculated by using Scherrer equation for as-prepared pure and polyphosphate grafted nano-magnets are found to be ~10 and ~11 nm, respectively. The lattice parameter obtained was equal to 8.378Å, is very close to the reported value of magnetite (JCPDS Card No. 19-0629, a = 8.396 Å). There is no substantial change in lattice parameters and XRD patterns when magnetite core is grafted using polyphosphate shells.

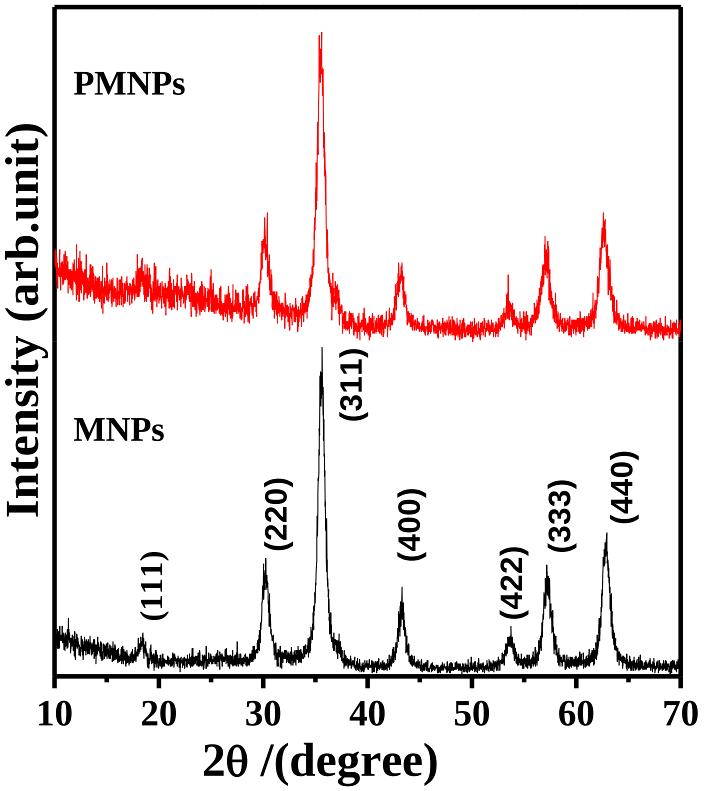

Figure 9.1: (a) XRD pattern of Pure (MNPs) and Polyphosphate grafted nano-magnets (PPNMs).

TEM images (**Figure 9.2(a)**) of PPNM clearly show the formation of almost spherical Fe_3O_4 nanoparticles of size about ~10 nm. The selected area electron diffraction pattern (**Figure 9.2(b)**) also confirmed the high crystallinity of PPNM. It can be indexed to crystalline reflections, from planes like (220), (311), (400), (422), (511) and (440) of cubic inverse spinel Fe_3O_4 structure, which is consistent with the XRD result. HRTEM, indicated that the lattice spacing (d_{hkl}) of Fe_3O_4 is 2.52 Å (**Figure 9.2(b))** which corresponds to the d spacing of the (311) plane.

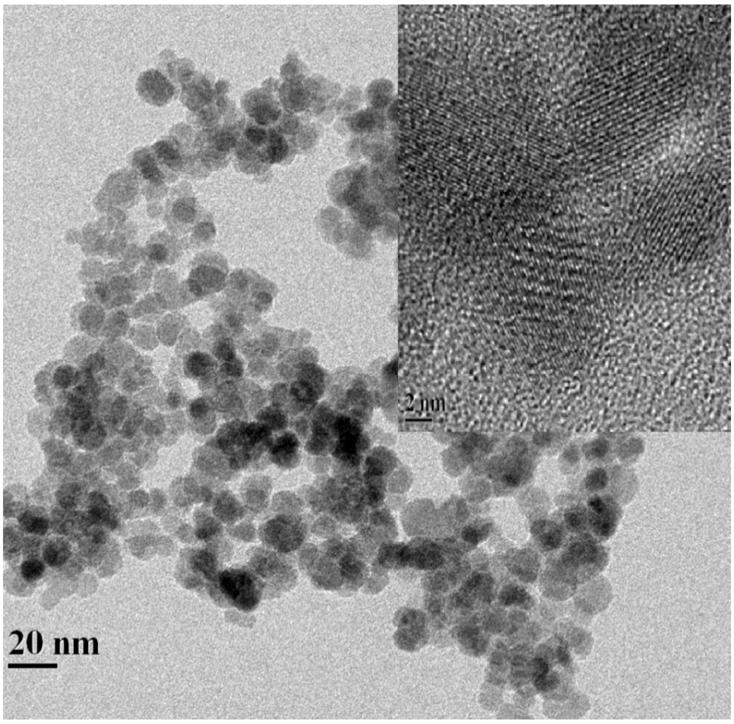

Figure 9.2: (a) TEM and (b) HRTEM image of PPNM.

FTIR spectroscopy is a useful tool to identify the functional groups present. In the present case, it is applied to find out whether there are any vibrational bands owing to the presence of the phosphate group on MNPs and to confirm the surface capping of the MNPs by STPP. FTIR spectra of STP, and PPNM and their peak assignments are shown in **Figure 9.3,** which indicates that the IR bands for pure STPP are well resolved, while those of the PPNM are rather broad and less intense.The intense peak at around 570 cm^{-1} in PPNM can be attributed to the Fe-O stretching vibrational mode of Fe_3O_4. The broad peaks observed in the range of 800 to 1250 cm^{-1} with band at 895, 915, 1026, 1087 and 1167 cm^{-1} in PPNM can be assigned to P-O$^-$ vibrations of STPP [518, 519]. Further, the IR bands observed at around 1400 cm^{-1} and shoulder at 710 cm^{-1} can be associated with P=O and P-O-P stretching vibrations, respectively [520]. These results clearly suggested the successful anchoring/grafting of phosphate groups of SHMP onto the surface of Fe_3O_4 nanoparticles. The solid bands observed at ∼3430 and 1630 cm^{-1}correspond to the stretching and bending vibrations of water (H_2O) on the surface of the particles.

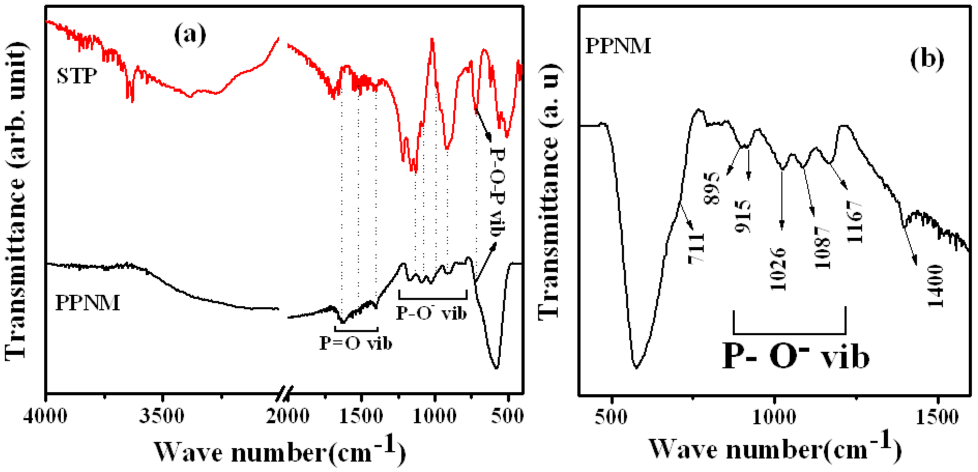

Figure 9.3: (a) FTIR spectra of STPP and PPNM with their peaks assignments and (b) expanded FTIR spectrum of PPNM in the range of 400 – 1600 cm^{-1}.

Thermogravimetric analysis curves of PPNMs are shown in **Figure 9.4**. The thermogravimetric analysis of the nanomagnets revealed about 5–6% weight loss when heated between room temperature and 400 °C. A three-phase decomposition profile is apparent for phosphate grafted NMs, an initial weight loss of about 2%

below 100 °C is associated with the removal of residual water and surface hydroxyl group present in particles. The second and third weight loss steps (3.5%) was observed due to decomposition of polyphosphate moieties present on the surface at around 100-300 °C. The two stage of mass loss appearing during decomposition of phosphate moieties, which means that the adsorption of phosphate molecules is not in a single layer.

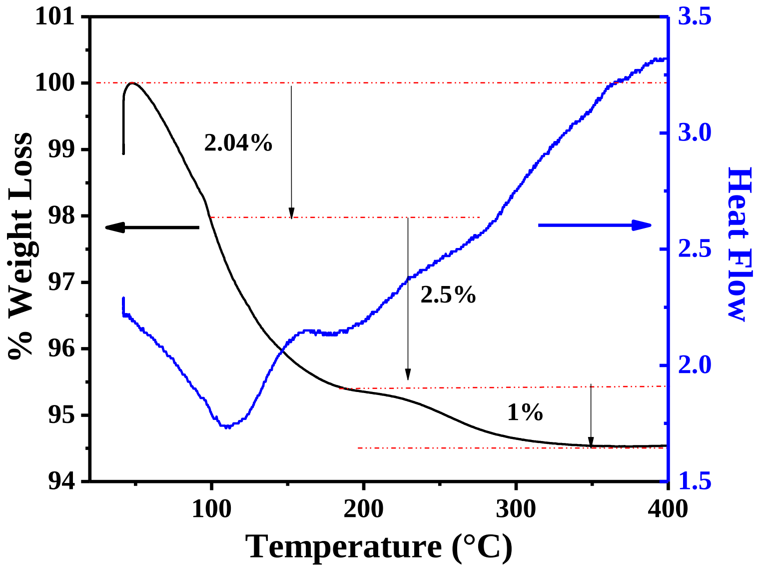

Figure 9.4: (a) TGA curve of polyphosphate grafted nanomagnets samples in argon with a scanning rate of 10 °C min-1 up to 400 °C.

After the structural and morphological analysis confirming the presence of polyphosphate moieties on the surface of the nano-magnets, it is important to check the colloidal stability for their practical applications. The colloidal stability of the nano-magnets was determined using zeta potential measurements and UV absorbance spectra. The variation in the zeta-potential of PPNM suspensions with varying pH values (0.05 mg/ml) are depicted in **Figure 9.5.** From Zeta potential measurements, no isoelectric point (pH_{zpc}/pH of zero-point charge) were observed in the pH range of 2-

12 and found that the particles are negatively charged even at highly acidic pH. Moreover, the high negative value of these particles at pH > 4 makes these particles colloidally stable. The high negative charge on these particles arises from the grafting of phosphate groups on MNPs.

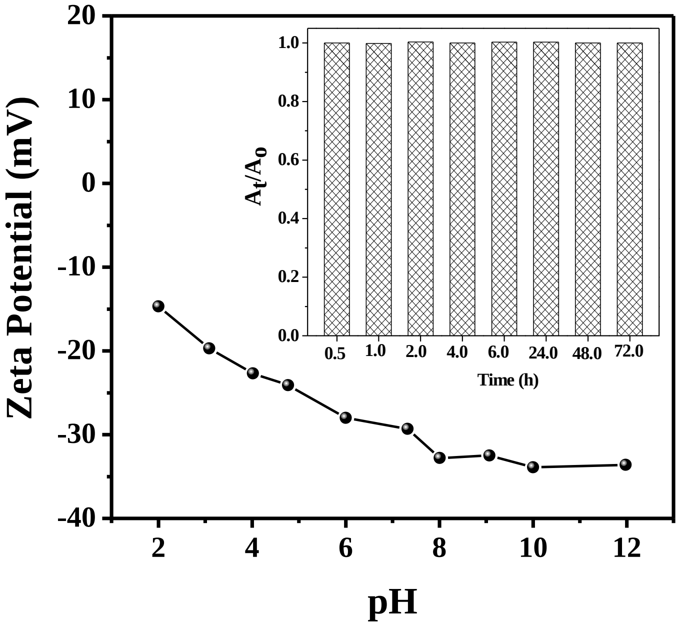

Figure 9.5: Variation in the zeta-potential of PPNM suspensions at varying pH values (0.05 mg/ml). Inset shows normalized UV absorbance (A_t/A_0) vs. time plot of PPNM (0.05 mg/ml) at wavelength of 350 nm in aqueous (A_t = absorbance at time't' and A_0 = Absorbance at t=0).

The colloidal stability of the PPNM was also assessed from the changes in light scattering intensity as well as extinction changes with time. The insignificant change in absorbance of PPNM suspensions in aqueous media even up to 72 h indicates their good colloidal stability (inset **Figure 9.5**). These nanoparticles are hydrophilic in nature due to the solvation of or hydrogen bonding assosiation of surface functional groups and water. In addition, the electrostatic repulsive force originating from the ionization of the surface groups provide additional stability to the particles. Furthermore, the negative zeta-potential of PPNM at physiological medium could decrease the possibility of their combination with hemoglobin, which would play a significant role in improving the stability and blood compatibility.

In order to assess the potential of polyphosphate grafted nano-magnets in targeted drug delivery and hyperthermia, further investigations were done on their magnetic and thermo-magnetic properties. The field-dependent magnetization plots of PPNM at 300 K and 5 K are shown in **Figure 9.6**. These nano-magnets exhibit superparamagnetic behavior without magnetic hysteresis and remanence at 300 K, whereas ferromagnetic behavior with a coercivity of about 80 Oe and a remanence of 11.85 emu/g is observed at 5 K (**Figure 9.6**).

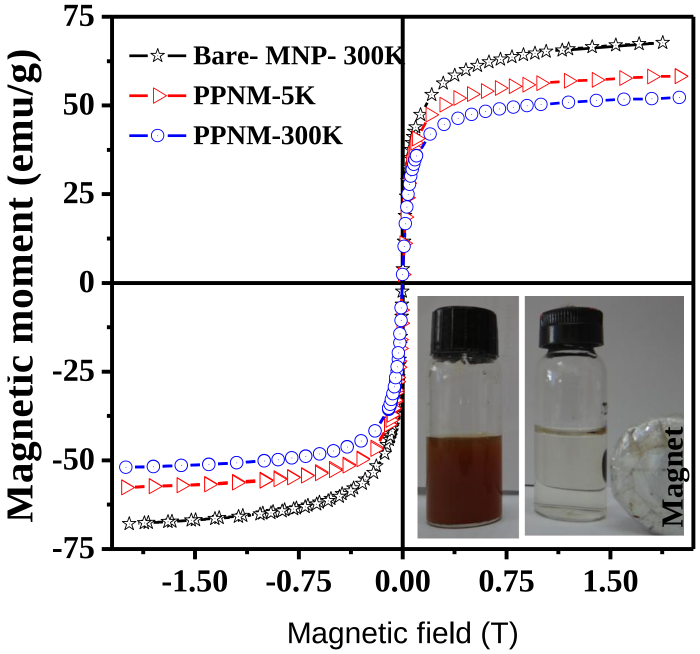

Figure 9.6:Field dependent magnetization plots of PPNM at 280 K (inset shows the photographs of PPNM in presence and absence of permanent magnet of field strength ~2.5 kOe).

The appearance of the hysteresis loop at lower temperature points to the magnetic ordering of the sample at lower temperature. The transition from superparamagneticbehavior to ferromagneticbehavior below the particular temperature, i.e.,blocking temperature (T_B) is usually observed in MNPs [521]. The ZFC-FC plots (**Figure 9.7**) shows that the blocking temperature (T_B) of the PPNM is 75 K at an applied field of 400 Oe. However, T_B is found to decrease with the increase of the applied field (**Figure 9.7**).

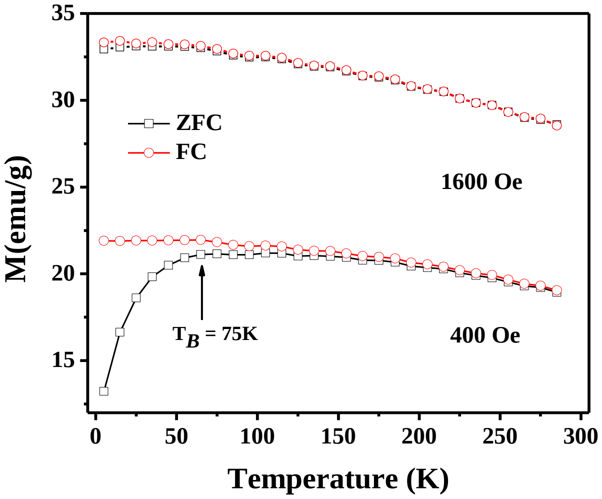

Figure 9.7:Field M vs. Temperature plots of PPNM at 400 and 1600 Oe and (ZFC-FC plot).

The magnetization values of PPNM were found to be 40.5 and 34.5 emu g^{-1}, at 6×10^{-4} Oe for 5 K and 300 K, respectively. The saturation magnetization of bulk Fe_3O_4 is 92 emu g^{-1} [479], which are much more than the PPNMs. The MNPs prepared by the similar route gave a saturation magnetization of 67emu/g. The magnetization in the case of PPNMs is reduced by 20 % as compared to the MNPs, although TGA showed a reduction of only 6% weight loss and ICP-MS showed a coating of ~15% STPP on to the surface. The magnetization of MNPs could be possibly arising from the clustering behavior of the uncapped MNPs, which will contribute to the increase in magnetization due to the exchange coupling and dipolar interaction among the surface ions [522]. Whereas in the case of PPNMs the presence of bulkier nonmagnetic polyphosphate group on the surface of MNPs, will suppress the contribution from exchange coupling as well as dipolar interactions among particles.

At room temperature, thermal energy (kT = 0.03 eV) can surpass the particle/crystalline anisotropic energy [523] of particles [524]. In the case of single-domain particles, the magnetization vector tends to align in a particular direction called the easy axis, which gives the minimum magnetocrystalline anisotropy energy (an energy barrier for free rotation of magnetic moment away from easy direction/axis).

When thermal energy overcomes the anisotropic energy KV, the magnetization vector can rotate to the opposite direction (0 → 180°) in a time scale of 10^{-8}–10^{-10} s. In such situation, particles exhibit superparamagnetic behavior because relaxation is so fast compared to the measurement time for VSM, i.e., 10^{-1} s. At zero applied magnetic field, domain rotation could not be detected by VSM, which led to zero moment. Further supported by the zero coercivity (Hc) value. When applied magnetic field increases, the magnetization vector of domain will try to align towards the field direction because thermal energy is dominated by applied magnetic field. This leads to an increase in blocking temperature with increase in the applied field.

9.2.2. Induction heating study

The effect of magnetic field strength and particle concentration on heating ability of PPNMs were evaluated. The magnetic field induced in the induction coil is propotional to current passing through the coil. The temperature *vs.* time plots of

PPNM suspension (**Figure 9.8)** showed a time-dependent gradual increase in temperature under AC magnetic fields for time up to 20 minutes. A magnetic field of 0.251 kOe at fixed frequency of 265 kHz was enough for raising the temperature of the magnetic suspension of 2.3 mg/ml to 41-43 °C within 20 min.

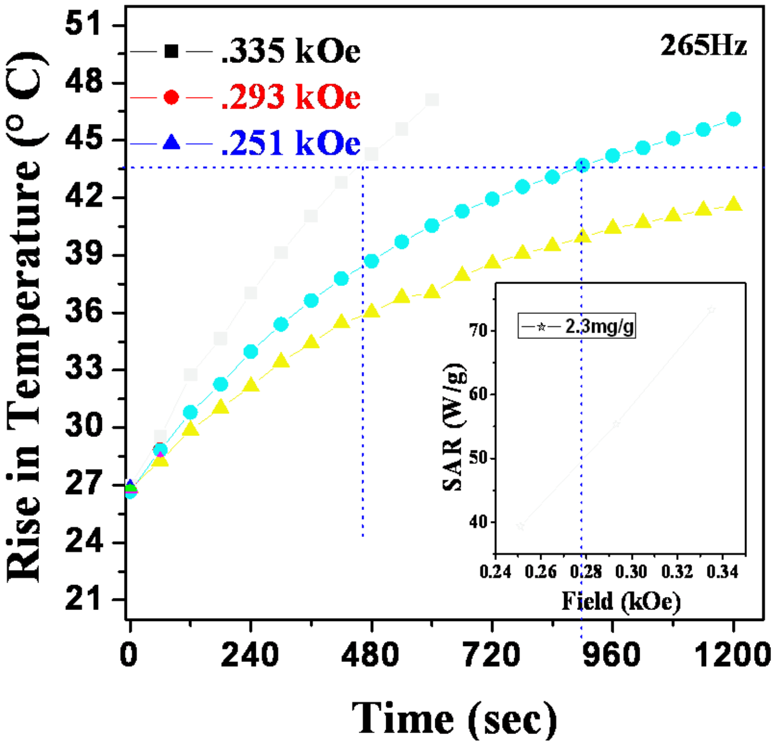

Figure 9.8:Temperature vs. time plots of 1 ml aqueous suspension of PPNM (2.3 mg/ml of Fe) at different applied field (inset shows the linear relationship between SAR and the applied AC magnetic field).

Further, the required hyperthermia temperature of 43 °C was achieved much faster with increasing field strength, which is apparent as the heat generation/dissipation (*P*) is proportional to the square of applied AC magnetic field. The temperature achieved by PPNM at different concentration and an applied field of .335 kOe for 20 min is shown in **Figure 9.9**. Even 1 mg of the sample could achieve the hyperthermia temperature (i.e., 41-43 °C) at 0.335 kOe within 20 min.; 0.64 and

2.3 mg of the samples can achieve the temperature of 38 and 47 °C respectively even at 0.335 kOe.

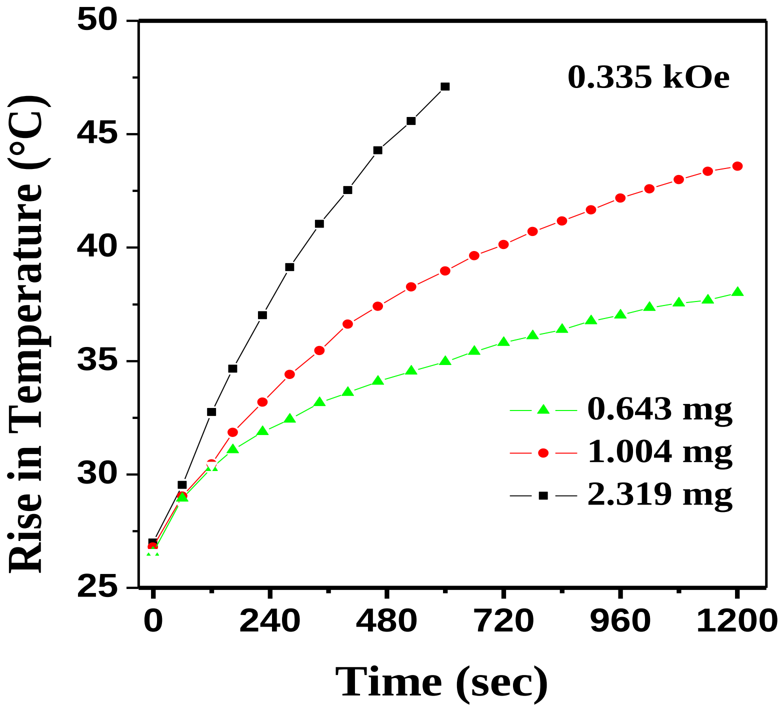

Figure 9.9: Temperature *vs.* time plots of 1ml of the aqueous suspension containing various amounts of PPNM at an applied field of 0.335 kOe.

Generally, ferrofluids undergo heat loss or power dissipation as a result of (1) Néels spin relaxation, Brownian rotation loss, (3) hysteresis loss and (4) Eddy current [242].

Susceptibility (χ) can be defined as the ratio of magnetisation M to the applied magnetic field H and in presence of AC field, it can be expressed as real (χ′) and imaginary (χ″) terms, of which the imaginary part is associated with the heat dissipation in the system. Heat-generation/dissipation is dependent on frequency and applied magnetic field. The dissipated thermal power per unit mass of magnetic material can be expressed in terms of the specific absorption rate (SAR), given by:

$$SAR = c\,\frac{\Delta T}{\Delta t}\frac{1}{m_{Fe}} \qquad ((9.1)$$

Where c is the sample specific heat capacity, (4.18 J g^{-1} K^{-1} as contribution from sample is negligible). ΔT/Δt is the slope of the time dependent temperature curve obtained at a particular field and weight of the sample, $M_{magn}$is the amount of magnetite or Fe in the 1 mL system.

The SAR values of PPNM were found to be 39.3, 52.4 and 73.5 W/g of Fe with an applied field of 0.251, 0.293 and 0.335 k Oe, respectively. As the SAR values and heat-generation/dissipation is dependent on frequency and applied magnetic field, direct comparison of SAR values can only be done for experiments performed at same frequency and field strength. The frequency and field independent power dissipation can be expressed as intrinsic power loss (ILP), i.e., [243]:

$$ILP = \frac{SAR}{H^2 f} \qquad ((9.2)$$

This equation is valid under frequencies of up to several MHz; provided the applied field strength H is well below the saturation field of the magnetic nanoparticles. Thus the ILP values obtained were 2.4, 2.43 and 2.46 nHm^2/kg with an applied field of 0.251, 0.293 and 0.335 keep, respectively for 2.3 mg/ml of the sample, which itself shows the normalization ineffective of the different applied field. Whereas, with increasing concentration, a decrease in ILP values, 3.9, 3.5 and 2.5nHm^2/kg was obtained with an applied field of 0.335 keep for 0.64, 1.004, and 2.3 mg/ml of the sample. This might be due to the reduction in Brownian and Neel contribution to hyperthermia. Brownian contribution decreases as the amount of the sample present per ml increases, Neel contribution decreases as there will be an increase in magnetic dipole-dipole interactions between nanoparticles in suspension as a result of increase in local concentration [481].

Table 9.1:Comparison between ILP of PPNMs with ILP of some commercial ferrofluids reported in literature.

Manufacturer	**Name**	**Coating**	**DLS Size (nm)**	**Crystallite size (nm)**	**ILP (nHm^2/kg)**
Chemicell	Fluidmag-D	Starch	42	9.8	1.31
Micromod	Nanomag-D-Spio	Carboxyl	91	11.8	3.12
Micromod	BNF-01908	Starch	108	7.7	0.35
Chemicell	Fluidmag-D	Starch	109	10	2.01
Chemicell	Fluidmag-D	Starch	160	9.6	1.41
Chemicell	Fluidmag-NC-D	Starch	177	9.5	1.31
Chemicell	Fluidmag-NY-D	Starch	212	9.6	1.53
Chemicell	Fluidmag-CMX	Carboxy methyl dextran	220	9.9	1.71
Micromod	Nanomag-D-Spio	Carboxyl	346	8.9	0.37
Micromod	BNF-02008	Carboxyl	512	7.6	0.16
Bayer-Schering	Resovist	Carboxy dextran	61	10.5	3.1
Micromod	BNF-01708	Carboxyl	130	7.1	0.15
Micromod	Nanomag-D-Spio	Carboxyl	84	11.2	2.31
Micromod	Nanomag-D-Spio	Carboxyl	165	8.3	0.23
Chemicell	Fluidmag-D	Starch	39	12.6	2.67
Micromod	BNF-01808	Carboxyl	129	8.2	0.17
This work	PPNM	Polyphosphate	44	10	2.4

The preeminent synthetic iron oxide particles reported in the literature to date were those by Hergt et al. [525] and Fortin et al. [526]. The former had a reported SLP parameter of 600 W/g at 11.2 kA/m and 410 kHz, while the latter had a SLP of 1650 W/g at H=24.8 kA/m and f= 700 kHz. The normalized ILP parameters for these samples are 11.7 and 3.8 nHm^2/kg, respectively. Further, Kallumadil et al. [243] compared the ILP of some commercial ferro fluids with different hydrodynamic sizes. The values are represented in **Table 9.1**. Comparing our results with that in literature shows that the ILP of PPNMs is comparable or even higher than ILPs of commercial ones with similar hydrodynamic sizes (**Table 9.1**).

9.2.3. Drug delivery studies:

These negatively charged surfaces of polyphosphate grafted NMs make it an attractive vehicle for the delivery of electrostatically bound drug molecules. DOX a cationic drug used in chemotherapy is chosen as a model to estimate the drug loading and release behavior of the PPNMs. Zeta-potential, DLS and fluorescence spectroscopic analysis were employed to investigate the binding of DOX with PPNMs. The variation in the zeta-potential is depicted in **Figure 9.10**. The variation in hydrodynamic radius and the fluorescence spectra of aqueous suspension of PPNMs with and without drug are shown in **Figure 9.11**and **Figure 9.12**, respectively. The zeta-potential of the PPNMs (100 μg/ml suspension) increased from −41.3 mV to–17.6 mV upon loading with an aqueous solution of 10 μg/ml of DOX. This change in surface potential can be attributed to the binding of cationic DOX with negatively charged nanomagnets through electrostatic interactions, thus partially passivating the surface.

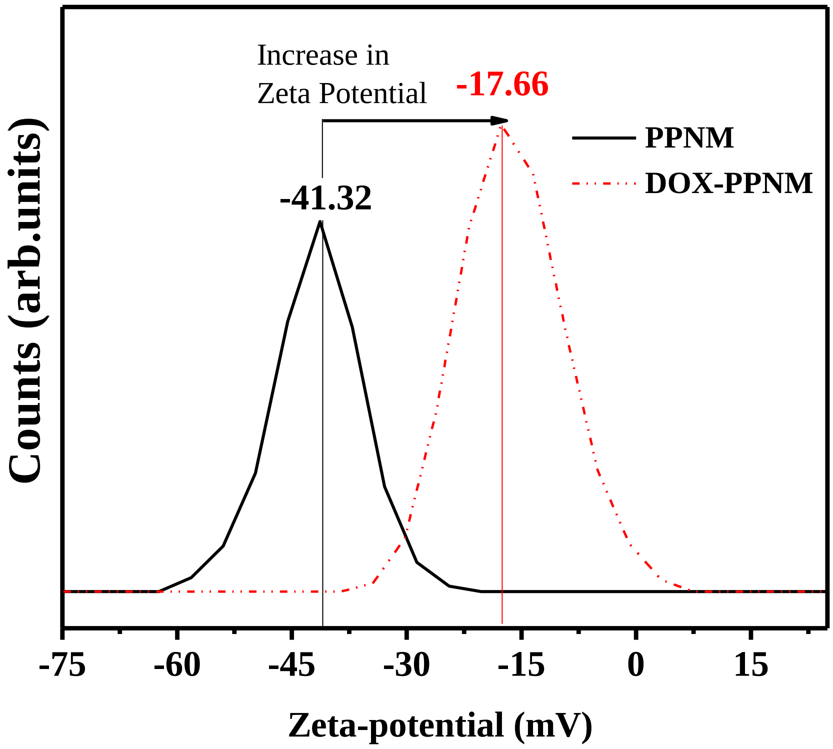

Figure 9.10:Zeta-potential of aqueous suspension of PPNMs and DOX-PPNMs.

These interaction was further proved by intensity weighted (z-average) hydrodynamic diameter measurements in DLS plot as shown in **Figure 9.11**. DLS measurements indicate a mono-modal distribution with mean hydrodynamic diameter of 43 nm and 236 nm (polydispersity index ~ 0.2) for PPNMs and DOX-PPNMS respectively. The larger hydrodynamic diameter of DOX- PPNMs as compared to PPNMs clearly indicates the loading of DOX on to the surface of PPNMs. It may be noted that the large shift in the average dimension by the adsorption of drug molecules is rather unexpected. This could rise from the effect of intra particle interaction on particle diffusion. Addition of the drug molecule decreases the intraparticle interaction and makes the particles amenable for aggregation, which leads to an increase in the apparent size of the suspensions.

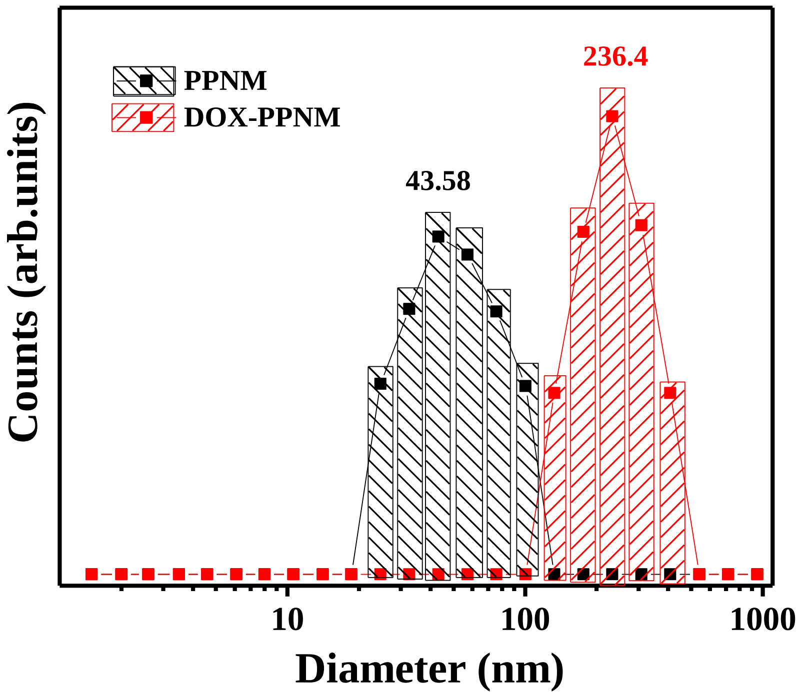

Figure 9.11:DLS plot of aqueous suspension of PPNMs and DOX-PPNMs.

The interaction of DOX molecules with PPNMs was also apparent from the variation in fluorescence intensity of the supernatant liquid after removal of DOX linked-PPNM through magnetic separation (**Figure 9.12**). The fluorescence intensity of supernatant liquid drops with increasing concentration of PPNM, due to increase in available surface area for drug adsorption. From the plot of loading efficiency versus concentration (inset of **Figure 9.12**) a strong dependence between weight ratio of PPNM to DOX is observed and a drug loading efficiency (w/w) of about 67% is achieved at PPNM to DOX weight ratio of 14 (no significant increase in loading efficiency is observed above this ratio).The affinity of DOX for negatively charged molecules has been the subject of numerous earlier investigations [207, 217, 533, 544].

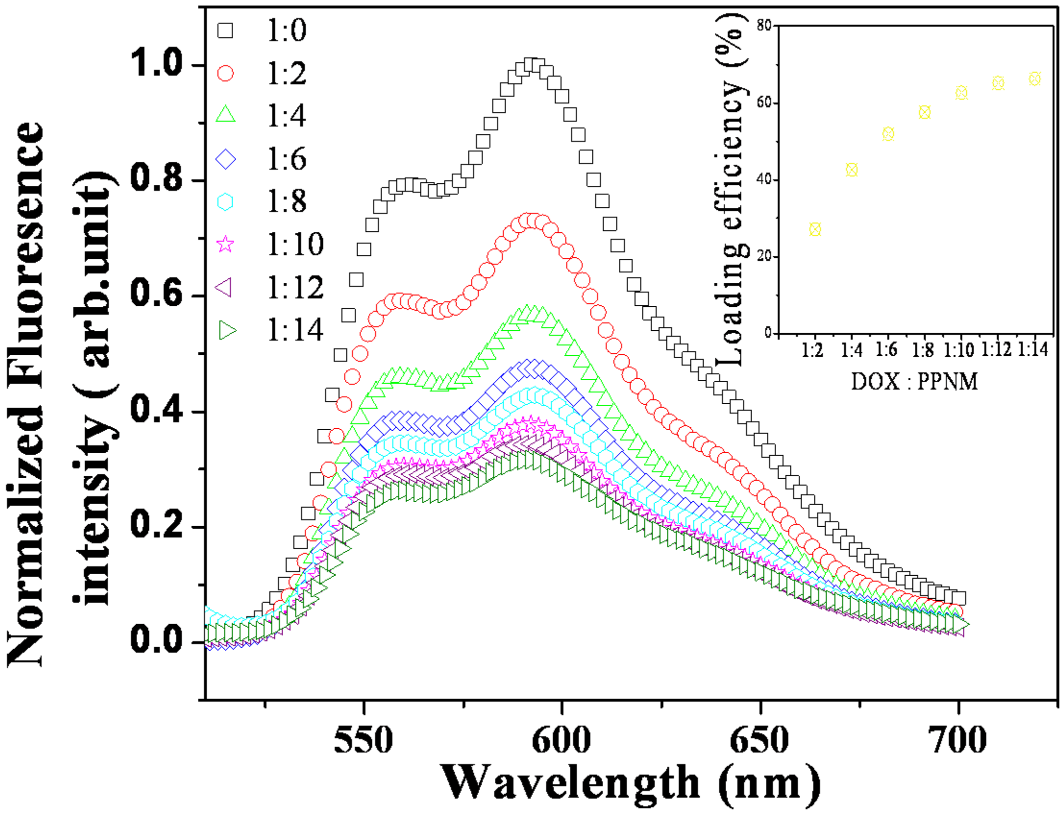

Figure 9.12: Fluorescence spectra of 1 ml aqueous solution of pure DOX (10 µg/ml) and after interaction with various amount of PPNM (inset of Figure 9.12 shows the loading efficiency of DOX onto PPNM surface after considering the washed drug molecules for calculations).

The release rate of DOX from loaded PPNM increased with decreasing environmental pH, such that 54 and 60.5% of the loaded DOX were released from the DOX-PPNMs within 48 h when stored in phosphate buffered saline (PBS) solutions of pH 5.0, and 4.0, respectively (**Figure 9.13**). Similar reports were found in literature [527-529] pH-triggered DOX release thus occurs across the range of pH values usually found in intracellular matrix (pH~4), or the local environment in some cancerous tissues, thereby enabling targeted therapeutics by passive release at the clinically relevant sites [527-529].

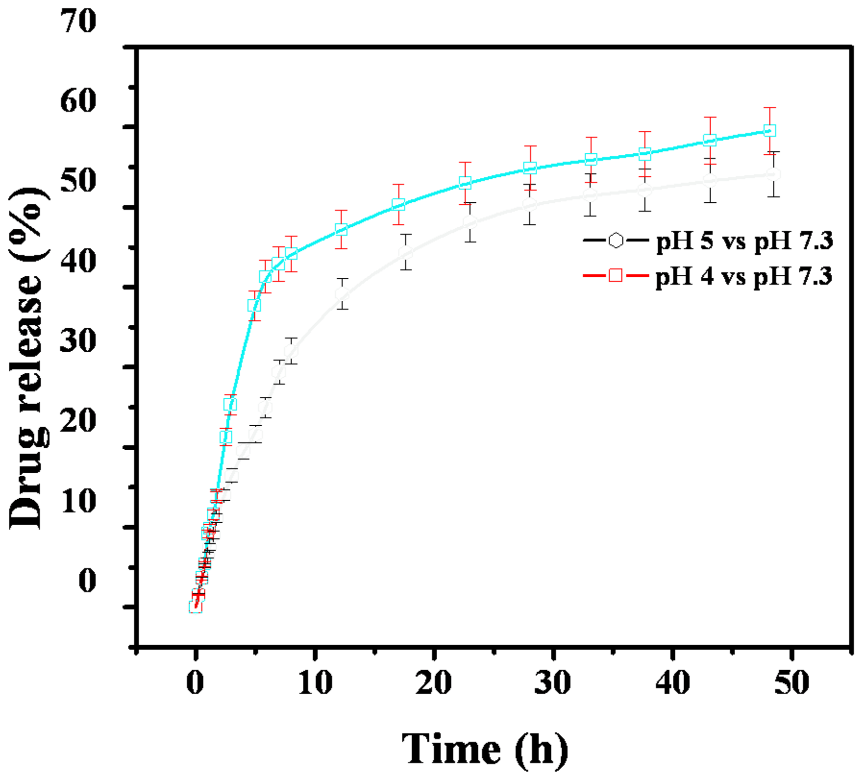

Figure 9.13:Drug release profile of DOX-PPNM in cell mimicking environment (reservoir: pH 5 and sink: pH 7.3) at 37 °C.

9.2.4. Cyto-combatibility studies:

The positive results obtained from drug release studies further led to explore the cellular uptake of PPNMs/ DOX-PPNMs by cancer cells. Hence, their interaction with mouse fibro sarcoma (WEHI 164)cells by Prussian blue staining and light microscopy were carried out. Without nanoparticles, there are no blue spots in WEHI 164 cells (**Figure 9.14**). The WEHI 164 cells treated with PPNMs/ DOX-PPNMs show the presence of a number of blue spots, suggesting that the drug loaded nanomagnets/ nanomagnets were internalized in the tumor cells (**Figure 9.14**). This study demonstrates that the use of these nanoparticles as drug delivery vehicles could significantly enhance the accumulation of drug (DOX) in target cancer cells leading to a high therapeutic efficacy.

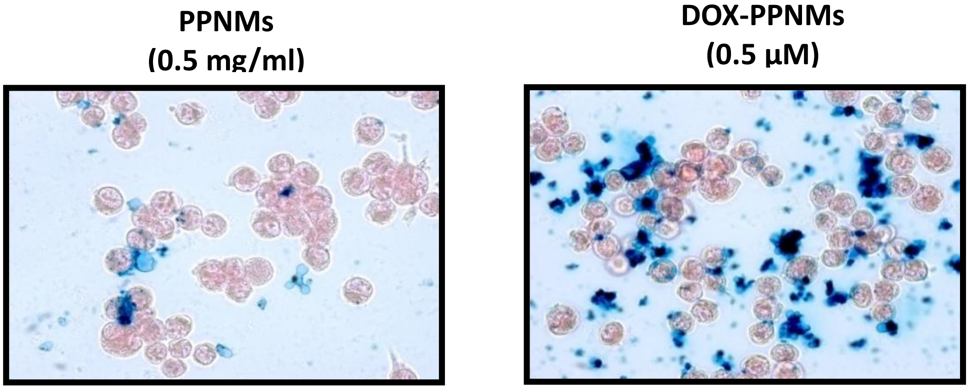

Figure 9.14: Prussian blue staining of the Wehi 164 cells (a) cell media with PPNMs (0.5 mgml−1) (b) cells treated with DOX-PPNMs for 6 h.

The cyto-compatibility was investigated using MTT assay to assess whether these samples had any deleterious biological properties, for further in vivo use. The cytotoxicity of PPNMs and DOX-loaded PPNMs was evaluated and compared with free DOX via the MTT (3-4, 5-dimethylthiazol-2-yl)-2, 5-diphenyltetrazolium bromide) assay. Even at concentrations as high as 2mgmL^{-1}, the PPNMs had negligible effect on the mouse fibro sarcoma (WEHI 164)cells viability (**Figure 9.15**), indicating that the unloaded PPNMs are highly biocompatible. In contrast, low total concentrations (0.2 to 200μg mL^{-1}) of DOX-loaded PPNMs exhibit significant cytotoxicity and a distinct advantage over free DOX. The relatively lower cytotoxicity of DOX-loaded PPNMs, compared to DOX, can be attributed to the sustained release behavior of the nanomagnets (loaded drug is expected to release slowly over a period of time). In addition, the percentage of hemolysis was found to be around 3% after incubation of 0.5 mg of PPNM, which indicates their good haemocompatibility.

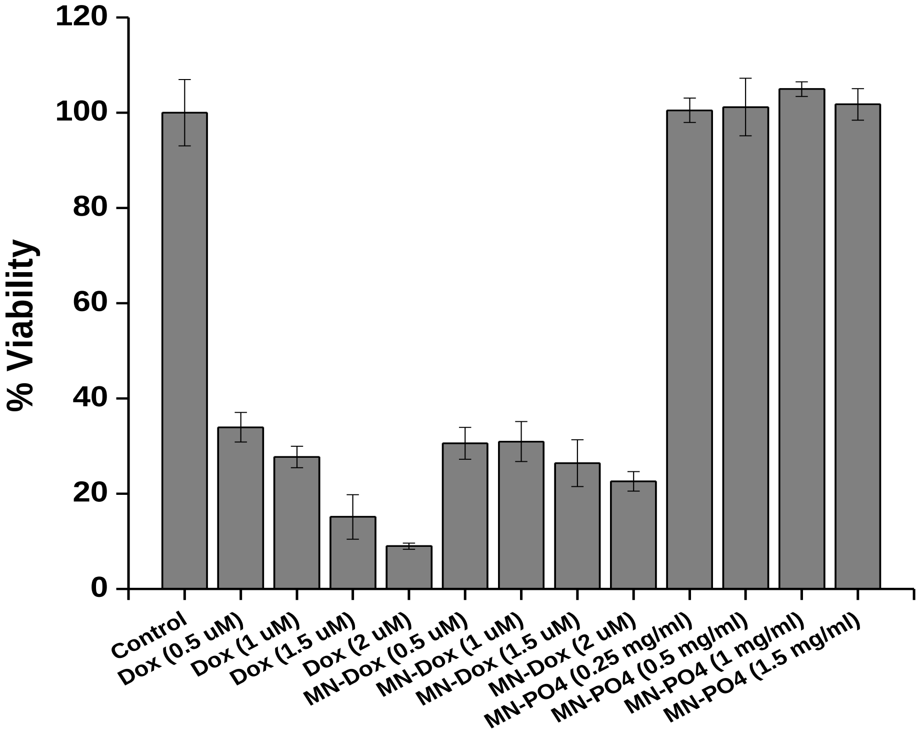

Figure 9.15: Viabilities of mouse fibro sarcoma (WEHI-164)cells incubated in medium containing difference concentrations of (a) PPNM, DOX and DOX-PAMN at 37 °C for 48 h.

Thus, the viabilities of cells are not affected by the mere presence of PPNMs, registering normal growth in the cells, suggesting that these samples are biocompatible and do not have toxic effect for further in vivo use. Specifically, the present study demostrates the formation of stable, highly crystalline, biocompatible, protein resistance polyphosphate grafted nanomagnets having good magnetization and excellent intrinsic loss power. This makes it amenable for promising applications in hyperthermia treatment of cancer as well as pH triggered release of DOX for combination therapy involving hyperthermia and chemotherapy.

9.3. Summary

In summary, the synthesis of a hydrophilic multifunctional polyphosphate grafted nanomagnets of average size 10 nm using co-precipitation method is reported. XRD and TEM analysis confirmed the formation of highly crystalline single phase Fe_3O_4 nanostructures. The detailed structural analysis by FTIR, TGA, DLS and zeta-potential confirmed the successful grafting of nanomagnets with polyphosphate moieties. These superparamagnetic nanomagnets exhibit colloidal stability and biocompatibility along with self-heating efficacy under AC magnetic field. Drug delivery capability of the stable colloidal nanomagnets was explored. Cytotoxicity and cell imaging experiments reveal that the nanomagnets are biocompatible and easily endocytosed by cells. Drug loading efficiency and the pH triggered intracellular drug releaseof the PPNMs was also done by using DOX as a model drug. The multifunctional nanomagnets show additional benefits by enhancementof *in vivo* therapeutic efficacy *via* decreasing systemic toxicity of antitumor drugs both through protection of the drug throughout circulation and by means of magnetic fields to target the nanomagnets to the infected area.

Chapter 10

Luminescent–magnetic materials

1. *Facile synthesis of flower like FePt@ZnO core–shell structure and its bifunctional properties*
   Jerina Majeed, O.D. Jayakumar, B.P. Mandal, H.G. Salunke, R. Naik and A.K. Tyagi
   J. Alloys Comp., 2014, 59, 95–100.

2. *Direct synthesis of partially ordered tetragonally structured FePt nanoparticles by polyol method for biomedical application*
   Jerina Majeed, F. Sayed, O. D. Jayakumar, C. Sudakar and A. K. Tyagi
   Int.J.Nano Dim.,2011, 2, 61-65.

10.1. Introduction

Recently, the relevance of luminescent and magnetic nanoparticles has been highly increased in the bio-imaging technologies [530, 531]. The integration of fluorescent as well as magnetic nanoparticles further offers a new perspective for in vitro and in vivo imaging. Magnetic–fluorescent nanoparticles assist both as a contrast agents for magnetic resonance imaging (MRI) and optical probes in case of intravital fluorescence microscopy [532].

Iron-platinum alloy nanoparticles (FePt NPs) are extremely promising candidates for the next generation of magnetic nanomaterial for nanomedicine applications like magnetic hyperthermia and magnetic resonance imaging (MRI) [114, 124, 218, 533, 534] because of their high Curie temperature (T_c), saturation magnetic moment (M_s), magnetocrystalline anisotropy, and chemical stability. Recently, superparamagnetic chemically disordered face-centered cubic (fcc) FePt nanoparticles have been demonstrated as superior negative contrast agents for MRI [533]. Superparamagnetic FePt nanoparticles, which show high saturation magnetization compared to superparamagnetic ironoxide nanoparticles (SPION), are expected to be ahigh-performance nanomagnet for magnetic medicine [121-123]. Even though, FePt NPs exists both in disordered fcc and ordered fct structures, the synthesis of fct FePt NPs is not so easy. Further, such structural difference in fcc-FePt and fct-FePt NPs leads to distinctive property change not only in magnetism [535-537] but also in the chemical stability. Conventionally, as prepared fcc FePt NPs are converted into fct NPs by a slow rate heating of fcc structure above 550 ˚C for 4-6 h [535, 536], which results in agglomeration of these NPs. This conventional, complicated synthesis procedure and hydrophobicity have limited the potential usage of both forms of FePt

NPs in vitro, in vivo and in the clinic. In this work, attempts were made for the direct soft chemical synthesis and characterization of a family of fcc and partially ordered fct-FePt NPs dispersible in aqueous media suitable for biomedical applications. Both fcc and partially ordered fct-FePt NPs are synthesized by employing a simple polyol method. By variying the ratios of Polyvinylpyrolidone (PVP) used during synthesis, fcc-FePt NPs have been converted into partially ordered fct-FePt NPs. The benefits of this process are its facile chemistry, the short reaction time, and simplicity.

Most of the optical imaging agents based on nanoparticles are further subdivided into two categories: dye–doped and quantum dots (QDs) [183, 215, 538, 539]. Generally, dye molecules undergo photo-bleaching as well as quenching upon interacting with solvent molecules and reactive species like oxygen, or other ions dissolved in solution [540, 541]. In contrast to dye molecules, QDs are more photochemically stable [542, 543] with narrow and tunable emission spectra [544], and are more metabolically stable [545]. Nevertheless, toxicity, photo-oxidation, and intricate surface conjugation chemistry allied with them limit their applications, and usually a shielding shell of insulating material or semiconductor is introduced to overcome these problems [546], which indeed complicates the fabrication process.

In the past decade, ZnO has been explored for new device applications when extra functionalities like magnetism [547-549] and photoluminescence [38, 550-552] which are deliberately introduced through proper doping or alloying with appropriate ions. In order to meet the demands of practical applications, there has been ever-increasing interest in the realization of ZnO-based hybrid materials, which can generally combine the advantages of luminescence, piezoelectricity, ferroelectricity and ferromagnetism [553-556]. It is expected that the core-shell or hybrid nanostructure of ZnO and FePt, arranged in a well-controlled way, would be multifunctional with unique applications. However, it is challenging to grow the two materials together in a controlled manner due to lattice mismatch and a large difference in their surface free energies. However, Liu et al. reported the enhancement of near-band-edge (NBE) emission of ZnO when ZnO nanowires were covered with a polymer [31]. Hwang et al. demonstrated substantially enhanced photoluminescence (PL) at the bandgap energy of ZnO (3.3 eV) in hybrid graphene/ZnO films due to the resonant excitation of graphene plasmon [557]. Zhou et al. [558] synthesized FePt/ZnO core/shell nanoparticles exhibiting ferromagnetism and luminescence. Lu et al. [559] observed luminescent properties in ferromagnetic nano-composites of FePt and ZnO nanoparticles. However, in all these methods mentioned above, spherical FePt nanoparticles were used for the synthesis. Herein, a successful methodology for multifunctional flower shaped core-shell type of nanostructures of ZnO coated FePt, synthesized by a facile chemical method using preformed flower shaped FePt nanostructures and zinc acetate is demonstrated. Preformed FePt nanoflowers dispersed in tri-n-octylamine solvent has been coated with ZnO with different thickness by synthesizing ZnO in FePt dispersed tri-n-octylamine solvent by a wet chemical method.

In this chapter, the synthesis of FePt decorated ZnO nanorod by synthesizing FePt on preformed ZnO nanorods dispersed in tri-n-octylamine was also explored. These nanoparticles are further studied for their magnetic and optical properties.

10.2. Results and discussion

10.2.1. FePt: PVP

The FePt nanoparticles were prepared by simple solvothermal method using variing ratios of PVP as stabilizing agent. The XRD pattern of fcc-FePt samples showed the peaks (111), (200) and (220) with the lattice constant a = 3.848 Å, corresponding to cubic phase (fcc) of FePt (**Figure 10.1(a and d)**). The emergence of additional peaks (001) and (110) in the XRD pattern (**Figure 10.1(b and c)**) confirms the partial transformation of fcc-FePt to tetragonal structured fct-FePt. Analysis of the X-ray diffraction pattern of fct-FePt revealed that the lattice constant is 3.862 Å and c is 3.722 Å, with c/a ratio being 0.964. This is relatively consistent with the lattice constants for near-equiatomic FePt bulk material with L10 phase [535].

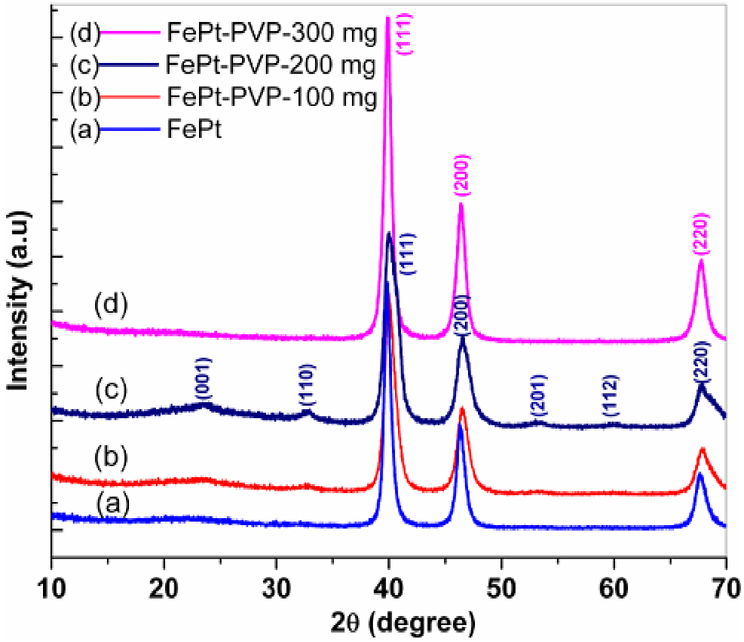

Figure 10.1: Room temperature XRD patterns of FePt (a) without PVP, (b) with FePt: PVP = 1:1, (c) with FePt: PVP = 1:2 and (d) with FePt: PVP = 1:3.

It is worth to note that the sample without PVP is fcc structured, and the fct-FePt phase started to form only in the presence of PVP (**Figure 10.1 (b and c)**). However, it is observed that the fct phase formation is PVP ratio dependent and above FePt:PVP = 1:3 ratio, the fct phase disappears and the fcc phase re-emerges (**Figure 10.1(d)**). The crystallite size calculated for these samples using Scherrer's equation (after correction for broadening due to the standard sample) is approximately in the range 7-10 nm. It is worth to note that the crystallite size is marginally smaller for PVP stabilized samples. A marginal shift in the peak positions to higher angles (**Figure 10.1**) is observed in the case of fct phased FePt samples (**Figure 10.1(b and c)**).

The TEM, HRTEM and SAED pattern of fcc phased FePt NPs synthesized without adding PVP are shown in **Figure 10.2**.

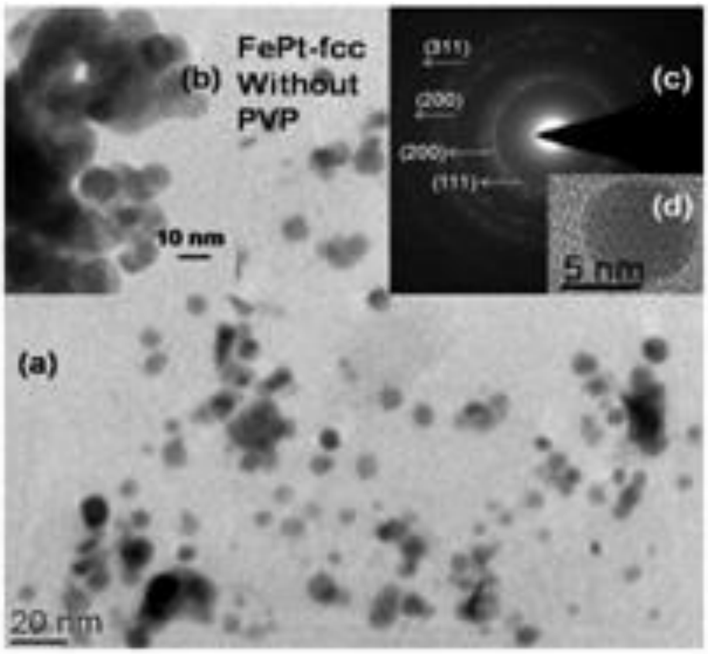

Figure 10.2: (a, b) TEM image (c) SAED pattern and (d) HRTEM image of fcc-FePt nanoparticles without PVP coating.

The TEM (**Figure 10.2.(a and b)**) shows that the particle diameter is about 10 nm in agreement with the XRD results.The HRTEM and indexed SAED pattern show that the samples are highly crystalline fcc structured FePt. FePt NPs with fct structure prepared using PVP (FePt: PVP=1:2) showed particle diameter of about 8 nm (**Figure10.3 (a and b)**). The indexed SAED pattern (**Figure 10.3(c)**) shows that the FePt particles are highly crystalline with fct structure. On increasing the PVP ratio to FePt: PVP = 1:3, the particle size marginally decreased to about 6-7 nm as is evident from **Figure 10.3(d)**.

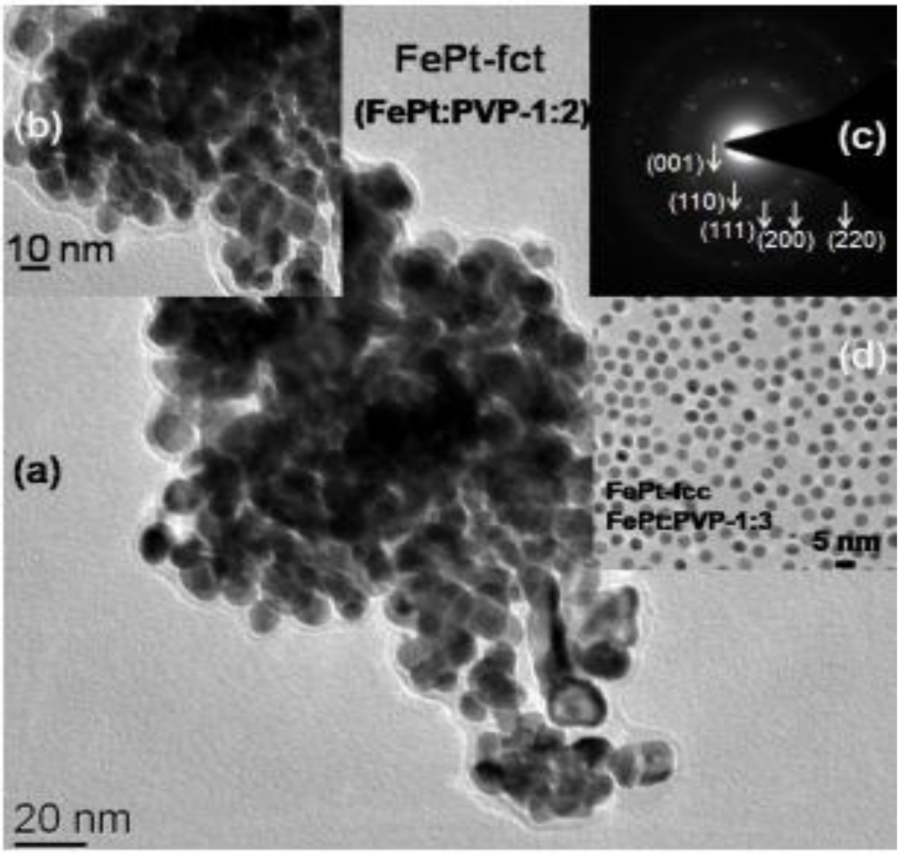

Figure 10.3:(a, b) TEM images, (c) SAED pattern of fct-FePt nanoparticles with FePt:PVP = 1:2 and (d) TEM image of fcc-FePt nanoparticles with FePt:PVP = 1:3.

The magnetic hysteresis loops and magnetization as a function of temperature of fcc and fct phased FePt NPs prepared using different ratios of PVP are given in **Figure 10.4**.

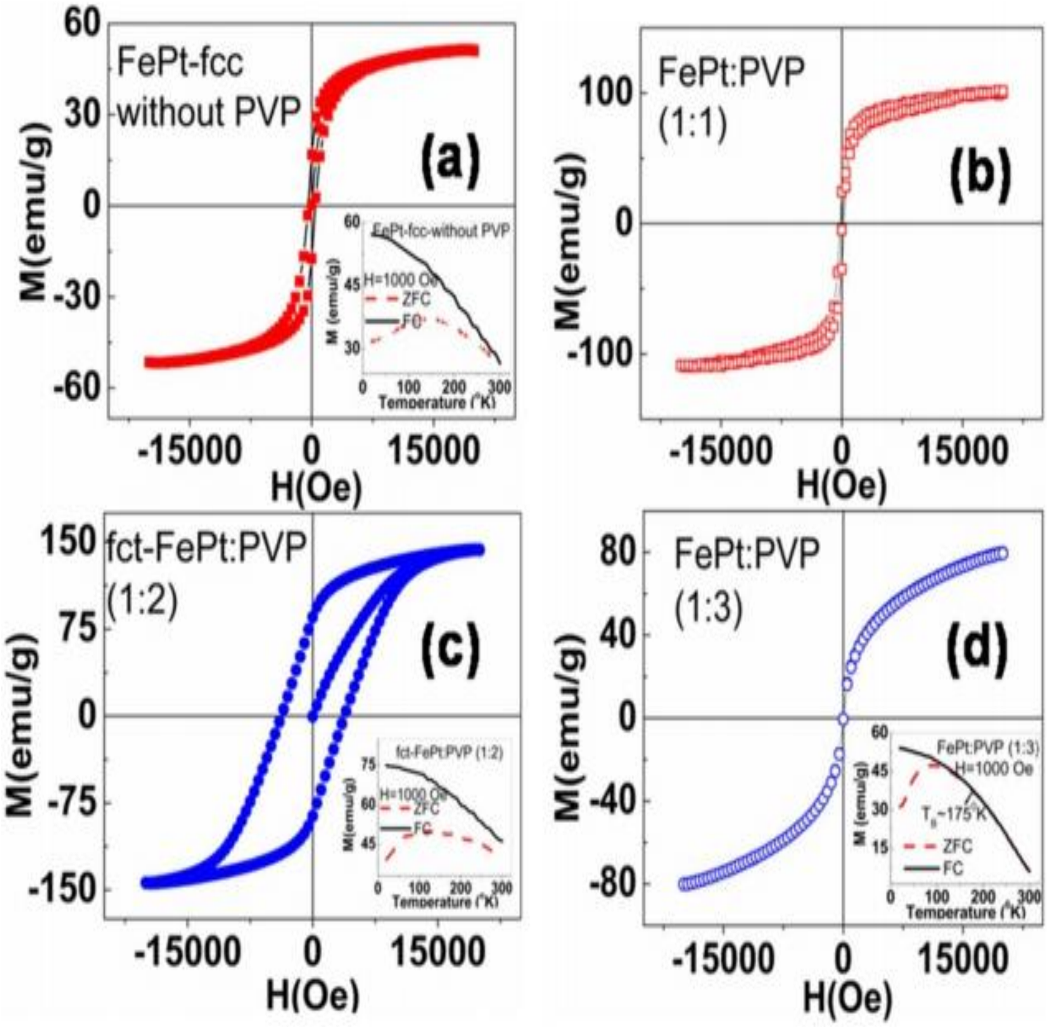

Figure 10.4: M *vs* H curves of (a) FePt without PVP and inset shows its M *vs.* T curve, (b) FePt with FePt:PVP = 1:1, (c) fct-FePt with FePt:PVP = 1:2 and inset shows M vs. T (ZFC-FC) curve and (d) fcc-FePt with FePt:PVP = 1:3 and inset shows the M vs. T (ZFC-FC) curve.

The saturation magnetization (M_S) of fcc phased FePt NPs synthesized without PVP is ~50 emu/g. It is worth to note that the saturation magnetization increases systematically as a function of increasing PVP ratio up to an optimum value of FePt: PVP = 1:2. The M_s value observed for FePt nanoparticles prepared using PVP ratios FePt:PVP = 1:1 and FePt:PVP = 1:2 were 105 and 142 emu/g, respectively. Above PVP ratio of 1:2 (e.g.,. FePt: PVP = 1:3), the saturation magnetization decreases, and the M vs. H curve showed a superparamagnetic type of behavior. Both FePt without PVP (fcc-FePt) and with PVP (FePt:PVP = 1:1) showed ferromagnetic behavior with weak coercivities (Hc=430 and 250 Oe respectively) and remanences (Mr=16 and 26 emu/g respectively) (**Figure 10.4(a and b)**). The M vs. T (FC-ZFC) curve (inset of **Figure 10.4(a))** of fcc-FePt NPs, synthesized without PVP, further confirmed their ferromagnetic behavior.

However, in the case of fct-FePt NPs obtained by using higher PVP ratio (FePt:PVP = 1:2), the saturation magnetization (Ms~142 emu/g), coercivity (Hc~4 kOe) and remanence (Mr~90 emu/g) are high, which is expected for fct phased FePt NPs. Its ferromagnetic behavior at room temperature is further confirmed from the M vs. T plot (inset of **Figure 10.4(c)**). The interesting aspect is that the fcc to fct phase transformation in FePt NPs is found to be PVP ratio dependent for a given concentration of Fe and Pt salts. When the PVP ratio is increased to 1:3 (FePt:PVP = 1:3) by keeping other conditions same, the FePt NPs showed fcc phase (**Figure 10.1(d))** with superparamagnetic type of behavior (**Figure 10.4(d)**) with blocking temperature (T_B) ~175 K (inset of **Figure10.4(d)).** Preliminary studies on FePt, for their effects on the metabolic activity and viability of human endothelial cells was also carried out. Considering the magnetic properties shown by this material, it appears to be promising for T_2 weighted imaging in MRI applications. It may be noted that FePt nanoparticles without PVP showed slight toxicity character wherein at 10µg/ml, cell started showing adverse effects on their viability leading to apoptosis. It is believed that the presence of platinum contributed to the toxicity character for this material. However, considering the clinical use of platinum based chemodrugs such as cisplatin and oxaliplatin, it is possible that, with proper surface chemistry modifications, it will be appropriate to test for the anticancer activity of this materials at lower doses (< 10µg/ml). The PVP coated FePt samples showed promising results in this respect and further studies on these materials using different size-scale, shape, composition and surface chemistry are in progress for better understanding of the properties and their possible bio-medical applications.

10.2.2. FePt@ZnO

The steps followed to synthesize the flower shaped FePt and ZnO coated FePt core-shell structure are shown in **Schemes 10.1 and 10.2** , respectively. Two compositions with different concentrations of ZnO over FePt (FePt : ZnO = 1:3 and 1: 6 molar ratio) were synthesized. Tri-n-octylamine forms complex with zinc and then get absorbed on predispersed FePt nanoparticles. The complex, subsequently, decomposes on FePt particles leading to core-shell structure of FePt@ZnO. Slow heating rate has immense influence over the formation of core-shell nanoparticles. It has been shown by Winkler et al. [560] that the energy required for the formation of the embryo on a seed particle is smaller than that of Kelvin size embryo in homogeneous solution. In this case also, slow heating rate leads to the lower concentration of ZnO monomer which could be below the homogeneous nucleation thresold [561]. These ZnO monomers are adsorbed on the surface of the heterogeneous phase i.e., FePt nanoparticle which is energetically more favorable than nucleate homogenously to form separate ZnO nanoparticles.

X-ray diffraction (XRD) pattern of the as-synthesized FePt@ZnO nanostructures with different compositions, along with those of the pure ZnO and FePt nanostructures are shown in **Figure 10.5** for comparison. The room temperature X-ray diffraction pattern of as-prepared FePt nanoflowers are displayed in **Figure 10.5(a)**. Peaks in the XRD pattern of FePt correspond to a partially ordered face centered tetragonal (fct) $L1_0$ phase (JCPDS Card-02-1167). Analysis of the X-ray diffraction pattern of fct-FePt revealed that the lattice constant ‘a’ is 3.862 (1) Å and ‘c’ is 3.722 (1) Å, with c/a ratio being 0.964. This is quite consistent with the lattice constant for near-equiatomic FePt bulk material with $L1_0$ phase.

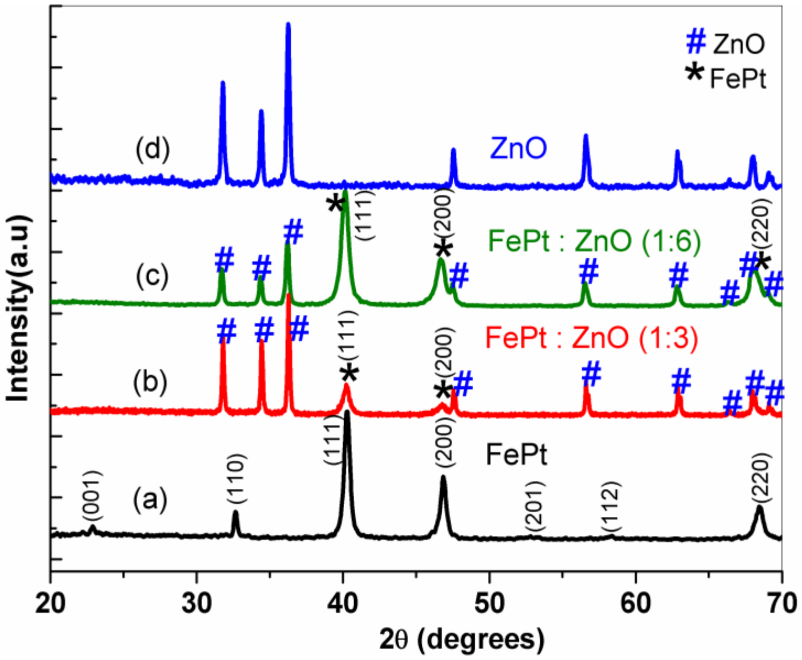

Figure 10.5:XRD patterns of (a) FePt, (b) FePt: ZnO (1:3), (c) FePt: ZnO (1:6) and (d) ZnO.

X-ray diffraction patterns of two compositions of FePt@ZnO (FePt :ZnO =1:3 and FePt : ZnO = 1:6) nanostructures exhibited peaks corresponding to hexagonal ZnO (JCPDS 36-1451) and fcc phase of FePt (**Figure 10.5(b,c)**). It may be noted that the intensities of peaks corresponding to FePt and ZnO are in different ratios in both FePt: ZnO =1:3 and FePt: ZnO = 1:6 samples. This is in agreement with the lower (1:6) and higher (1:3) concentrations of FePt with respect to ZnO. It is noteworthy that, while pure ZnO retains wurtzite hexagonal phase (**Figure 10.5(d)**), FePt shows peaks corresponding to fcc phase in the ZnO coated FePt core-shell nanostructures (**Figure 10.5(b,c)**). The reason for this transformation is not well understood at present. This could be due to the presence of ZnO along with FePt. To confirm this and to see whether the reverse structure (FePt coated ZnO nanostructure) also gives similar XRD patterns for FePt in presence of ZnO, attempts were made to synthesize core-shells of FePt coated ZnO (ZnO@FePt) nanorods, which resulted in the formation of FePt decorated ZnO nanorods.

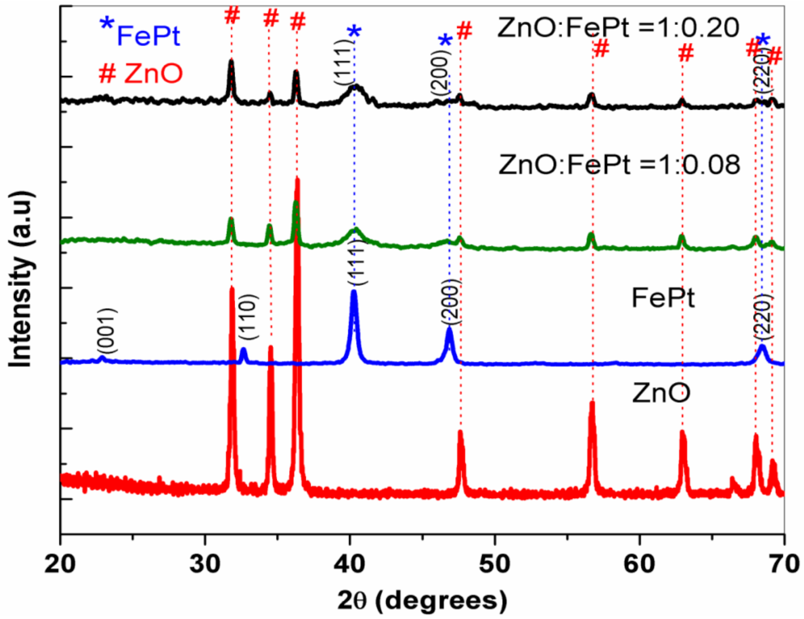

Figure 10.6. XRD patterns of ZnO, FePt and FePt decorated ZnO [ZnO: FePt (1:0.08) and ZnO: FePt (1:0.2)].

Here too, while pure FePt showed partially ordered face center tetragonal phase (fct phase), the FePt decorated ZnO nanorods showed the presence of FePt in disordered fcc cubic phase (**Figure 10.6**). Several different routes to synthesize FePt nanoparticles have been described in the literature [114, 123, 533, 535-537]. The vast majority of these methods use solution-based methods to produce fcc phase of FePt particles that are subsequently transformed by thermal annealing to the highly anisotropic fct phase [535, 536]. In the present method, partially ordered fct phase of FePt nanoflowers was directly synthesized by heating the Fe and Pt salts in oleylamine at 320 °C for 2 h. This temperature is found to be sufficient to get the partially ordered fct phase of FePt (**Figure 10.5**).

The TEM image of pure FePt nanostructures under different resolutions are shown in **Figure 10.7(a,b)** which clearly displays the formation of FePt in flower form. The indexed SAED pattern (**Figure 10.7(c)**) and the HRTEM image (**Figure 10.7(d)**) shows that the FePt particles are fct structured in agreement with the XRD results (**Figure 10.5(a)**) and are highly crystalline in nature. TEM image of pure ZnO particles confirmed the nanorod morphology for them as can be seen from **Figure 10.8**. However, TEM images of both concentrations of FePt@ZnO nanostructures with FePt : ZnO = 1:3 and FePt : ZnO = 1:6 (**Figures 10.9 and 10.10**) showed formation of core-shell type flower shaped nanostructures with high crystallinity (**Figure 10.9(c) and 10.10(c)**), similar to the morphology observed for pure FePt (**Figure 10.7(a,b)**), with ZnO covering the FePt flowers. The centre or core part of TEM appear darker (**Figure 10.9(d), 10.10(d)**), while the outer part or shells appear lighter in the images due to the large difference in electron scattering abilities (Z-contrast) of FePt and ZnO. The ZnO thickness (7-8 nm) is on higher side for FePt : ZnO = 1:6 sample (**Figure 10.10(d)**), compared to ZnO thickness (3-4 nm) in FePt : ZnO = 1:3 sample (**Figure 10.9(d)**), due to the lower amount of FePt taken during the synthesis of former sample.

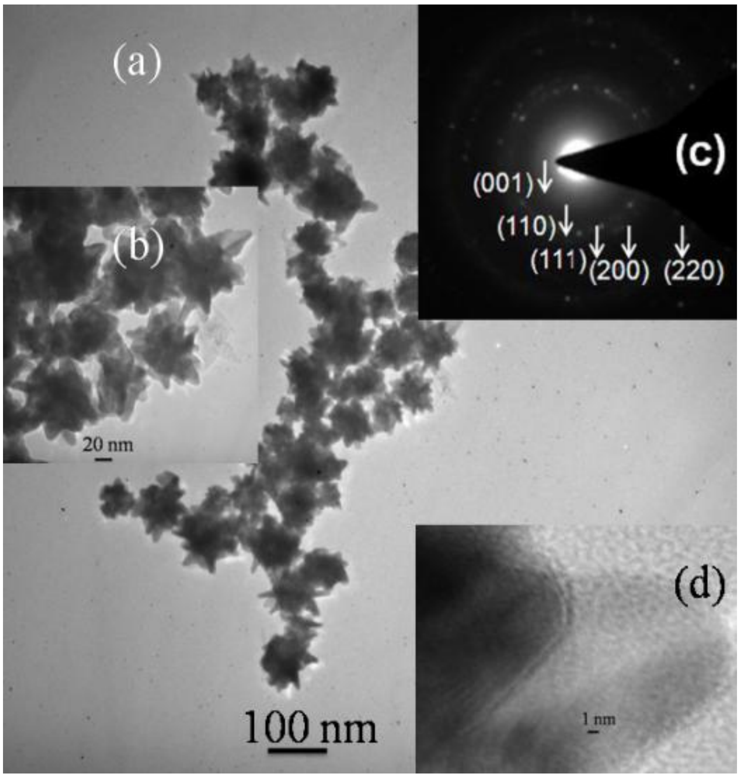

Figure 10.7:(a, b) TEM image (c) SAED pattern and (d) HRTEM image of FePt.

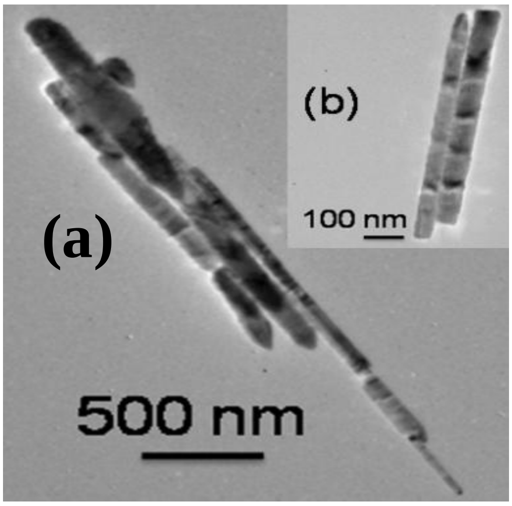

Figure 10.8: TEM images of pure ZnO.

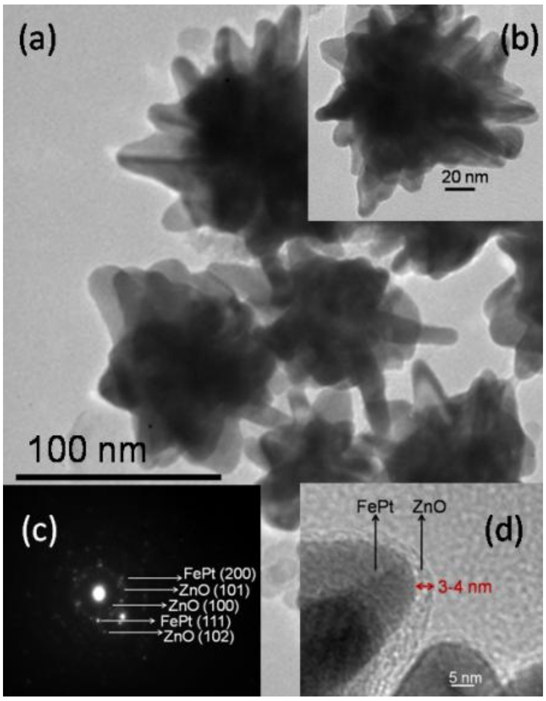

Figure 10.9: (a, b) TEM image (c) SAED pattern and (d) HRTEM image of FePt: ZnO (1:3).

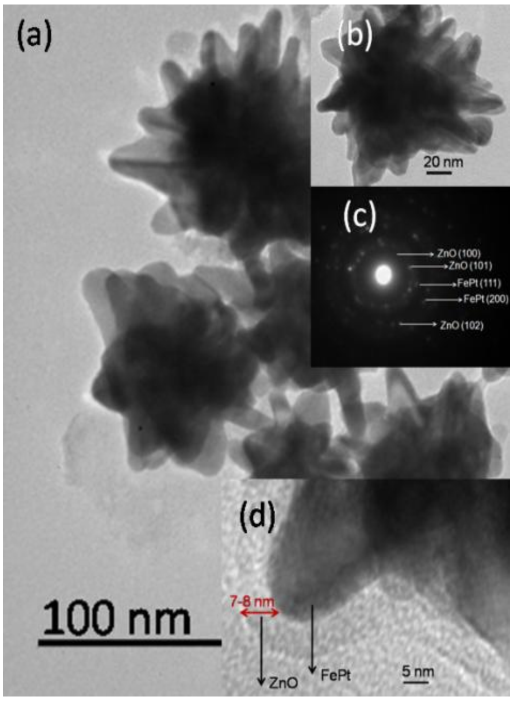

Figure 10.10:(a, b) TEM image (c) SAED pattern and (d) HRTEM image of FePt: ZnO (1:6) nano hybrids.

The mechanism for the formation of ZnO over FePt (FePt@ZnO), with flower shape, could be due to the catalytic action of both Fe and Pt present in FePt, thus preventing ZnO from growing as independent nanorods as has been observed for pure ZnO (**Figure 10.8**).

Thus, it can be presumed that though ZnO tries to grow as rods with high aspect ratio, the presence of FePt hinders the growth of ZnO into rod and activate them to form into flower shaped.particles (**Figure 10.9(d),10.10(d)**). This mechanism is further confirmed by the synthesis of FePt coated ZnO (as shown in **Scheme 10.3**), where instead of core-shell type of structure formation of FePt over ZnO, FePt nanoparticles decorated ZnO nanorods (**Figure 10.11**) were formed. Here, FePt particles were grown on preformed ZnO surface and, therefore, the catalytic activity of FePt on ZnO growth is ruled out.

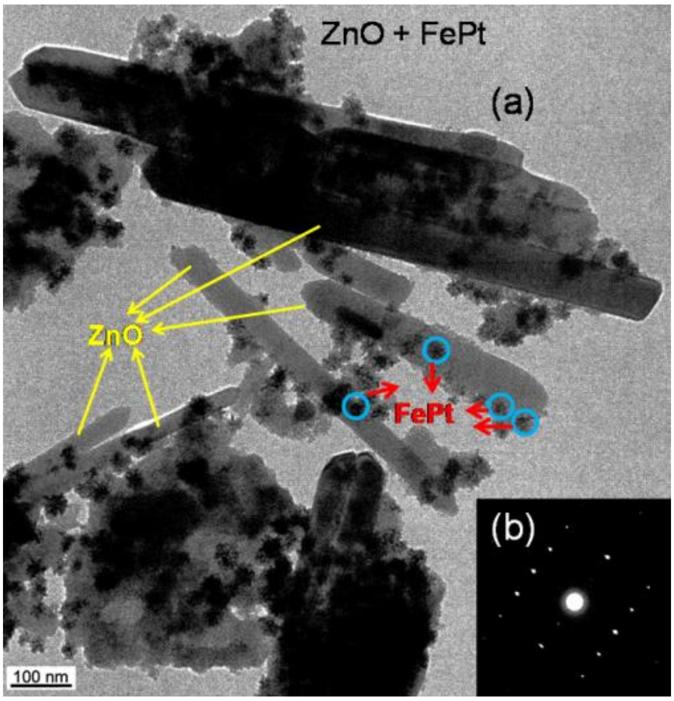

Figure 10.11:(a) TEM image and (b) SAED pattern for FePt decorated ZnO nanorod (ZnO: FePt (1:0.08) composition).

For the magnetic fct FePt alloy, the preferential growth direction follows the route of the minimum magnetic anisotropic energy or surface free energy [562]. Spherical nanoparticles could be obtained when the rate of reaction is very high. At slower rate of reaction, growth could take place along the magnetic easy axis to minimize the magnetic anisotropic energy [563] or the high energy facets could also grow easily to minimize the surface free energy [564].

Scheme 10.1: Steps followed to synthesize FePtnanoflower.

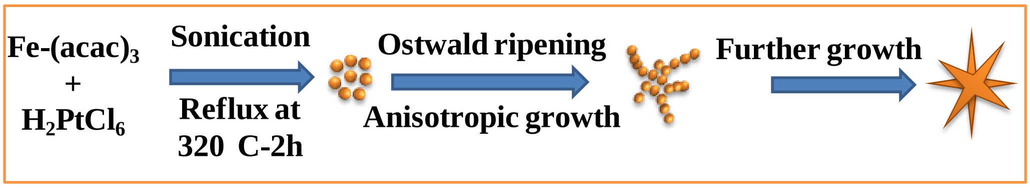

Scheme 10.2: Steps followed to synthesize ZnO coated FePt (FePt @ZnO).

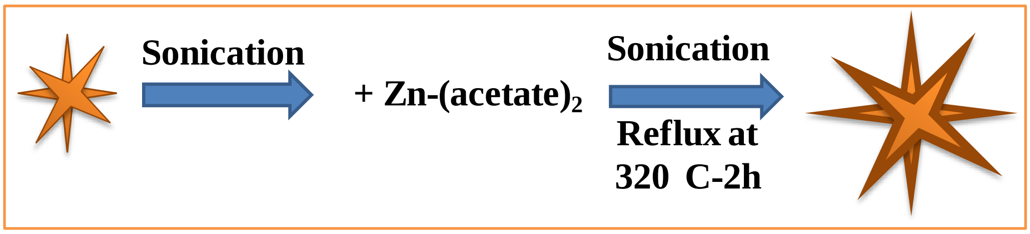

Scheme 10.3: Steps to synthesize FePt decorated ZnO (ZnO@FePt).

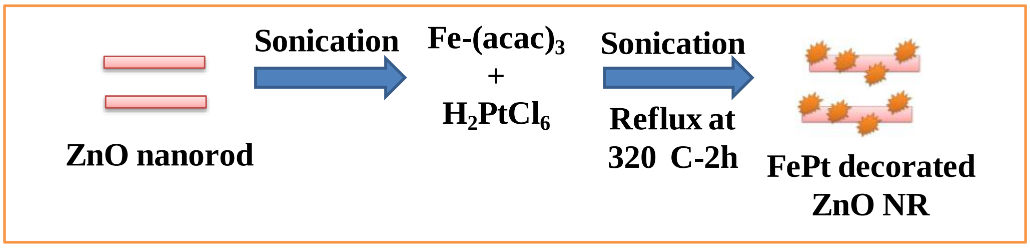

In case of fct FePt, magnetic easy axis is [001] and the surface free energy follows the trend σ{111} (0.701 eV/ atom) < σ {001} (0.991 eV/ atom) < σ {011}(1.342eV/ atom) [565]. At the begining of the reaction, the concentration of reactants is high, therefore, the rate of reaction is faster which facilitates to form the spherical core of the nanoflower. However, as the time proceeds, the concentration of the reactants decreases which decelerate the rate of reaction. At very slow rate, the difference in growth of different facets become more prominent, and the growth follows the above-mentioned energy minimization principles. The growth rate of {111} facets is much lower (or may be nil) than that of {011} because of their lowest surface free energy [566]. The petals of the nanoflowers follow a preferential growth, possibly along the [011] or [001] direction, keeping the core nearly spherical as shown in **Scheme 1**.

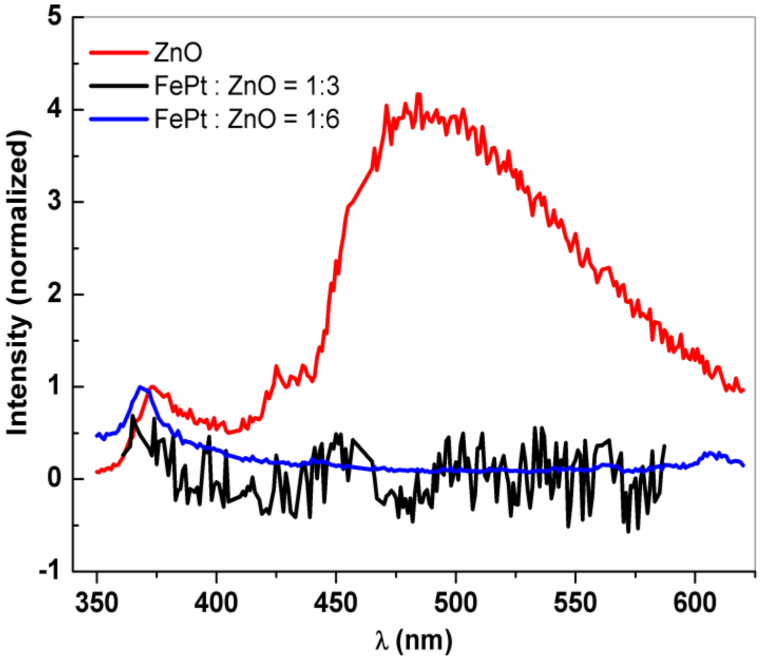

Figure 10.12: Room temperature photoluminescence spectra of ZnO, FePt: ZnO (1:3) and FePt: ZnO (1:6).

The optical properties of the FePt@ZnO nanostructures with two different compositions are presented in **Figure 10.12**, along with the photoluminescence spectrum of pure ZnO nanorods for comparison. Emission spectrum of pure ZnO sample is characterized by a sharp emission around 370 nm along with a broad Gaussian-like emission in the 450–550 nm regions. The sharp peak at 370 nm is attributed to the near band edge emission (NBE) and the broad peak to either oxygen or zinc vacancies [557, 567-571]. ZnO coated with FePt (FePt@ZnO 1:6 composition), exhibited near-band edge emission with a slight blue shift and the defect related emission got suppressed in this sample.

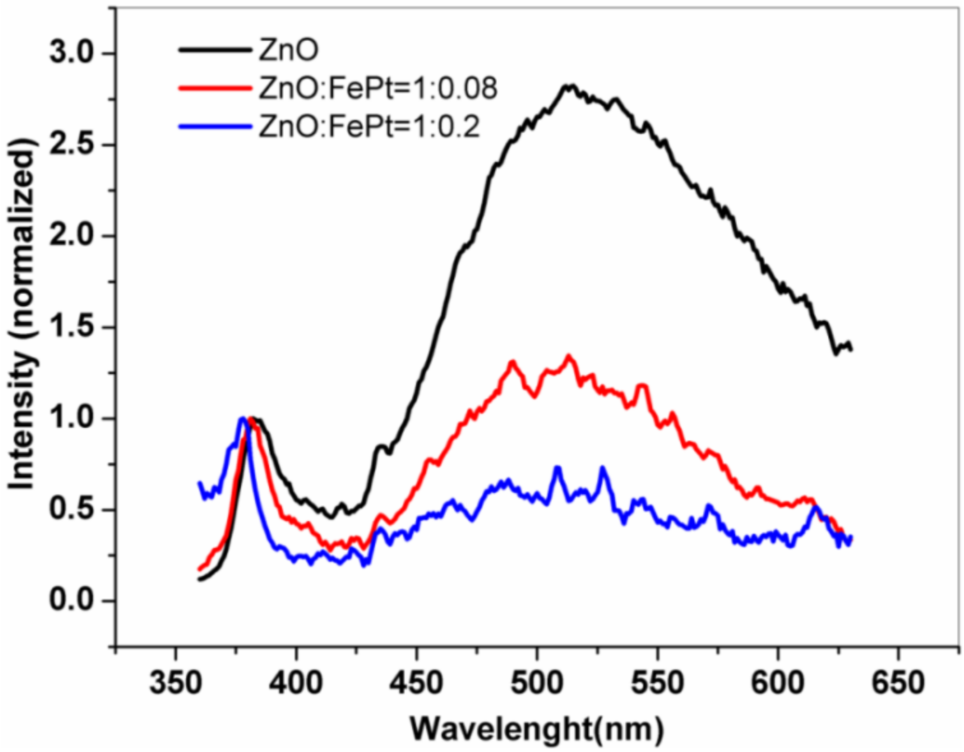

Figure 10.13: Room temperature photoluminescence spectra of ZnO and FePt decorated ZnO (ZnO: FePt = 1:0.08 and ZnO: FePt = 1:0.20).

However, on further increasing the FePt content (with 1:3 composition), the near band edge emission as well as emission due to defects disappeared. This is due to the increased FePt content which is metallic nature. It is worth to mention here that both the compositions of FePt decorated ZnO nanorods (ZnO : FePt = 1:0.08 and ZnO : FePt = 1:0.20) also showed near band edge emission with decreased intensity for defect related emission (**Figure 10.13**). However, a complete disappearance of band edge or defect related emission in FePt decorated

ZnO nanorods were not observed. This can be due to the presence of partially exposed region of ZnO nanorods (**Figure 10.11**) when small amount FePt is decorated over ZnO nanorods.

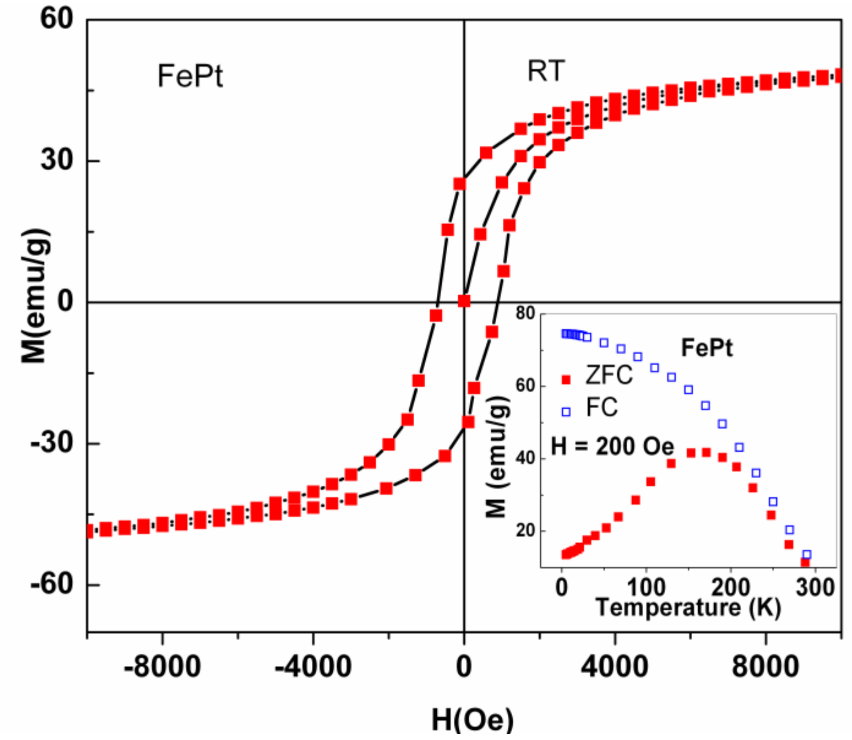

Figure 10.14: Magnetization vs. Field and Magnetization vs. Temperature (inset) of FePtnanoflowers.

Room temperature hysteresis loop of FePt nanostructures (**Figure 10.14**) shows ferromagnetic behavior with coercivity (Hc) ~ 750 Oe and remanence (Mr) ~27 emu/g at RT. FePt nanostructures with fct phase are known to be ferromagnetic at room temperature with large coercivity and remanence [535-537]. It is well known that temperature dependent magnetization studies under field cooled (FC) and zero field cooled (ZFC) conditions show the type of magnetism present in the material and also depicts the transition temperature (T_C) for ferromagnetic and blocking temperature (T_B) for superparamagnetic materials.

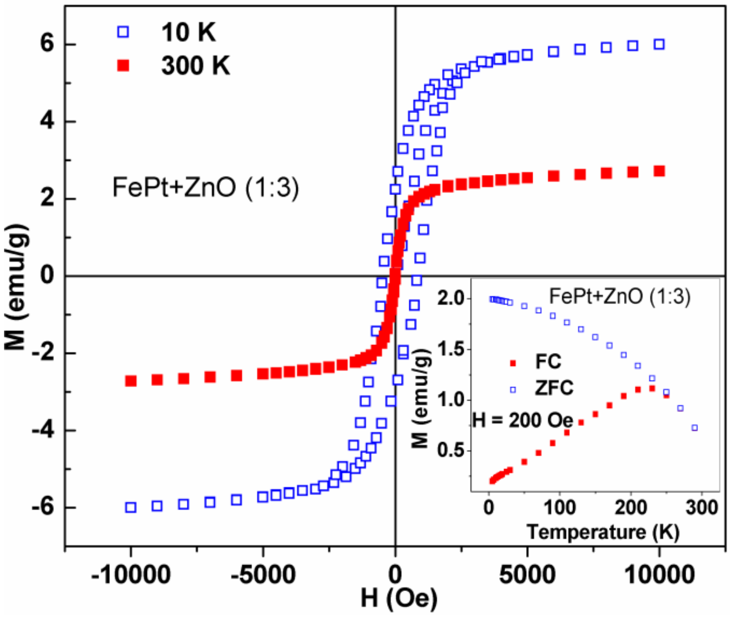

Figure 10.15: Magnetization vs. Field and Magnetization vs. Temperature (inset) of FePt: ZnO (1:3) nanoflowers.

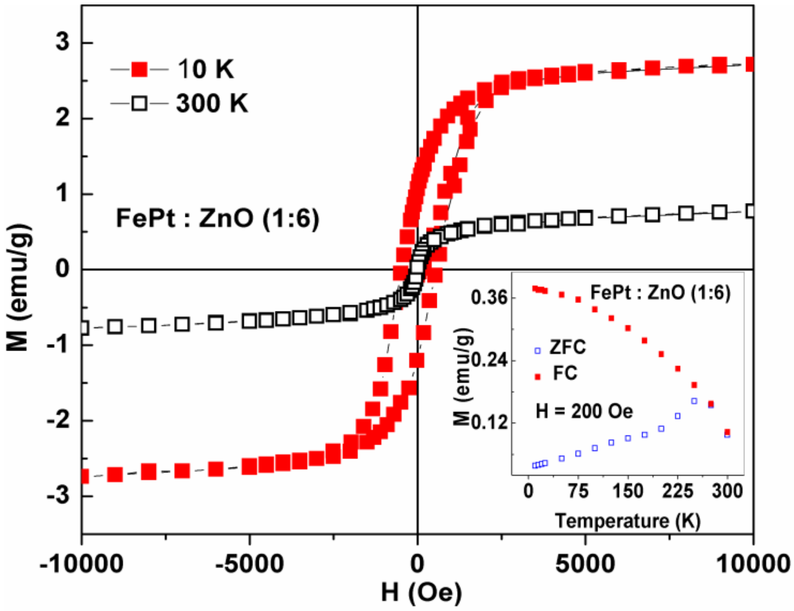

Figure 10.16: Magnetization vs Field and Magnetization vs Temperature (inset) of FePt: ZnO (1:6) nanoflowers.

The ZFC-FC curves of FePt nanostructures (inset **Figure 10.14**), measured under an applied field of 200 Oe shows that they are ferromagnetic above room temperature. The magnetization as a function of field (M vs. H) for ZnO showed a diamagnetic behavior as expected (figure not shown). The hysteresis loops of both the structures of FePt@ZnO with different concentrations of FePt@ZnO (1:3 and 1:6), measured at room temperature and at lower temperatures are shown in **Figure 10.15 and 10.16**, respectively. It is clear from these loops that these nanostructures are superparamagnetic at room temperature and ferromagnetic at lower temperatures. The superparamagnetic nature of FePt@ZnO nanostructures with varying FePt concentrations is further confirmed from their ZFC-FC curves with T_B near room temperature (inset of **Figures 10.15 and 10.16**). It is worth to mention here that the broad gap between the ZFC-FC curves observed at low temperature could be due to the presence of very low concentration of magnetically anisotropic $L1_0$ fct phase of FePt in the FePt- ZnO hybrids. It is noteworthy that fct-FePt is ferromagnetic and hexagonal ZnO is diamagnetic at room temperature. Nevertheless, their hybrids exhibit superparamagnetic behavior with $T_B \sim 300$ K. It can be due to the existence of FePt in fcc phase (as fcc - FePt is known to show superparamagnetism) as is evidenced by the XRD pattern of FePt@ZnO composite (**Figure 10.5(b,c)**). The change of phase of FePt from fct to fcc in the FePt@ZnO composite clearly shows that there is an interaction between ZnO and FePt nanostructures. If FePt existed as an independent phase in the hybrids, without any interaction with ZnO, it should have shown the fct phase and hence the M vs H curve of FePt@ZnO composite should have exhibited the ferromagnetic behavior at RT. However, the hybrid showed superparamagnetic behavior with T_B near room temperature (**Figure 10.15, 10.16**). Hence, the magnetic properties show that there is an interaction between the FePt and ZnO nanostructures. Further, the decreased saturation magnetization (M_s) values at 10 K of FePt@ZnO nanostructures (~ 6 and 3 emu/g for 1:3 and 1:6 ratio) compared to FePt nanostructures (48 emu/g) is partly due to this interaction and also because of the small concentration of FePt in the FePt@ZnO nanostructures. Further, it is interesting to note that the decreased FePt content in FePt@ZnO (1:6) sample, decreased its saturation magnetization (3 emu/g) compared to FePt@ZnO (1:3) sample with saturation magnetization 6 emu/g. It is appropriate to mention here that the FePt decorated ZnO nanorods also showed superparamagnetic (**Figure 10.17**, shown for representative ZnO:FePt=1:0.08 sample) behaviour with blocking temperature (T_B) around 150 K (**Figure 10.17**).

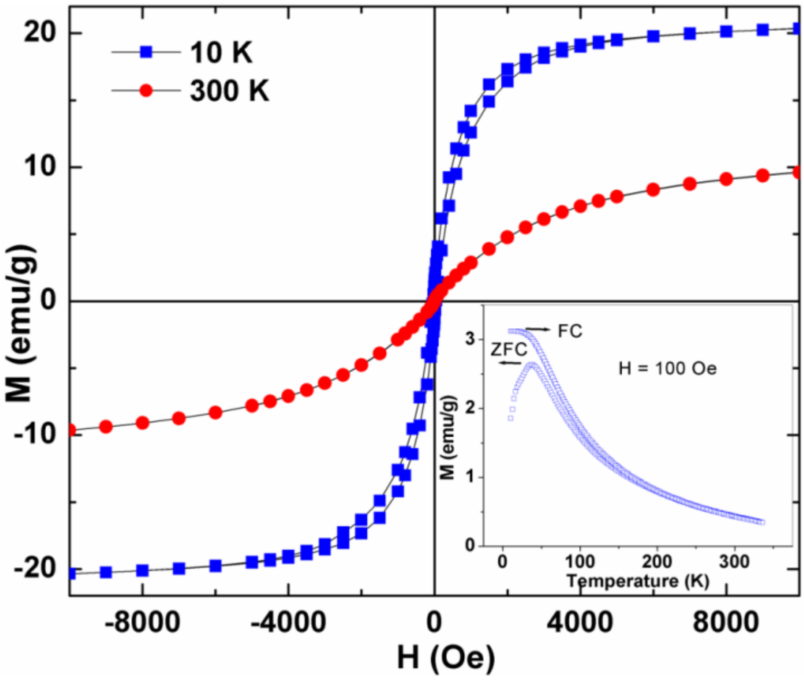

Figure 10.17: Magnetization *vs.* Field and Magnetization *vs* Temperature (inset) of FePt decorated ZnO nanorods (ZnO: FePt = 1:0.08 composition).

Characteristic of FePt in fcc phase as is evident from **Figure 10.6** and **Figure**

10.11. This shows that the presence of ZnO along with FePt plays a crucial role in converting fct - FePt into fcc - FePt. This behavior needs further studies to elucidate the nature of the interaction between ZnO and FePt during synthesis.

10.3 Summary

In summary, a solvothermal method, of preparing fct phased FePt from fcc phased FePt nanoparticles at low temperature, has been developed using PVP as a protective agent. The preliminary results suggest that, in addition to unique functional properties, these nanomaterials also show typical nano-bio interactions leading to varied toxicity characteristics.

Flower shaped FePt and ZnO coated FePt with core-shell nanostructures are synthesized by a facile solvothermal procedure. Two different compositions (molar ratio) of FePt and ZnO (FePt: ZnO = 1:3 and FePt: ZnO = 1:6) were synthesized by varying FePt concentration with respect to ZnO thereby changing the ZnO shell thickness. Hybrid structure with lower FePt concentration (FePt: ZnO = 1:6) exhibited bifunctionality such as near room temperature ferromagnetism and photoluminescence. However, attempts to make FePt coated ZnO core-shells by a similar method resulted in the formation of luminescent and superparamagnetic ZnO nanorods decorated with FePt nanoparticles. Further toxicity studies and other bioapplications are yet to be conducted.

Chapter 11

Summary and future scope

11.1. Summary of the thesis

The present thesis demonstrates the facile synthesis, characterization and property evaluation of various nanostructures with wider range of applications like removal of toxic species (heavy metal ions, organic species, organic dyes etc) as well as in bioapplications like hyperthermia therapy, drug delivery, etc. A broad range of nanostructures was synthesized and studied in this research.

To begin with an introduction and basis of the research work carried out under the title of "Nanostructures for environmental remediation and bio applications" is briefed. Origin of nanostructured materials, their various properties, and societal applications, which are under exploration by the researchers worldwide, have been discussed in detail.

The surface charge of nano sorbents is acrucial factor which affects applications. The surface charge of ZnO NPs was tailored by adopting different synthesis protocols. The synthesized nanoparticles were characterized and zeta potential measurements showed that the ZnO NPs synthesized by pyrolysis method (ZnO (PY)) and gel combustion method (ZnO (GC) posses a positive charge while the co-precipitation method results in nanoparticles (ZnO (CP)) with negative surface charge. X-ray diffraction analysis reveals the formation of wurtzite hexagonal structure of ZnO nanostructures. These ZnO nanostructures were found to be efficient to remediate organic pollutants and heavy metal ions present in wastewater. In comparison to other ZnO, ZnO CP exhibits excellent sorption efficiency for Cu(II)ions while the other two with positive surface charge showed sorption efficiency for chromate species.

Surface functionalizations of moieties such as thiol, silanols and mercapto-silanol groups onto ZnO were prepared by one pot coprecipitation method. The functionalization of ZnO nanoparticles with thiol (thiourea), silanol (TEOS) and thiol (MPTS) were evident from FTIR spectra, elemental analysis, and zeta-potential measurements. The efficiency of these nanoparticles have been explored for removal of toxic metal ions (Cu(II), Co(II), Ni(II), Zn(II), Pb(II) and Hg(II)) from water. Depending upon the surface functionality (Si-OH or SH), nano adsorbents capture metal ions either by forming chelate complexes or ion exchange process or electrostatic interaction. Almost 99% of Hg(II) was removed within the first 10 min, indicating fast sorption kinetics. The adsorption equilibrium isotherm showed the best fit to Freundlich model. The isotherm analysis and kinetic modeling revealed the process to be a favorable chemisorption phenomenon following pseudo second order kinetics.

Zircon-type Mo-substituted $CeVO_4$ solid solutions were synthesized by co-precipitation technique. The system was extensively characterized using X-ray diffraction, X-ray fluorescence, Raman spectroscopy and X-ray photoelectron spectroscopy. The solid solution formation mechanism was proposed which involves the partial reduction of Mo^{6+} to Mo^{5+} accompanied by Ce^{3+} vacancies. The particle size increased on Mo-substitution with a concomitant increase in surface area that can be attributed to the presence of mesopores as shown by the N_2-adsorption-desorption isotherms. The hierarchical morphology coupled with the mesoporous structure showed efficient uptake of Pb(II) ions by $CeVO_4$. Introduction of hetero-Mo network improved the uptake kinetics by five times wherein 100 mg/L of Pb(II) uptake was exhibited in 10 min. The adsorption equilibrium isotherm showed the best fit to

Freundlich model. The isotherm analysis and kinetic modeling revealed the process to be a favorable chemisorption phenomenon following pseudo second order kinetics. The study brings forth highly promising Pb(II) ion sorbents in a hitherto unexplored cerium molydovanadate system.

Porous nanocomposite of $Fe_3O_4@SiO_2$ was synthesized by one-pot co-precipitation process. These spherical porous structures comprise of a crystalline magnetic core of size~10nm and an amorphous silica shell as confirmed by detailed characterization techniques and this helps to have a composite with the combination of both the magnetic property of the Fe_3O_4 core and high surface area of silica shell (due to amorphous nature), thus can enhance the application in waste water treatment.The magnetic property of the Fe_3O_4 core, aids in easier and faster removal of the sorbent from its aqueous solution by external magnet as compared to the non-magnetic sorbents. The uptake process was found to be thermodynamically as well as kinetically favorable, and the extensive modeling of data showed that maximum adsorption capacity that is in agreement with experimental values and the chemisorption nature of uptake.

Photocatalytic activity of TiO_2 (anatase) is appreciably enhanced by doping of Mo in anatase lattice, in conjunction with the incorporation of nanostructured MoO_3 within the parent anatase lattice. The photocatalyst material was characterized in details using X-ray diffraction, Raman spectroscopy, diffuse reflectance (DR-UV–Vis spectroscopy), X-ray photoelectron spectroscopy, and electron microscopy. Photocatalysis experiments were conducted using a model rhodamine-B (Rh–B) dye degradation using both UV and visible irradiation sources. The observed trends in the case of visible irradiative source can be summarized as follows: Mo-1 < Mo-2 < Mo-5

≫ Mo-10. Attempts were made to delineate the structural factors that control photochemical behavior of these Mo–TiO_2 photocatalysts and to correlate photocatalytic activity with different structural aspects like oxidation state, band gap, surface species, etc. Mechanistic insights were acquired from ex situ ^1H NMR studies showing different intermediates and different probable routes for the Rh–B dye degradation with UV and visible radiations. The stable intermediates were formed by a direct oxidative fragmentation route, without any evidence of the initial de ethylation route. The intermediates were benzoic acid, different amines, diols, and certain acids (mostly formic and acetic acid). The adsorption of the Rh–B dye on the catalytic surface via the N-charge centers of the Rh–B was also observed.

Core–shell Fe_3O_4–SiO_2 magnetic nanoparticles (MNPs) have been synthesized using a simple synthesis procedure at different temperatures. These MNPs are used to investigate the effect of surface coating on specific absorption rate (SAR) under alternating magnetic field (AMF). The temperature attained by silica coated Fe_3O_4 is higher than that by uncoated MNPs (Fe_3O_4), which can be attributed to the extent of the increase in Brownian motion for silica coated MNPs. The sample prepared at optimized temperature of 80°C shows the highest SAR value of 111 W/g. It has been observed that SAR value decreases with an increment in the shell thickness. Further, the chemical stability of these samples was studied by leaching experiments over pH 2–7, indicating the stability of silica coated samples at pH 2 even up to seven days. Sulforhodamine-B assay was used to evaluate the biocompatibility of the MNPs *in vitro* by assessing their cytotoxicity in L929 and human cervical cancer cells (HeLa cells). Their hyperthermic efficacy was also assessed by the same method using HeLa cells. Cells containing MNPs when subjected to the induction heating showed lesser viability in contrast to those without induction heating. Furthermore, cell death was found to be 55% more in cells with silica coated MNPs under AMF, in comparison to the untreated control. These results demonstrate the efficacy of Fe_3O_4–SiO_2 prepared at 80 °C in cellular hyperthermia.

The synthesis of a hydrophilic multifunctional polyphosphate grafted nanomagnets of size ~ 10 nm using a facile simple co-precipitation method is reported. XRD and TEM analysis confirmed the formation of highly crystalline single phase Fe_3O_4 nanostructures. The detailed structural studies by FTIR, TGA, DLS and zeta-potential confirmed the successful grafting of nanomagnets with polyphosphate moieties. These superparamagneticnanomagnets exhibit better colloidal stability and good biocompatibility along with excellent heating efficacy under AC magnetic field. The drug delivery capability of these hydrophilic nanomagnets was investigated using DOX as model drug. Cytotoxicity and cell imaging experiments reveal the nanomagnetsas biocompatible and easily endocytosed by cells. Drug loading efficiency of the PPNMs was also done by using DOX as a model drug. In addition, pH triggered intracellular drug release was also observed. The multifunctional nanomagnets show an additional benefit of *in-vivo* enhancement of therapeutic efficacy by reducing the systemic toxicity of antitumour drugs either through protection of the drug during circulation or by targeting the material to the infected area using magnetic field.

A soft chemical method, of preparing fct phased FePt from fcc phased FePt nanoparticles at low temperature, has been developed using PVP as a protective agent. The preliminary results suggest that, in addition to unique functional properties, these nanomaterials also show typical nano-bio interactions leading to varied toxicity characteristics. Flower shaped FePt and ZnO coated FePt with core-shell nanostructures are synthesized by a facile solvothermal procedure. Two different compositions (molar ratio) of FePt and ZnO (FePt : ZnO = 1:3 and FePt : ZnO = 1:6) were synthesized by varying FePt concentration with respect to ZnO thereby changing the ZnO shell thickness. Hybrid structure with lower FePt concentration (FePt: ZnO = 1:6) exhibited bifunctionality such as near room temperature ferromagnetism and photoluminescence. However, attempts to make FePt coated ZnO core-shells by a similar method resulted in the formation of luminescent and superparamagnetic ZnO nanorods decorated with FePt nanoparticles. Further toxicity studies and other bioapplications are yet to be conducted.

11.2. Future scope of work

1. The column mode sorption experiment need to be performed to test the practicality of the synthesized sorbents under actual conditions.
2. The methodology used in the fabrication of ZnO nanostructures, and their functionalization can be extended to other functional oxides.
3. Fabrication of $Fe_3O_4@SiO_2$-Ag material for added advantage of antibacterial activity of Ag along with the sorption efficiency of highly efficient magnetic sorbent ($Fe_3O_4@SiO_2$).
4. In the area of oxide nanomaterials for water purification, magnetic separation system designs need to be in the frontier area of research.
5. *In vivo* studies of FePt-ZnO nano-composites for biomedical applications such as MRI, hyperthermia therapy and targeted drug delivery.

References

References

1. C. N. R. Rao, A. Müller and A. K. Cheetham, *The Chemistry of Nanomaterials*, Wiley-VCH Verlag GmbH & Co. KGaA, **2005**,ch1, 1.
2. A. K. Bandyopadhyay, *Nano Materials: Architecture, Interior Architecture and Design*, New Age International, New Delhi, **2008**.
3. M. Faraday, *Philos Trans R Soc London*, **1857**, 147.
4. A. Roucoux, J. Schulz and H. Patin, *Chem Rev*, **2002**, 102.
5. C. G. Granqvist and R. A. Buhrman, *J Appl Phys*, **1976**, 47, 2200.
6. D. E. Arnold, J. R. Branden, P. R. Williams, G. M. Feinman and J. P. Brown, *Antiquity*, **2008**, 82, 151.
7. M. Fernández-García and J. A. Rodriguez, *Encyclopedia of Inorganic Chemistry*, John Wiley & Sons, Ltd, **2006**.
8. G. Oskam, *J Sol-Gel Sci.Techn*, **2006**, 37, 161.
9. J. Ramkumar, R. Shukla, S. Chandramouleeswaran, T. Mukherjee and A. K. Tyagi, *NanosciNanotechnol Lett*, **2012**, 4, 693.
10. N. Kumar, A. Dorfman and J. I. Hahm, *J Nanosci Nanotechnol*, **2005**, 5, 1915.
11. D. S. Bohle and C. J. Spina, *J Am Chem Soc*, **200**9, 131, 4397.
12. A. N. Rao, B. Sivasankar and V. Sadasivam, *J Hazard Mater*, **2009**, 166, 1357.
13. B. Santara, P. K. Giri, K. Imakita and M. Fujii, *Nanoscale*, **2013**, 5, 5476.
14. N. C. Selvam, J. J. Vijaya and L. J. Kennedy, *J Nanosci Nanotechnol*, **2014**, 14, 2317.
15. J. C. Sin, S. M. Lam, K. T. Lee and A. R. Mohamed, *J Colloid Interface Sci*, **2013**, 401, 40.

16. A. K. Raj, P. Prabhakar Rao, T. S. Sreena, S. Sameera, V. James and U. A. Renju, *Phys Chem Chem Phys*, **2014**, 16, 23699.

17. F. Zheng, M. He, Y. Yang and Q. Chen, *Nanoscale*, **2015**, DOI: 10.1039/c4nr06321j.

18. X. H. Zhou, B. C. Huang, T. Zhou, Y. C. Liu and H. C. Shi, *Chemosphere*, **2015**, 119, 568.

19. C. Y. Chen, J. H. Huang, K. Y. Lai, Y. J. Jen, C. P. Liu and J. H. He, *Opt Express*, **2012**, 20, 2015.

20. W. J. E. Beek, M. M. Wienk and R. A. J. Janssen, *Adv Mater*, **2004**, 16, 1009.

21. S. Li, M. S. Toprak, Y. S. Jo, J. Dobson, D. K. Kim and M. Muhammed, *Adv Mater*, **2007**, 19, 4347.

22. W. Y. Chen and Y. C. Chen, *Anal Bioanal Chem*, **2010**, 398, 2049.

23. Y. Kikuchi, Q. Qian, M. Machida and H. Tatsumoto, *Carbon*, **2006**, 44, 195.

24. O. D. Jayakumar, C. Sudakar, C. Persson, V. Sudarsan, T. Sakuntala, R. Naik and A. K. Tyagi, *Cryst Growth Des*, **2009**, 9, 4450.

25. M. Pashchanka, R. C. Hoffmann, A. Gurlo, J. C. Swarbrick, J. Khanderi, J. Engstler, A. Issanin and J. J. Schneider, *Dalton Trans*, **2011**, 40, 4307.

26. X. Sun, X. Qiu, L. Li and G. Li, *Inorg Chem*, **2008**, 47, 4146.

27. J. H. He, C. S. Lao, L. J. Chen, D. Davidovic and Z. L. Wang, *J Am Chem Soc*, **2005**, 127, 16376.

28. W. Liu, F. Xiu, K. Sun, Y. H. Xie, K. L. Wang, Y. Wang, J. Zou, Z. Yang and J. Liu, *J Am Chem Soc*, **2010**, 132, 2498.

29. K. Matsuyama, N. Ihsan, K. Irie, K. Mishima, T. Okuyama and H. Muto, *J Colloid Interface Sci*, **2013**, 399, 19.

30. T. Omata, K. Takahashi, S. Hashimoto, Y. Maeda, K. Nose, S. Otsuka-Yao-Matsuo and K. Kanaori, *J Colloid Interface Sci*, **2011**, 355, 274.

31. Q. Yang, Y. Liu, C. Pan, J. Chen, X. Wen and Z. L. Wang, *Nano Lett*, **2013**, 13, 607.

32. K. Bhattacharyya, J. Majeed, K. K. Dey, P. Ayyub, A. K. Tyagi and S. R. Bharadwaj, *J Phys Chem C*, **2014**, 118, 15946.

33. I. Concina and A. Vomiero, *Small*, **2014**, DOI: 10.1002/smll.201402334.

34. S. Y. Jung, H. K. Jun, S. J. Lee, T. J. Lee, C. K. Ryu and J. C. Kim, *Environ Sci Technol*, **2005**, 39, 9324.

35. B. O'Regan and M. Grätzel, *Nature*, **1991**, 353, 737.

36. L. N. Quan, Y. H. Jang, K. A. Stoerzinger, K. J. May, Y. J. Jang, S. T. Kochuveedu, Y. Shao-Horn and D. H. Kim, *Phys Chem Chem Phys*, **2014**, 16, 9023.

37. R. K. Biroju, P. K. Giri, S. Dhara, K. Imakita and M. Fujii, *ACS Appl Mater Interfaces*, **2014**, 6, 377.

38. Y. W. Chen, Y. C. Liu, S. X. Lu, C. S. Xu, C. L. Shao, C. Wang, J. Y. Zhang, Y. M. Lu, D. Z. Shen and X. W. Fan, *J Chem Phys*, **2005**, 123, 134701.

39. A. Yoon, W. K. Hong and T. Lee, *J Nanosci Nanotechnol*, **2007**, 7, 4101.

40. G. Shen, Y. Bando, D. Chen, B. Liu, C. Zhi and D. Golberg, *J Phys Chem B*, **2006**, 110, 3973.

41. J. Kang, T. Moon, Y. Jeon, H. Kim and S. Kim, *J Nanosci Nanotechnol*, **2013**, 13, 3526.

42. H. Li, Y. Huang, Q. Zhang, Y. Qiao, Y. Gu, J. Liu and Y. Zhang, *Nanoscale*, **2011**, 3, 654.

43. R. Sridhar, C. Manoharan, S. Ramalingam, S. Dhanapandian and M. Bououdina, *Spectrochim Acta A Mol Biomol Spectrosc,* **2014**, 120, 297.

44. Q. Hou, F. Meng and J. Sun, *Nanoscale Res Lett,* **2013**, 8, 144.

45. R. Ullah and J. Dutta, *J Hazard Mater*, **2008**, 156, 194.

46. S. J. Pearton, D. P. Norton, K. Ip, Y. W. Heo and T. Steiner, *SuperlattMicrostruc*, **2003**, 34, 3.

47. X. Wang, W. Cai, Y. Lin, G. Wang and C. Liang, *J Mater Chem*, **2010**, 20, 8582.

48. X. Wang, W. Cai, S. Liu, G. Wang, Z. Wu and H. Zhao, *Colloids SurfA*, **2013**, 422, 199.

49. S. P. Singh, L. Q. Ma and M. J. Hendry, *J Hazard Mater*, **2006**, 136, 654.

50. S. Ma, R. Li, C. Lv, W. Xu and X. Gou, *J Hazard Mater*, **2011**, 192, 730.

51. T. Zhai, S. Xie, Y. Zhao, X. Sun, X. Lu, M. Yu, M. Xu, F. Xiao and Y. Tong, *CrystEngComm*, **2012**, 14, 1850.

52. J. Zheng, Z.-Y. Jiang, Q. Kuang, Z.-X. Xie, R.-B. Huang and L.-S. Zheng, *J Solid State Chem*, **2009**, 182, 115.

53. M. Landmann, E. Rauls and W. G. Schmidt, *J Phys: Condens Matter*, **2012**, 24, 195503.

54. N. Nataraj, G. S. Anjusree, A. A. Madhavan, P. Priyanka, D. Sankar, N. Nisha, S. V. Lakshmi, R. Jayakumar, A. Balakrishnan and R. Biswas, *J Biomed Nanotechnol*, **2014**, 10, 864.

55. K. Naik and M. Kowshik, *Mater Sci Eng C Mater Biol Appl*, **2014**, 34, 62.

56. Q. Mu, Y. Li, Y. Ma and X. Zhong, *Analyst*, **2014**, 139, 996.

57. C. Larue, H. Castillo-Michel, S. Sobanska, N. Trcera, S. Sorieul, L. Cecillon, L. Ouerdane, S. Legros and G. Sarret, *J Hazard Mater*, **2014**, 273, 17.

58. P. Kongsong, L. Sikong, S. Niyomwas and V. Rachpech, *ScientWorldJ*, **2014**, 2014, 869706.

59. J. H. Kim, F. A. Sheikh, H. W. Ju, H. J. Park, B. M. Moon, O. J. Lee and C. H. Park, *Int J Biol Macromol*, **2014**, 68, 158.

60. S. Kato, H. Aoshima, Y. Saitoh and N. Miwa, *J Nanosci Nanotechnol*, **2014**, 14, 3285.

61. Y. Hou, M. Lai, X. Chen, J. Li, Y. Hu, Z. Luo, X. Ding and K. Cai, *J Biomed Mater Res A*, **2014**, 102, 1726.

62. W. J. Ong, L. L. Tan, S. P. Chai, S. T. Yong and A. R. Mohamed, *Nanoscale*, **2014**, 6, 1946.

63. K. Parida, K. G. Mishra and S. K. Dash, *J Hazard Mater*, **2012**, 241-242, 395.

64. T. Luo, J. Cui, S. Hu, Y. Huang and C. Jing, *Environ Sci Technol*, **2010**, 44, 9094.

65. Y. L. Pang and A. Z. Abdullah, *App Catal, B*, **2013**, 129, 473.

66. J. Yu, G. Dai, Q. Xiang and M. Jaroniec, *J Mater Chem*, 2011, 21, 1049.

67. J. Ju, X. Chen, Y. Shi, J. Miao and D. Wu, *Powder Technol*, **2013**, 237, 616.

68. F. Luo, C.-J. Jia, R. Liu, L.-D. Sun and C.-H. Yan, *Mater Res Bull*, **2013**, 48, 1122.

69. S. Lahiri, K. Roy, S. Bhattacharya, S. Maji and S. Basu, *Appl Radiat Isot*, **2005**, 63, 293.

70. F. Luo, C.-J. Jia, W. Song, L.-P. You and C.-H. Yan, *Cryst Growth Des*, **2005**, 5, 137.

71. R. Jindal, M. M. Sinha and H. C. Gupta, *Spectrochim Acta Part A*, **2013**, 113, 286.

72. F. Liu, X. Shao, Y. Yin, L. Zhao, Q. Sun, Z. Shao, X. Liu and X. Meng, *J Rare Earths*, **2011**, 29, 97.

73. A. B. Garg, K. V. Shanavas, B. N. Wani and S. M. Sharma, *J Solid State Chem*, **2013**, 203, 273.

74. S. Mahapatra, S. K. Nayak, G. Madras and T. N. Guru Row, *IndEng Chem Res*, **2008**, 47, 6509.

75. L. Zhu, Q. Li, J. Li, X. Liu, J. Meng and X. Cao,*J Nanopart Res*, **2007**, 9, 261.

76. H. Wang, Y. Meng and H. Yan, *Inorg Chem Commun*, **2004**, 7, 553.

77. L. Chen, *Mater Lett*, **2006**, 60, 1859.

78. J. L. F. Da Silva, M. V. Ganduglia-Pirovano and J. Sauer, *Phys Rev B: Condens Matter*, **2007**, 76.

79. L. Chen, *Hydrothermal synthesis and ethanol sensing properties of* $CeVO_4$ *and* $CeVO_4$-CeO_2 *powders*, Elsevier, Amsterdam, **2006**.

80. E. V. Tsipis, M. V. Patrakeev, V. V. Kharton, N. P. Vyshatko and J. R. Frade, *J Mater Chem*, **2002**, 12, 3738.

81. K.-T. Li and Z.-H. Chi, *Appl Catal A*, **2001**, 206, 197.

82. M. P. Alvarez-Berrios, A. Castillo, C. Rinaldi and M. Torres-Lugo, *Int J Nanomedicine*, **2014**, 9, 145.

83. P. Cantillon-Murphy, L. L. Wald, E. Adalsteinsson and M. Zahn, *J Magn Magn Mater*, **2010**, 322, 727.

84. A. Jordan, R. Scholz, P. Wust, H. Fähling and F. Roland, *J Magn Magn Mater*, **1999**, 201, 413.

85. R. E. Rosensweig, *J Magn Magn Mater*, **2002**, 252, 370.

86. T. M. Liu, J. Yu, C. A. Chang, A. Chiou, H. K. Chiang, Y. C. Chuang, C. H. Wu, C. H. Hsu, P. A. Chen and C. C. Huang, *Sci Rep*, **2014**, 4, 5593.

87. Y. Ling, M. Long, P. Hu, Y. Chen and J. Huang, *J Hazard Mater*, **2014**, 264, 195.

88. L. Zhou, B. He and J. Huang, *ACS Appl Mater Interfaces*, **2013**, 5, 8678.

89. L. Zhang, S. Guo and S. Dong, *J Biomed Nanotechnol*, **2009**, 5, 586.

90. J. Mukherjee, K. Solanki and M. N. Gupta, *Methods Mol Biol*, **2013**, 1051, 117.

91. Q. A. Pankhurst,N. T. K. Thanh, S. K. Jones and J. Dobson, *J Phys D: Appl Phys*,**2009**, 42, 224001.

92. Q. A. Pankhurst, J. Connolly, S. K. Jones and J. Dobson, *J Phys D: Appl Phys*, **2003**, 36, R167.

93. V. K. Verma, S. R. Kamaraju, R. Kancherla, L. K. Kona, S. S. Beevi, T. Debnath, S. P. Usha, R. Vadapalli, A. S. Arbab and L. K. Chelluri, *Int J Nanomedicine*, **2015**, 10, 711.

94. H. Nejadnik, D. Ye, O. D. Lenkov, J. S. Donig, J. E. Martin, R. Castillo, N. Derugin, B. Sennino, J. Rao and H. Daldrup-Link, *ACS Nano*, **2015**, DOI: 10.1021/nn504494c.

95. K. Yang, G. Yang, L. Chen, L. Cheng, L. Wang, C. Ge and Z. Liu, *Biomaterials*, **2015**, 38, 1.

96. P. Hua, Y. Y. Wang, L. B. Liu, J. L. Liu, J. Y. Liu, Y. Q. Yang and S. R. Yang, *Mol Med Rep*, **2015**, 11, 113.

97. F. Azzabi, M. Rottmar, V. Jovaisaite, M. Rudin, T. Sulser, A. Boss and D. Eberli, *Tissue Eng Part C Methods*, **2015**, 21, 182.

98. S. H. Sun, *Adv Mater*, **2006**, 18, 393.

99. H. B. He, B. Li, J. P. Dong, Y. Y. Lei, T. L. Wang, Q. W. Yu, Y. Q. Feng and Y. B. Sun, *ACS Appl Mater Interfaces*, **2013**, 5, 8058.

100. W. Jiang, X. Chen, Y. Niu and B. Pan, *J Hazard Mater*, **2012**, 243, 319.

101. Y. Liu, Y. Wang, S. Zhou, S. Lou, L. Yuan, T. Gao, X. Wu, X. Shi and K. Wang, *ACS Appl Mater Interfaces*, **2012**, 4, 4913.

102. S. Zhang, Y. Zhang, G. Bi, J. Liu, Z. Wang, Q. Xu, H. Xu and X. Li, *J Hazard Mater*, **2014**, 270, 27.

103. R. S. Ningthoujam, R. K. Vatsa, A. Kumar and B. N. Pandey,*Functional Materials*, ed. S. Banerjee. A. K. Tyagi, Elsevier, London, **2012**, 229.

104. J. P. Da Silva, R. Kulasekharan, C. Cordeiro, S. Jockusch, N. J. Turro and V. Ramamurthy, *Org Lett*, **2012**, 14, 560.

105. M. Okube and S. Sasaki, *J Appl Crystallogr*, **2014**, 47, 1387.

106. Y. S. Kang, S. Risbud, J. F. Rabolt and P. Stroeve, *Chem Mater*, **1996**, 8, 2209.

107. Q. A. Pankhurst and R. J. Pollard, *Phys Rev Lett*, **1991**, 67, 248.

108. A. A. Allam, M. E. Sadat, S. J. Potter, D. B. Mast, D. F. Mohamed, F. S. Habib and G. M. Pauletti, *Nanoscale Res Lett*, **2013**, 8, 426.

109. K. C. Barick, S. Singh, D. Bahadur, M. A. Lawande, D. P. Patkar and P. A. Hassan, *J Colloid Interface Sci*, **2014**, 418, 120.

110. G. H. Du, Z. L. Liu, X. Xia, Q. Chu and S. M. Zhang, *J Sol-Gel Sci Technol*, **2006**, 39, 285.

111. O. D. Jayakumar, B. P. Mandal, J. Majeed, G. Lawes, R. Naik and A. K. Tyagi, *J Mater Chem C,***2013**, 1, 3710.

112. C. Kacar, P. E. Erden, S. Pekyardimci and E. Kilic, *Artif Cells Nanomed Biotechnol*, **2013**, 41, 2.

113. D. H. Kim, Y. Tamada, T. Ono, S. D. Bader, E. A. Rozhkova and V. Novosad, *J Nanosci Nanotechnol*, **2014**, 14, 2648.

114. C. W. Lai, Y. H. Wang, B. P. Uttam, Y. C. Chen, J. K. Hsiao, C. L. Liu, H. M. Liu, C. Y. Chen and P. T. Chou, *Chem Commun (Camb)*, **2008**, 5342.

115. J. Li, S. Zhang, C. Chen, G. Zhao, X. Yang, J. Li and X. Wang, *ACS Appl Mater Interfaces*, **2012**, 4, 4991.

116. R. Ghosh, L. Pradhan, Y. P. Devi, S. S. Meena, R. Tewari, A. Kumar, S. Sharma, N. S. Gajbhiye, R. K. Vatsa, B. N. Pandey and R. S. Ningthoujam, *J Mater Chem*, **2011**, 21, 13388.

117. O. Kalogirou, M. Angelakeris, C. Dendrinou-Samara, S. Mourdikoudis, K. Simeonidis, K. Gloystein, A. Vilalta-Clemente and I. Tsiaoussis, *J Nanosci Nanotechnol*, **2010**, 10, 6017.

118. D. Weller and M. F. Doerner, *Annu Rev Mater Sci*, **2000**, 30, 611.

119. G. Brown, B. Kraczek, A. Janotti, T. C. Schulthess, G. M. Stocks and D. D. Johnson, *Phys Rev B: Condens. Matter*, **2003**, 68, 052405.

120. K. Osamu, S. Takehito, O. Satoshi, S. Yutaka and A. Hajime, *Jpn J Appl Phys*, **2004**, 43, L115.

121. J. Gao, G. Liang, J. S. Cheung, Y. Pan, Y. Kuang, F. Zhao, B. Zhang, X. Zhang, E. X. Wu and B. Xu, *J Am Chem Soc*, **2008**, 130, 11828.

122. J. Gao, G. Liang, B. Zhang, Y. Kuang, X. Zhang and B. Xu, *J Am Chem Soc*, **2007**, 129, 1428.

123. D. Ho, X. Sun and S. Sun, *Acc Chem Res*, **2011**, 44, 875.

124. Y. Liu, K. Yang, L. Cheng, J. Zhu, X. Ma, H. Xu, Y. Li, L. Guo, H. Gu and Z. Liu, *Nanomedicine (Lond)*, **2013**, 9, 1077.

125. J. Kim, Y. Lee and S. Sun, *J Am Chem Soc*, **2010**, 132, 4996.

126. S. Zhang, S. Guo, H. Zhu, D. Su and S. Sun, *J Am Chem Soc*, **2012**, 134, 5060.

127. S. Zhang, X. Zhang, G. Jiang, H. Zhu, S. Guo, D. Su, G. Lu and S. Sun, *J Am Chem Soc*, **2014**, 136, 7734.

128. S. Sun, C. B. Murray, D. Weller, L. Folks and A. Moser, *Science*, **2000**, 287, 1989.

129. H. Zeng, J. Li, Z. L. Wang, J. P. Liu and S. H. Sun, *Nano Lett*, **2004**, 4, 187.

130. H. Gu, P. L. Ho, K. W. Tsang, L. Wang and B. Xu, *J Am Chem Soc*, **2003**, 125, 15702.

131. H. Gu, P. L. Ho, K. W. Tsang, C. W. Yu and B. Xu, *Chem Commun (Camb)*, **2003**, 1966.

132. Y. Zhu, E. Kockrick, S. Kaskel, T. Ikoma and N. Hanagata, *J Phys Chem C*, **2009**, 113, 5998.

133. J. A. Dirksen and T. A. Ring, *Chem Eng Sci*, **1991**, 46, 2389.

134. V. K. LaMer and R. H. Dinegar, *J Am Chem Soc*, **1950**, 72, 4847.

135. *Handbook of Nanophase and Nanostructured Materials*, Springer US, **2003**, ch. 3, 55.

136. S. D. Lubetkin, *Controlled Particle, Droplet and Bubble Formation*, Oxford, **1994**,159.

137. D. Sordelet and M. Akinc, *J Colloid Interface Sci*, **1988**, 122, 47.

138. J. N. Sahu, K. Mahalik, A. V. Patwardhan and B. C. Meikap, *Ind Eng Chem Res*, **2008**, 47, 4689.

139. C. J. Brinker and G. W. Scherer, *Sol–Gel Science*, Academic Press,**1990.**

140. J. D. Wright and N. A. J. M. Sommerdijk, *Sol–Gel Materials: Chemistry and Applications*, CRC Press, **2000**.

141. L. Akhigbe, S. Ouki, D. Saroj and X. M. Lim, *Environ Sci Pollut Res Int*, **2014**, 21, 10940-10948.

142. G. Carre, E. Hamon, S. Ennahar, M. Estner, M. C. Lett, P. Horvatovich, J. P. Gies, V. Keller, N. Keller and P. Andre, *Appl Environ Microbiol*, **2014**, 80, 2573.

143. K. I. Dhanalekshmi and K. S. Meena, *Spectrochim Acta A Mol Biomol Spectrosc*, **2014**, 128, 887.

144. F. Dong, S. Guo, H. Wang, X. Li and Z. Wu, *J Phys Chem C*, **2011**, 115, 13285.

145. M. Ito, S. Fukahori and T. Fujiwara, *Environ Sci Pollut Res Int*, **2014**, 21, 834.

146. S. Pal, Y. K. Tak, J. Joardar, W. Kim, J. E. Lee, M. S. Han and J. M. Song, *J Nanosci Nanotechnol*, **2009**, 9, 2092.

147. A. Shrestha, M. Cordova and A. Kishen, *J Endod*, **2015**, DOI: 10.1016/j.joen.2014.12.007.

148. S. Kang, M. Herzberg, D. F. Rodrigues and M. Elimelech, *Langmuir*, **2008**, 24, 6409.

149. X. H. Yang, W. J. Kong, M. H. Yang, S. L. Chen, M. Zhao and Z. Ouyang, *Zhongguo Zhong Yao Za Zhi*, **2013**, 38, 3997.

150. J. P. Lafleur, S. Senkbeil, T. G. Jensen and J. P. Kutter, *Lab Chip*, **2012**, 12, 4651.

151. N. Zhang, H. Peng and B. Hu, *Talanta*, **2012**, 94, 278.

152. C. Cheng, A. Amini, C. Zhu, Z. Xu, H. Song and N. Wang, *Sci Rep*, **2014**, 4, 4181.

153. A. Hernandez-Gordillo, M. Arroyo, R. Zanella and V. Rodriguez-Gonzalez, *J Hazard Mater*, **2014**, 268, 84.

154. Y. Yang, Y. Li, L. Zhu, H. He, L. Hu, J. Huang, F. Hu, B. He and Z. Ye, *Nanoscale*, **2013**, 5, 10461.

155. F. Fu and Q. Wang, *J Environ Manage*, **2011**, 92, 407.

156. F. J. Perez-Vazquez, R. Flores-Ramirez, A. C. Ochoa-Martinez, S. T. Orta-Garcia, B. Hernandez-Castro, L. Carrizalez-Yanez and I. N. Perez-Maldonado, *Environ Monit Assess*, **2015**, 187, 4119.

157. E. Peruzzi, C. Macci, S. Doni, M. Volpi and G. Masciandaro, *Environ Sci Pollut Res Int*, **2015**, 22, 2447.

158. A. Sapkota, A. R. Sapkota, M. Kucharski, J. Burke, S. McKenzie, P. Walker and R. Lawrence, *Environ Int*, **2008**, 34, 1215.

159. X. Tan, Y. Liu, G. Zeng, X. Wang, X. Hu, Y. Gu and Z. Yang, *Chemosphere*, **2015**, DOI: 10.1016/j.chemosphere.2014.12.058.

160. F. P. Tsague Manfo, E. A. Nantia and P. P. Mathur, *Curr Mol Pharmacol*, **2015,** 8, 119.

161. Y. Hu, X. Liu, J. Bai, K. Shih, E. Y. Zeng and H. Cheng, *Environ Sci Pollut Res Int*, **2013**, 20, 6150.

162. D. L. Villeneuve, L. R. Curtis, J. J. Jenkins, K. E. Warner, F. Tilton, M. L. Kent, V. G. Watral, M. E. Cunningham, D. F. Markle, D. Sethajintanin, O. Krissanakriangkrai, E. R. Johnson, R. Grove and K. A. Anderson, *Environ Sci Technol*, **2005**, 39, 3495.

163. F. Zan, S. Huo, B. Xi, J. Su, X. Li, J. Zhang and K. M. Yeager, *J Environ Monit*, **2011**, 13, 2788.

164. S. Srinivasa Gowd, M. Ramakrishna Reddy and P. K. Govil, *J Hazard Mater*, **2010**, 174, 113.

165. H. H. Lin and A. Y. Lin, *Water Res*, **2014**, 48, 559.

166. R. Yuan, B. Zhou and L. Ma, *Water Sci Technol*, **2014**, 70, 642.

167. S. W. Hong, Y. S. Choi, G. Kwon and K. Y. Park, *Water Sci Technol*, **2005**, 52, 107.

168. Y. Chen, H. Li, W. Liu, Y. Tu, Y. Zhang, W. Han and L. Wang, *Chemosphere*, **2014**, 113, 48.

169. Q. Li, C. Batchelor-McAuley and R. G. Compton, *J Phys Chem B*, **2010**, 114, 9713.

170. Q. Li, C. Batchelor-McAuley and R. G. Compton, *J Phys Chem B*, **2010**, 114, 7423.

171. A. Mishra, J. S. Melo, D. Sen and S. F. D'Souza, *J Colloid Interface Sci*, **2014**, 414, 33.

172. M. A. Khan, R. Bushra, A. Ahmad, S. A. Nabi, D. A. Khan and A. Akhtar, *Arch Environ Contam Toxicol*, **2014**, 66, 259.

173. L. M. Blaney, S. Cinar and A. K. SenGupta, *Water Res*, **2007**, 41, 1603.

174. Q. Y. Sun, P. Lu and L. Z. Yang, *Environ Geochem Health*, **2004**, 26, 311.

175. M. H. Khan, D. H. Ha and J. Jung, *J Environ Sci Health A Tox Hazard Subst Environ Eng*, **2013**, 48, 534.

176. S. Babel and T. A. Kurniawan, *J Hazard Mater,* **2003**, 97, 219.

177. D. Banerjee, A. J. Cairns, J. Liu, R. K. Motkuri, S. K. Nune, C. A. Fernandez, R. Krishna, D. M. Strachan and P. K. Thallapally, *Acc Chem Res*, **2014**, DOI: 10.1021/ar5003126.

178. M. O. Omorogie, J. O. Babalola, E. I. Unuabonah and J. R. Gong, *Environ Technol*, **2014**, 35, 611.

179. S. Singh, K. C. Barick and D. Bahadur, *J Hazard Mater*, **2011**, 192, 1539.

180. F. Yu, J. Chen, L. Chen, J. Huai, W. Gong, Z. Yuan, J. Wang and J. Ma, *J Colloid Interface Sci*, **2012**, 378, 175.

181. J. G. Yu, L. Y. Yu, H. Yang, Q. Liu, X. H. Chen, X. Y. Jiang, X. Q. Chen and F. P. Jiao, *Sci Total Environ*, **2015**, 502, 70.

182. A. Ayati, A. Ahmadpour, F. F. Bamoharram, B. Tanhaei, M. Manttari and M. Sillanpaa, *Chemosphere*, **2014**, 107, 163.

183. M. Mahmoudi, V. Serpooshan and S. Laurent, *Nanoscale*, 2011, 3, 3007.

184. T. Neuberger, B. Schöpf, H. Hofmann, M. Hofmann and B. von Rechenberg, *J Magn Magn Mater*, **2005**, 293, 483.

185. D. Singh, J. M. McMillan, A. V. Kabanov, M. Sokolsky-Papkov and H. E. Gendelman, *Nanomedicine (Lond)*, **2014**, 9, 501.

186. J. Zhong, W. Liu, L. Jiang, M. Yang and P. C. Morais, *Rev Sci Instrum*, **2014**, 85, 094905.

187. M. Chanana, Z. Mao and D. Wang, *J Biomed Nanotechnol*, **2009**, 5, 652.

188. E. K. Efthimiadou, C. Tapeinos, A. Chatzipavlidis, N. Boukos, E. Fragogeorgi, L. Palamaris, G. Loudos and G. Kordas, *Int J Pharm*, **2014**, 461, 54.

189. M. Heidari Majd, D. Asgari, J. Barar, H. Valizadeh, V. Kafil, G. Coukos and Y. Omidi, *J Drug Target*, **2013**, 21, 328.

190. C. Tao and Y. Zhu, *Dalton Trans*, **2014**, 43, 15482.

191. B. Sahoo, K. S. Devi, S. Dutta, T. K. Maiti, P. Pramanik and D. Dhara, *J Colloid Interface Sci*, **2014**, 431, 31.

192. R. Liang, M. Wei, D. G. Evans and X. Duan, *Chem Commun (Camb)*, **2014**, 50, 14071.

193. M. Xie, H. Shi, K. Ma, H. Shen, B. Li, S. Shen, X. Wang and Y. Jin, *J Colloid Interface Sci*, **2013**, 395, 306.

194. M. Xie, H. Shi, Z. Li, H. Shen, K. Ma, B. Li, S. Shen and Y. Jin, *Colloids Surf B Biointerf*, **2013**, 110, 138.

195. W. Guo, C. Yang, H. Lin and F. Qu, *Dalton Trans*, **2014**, 43, 18056.

196. E. Alphandery, *J Cancer*, **2014**, 5, 472.

197. A. Hervault and N. T. Thanh, *Nanoscale*, **2014**, 6, 11553.

198. J. Owen, Q. Pankhurst and E. Stride, *Int J Hyperthermia*, **2012**, 28, 362.

199. M. L. Etheridge, K. R. Hurley, J. Zhang, S. Jeon, H. L. Ring, C. Hogan, C. L. Haynes, M. Garwood and J. C. Bischof, *Technology (Singap World Sci)*, **2014**, 2, 214.

200. A. Hardiansyah, L. Y. Huang, M. C. Yang, T. Y. Liu, S. C. Tsai, C. Y. Yang, C. Y. Kuo, T. Y. Chan, H. M. Zou, W. N. Lian and C. H. Lin, *Nanoscale Res Lett*, **2014**, 9, 497.

201. N. V. Jadhav, A. I. Prasad, A. Kumar, R. Mishra, S. Dhara, K. R. Babu, C. L. Prajapat, N. L. Misra, R. S. Ningthoujam, B. N. Pandey and R. K. Vatsa, *Colloids Surf B Biointerfaces*, **2013**, 108, 158.

202. M. K. Jaiswal, A. Pradhan, R. Banerjee and D. Bahadur, *J Nanosci Nanotechnol*, **2014**, 14, 4082.

203. J. Kolosnjaj-Tabi, R. Di Corato, L. Lartigue, I. Marangon, P. Guardia, A. K. Silva, N. Luciani, O. Clement, P. Flaud, J. V. Singh, P. Decuzzi, T. Pellegrino, C. Wilhelm and F. Gazeau, *ACS Nano*, **2014**, 8, 4268.

204. S. Kossatz, R. Ludwig, H. Dahring, V. Ettelt, G. Rimkus, M. Marciello, G. Salas, V. Patel, F. J. Teran and I. Hilger, *Pharm Res*, **2014**, 31, 3274.

205. M. Lin, J. Huang and M. Sha, *J Nanosci Nanotechnol*, **2014**, 14, 792.

206. A. I. Prasad, A. K. Parchur, R. R. Juluri, N. Jadhav, B. N. Pandey, R. S. Ningthoujam and R. K. Vatsa, *Dalton Trans*, **2013**, 42, 4885.

207. S. Rana, N. V. Jadhav, K. C. Barick, B. N. Pandey and P. A. Hassan, *Dalton Trans*, **2014**, 43, 12263.

208. T. Sadhukha, T. S. Wiedmann and J. Panyam, *Biomaterials*, **2014**, 35, 7860.

209. H. S. Sharma, P. K. Menon, J. V. Lafuente, Z. P. Aguilar, Y. A. Wang, D. F. Muresanu, H. Mossler, R. Patnaik and A. Sharma, *J Nanosci Nanotechnol*, **2014**, 14, 577.

210. C. Yuan, Y. An, J. Zhang, H. Li, H. Zhang, L. Wang and D. Zhang, *Nanotechnology*, **2014**, 25, 345101.

211. H. Gu, K. Xu, Z. Yang, C. K. Chang and B. Xu, *Chem Commun (Camb)*, **2005**, 4270.

212. D. S. Luo, Q. W. Mi, X. J. Meng, Y. Gao, Y. P. Dai and C. H. Deng, *Beijing Da Xue Xue Bao*, **2012**, 44, 524.

213. J. Shi, X. Yu, L. Wang, Y. Liu, J. Gao, J. Zhang, R. Ma, R. Liu and Z. Zhang, *Biomaterials*, **2013**, 34, 9666.

214. H. J. Yoon, T. G. Lim, J. H. Kim, Y. M. Cho, Y. S. Kim, U. S. Chung, J. H. Kim, B. W. Choi, W. G. Koh and W. D. Jang, *Biomacromolecules*, **2014**, 15, 1382.

215. P. Sharma, S. Brown, G. Walter, S. Santra and B. Moudgil, *Adv Colloid Interface Sci*, **2006**, 123-126, 471.

216. S. Maenosono, T. Suzuki and S. Saita, *J Magn Magn Mater*, **2008**, 320, L79.

217. Q. Pankhurst, D. Hautot, N. Khan and J. Dobson, *J Alzheimers Dis*, **2008**, 13, 49.

218. S. W. Chou, Y. H. Shau, P. C. Wu, Y. S. Yang, D. B. Shieh and C. C. Chen, *J Am Chem Soc*, **2010**, 132, 13270.

219. X. Ma, A. Gong, B. Chen, J. Zheng, T. Chen, Z. Shen and A. Wu, *Colloids Surf B Biointerfaces*, **2014**, 126C, 44.

220. W. S. Seo, J. H. Lee, X. Sun, Y. Suzuki, D. Mann, Z. Liu, M. Terashima, P. C. Yang, M. V. McConnell, D. G. Nishimura and H. Dai, *Nat Mater*, **2006**, 5, 971.

221. H. Kosuge, S. P. Sherlock, T. Kitagawa, M. Terashima, J. K. Barral, D. G. Nishimura, H. Dai and M. V. McConnell, *PLoS One*, **2011**, 6, e14523.

222. T. Kawano and H. Imai, *Colloids Surf A*, **2008**, 319, 130.

223. K. Bhattacharyya, S. Varma, A. K. Tripathi, S. R. Bharadwaj and A. K. Tyagi, *J. Phys. Chem. C*, **2008**, 112, 19102.

224. V. S. Jakkal, Private Communication.

225. S. Brunauer, P. H. Emmett and E. Teller, *J Am Chem Soc*, **1938**, 60, 309.

226. F. Rouquerol, R. J. and K. Sing, *Adsorption by Powder & Porous Solid*, Academic Press, London, **1999**.

227. I. Langmuir, *J Am Chem Soc*, **1917**, 39, 1848.

228. K. K. H. Choy, G. McKay and J. F. Porter, *Resources, Conservation and Recycling*, **1999**, 27, 57.

229. H. Freundlich, *Z Phys Chem*, **1906**, 57, 385.

230. M. I. Tempkin, *V. Pyzhev, Acta Phys. Chim. USSR*, **1940**, 12, 327.

231. S. J. Allen, Q. Gan, R. Matthews and P. A. Johnson, *Bioresour Technol*, **2003**, 88, 143.

232. M. M. Dubinin, E. D. Zaverina and L. V. Radushkevich, *Zh. Fiz. Khim.*, **1947**, 21, 1362.

233. S. Lagergren, *Handlingar*, **1898**, 24, 1.

234. S. Lagergren, *Kungliga Svenska Vetenskapsakademiens Handlingar*, **1898**, 24.

235. Y. S. Ho and G. McKay, *Proc Safety Environ Protect*, **1998**, 76, 183.

236. Y. S. Ho and G. McKay, *Water Res*, **2000**, 34, 735.

237. J. W. Weber and J. C. Morris, *J. Sanit. Eng. Div. ACSE*, **1963**, 89, 31.

238. W. H. Cheung, Y. S. Szeto and G. McKay, *Bioresour Technol*, **2007**, 98, 2897.

239. G. E. Boyd, A. W. Adamson and L. S. Myers, Jr., *J Am Chem Soc*, **1947**, 69, 2836.

240. M. Sankar, G. Sekaran, S. Sadulla and T. Ramasami, *J ChemTechnolBiotechnol*, **1999**, 74, 337.

241. N. M. Hassan and K. Adu-Wusu, *Solvent Extr Ion Exch*, **2005**, 23, 375.

242. L. L. Lao and R. V. Ramanujan, *J Mater Sci Mater Med*, **2004**, 15, 1061.

243. M. Kallumadil, M. Tada, T. Nakagawa, M. Abe, P. Southern and Q. A. Pankhurst, *J Magn Magn Mater,* **2009**, 321, 1509.

244. C. D. Klaassen, *Casarett And Doull's Toxicology: The Basis Science Of Poisons*, Macmillan: New York, **1986**.

245. T. R. Sandrin and R. M. Maier, *Environ Health Perspect*, **2003**, 111, 1093.

246. J. Y. Choi, D. S. Kim and J. Y. Lim, *J Environ Sci Health A Tox Hazard Subst Environ Eng*, 2006, 41, 1155.

247. F. M. Koehler, M. Rossier, M. Waelle, E. K. Athanassiou, L. K. Limbach, R. N. Grass, D. Gunther and W. J. Stark, *Chem Commun (Camb)*, **2009**, 4862.

248. Y.-H. Li, J. Ding, Z. Luan, Z. Di, Y. Zhu, C. Xu, D. Wu and B. Wei, *Carbon*, **2003**, 41, 2787.

249. A. Sarı, M. Tuzen, D. Cıtak and M. Soylak, *J Hazard Mater*, **2007**, 148, 387.

250. A. J. Romero-Anaya, M. A. Lillo-Ródenas and A. Linares-Solano, *Carbon*, **2010**, 48, 2625.

251. N. Kawasaki, F. Ogata and H. Tominaga, *J Hazard Mater*, **2010**, 181, 574.

252. N. S. Shcherbina, S. S. Kalmykov, L. A. Karpiouk, S. A. Ponomarenko, K. Hatfield, R. Haire and I. V. Perminova, *Environ Sci Technol*, **2014**, 48, 2226.

253. J. Ramkumar, S. Chandramouleeswaran, V. Sudarsan, R. K. Mishra, C. P. Kaushik, K. Raj and A. K. Tyagi, *J Hazard Mater*, **2009**, 172, 457.

254. S. Zang, Y. Su, Y. Li, H. Zhu and Q. Meng, *Inorg Chem*, **2006**, 45, 2972.

255. D. Wang, Y. Duan, Q. Luo, X. Li, J. An, L. Bao and L. Shi, *J Mater Chem*, **2012**, 22, 4847.

256. J. Yu and X. Yu, *Environ Sci Technol*, **2008**, 42, 4902.

257. H. Fu, T. Xu, S. Zhu and Y. Zhu, *Environ Sci Technol*, **2008**, 42, 8064.

258. S. W. Choi, A. Katoch, G. J. Sun, J. H. Kim, S. H. Kim and S. S. Kim, *ACS Appl Mater Interfaces*, **2014**, 6, 8281.

259. C. Cheng, B. Liu, H. Yang, W. Zhou, L. Sun, R. Chen, S. F. Yu, J. Zhang, H. Gong, H. Sun and H. J. Fan, *ACS Nano*, **2009**, 3, 3069.

260. D. Gedamu, I. Paulowicz, S. Kaps, O. Lupan, S. Wille, G. Haidarschin, Y. K. Mishra and R. Adelung, *Adv Mater*, **2014**, 26, 1541.

261. S. L. Shinde and K. K. Nanda, *Angew Chem Int Ed Engl*, **2013**, 52, 11325.

262. H. P. Kim, A. R. Yusoff, H. J. Lee, S. J. Lee, H. M. Kim, G. J. Seo, J. H. Youn and J. Jang, *Nanoscale Res Lett*, **2014**, 9, 323.

263. A. Gadisa, T. Hairfield, L. Alibabaei, C. L. Donley, E. T. Samulski and R. Lopez, *ACS Appl Mater Interfaces*, **2013**, 5, 8440.

264. S. Chakraborti, P. Joshi, D. Chakravarty, V. Shanker, Z. A. Ansari, S. P. Singh and P. Chakrabarti, *Langmuir*, **2012**, 28, 11142.

265. C. Bressy, V. G. Ngo, F. Ziarelli and A. Margaillan, *Langmuir*, **2012**, 28, 3290.

266. T. Le Bahers, T. Pauporte, F. Labat, G. Lefevre and I. Ciofini, *Langmuir*, **2011**, 27, 3442.

267. J. F. Gnichwitz, R. Marczak, F. Werner, N. Lang, N. Jux, D. M. Guldi, W. Peukert and A. Hirsch, *J Am Chem Soc*, **2010**, 132, 17910.

268. L. J. Wang, H. L. Fan, J. Shangguan, E. Croiset, Z. Chen, H. Wang and J. Mi, *ACS Appl Mater Interfaces*, **2014**, 6, 21167.

269. P. Dhage, A. Samokhvalov, D. Repala, E. C. Duin and B. J. Tatarchuk, *Phys Chem Chem Phys*, **2011**, 13, 2179.

270. P. Kannusamy and T. Sivalingam, *Colloids Surf B: Biointerfaces*, **2013**, 108, 229.

271. A. Sharma, B. P. Singh, S. Dhar, A. Gondorf and M. Spasova, *Surf Sci*, **2012**, 606, L13.

272. S. Sakohara, L. D. Tickanen and M. A. Anderson, *J Phys Chem*, **1992**, 96, 11086.

273. C. D. Palmer and R. W. Puls, *Natural Attenuation of Hexavalent Chromium in ground water and soils*, U.S. Environment Protection Agency, **1994**.

274. F. L. Arbeloa, I. L. Gonzalez, P. R. Ojeda and I. L. Arbeloa, *J Chem Soc, Faraday Trans 2: MolecChem Phys*, **1982**, 78, 989.

275. M. Muthukrishnan and B. K. Guha, *Desalination*, **2008**, 219, 171.

276. W. S. Wan Ngah, A. Kamari and Y. J. Koay, *Int J Biol Macromol*, **2004**, 34, 155.

277. B. Singha and S. K. Das, *Colloids Surf B Biointerfaces*, **2013**, 107, 97.

278. L. Zhang, X. Q. Jiang, T. C. Xu, L. J. Yang, Y. Y. Zhang and H. J. Jin, *Ind Eng Chem Res*, **2012**, 51, 5577.

279. M. Pérez-Candela, J. Martín-Martínez and R. Torregrosa-Maciá, *Water Res*, **1995**, 29, 2174.

280. M. Kobya, *Bioresour Technol*, **2004**, 91, 317.

281. N. K. Hamadi, X. D. Chen, M. M. Farid and M. G. Q. Lu, *Chem Eng J*, **2001**, 84, 95.

282. D. C. Sharma and C. F. Forster, *Bioresour Technol*, **1994**, 49, 31.

283. G. J. Alaerts, V. Jitjaturant and P. Kelderman, *Water Sci Technol*, **1989**, 21, 1701.

284. G. Cimino, A. Passerini and G. Toscano, *Water Res*, **2000**, 34, 2955.

285. S. Babel and T. A. Kurniawan, *Chemosphere,* **2004**, 54, 951.

286. V. K. Garg, R. Gupta, R. Kumar and R. K. Gupta, *Bioresour Technol*, **2004**, 92, 79.

287. K. Selvi, S. Pattabhi and K. Kadirvelu, *Bioresour Technol*, **2001**, 80, 87.

288. Y. Zeng, H. Woo, G. Lee and J. Park, *Desalination*, **2010**, 257, 102.

289. Z. Li and R. S. Bowman, *Water Res*, **2001**, 35, 3771.

290. X. S. Wang, Y. Li, L. P. Huang and J. Chen, *CLEAN – Soil, Air, Water*, **2010**, 38, 500.

291. Y. Zhu, H. Zhang, H. Zeng, M. Liang and R. Lu, *Int J Environ Sci Technol*, **2012**, 9, 463.

292. A. A. Atia, *Appl Clay Sci*, **2008**, 41, 73.

293. Y. S. Ho and G. McKay, *Process Biochem*, **1999**, 34, 451.

294. R. Gündoğan, B. Acemioğlu and M. H. Alma, *J Colloid Interface Sci*, **2004**, 269, 303.

295. C. Christophi and L. Axe, *J Environ Eng*, **2000**, 126, 66.

296. Z. Xiao, F. Peng, X. Li, R. Zhang, W. He and T. Zhou, *Surf Interf Analysis*, **2013**, 45, 1869.

297. A. Barati, M. Asgari, T. Miri and Z. Eskandari, *Environl Sci Pollut Res*, **2013**, 20, 6242.

298. M. R. Awual, T. Yaita, S. A. El-Safty, H. Shiwaku, S. Suzuki and Y. Okamoto, *Chem Eng J,* **2013**, 221, 322.

299. J. L. Gong, X. Y. Wang, G. M. Zeng, L. Chen, J. H. Deng, X. R. Zhang and Q. Y. Niu, *Chem Eng J*, **2012**, 185, 100.

300. D. Nandi, T. Basu, S. Debnath, A. K. Ghosh, A. De and U. C. Ghosh, *J Chem Eng Data*, **2013**, 58, 2809.

301. S. E. Bailey, T. J. Olin, R. M. Bricka and D. D. Adrian, *Water Res*, **1999**, 33, 2469.

302. X. Ge, C. D. Gu, X. L. Wang and J. P. Tu, *J Colloid Interface Sci*, **2015**, 438, 149.

303. J. Wu, Y. J. Zhu and F. Chen, *Small*, **2013**, 9, 2911.

304. S. J. Yang, J. H. Im, T. Kim, K. Lee and C. R. Park, *J Hazard Mater*, **2011**, 186, 376.

305. V. Vimonses, B. Jin and C. W. Chow, *J Hazard Mater*, **2010**, 177, 420.

306. K. Riahi, B. B. Thayer, A. B. Mammou, A. B. Ammar and M. H. Jaafoura, *J Hazard Mater*, **2009**, 170, 511.

307. C. D. Johnson and F. Worrall, *Water Res*, **2007**, 41, 2229.

308. I. Ali and V. K. Gupta, *Nat Protoc*, **2006**, 1, 2661.

309. B. Bayat, *J Hazard Mater*, **2002**, 95, 275.

310. A. S. Jalilov, G. Ruan, C. C. Hwang, D. E. Schipper, J. J. Tour, Y. Li, H. Fei, E. L. Samuel and J. M. Tour, *ACS Appl Mater Interfaces*, **2015**, 7, 1376.

311. J. Altmann, F. Zietzschmann, E. L. Geiling, A. S. Ruhl, A. Sperlich and M. Jekel, *Chemosphere*, **2015**, DOI: 10.1016/j.chemosphere.2014.12.061.

312. M. C. Pereira, F. S. Coelho, C. C. Nascentes, J. D. Fabris, M. H. Araujo, K. Sapag, L. C. Oliveira and R. M. Lago, *Chemosphere*, **2010**, 81, 7.

313. J. Brown, R. Richer and L. Mercier, *Microporous Mesoporous Mater*, **2000**, 37, 41.

314. P. Janos, H. Buchtova and M. Ryznarova, *Water Res*, **2003**, 37, 4938.

315. M. G. da Fonseca, M. M. de Oliveira and L. N. Arakaki, *J Hazard Mater*, **2006**, 137, 288.

316. M. Panayotova and B. Velikov, *J Environ Sci Health A Tox Hazard Subst Environ Eng*, **2002**, 37, 139.

317. L. Ringqvist, A. Holmgren and I. Oborn, *Water Res*, **2002**, 36, 2394.

318. W. Clayton, *J Soc Chem Ind*, **1926**, 45, 797.

319. C. Green-Ruiz, *Environ Technol*, **2008**, 30, 63.

320. K. Hahn, J. Kärger and V. Kukla, *Phys Rev Lett*, **1996**, 76, 2762.

321. M. G. Warner, C. L. Warner, R. S. Addleman and W. Yantasee, *Magnetic Nanomaterials for Environmental Sensing, Magnetic Nanomaterials:*, Wiley-VCH, **2010**.

322. S. Xu, Y. Wei, M. Kirkham, J. Liu, W. Mai, D. Davidovic, R. L. Snyder and Z. L. Wang, *J Am Chem Soc*, **2008**, 130, 14958.

323. K. Senthil, Y. Tak, M. Seol and K. Yong, *Nanoscale Res Lett*, **2009**, 4, 1329.

324. R. K. Upadhyay, N. Soin and S. S. Roy, *RSC Adv*, **2014**, 4, 3823.

325. T. S. Anirudhan, S. Jalajamony and S. S. Sreekumari, *Appl Clay Sci*, **2012**, 65-66, 67.

326. S. A. Idris, S. R. Harvey and L. T. Gibson, *J Hazard Mater*, **2011**, 193, 171.

327. M. C. Bruzzoniti, C. Sarzanini, A. M. Torchia, M. Teodoro, F. Testa, A. Virga and B. Onida, *J Mater Chem*, **2011**, 21, 369.

328. M. C. Bruzzoniti, A. Prelle, C. Sarzanini, B. Onida, S. Fiorilli and E. Garrone, *J Sep Sci*, **2007**, 30, 2414.

329. A. Walcarius and C. Delacôte, *Anal Chim Acta*, **2005**, 547, 3.

330. A. Dąbrowski, *Adv Colloid Interface Sci*, **2001**, 93, 135.

331. N. Mohammadpourdounighi, A. Behfar, A. Ezabadi, H. Zolfagharian and M. Heydari, *Nanomedicine (Lond)*, **2010**, 6, 137.

332. X. Feng, G. E. Fryxell, L.-Q. Wang, A. Y. Kim, J. Liu and K. M. Kemner, *Science*, **1997**, 276, 923.

333. R. S. McDonald, *J Phys Chem*, **1958**, 62, 1168.

334. V. Marjanović, S. Lazarević, I. Janković-Častvan, B. Potkonjak, Đ. Janaćković and R. Petrović, *Chem Eng J*, **2011**, 166, 198.

335. P. Bladon, *Org Magn Reson*, **1969**, 1, 277.

336. R. M. Silverstein and F. X. Webster, *Spectrometric Identification of Organic Compounds, Wiley Student Edition*, **2005**.

337. W. D. Harkins and G. Jura, *J. Amer. Chem. Soc.*, **1944**, 66, 603

338. R. G. Pearson, *J Am Chem Soc*, **1963**, 85, 3533.

339. S. V. Mattigod, G. E. Fryxell and K. E. Parker, *Environmental Applications of Nanomaterials: synthesis, sorbents and sensors, Imperial College Press*, **2007**, 275.

340. B. Agula, T. Z. Ren, X. Zhao, B. Zhaorigetu and Z. Y. Yuan, *J Nat Gas Chem*, **2011**, 20, 232.

341. P. A. Deshpande and G. Madras, *Chem Eng J*, **2010**, 158, 571.

342. S. Mahapatra, R. Vinu, T. N. G. Row and G. Madras, *App Cat A: General*, **2008**, 351, 45.

343. H. Fuess and A. Kallel, *J. Solid State Chem*, 1972, 5, 11.

344. S. Mahapatra, G. Madras and T. N. Guru Row, *Ind Eng Chem Res*, **2007**, 46, 1013.

345. M. D. Guo, A. T Aldred and S. K. Chan, *J Phys Chem Solids*, **1987**, 48, 229.

346. U. Kolitsch and D. Holtstam, *Eur J Mineral*, **2004**, 16, 117.

347. Y. Hirano, N. Wakabayashi, C.-K. Loong and L. A. Boatner, *Phys Rev B*, **2003**, 67, 014423.

348. L. H. Mason, J. P. Harp and D. Y. Han, *Bio Med Res Inter*, **2014**, DOI: doi:10.1155/2014/840547.

349. M. M. Khin, A. S. Nair, V. J. Babu, R. Murugan and S. Ramakrishna, *Energy Environ Sci*, **2012**, 5, 8075.

350. A. Singh, D. P. Dutta, J. Ramkumar, K. Bhattacharya, A. K. Tyagi and M. H. Fulekar, *RSC Adv*, **2013**, 3, 22580.

351. Jerina Majeed, Jayshree Ramkumar, S. Chandramouleeswaran, O. D. Jayakumar and A. K. Tyagi, *RSC Adv,* **2013**, 3, 3365.

352. Jayshree Ramkumar, S. Chandramouleeswaran, B. S. Naidu and V. Sudarsan, *J Radioanal Nucl Chem*, **2013**, 298, 1845.

353. T. Yousefi, A. R. Khanchi, S. J. Ahmadi, M. K. Rofouei, R. Yavari, R. Davarkhah and B. Myanji, *J Hazard Mater*, **2012**, 215.

354. R. D. Shannon, *Acta Cryst B*, **1976**, A32.

355. P. Porta, N. Franceschini and G. Minelli, *Mater Chem Phys*, **2001**, 70, 17.

356. M. Cesari, G. Perego, A. Zazzetta, G. Manara and B. Notari, *J Inorg Nucl Chem*, **1971**, 33, 3595.

357. D. Briggs and M. P. Seah, *Practical Surface Analysis*, John Wiley and Sons, **1987**.

358. B.A. Reddy, A. Khan, Y. Yamada, T. Kobayashi, S. Loridant and J.C. Volta, *J Phys Chem B*, **2002**, 106, 10964.

359. J. F. Moulder, W. F. Stickle, P. E. Sobol and K. D. Bomben, *Handbook of X-Ray Photoelectron Spectroscopy*, **1995**.

360. A. Pfau and K. D. Schierbaum, *Surf Sci*, **1994**, 321**,** 71.

361. D. Marrocchelli, S. R. Bishop, H. L. Tuller, G. W. Watson and B. Yildiz, *Phys Chem Chem Phys*, 2012, 14.

362. C. Banerjee, N. Dudwadkar, S. C. Tripathi, P. M. Gandhi, V. Grover, C. P. Kaushik and A. K. Tyagi, *J Hazard Mater*, **2014**, 280, 63.

363. Y. H. Zheng, C. Q. Chen, Y. Y. Zhan, X. Y. Lin, Q. Zheng, K. M. Wei, J. F. Zhu and Y. J. Zhu, *Inorg Chem*, **2007**, 46, 6675.

364. C. Scherdel, G. Reichenauer and M. Wiener, *Micro Meso Mater*, **2010**, 132, 572.

365. T. K. Naiya, A. K. Bhattacharya and S. K. Das, *J Colloid Interface Sci*, **2009**, 333, 14.

366. Z. Wu, Z. Gu, X. Wang, L. Evans and H. Guo, *Environ Pollut*, **2003**, 121, 469.

367. Y.-H. Huang, C.-L. Hsueh, C.-P. Huang, L.-C. Su and C.-Y. Chen, *Sep Purif Technol*, **2007**, 55, 23.

368. S.-G. Wang, W.-X. Gong, X.-W. Liu, Y.-W. Yao, B.-Y. Gao and Q.-Y. Yue, *Sep Purif Technol*, **2007**, 58, 17.

369. Y. Ni, K. Mi, C. Cheng, J. Xia, X. Ma and J. Hong, *Chem Commun*, **2011**, 47, 5891.

370. X. Wang, X. Yang, J. Cai, T. Miao, L. Li, G. Li, D. Deng, L. Jiang and C. Wang, *J Mater Chem A*, **2014**, 2, 6718.

371. *Guidelines for Drinking-Water Quality*, **2008**.

372. *National Recommended Water Quality Criteria*, **2006**.

373. J. S. Liu, L. Song and G. Q. Shao, *J Chem Eng Data*, **2011**, 56, 2119.

374. P. Kijjanapanich, A. P. Annachhatre, G. Esposito and P. N. Lens, *Environ Technol*, **2014**, 35, 1989.

375. D. Claveau-Mallet, B. Courcelles and Y. Comeau, *Environ Sci Technol*, **2014**, 48, 7486.

376. T. Zhang, K. Gregory, R. W. Hammack and R. D. Vidic, *Environ Sci Technol*, **2014**, 48, 4596.

377. A. Dabrowski, Z. Hubicki, P. Podkoscielny and E. Robens, *Chemosphere*, **2004**, 56, 91.

378. R. S. Juang, S. H. Lin and T. Y. Wang, *Chemosphere*, **2003**, 53, 1221.

379. C. Blocher, J. Dorda, V. Mavrov, H. Chmiel, N. K. Lazaridis and K. A. Matis, *Water Res*, **2003**, 37, 4018.

380. M. M. Khin, A. S. Nair, V. J. Babu, R. Murugan and S. Ramakrishna, *Energy Environ Sci*, **2012**, 5, 8075.

381. M. Hua, S. Zhang, B. Pan, W. Zhang, L. Lv and Q. Zhang, *J Hazard Mater*, **2012**, 211–212, 317.

382. H. Matsuda, T. Ito, D. Kuchar, N. Tanahashi and C. Watanabe, *Chemosphere*, **2009**, 74, 1348.

383. K. Singh, A. Ohlan, V. H. Pham, B. R, S. Varshney, J. Jang, S. H. Hur, W. M. Choi, M. Kumar, S. K. Dhawan, B. S. Kong and J. S. Chung, *Nanoscale*, **2013**, 5, 2411.

384. J. D. Ostergren, J. R. Bargar, G. E. Brown, Jr. and G. A. Parks, *J Synchrotron Radiat*, **1999**, 6, 645.

385. J. D. Ostergren, G. E. Brown, Jr., G. A. Parks and P. Persson, *J Colloid Interface Sci*, **2000**, 225, 483.

386. Z. Bacsik, N. Ahlsten, A. Ziadi, G. Zhao, A. E. Garcia-Bennett, B. Martin-Matute and N. Hedin, *Langmuir*, **2011**, 27, 11118.

387. J. Chung, J. Chun, J. Lee, S. H. Lee, Y. J. Lee and S. W. Hong, *J Hazard Mater*, **2012**, 239-240, 183.

388. M. L. Kim and M. B. Tudino, *Talanta*, **2010**, 82, 923.

389. L. Cui, X. Guo, Q. Wei, Y. Wang, L. Gao, L. Yan, T. Yan and B. Du, *J Colloid Interface Sci*, **2015**, 439, 112.

390. G. Liu, Y. Wang, L. Jiao and H. Yuan, *ACS Appl Mater Interfaces*, **2014**, 6, 11038.

391. A. S. Moscofian and C. Airoldi, *J Hazard Mater*, **2008**, 160, 63.

392. M. N. Luwang, R. S. Ningthoujam, S. K. Srivastava and R. K. Vatsa, *J Mater Chem*, **2011**, 21, 5326.

393. J. Ramkumar, S. Chandramouleeswaran, V. Sudarsan, R. K. Mishra, C. P. Kaushik, K. Raj, T. Mukherjee and A. K. Tyagi, *J Hazard Mater*, **2008**, 154, 513.

394. J. Sobkowski and A. Czerwiński, *J Electroanal Chem Interfacial Electrochem*, **1974**, 55, 391.

395. M. R. Hoffmann, S. T. Martin, W. Choi and D. W. Bahnemann, *Chem Rev*, **1995**, 95, 69.

396. M. Kitano, M. Matsuoka, M. Ueshima and M. Anpo, *App Cata, A*, **2007**, 325, 1.

397. B. O’Regan and M. Grätzel, *Nature*, **1991**, 353, 737.

398. A. L. Linsebigler, G. Lu and J. T. Yates, *Chem Rev*, **1995**, 95, 735.

399. O. Carp, C. L. Huisman and A. Reller, *Prog Solid State Chem*, **2004**, 32, 33.

400. A. Fujishima, T. N. Rao and D. A. Tryk, *J. Photochem Photobio, C*, **2000**, 1, 1.

401. A. Fujishima, X. Zhang and A. D, *Surf Sci Rep*, **2008**, 63, 515.

402. F. Bregani, C. Casale, L. E. Depero, I. Natali-Sora, D. Robba, L. Sangaletti and G. P. Toledo, *Sens Actuators, B*, **2004**, 31, 25.

403. A. Kubacka, G. Colón and M. Fernández-García, *Catal Today*, **2009**, 143, 286.

404. N. U. Silva, T. G. Nunes, M. S. Saraiv, M. S. Shalamzari, P. D. Vaz, O. C. Monteiro and C. D. Nunes, *Appl Catal, B*, **2012**, 113– 114, 180.

405. Y. X. Li, J. Chen and L. Wang, *J Photochem Photobiol A*, **2004**, 163, 517.

406. K. Tan, H. Zhang, C. Xie, H. Zheng, Y. Gu and W. F. Zhang, *Catal Commun*, **2000**, 11, 331.

407. V. Štengl and S. Bakardjieva, *J Phys Chem C*, **2010**, 114, 19308.

408. L. Gomathi Devi, S. G. Kumar, B. Narasimha Murthy and N. Kottam, *Catal Commun*, **2009**, 10, 794.

409. L. Gomathi Devi and B. Narasimha Murthy, *Catal Lett*, **2008**, 125, 320.

410. L. Gomathi Devi, B. Narasimha Murthy and S. G. Kumar, *Chemosphere*, **2009**, 76, 1163.

411. K. Y. Song, M. K. Park, Y. T. Kwon, H. W. Lee, W. J. Chung and W. I. Lee, *Chem Mater*, **2001**, 13, 2349.

412. L. Ayed, K. Chaieb, A. Cheref and A. Bakhrouf, *World J Microbiol Biotechnol*, **2009**, 25, 705.

413. K. N. Vinod, T. K. Puttaswamy and N. N. Gowda, *J Mol Catal A: Chem*, **2009**, 298, 60.

414. C. Chen and C. S. Lu, *Environ Sci Technol*, **2007**, 41, 4389.

415. H. Park and W. Choi, *J Phys Chem B*, **2005**, 109, 11667.

416. T. Wu, G. Liu, J. Zhao, H. Hidaka and N. Serpone, *J Phys Chem B*, **1998**, 102, 5845.

417. N. Banwell and E. M. McCash, *Fundamentals of Molecular Spectroscopy*, **1994**.

418. L. Seguin, M. Figlarz, I. R. Cavagnat and J. C. Lasskgues, *Spectrochim Acta, Part A*, **1995**, 51, 1323.

419. T. Ohsaka, F. Izumi and Y. Fujiki, *J Raman Spectrosc*, **1978**, 7, 321.

420. Y. H. Zhang, C. K. Chan, J. F. Porter and W. Guo, *J Mater Res*, **1998**, 13, 2602.

421. G. Busca, G. Ramis, J. M. G. Amores, V. S. Escribano and P. Piaggio, *J Chem Soc: Faraday Trans*, **1994**, 90, 3181.

422. S. Kelly, F. H. Pollak and M. Tomkiewicz, *J Phys Chem B*, **1997**, 101, 2730.

423. A. Kubacka, M. Fernández-García and G. Colónb, *J Catal*, **2008**, 254, 272.

424. X. Gao and I. E. Wachs, *Catal Today*, **1999**, 51, 233.

425. Y. H. Hsien, C. F. Chang, Y. H. Chen and S. Cheng, *Appl Catal: B*, **2001**, 31, 241.

426. L. Tuel and G. Hubert-Pfalzgraf, *J Catal*, **2003**, 217, 343.

427. M. R. Tubbs, *Phys Status Solidi A*, **1974**, 21, 253.

428. S. K. Deb and J. A. Chopoorian, *J Appl Phys*, **1966**, 37, 4818.

429. O. F. Schirmer, V. Wittwer, G. Baur and G. Brandt, *J Electrochem Soc*, **1977**, 124, 749.

430. P. Kubelka and F. Munk-Aussig, *Z Techn Phys*, **1931**, 12, 593.

431. A. Kubacka, M. Fernandez Garcia and G. Colónb, *Chem Rev*, **2012**, 112, 1555.

432. P. M. Kumar, S. Badrinarayanan and M. Sastry, *Thin Solid Films*, **2000**, 358, 122.

433. P. A. Bertrand, *J Vac Sci Technol*, **1981**, 18, 28.

434. A. Gutierrez and B. T. Johansson, *Phys Rev B*, **2001**, 65, 1.

435. S. Zhang, S. B. Ogale, W. Yu, X. Gao, T. Liu, S. Ghosh, G. P. Das, A. T. S. Wee, R. L. Greene and T. Venkatesan, *Adv Mater*, **2009**, 21, 2282.

436. V. A. Alyoshin, I. P. Romanova, D. Mikhailova, S. Oswald, A. Senyshyn and H. Ehrenberg, *J Phys Chem A*, **2010**, 114, 13362.

437. K. Kollbek, M. Sikora, C. Kapusta, J. Szlachetko, K. Zakrzewska, K. Kowalski and M. Radecka, *Appl Surf Sci*, **2013**, 281, 100.

438. N. V. Kosova, V. V. Kaichev, V. I. Bukhtiyarov, D. G. Kellerman, E. T. Devyatkina and T. V. Larina, *J Power Sources*, **2003**, 119–121, 669.

439. N. A. Merino, B. P. Barbero, P. Eloy and L. E. Cadus, *Appl Surf Sci*, **2006**, 253, 1489.

440. S. Oswald and W. Brückner, *Surf Interface Anal*, **2004**, 36, 17.

441. K. Tabata, Y. Hirano and E. Suzuki, *Appl Catal: A*, **1998**, 170, 245.

442. T. Watanabe, T. Takizawa and K. Honda, *J Phys Chem*, **1977**, 81, 1845.

443. T. Albaret, F. Finocchi and C. Noguera, *Faraday Discuss*, **2000**, 114, 285.

444. B. M. Reddy, B. Chowdhury and P. G. Smirniotis, *Appl Catal: A*, **2001**, 211, 19.

445. J. A. Rodriguez and A. Maiti, *J Phys Chem B*, **2000**, 104, 3630.

446. T. Bredow, E. Apra, M. Catti and G. Pacchioni, *Surf Sc.*, **1998**, 418, 150.

447. M. Casarin, C. Maccato and A. Vittadini, *Surf Sci*, **1997**, 377–379, 587.

448. M. J. Potrzebowski, J. Blaszczyk, M. W. Wieczorek and J. Klinowski, *J Chem Phys*, **1999**, 101, 8077.

449. K. Fajans, *Naturwissenschaften*, **1923**, 11, 165.

450. K. Fajans, *Z Kristallogr.*, **1925**, 61, 18.

451. K. Fajans and G. Joos, *Z Phys*, **1924**, 23, 1.

452. J. Li, W. Ma, P. Lei and J. Zhao, *J Environ Sci*, **2007**, 19, 892.

453. G. Liu and J. Zhao, *New J Chem*, **2000**, 24, 411.

454. S. Yu, H. Yang, C. He, C. Sun and Y. Ju, *J Phys Chem A*, **2009**, 113, 10024.

455. H. Fu, C. Pan, W. Yao and Y. Zhu, *J Phys Chem B*, **2005**, 109, 22432.

456. C. A. Scamehorn, N. M. Harrison and M. I. McCarthy, *J Chem Phys*, **1994**, 101, 1547.

457. R. E. Dawson, A. Hennig, D. P. Weimann, D. Emery, V. Ravikumar, J. Montenegro, T. Takeuchi, S. Gabutti, M. Mayor and J. Mareda, *Nat Chem*, **2010**, 2, 533.

458. Z. Cheng, Y. Dai, X. Kang, C. Li, S. Huang, H. Lian, Z. Hou, P. Ma and J. Lin, *Biomaterials*, **2014**, 35, 6359.

459. X. Liu, I. Marangon, G. Melinte, C. Wilhelm, C. Menard-Moyon, B. P. Pichon, O. Ersen, K. Aubertin, W. Baaziz, C. Pham-Huu, S. Begin-Colin, A. Bianco, F. Gazeau and D. Begin, *ACS Nano*, **2014**, 8, 11290.

460. Y. Tsukasaki, A. Komatsuzaki, Y. Mori, Q. Ma, Y. Yoshioka and T. Jin, *Chem Commun (Camb)*, **2014**, 50, 14356.

461. L. Wang, J. Liu, Y. Dai, Q. Yang, Y. Zhang, P. Yang, Z. Cheng, H. Lian, C. Li, Z. Hou, P. Ma and J. Lin, *Langmuir*, **2014**, 30, 13042.

462. X. Zhu, Y. Ma, C. Zhao, Z. Lin, L. Zhang, R. Chen and W. Yang, *Langmuir*, **2014**, 30, 15229.

463. N. Erathodiyil and J. Y. Ying, *Acc Chem Res*, **2011**, 44, 925.

464. M. Mahmoudi, H. Hosseinkhani, M. Hosseinkhani, S. Boutry, A. Simchi, W. S. Journeay, K. Subramani and S. Laurent, *Chem Rev*, **2011**, 111, 253.

465. A. I. Prasad, A. K. Parchur, R. R. Juluri, N. Jadhav, B. N. Pandey, R. S. Ningthoujam and R. K. Vatsa, *Dalton Trans*, **2013**, 42, 4885.

466. H. Amiri, M. Mahmoudi and A. Lascialfari, *Nanoscale*, **2011**, 3, 1022.

467. Y. Jin, C. Jia, S. W. Huang, M. O'Donnell and X. Gao, *Nat Commun*, **2010**, 1, 41.

468. Y. Zhang, N. Kohler and M. Zhang, *Biomaterials*, **2002**, 23, 1553.

469. C. Yi, L. Liu, C. W. Li, J. Zhang and M. Yang, *Mater Sci Eng C Mater Biol Appl*, **2015**, 46, 32.

470. A. L. Morel, S. I. Nikitenko, K. Gionnet, A. Wattiaux, J. Lai-Kee-Him, C. Labrugere, B. Chevalier, G. Deleris, C. Petibois, A. Brisson and M. Simonoff, *ACS Nano*, **2008**, 2, 847.

471. C. S. Lee, H. H. Chang, P. K. Bae, J. Jung and B. H. Chung, *Macromol Biosci*, **2013**, 13, 321.

472. R. Bakalova, Z. Zhelev, D. Kokuryo, L. Spasov, I. Aoki and T. Saga, *Int J Nanomedicine*, **2011**, 6, 1719.

473. H. Yang, Y. Zhuang, Y. Sun, A. Dai, X. Shi, D. Wu, F. Li, H. Hu and S. Yang, *Biomaterials*, **2011**, 32, 4584.

474. X. L. Liu, H. M. Fan, J. B. Yi, Y. Yang, E. S. G. Choo, J. M. Xue, D. D. Fan and J. Ding, *J Mater Chem*, **2012**, 22, 8235.

475. G. H. Du, Z. L. Liu, X. Xia, Q. Chu and S. M. Zhang, *JSol-Gel SciTechnol,***2006**, 39, 285.

476. M. N. Luwang, R. S. Ningthoujam, S. K. Srivastava and R. K. Vatsa, *J Mater Chem*, **2011**, 21, 5326.

477. R. N. Panda, N. S. Gajbhiye and G. Balaji, *J Alloys Compd*, **2001**, 326, 50.

478. C. N. Chinnasamy, A. Narayanasamy, N. Ponpandian, K. Chattopadhyay, H. Guérault and J. M. Greneche, *J Phys: Condens Matter*, **2000**, 12, 7795.

479. B. D. Cullity, *Introduction to magnetic materials*, Addison-Wesley Pub. Co., **1972**.

480. R. Ghosh, L. Pradhan, Y. P. Devi, S. S. Meena, R. Tewari, A. Kumar, S. Sharma, N. S. Gajbhiye, R. K. Vatsa, B. N. Pandey and R. S. Ningthoujam, *J Mater Chem*, **2011**, 21, 13388.

481. K. C. Barick and P. A. Hassan, *J Colloid Interface Sci*, **2012**, 369, 96.

482. K. C. Barick, S. Singh, N. V. Jadhav, D. Bahadur, B. N. Pandey and P. A. Hassan, *Adv Funct Mater*, **2012**, 22, 4975.

483. J. P. Fortin, C. Wilhelm, J. Servais, C. Menager, J. C. Bacri and F. Gazeau, *J Am Chem Soc*, **2007**, 129, 2628.

484. B. Samanta, H. Yan, N. O. Fischer, J. Shi, D. J. Jerry and V. M. Rotello, *J Mater Chem*, **2008**, 18, 1204.

485. A. K. Gupta and M. Gupta, *Biomaterials*, **2005**, 26, 3995.

486. J. Cheon and J. H. Lee, *Acc Chem Res*, **2008**, 41, 1630.

487. C. Boyer, M. R. Whittaker, V. Bulmus, J. Liu and T. P. Davis, *NPG Asia Mater*, **2010**, 2, 23.

488. J. Majeed, L. Pradhan, R. S. Ningthoujam, R. K. Vatsa, D. Bahadur and A. K. Tyagi, *Colloids Surf B Biointerfaces*, **2014**, 122, 396.

489. Y.-K. Peng, C. N. P. Lui, T.-H. Lin, C. Chang, P.-T. Chou, K. K. L. Yung and S. C. E. Tsang, *Faraday Discuss*, **2014**, DOI: 10.1039/C4FD00132J.

490. M. Das, D. Mishra, P. Dhak, S. Gupta, T. K. Maiti, A. Basak and P. Pramanik, *Small*, **2009**, 5, 2883.

491. D. Portet, B. Denizot, E. Rump, J. J. Lejeune and P. Jallet, *J Colloid Interface Sci*, **2001**, 238, 37.

492. Y. Sahoo, H. Pizem, T. Fried, D. Golodnitsky, L. Burstein, C. N. Sukenik and G. Markovich, *Langmuir*, **2001**, 17, 7907.

493. J. Wang, C. Gong, Y. Wang and G. Wu, *Colloids Surf B Biointerfaces*, **2014**, 118, 218.

494. S. Nigam, S. Chandra, D. F. Newgreen, D. Bahadur and Q. Chen, *Langmuir*, **2014**, 30, 1004.

495. J. Xie, K. Chen, H. Y. Lee, C. Xu, A. R. Hsu, S. Peng, X. Chen and S. Sun, *J Am Chem Soc*, **2008**, 130, 7542.

496. M. Gogoi, H. D. Sarma, D. Bahadur and R. Banerjee, *Nanomedicine (Lond)*, **2014**, 9, 955.

497. K. Yan, H. Li, P. Li, H. Zhu, J. Shen, C. Yi, S. Wu, K. W. Yeung, Z. Xu, H. Xu and P. K. Chu, *Biomaterials*, **2014**, 35, 344.

498. C. Tudisco, F. Bertani, M. T. Cambria, F. Sinatra, E. Fantechi, C. Innocenti, C. Sangregorio, E. Dalcanale and G. G. Condorelli, *Nanoscale*, **2013**, 5, 11438.

499. K. Loster, S. Seidel, D. Kirstein, F. Schneider and F. Noll, *J Immunol Methods*, **1992**, 148, 41.

500. N. N. Rao, M. R. Gomez-Garcia and A. Kornberg, *Annu Rev Biochem*, **2009**, 78, 605.

501. R. Palmeira-de-Oliveira, A. Palmeira-de-Oliveira, C. Gaspar, S. Silvestre, J. Martinez-de-Oliveira, M. H. Amaral and L. Breitenfeld, *Int J Pharm*, **2011**, 421, 130.

502. S. Vimal, S. Abdul Majeed, G. Taju, K. S. Nambi, N. Sundar Raj, N. Madan, M. A. Farook, T. Rajkumar, D. Gopinath and A. S. Sahul Hameed, *Acta Trop*, **2013**, 128, 486.

503. K. Konecsni, N. H. Low and M. T. Nickerson, *Food Chem*, **2012**, 134, 1775.

504. S. Tripathy, S. Das, S. P. Chakraborty, S. K. Sahu, P. Pramanik and S. Roy, *Int J Pharm*, **2012**, 434, 292.

505. C. Yee, G. Kataby, A. Ulman, T. Prozorov, H. White, A. King, M. Rafailovich, J. Sokolov and A. Gedanken, *Langmuir*, **1999**, 15, 7111.

506. G. Lamanna, M. Kueny-Stotz, H. Mamlouk-Chaouachi, C. Ghobril, B. Basly, A. Bertin, I. Miladi, C. Billotey, G. Pourroy, S. Begin-Colin and D. Felder-Flesch, *Biomaterials*, **2011**, 32, 8562.

507. J. Auernheimer, D. Zukowski, C. Dahmen, M. Kantlehner, A. Enderle, S. L. Goodman and H. Kessler, *ChemBioChem*, **2005**, 6, 2034.

508. J. Usui, I. G. Glezerman, S. P. Salvatore, C. B. Chandran, C. D. Flombaum and S. V. Seshan, *Hum Pathol*, **2014**, 45, 1918.

509. G. Xie, H. Wang, Z. Yan, L. Cai, G. Zhou, W. He, R. Paus and Z. Yue, *J Invest Dermatol*, **2015**, 135, 690.

510. G. M. Shepherd, *Clin Rev Allergy Immunol*, **2003**, 24, 253.

511. B. G. Peters, *Top Hosp Pharm Manage*, **1994**, 14, 59.

512. M. A. Moses, H. Brem and R. Langer, *Cancer Cell*, **2003**, 4, 337.

513. Z. S. Al-Ahmady, O. Chaloin and K. Kostarelos, *J Control Release*, **2014**, 196, 332.

514. S. T. Heijkoop, H. C. van Doorn, L. J. Stalpers, I. A. Boere, J. van der Velden, M. Franckena and A. M. Westermann, *Int J Hyperthermia*, **2014**, 30, 6.

515. Z. Liang, X. Li, Y. Xie and S. Liu, *Biomed Mater*, **2014**, 9, 025012.

516. G. M. Hahn, J. Braun and I. Har-Kedar, *Proc Natl Acad Sci U S A*, **1975**, 72, 937.

517. P. Sharma, S. Rana, K. C. Barick, C. Kumar, H. G. Salunke and P. A. Hassan, *New J Chem*, **2014**, 38, 5500.

518. W. Yang, J. Fu, T. Wang and N. He, *J Biomed Nanotechnol*, **2009**, 5, 591.

519. W. Jastrzebski, M. Sitarz, M. Rokita and K. Bulat, *Spectrochim Acta A Mol Biomol Spectrosc*, **2011**, 79, 722.

520. A. Michelmore, W. Gong, P. Jenkins and J. Ralston, *Phys Chem Chem Phys*, **2000**, 2, 2985.

521. P. J. van der Zaag, Y. Ijiri, J. A. Borchers, L. F. Feiner, R. M. Wolf, J. M. Gaines, R. W. Erwin and M. A. Verheijen, *Phys Rev Lett*, **2000**, 84, 6102.

522. S. Chandra, S. Mehta, S. Nigam and D. Bahadur, *New J Chem*, **2010**, 34, 648.

523. M. Kilianova, R. Prucek, J. Filip, J. Kolarik, L. Kvitek, A. Panacek, J. Tucek and R. Zboril, *Chemosphere*, **2013**, 93, 2690.

524. Y. Lai, W. Yin, J. Liu, R. Xi and J. Zhan, *Nanoscale Res Lett*, **2009**, 5, 302.

525. R. Hergt, R. Hiergeist, I. Hilger, W. A. Kaiser, Y. Lapatnikov, S. Margel and U. Richter, *J Magn MagnMater*, **2004**, 270, 345.

526. J.-P. Fortin, C. Wilhelm, J. Servais, C. Ménager, J.-C. Bacri and F. Gazeau, *J Am Chem Soc*, **2007**, 129, 2628.

527. Y. Zhu, T. Ikoma, N. Hanagata and S. Kaskel, *Small*, **2010**, 6, 471.

528. L. Li, F. Tang, H. Liu, T. Liu, N. Hao, D. Chen, X. Teng and J. He, *ACS Nano*, **2010**, 4, 6874.

529. G. Helmlinger, F. Yuan, M. Dellian and R. K. Jain, *Nat Med*, **1997,** 3, 177.

530. D. Depan and R. D. Misra, *Nanoscale*, **2012**, 4, 6325.

531. S. K. Yen, D. Janczewski, J. L. Lakshmi, S. B. Dolmanan, S. Tripathy, V. H. Ho, V. Vijayaragavan, A. Hariharan, P. Padmanabhan, K. K. Bhakoo, T. Sudhaharan, S. Ahmed, Y. Zhang and S. Tamil Selvan, *ACS Nano*, **2013**, 7, 6796.

532. M. S. Martina, J. P. Fortin, L. Fournier, C. Menager, F. Gazeau, O. Clement and S. Lesieur, *Mol Imaging*, **2007**, 6, 140.

533. A. Figuerola, A. Fiore, R. Di Corato, A. Falqui, C. Giannini, E. Micotti, A. Lascialfari, M. Corti, R. Cingolani, T. Pellegrino, P. D. Cozzoli and L. Manna, *J Am Chem Soc*, **2008**, 130, 1477.

534. J. S. Choi, Y. W. Jun, S. I. Yeon, H. C. Kim, J. S. Shin and J. Cheon, *J Am Chem Soc*, **2006**, 128, 15982.

535. L. C. Varanda and M. Jafelicci, Jr., *J Am Chem Soc*, **2006**, 128, 11062.

536. L. E. Howard, H. L. Nguyen, S. R. Giblin, B. K. Tanner, I. Terry, A. K. Hughes and J. S. Evans, *J Am Chem Soc*, **2005**, 127, 10140.

537. X. Teng and H. Yang, *J Am Chem Soc*, **2003**, 125, 14559.

538. Y. Jin, F. Ye, M. Zeigler, C. Wu and D. T. Chiu, *ACS Nano*, **2011**, 5, 1468.

539. D. Janczewski, Y. Zhang, G. K. Das, D. K. Yi, P. Padmanabhan, K. K. Bhakoo, T. T. Tan and S. T. Selvan, *Microsc Res Tech*, **2011**, 74, 563.

540. J. Contreras, J. Xie, Y. J. Chen, H. Pei, G. Zhang, C. L. Fraser and S. F. Hamm-Alvarez, *ACS Nano*, **2010**, 4, 2735.

541. J. Herz, V. Siffrin, A. E. Hauser, A. U. Brandt, T. Leuenberger, H. Radbruch, F. Zipp and R. A. Niesner, *Biophys J*, **2010**, 98, 715.

542. M. A. Walling, J. A. Novak and J. R. Shepard, *Int J Mol Sci*, **2009**, 10, 441.

543. X. Gao and S. R. Dave, *Adv Exp Med Biol*, **2007**, 620, 57.

544. T. M. Samir, M. M. Mansour, S. C. Kazmierczak and H. M. Azzazy, *Nanomedicine (Lond)*, **2012**, 7, 1755.

545. H. M. Azzazy, M. M. Mansour and S. C. Kazmierczak, *Clin Biochem*, **2007**, 40, 917.

546. W. Liu, Z. He, J. Liang, Y. Zhu, H. Xu and X. Yang, *J Biomed Mater Res A*, **2008**, 84, 1018.

547. W. L. Ong, H. Huang, J. Xiao, K. Zeng and G. W. Ho, *Nanoscale*, **2014**, 6, 1680.

548. S. B. Ogale, *Adv Mater*, **2010**, 22, 3125.

549. D. A. Schwartz, N. S. Norberg, Q. P. Nguyen, J. M. Parker and D. R. Gamelin, *J Am Chem Soc*, **2003**, 125, 13205.

550. G. L. Song, *Guang Pu Xue Yu Guang Pu Fen Xi*, **2007**, 27, 2409.

551. J. Hays, K. M. Reddy, N. Y. Graces, M. H. Engelhard, V. Shutthanandan, M. Luo, C. Xu, N. C. Giles, C. Wang, S. Thevuthasan and A. Punnoose, *J Phys Condens Matter*, **2007**, 19, 266203.

552. H. Pan, Z. Ni, H. Sun, Z. Yong, Y. Feng, W. Ji, Z. Shen, A. T. Wee and J. Lin, *J Nanosci Nanotechnol*, **2006**, 6, 2529.

553. T. S. Herng, M. F. Wong, D. Qi, J. Yi, A. Kumar, A. Huang, F. C. Kartawidjaja, S. Smadici, P. Abbamonte, C. Sanchez-Hanke, S. Shannigrahi, J. M. Xue, J. Wang, Y. P. Feng, A. Rusydi, K. Zeng and J. Ding, *Adv Mater*, **2011**, 23, 1635.

554. I. Kaminska, B. Sikora, K. Fronc, P. Dziawa, K. Sobczak, R. Minikayev, W. Paszkowicz and D. Elbaum, *J Phys Condens Matter*, **2013**, 25, 194105.

555. O. D. Jayakumar, V. Sudarsan, K. Shashikala, C. Sudakar, R. Naik, R. K. Vatsa and A. K. Tyagi, *J Nanosci Nanotechnol*, **2011**, 11, 3273.

556. O. D. Jayakumar, S. N. Achary, C. Sudakar, R. Naik, H. G. Salunke, R. Rao, X. Peng, R. Ahuja and A. K. Tyagi, *Nanoscale*, **2010**, 2, 1505.

557. S. W. Hwang, D. H. Shin, C. O. Kim, S. H. Hong, M. C. Kim, J. Kim, K. Y. Lim, S. Kim, S. H. Choi, K. J. Ahn, G. Kim, S. H. Sim and B. H. Hong, *Phys Rev Lett*, **2010**, 105, 127403.

558. T. Zhou, M. Lu, Z. Zhang, H. Gong, W. S. Chin and B. Liu, *Adv Mater*, **2010**, 22, 403.

559. M. Lu, H. Gong, T. Song, J.-P. Wang, H.-W. Zhang and T. J. Zhou, *JMagn Magn Mater*, **2006**, 303, 323.

560. P. M. Winkler, G. Steiner, A. Vrtala, H. Vehkamaki, M. Noppel, K. E. Lehtinen, G. P. Reischl, P. E. Wagner and M. Kulmala, *Science*, **2008**, 319, 1374.

561. L. Liu, J. Guan, W. Shi, Z. Sun and J. Zhao, *JPhysChem C*, **2010**, 114, 13565.

562. J. Ye, Q.-W. Chen, H.-P. Qi and N. Tao, *Cryst Growth Des*, **2008**, 8, 2464.

563. R. Buonsanti, V. Grillo, E. Carlino, C. Giannini, F. Gozzo, M. Garcia-Hernandez, M. A. Garcia, R. Cingolani and P. D. Cozzoli, *J Am Chem Soc*, **2010**, 132, 2437.

564. H. J. Joyce, J. Wong-Leung, Q. Gao, H. H. Tan and C. Jagadish, *Nano Lett*, **2010**, 10, 908.

565. J. B. Staunton, S. Ostanin, S. S. Razee, B. L. Gyorffy, L. Szunyogh, B. Ginatempo and E. Bruno, *Phys Rev Lett*, **2004**, 93, 257204.

566. Z. L. Wang, *JPhysChemB*, **2000**, 104, 1153.

567. M. Li, G. Xing, L. F. Qune, G. Xing, T. Wu, C. H. Huan, X. Zhang and T. C. Sum, *Phys Chem Chem Phys*, **2012**, 14, 3075.

568. C. H. Ahn, Y. Y. Kim and H. K. Cho, *J Nanosci Nanotechnol*, **2011**, 11, 458.

569. X. L. Chen, C. S. Xu, Y. X. Liu, H. Q. Qiao, H. T. Xu, Y. H. Ning and Y. C. Liu, *J Nanosci Nanotechnol*, **2010**, 10, 2185.

570. K. Black, A. C. Jones, I. Alexandrou, P. N. Heys and P. R. Chalker, *Nanotechnology*, **2010**, 21, 045701.

571. J. A. Kim, I. K. Kim, T. W. Kim, J. H. Moon and J. H. Kim, *J Nanosci Nanotechnol*, **2008**, 8, 5485.